BIOGENESIS OF THE NEOPROTEROZOIC KREMYDILITE MANGANESE ORES FROM URUCUM (BRAZIL) – A NEW MANGANESE ORE TYPE.

Running title: Biogenesis of a Neoproterozoic manganese ore

João Carlos Biondi[1+], Márta Polgári[2,3*+], Ildikó Gyollai[2], Krisztián Fintor[4], Ivett Kovács[2], József Fekete[2], Stephen J. Mojzsis[2,5*]

[1]*Federal University of Paraná State, Polytechnic Center, Geology Department, 81531-980 Curitiba, Brazil, e-mail: biondiufpr@gmail.com*

[2]*Institute for Geological and Geochemical Research, RCAES, Hungarian Academy of Sciences, 1112 Budapest, Budaörsi u. 45, Hungary, e-mail: rodokrozit@gmail.com, gyildi@gmail.com, iv.kovacs@gmail.com, fekete.jozsef@csfk.mta.hu*

[3]*Eszterházy Károly University, Dept. of Natural Geography and Geoinformatics, 3300 Eger, Leányka u. 6, Hungary*

[4]*Szeged University, Dept. of Mineralogy, Geochemistry and Petrology, 6722 Szeged, Egyetem u. 2-6, Hungary, e-mail: efkrisz@gmail.com*

[5]*University of Colorado, Department of Geological Sciences, 2200 Colorado Avenue, UCB 399, Boulder, Colorado 80309-0399, United States of America, e-mail: mojzsis@colorado.edu*

**corresponding authors:*
rodokrozit@gmail.com
[+] The first two authors contributed equally to this work

mojzsis@colorado.edu

Significance statement

The Neoproterozoic Urucum manganese deposit (Brazil) is a ~600 Mt microbially-mediated sedimentary Mn ore. Proto-ore formation via sedimentation and diagenesis occurred under suboxic-oxic and semi-neutral pH conditions in the Ediacaran ocean, wherein microbial Mn(II) oxidation ensued from the fine-grained accumulation of Mn oxides and organic matter. Oxic conditions that facilitated enzymatic Mn oxidation and overwhelmed microbial Fe oxidation appears as a sharp contact between manganese and iron beds. The Urucum deposit arose from a complex suite of diagenetic processes, including decomposition and mineralization of microbially-derived organic matter involving extracellular polymeric substances. *Kremydilite* – a new type of diagenetic concentric Mn mineral structure – formed by randomly activated heterotrophic cell colonies that generated pores in the microbialite sediment after burial, coincident with lithification.

Highlights

1. Urucum Mn deposit formed in an Ediacaran marginal basin with more than 600 Mt of ore formed from manganiferous microbialite.
2. *Kremydilite* is diagenetic structure that comprises a new type of Mn ore.
3. Microbial mediation occurred during Mn ore sedimentation and diagenesis.
4. Cellular and extracellular polymeric substances from Fe and Mn bacteria and cyanobacteria were mineralized.

Abstract

The Urucum district in Mato Grosso do Sul (Brazil), hosts the youngest and largest sedimentary Mn ore of Neoproterozoic age; units Mn-1, Mn-2, and Mn-3 are found in jaspilites and ironstones, and represent approximately 600 Mt of extractable rock with 27–44% Mn and 12–30% Fe. High-resolution optical- and cathodoluminescence microscopy, as well as Raman and FTIR spectroscopy show that the lower Mn-1 is ferruginous, while the upper Mn-1 consists mainly of 30–75 vol.% braunite, < 0.5% aegirine, 3–15% quartz, 5–10% feldspar, and 1–5% clay minerals, including apatite, chlorite, and organic matter. Here, we model the control of this ore mineralogy by homogeneous oxidation and microbial processes. Layers Mn-2 and Mn-3 contain *kremydilite*, as a characteristic ore structure, with 77–95 vol.% cryptomelane, 0–23% hollandite, 9–19 % braunite, 7–21% hematite, and 0–5% pores filled with clay minerals and organic matter. These are present within a micro-nodule matrix composed of cryptomelane and hematite in varying proportions. The first syngenetic products of microbial enzymatic oxidation were, on the Fe side, ferrihydrite and lepidocrocite, and on the Mn side, vernadite, todorokite, birnessite, and manganite. These formed under obligatory oxic (Mn) and suboxic (Fe) conditions and close to neutral pH. We describe the genesis of Urucum via complex diagenetic processes, which include the decomposition and mineralization of cellular- and extracellular-polymeric substances from Fe and Mn bacteria and cyanobacteria. The kremydilite forms in successive stages of oxidation of organic matter mediated by microbes, which generate pores and produce methane and CO_2/H_2 bubbles. They are a unique type of diagenetic structure formed by heterotrophic cell colonies randomly activated in the microbialite milieu following burial in suboxic neutral/alkaline conditions, side-by-side with the lithification and stabilization of the mineral assemblages. (**294 words**)

Keywords:
(1) Urucum Ediacaran manganese deposit; (2) kremydilite; (3) microbialite; (4) enzymatic oxidation, cell and extracellular polymeric substance mineralization.

1. INTRODUCTION

The Urucum mining district occupies an area of approximately 800 km^2 and is located in the Pantanal swamps region of west-central Brazil. Three layers of massive manganese oxides, named Mn-1, Mn-2, and Mn-3, occur interbedded with massive jasper, banded iron formations (BIFs), and massive iron formations (IF) that comprise the Santa Cruz Formation of the Neoproterozoic Jacadigo Group (Urban et al. 1992; Frei et al. 2017; Fig. 1 and SI 1-Fig). It was estimated that the Urucum district originally contained more than 600 Mt of rock with the manganese content between 27–44 wt.% and iron content between 12–30 wt.% (Urban et al. 1992).

Fig. 1 HERE

The stratigraphic sequence of the Urucum region was first defined by Dorr (1945) and Almeida (1946), who also conducted the first systematic studies on the origin of iron and manganese deposits in the region. Urban et al. (1992) mapped the entire mining region, and since that time, the regional geological map has been minimally updated. Following the work of Urban et al. (1992), the most relevant changes to our understanding of the regional geology arose from the work of Freitas et al. (2011), who detailed the Jacadigo Group lithologies and defined their sedimentation environments. Biondi and Lopez (2017) identified faults that acted as conduits for hydrothermal fluids which altered the rocks of the Jacadigo Group basement, and exhaled fluids with iron and other elements at the base of the sedimentary sequence of the Urucum basin. They also correlated the Mn-1, Mn-2, and Mn-3 layers with those recognized at different Urucum sites.

Various and mutually-exclusive proposed genetic models for the Jacadigo Group iron and manganese rocks have been a topic of discussion and debate since their discovery. These models can be summarized as follows: (a) marine genesis with sediments of continental origin (Dorr 1945); (b) marine genesis with sediments of marine origin (Almeida 1946; Putzer, 1958; Haralyi and Walde, 1986); (c) volcanogenic marine genesis (Walde 1981; Walde et al. 1981; Leonardos and Walde 1982; O'Connor and Walde 1985); (d) formation in a glacio-marine sedimentary

106 environment followed by supergene enrichment (Schneider 1984; Schreck 1984; Leeuwen and
107 Graf 1987; Graf et al. 1994; Costa et al. 2005); (e) sedimentary genesis in a flooded graben with a
108 contribution of hydrothermal leaching from hidden mafic rocks (Haralyi and Walde 1986; Walde
109 1988; Trompette et al. 1998); (f) SEDEX, or sedimentary exhalation (Dardenne 1998); and (g)
110 sedimentary genesis in an oceanic environment with a deep-sea hydrothermal contribution (Klein
111 and Ladeira 2004). Recently, Angerer et al. (2016) proposed a biologically-mediated origin in a
112 glacio-marine environment for the carbonate BIFs of the Santa Cruz Mine region located on the
113 southeastern part of the Santa Cruz plateau. In a recent comprehensive study, Biondi and Lopez
114 (2017) (a) recognized the biogenic mediation during the genesis of manganese ore; (b) described
115 in detail mineral structures termed by them *kremydilites* and argued that they may represent
116 fossilized microbial colonies from organisms that mediated the formation of the manganese layers;
117 and (c) modified the region's stratigraphy based on the fossil assemblages, showing that the
118 Urucum iron-manganese rocks correlate to the carbonate rocks of the Bocaina Formation, of the
119 Corumbá Group, previously considered post-depositional to those of the Jacadigo Group.
120 The Ediacaran Period of formation is proposed by the authors based on the presence of the
121 *Corumbella Verneri* fossil, found amidst the ironstones separating Mn-2 from Mn-3 (Figs 2B and
122 Figs 4B to D, Biondi and Lopez 2017). This fossil has always been considered Ediacaran, which
123 establishes a wider interest concerning the Urucum Mn deposit.
124 Here, we explore the origin of kremydilites described in Biondi and Lopez (2017) and
125 present a model that explains the processes of sedimentation and diagenesis that facilitated the
126 origin of these structures and the manganese layers. Recent works have provided a geological
127 setting diagram, mineralogy (low magnification optical microscopy, X-ray diffraction, SEM-EDS-
128 based), and chemistry datasets based on bulk samples and in situ (SEM-EDS) data (e.g. Frei et al.
129 2017), but microbial mediation as a plausible mechanism for the genesis of these rocks is still
130 under debate (Biondi and Lopez 2017). We expand the results of these previous studies with more
131 detailed optical microscopy (OM), cathodoluminescence microscopy (CL), Raman- and Fourier-
132 transform infrared spectroscopy (FTIR) to document the micro-mineralogy, presence, and
133 distribution of embedded organic matter. The goal here is to explore the role of microorganisms

in the process of manganese ore genesis from Urucum, and to understand the diagenesis, structures, and process of formation of kremydilites.

2. GEOLOGICAL AND GEOCHRONOLOGICAL BACKGROUND

The Santa Cruz Formation is mainly composed of jaspilitic BIFs, (massive) iron formations (IFs), massive banded jasper, and ferruginous arkosic silt and sandstones. The greatest thickness of the Santa Cruz Formation, 396 m, is documented in drill hole (DH) 44-28, made at the Vetorial Mine, and bookended by a 40 m section at the northern end of the Rabicho plateau (Fig. 2). The massive manganese layers, Mn-1, Mn-2, and Mn-3, occur in the lower half of this formation and are interlayered with BIFs and massive jasper.

The Jacadigo and Corumbá Groups are considered coeval (Biondi and Lopez 2017) and of Ediacaran age, based on the presence of stromatolites below Mn-1 (Jacadigo Group) and *Corumbella* fossils in the rocks of the Bocaina and Santa Cruz Formations (respectively, Corumbá and Jacadigo Groups). The age of this fossil in the ironstones of the Santa Cruz Formations (Jacadigo Group) and limestones of the Tamengo Formation (Corumbá Group) was estimated at ca. 550 Ma (Germs 1972; Grant 1990; Grotzinger et al. 1990; Hofmann and Mountjoy 2001; Bengtson 2002). The proposed age of this horizon was 555–542 Ma by ichnofossils, identified by Parry et al. (2017), in the Bocaina Formation. These ages are consistent with U-Pb geochronology of detrital zircons from a volcanic ash layer intercalated with carbonate rocks of the Tamengo Formation, at 543±3 Ma (Babinski et al. 2008), and the $^{40}Ar/^{39}Ar$ age of 587±7 Ma for cryptomelane in the Mn-1 to Mn-3 layers (Piacentini et al. 2013; Frei et al. 2017 and references therein).

Dating braunite from the Mn-1 layer, Piacentini et al. (2013) interpreted the 547±3 to 513±4 Ma ($^{40}Ar/^{39}Ar$) age as a minimum age, arguing that the Ar/Ar thermo-chronological system was rejuvenated by tectonic warming, which was considered a consequence of the metamorphism underwent by the Jacadigo Group rocks. Also using the $^{40}Ar/^{39}Ar$ method, they dated 513±3 Ma some crystals of muscovite collected from the arkoses that are interlayered with the BIFs, which was also considered metamorphic. According to Piacentini et al. (2013), these ages are "*possibly*

related to disruption between the Amazon Craton and the Apa River cratonic fragment and they do not reflect the time of Jacadigo Group deposition", which would be greater than 590 Ma, and concluded that Jacadigo's rocks would have at least 587 ± 7 Ma.

To reconstruct the paleogeography of the sedimentary basin, Mn-2 and Mn-3 were leveled and used as stratigraphic markers. This procedure makes it possible to outline the geometrical differences between the Mn-layers. This reconstruction shows that stratigraphy observed within the Urucum plateaux always includes Mn-1, and that this stratum lines the basin floor wherever the Jacadigo Group is described (e.g., Urban et al. 1992; Biondi and Lopez 2017) (Fig. 2). Yet, unlike Mn-1, both the Mn-2 and Mn-3 layers occur only in the interpreted depocenter of the basin, in the region of Urucum, Santa Cruz and southeast of the Morro Grande plateaux (Fig. 1). In the interior of each plateau, mining of the manganese layers reveals that Mn-2 and Mn-3 are flat and parallel to one another, whereas the Mn-1 unit follows the contours of the basin floor. By positioning Mn-2 and Mn-3 in their respective stratigraphic horizons it is now possible to reconstruct Urucum marginal basin floor (Fig. 2).

The origin of the sediments of Urucum has been detailed elsewhere (Walde 1981; Walde et al. 1981; Leonardos and Walde 1982; O'Connor and Walde 1985, Haralyi and Walde 1986; Walde 1988; Trompette et al. 1998, Dardenne 1998, Klein and Ladeira 2004, Angerer et al. 2016; Biondi and Lopez 2017), and we provided a brief synopsis, here. The Santa Cruz Formation formed as an in-fill of an ancient graben with iron and manganese-rich sediments overlying fluvial deposits from the Urucum Formation, while limestones from the Bocaina and Tamengo Formations were deposited in the shallow marginal regions (Biondi and Lopez 2017; Fig. 2). As has been proposed for some Phanerozoic Mn ores (e.g. Polgári et al. 2012ab, 2016b), the most probable sources of the Mn and Fe was hydrothermal exhalations in a submarine environment. The Mn and Fe fluids were transported to the sedimentary basin via basement faults (SI 1-2-Figs) that became activated

each time the graben widened. During inundations attributed to sedimentation of the Mn-1, Mn-2, and Mn-3 units, Mn and Fe discharged on basin floor mixed with Mn and Fe brought in by water from the open ocean as well as with that originating from the exhalates located outside the Urucum basin.

Fig. 2.

A transition between the Urucum and Santa Cruz formations through the Mn-1 horizon exists in all mines from the area (Urban et al. 1992). Furthermore, Biondi and Lopez (2017) showed that there are typically two or more layers of Mn-1 manganese ore with meter- to decimeter-scale thicknesses, locally interlayered with jaspillite-rich clasts. We now describe these relationships in more detail.

The lower Mn-1 ore layer is relatively siliceous and composed mainly of braunite, cryptomelane cement and Mn–Fe-rich carbonate, whereas the Upper Mn-1 layer is a fine-grained, massive, clastic layer of manganese oxides with undulating parallel lamination and numerous decimeter-scale oblate structures, characterized by a massive core and silty clay and arkose wrap dubbed amygdalites (Fig. 3C). The ore layer is bounded by sharp planar contacts typically overlain by conglomerate consisting of angular granite pebbles in an arkosic matrix. Layers Mn-2 and Mn-3 contain mostly massive manganese ore with lamination. They are composed mainly of cryptocrystalline manganese oxides and hydroxides, commonly containing kremydilites (Figs. 3D-E and 4) with minor amygdalites (Biondi and Lopez 2017). In Mn-2 and Mn-3, what have been interpreted as the remains of microbial colonies form oblate, 5–15-cm sized concentric kremydilite structures, within the fine-grained and biomass-rich basin floor shale as well as intergranular, oblate gas structures (Figs. 4A, C, F, and H). The main features of the ore beds, including their mineralogical and selective element compositions are summarized in Table 1.

Fig. 3

Fig. 4.

Table 1.

The textures of the Mn-2 and Mn-3 layers express as 1–10 millimeter-sized spherical, often zoned manganese oxide micro-nodules that coalesce to form the massive ores. These probably involved the aforementioned kremydilite structures made solely of manganese and minor iron oxides. All observed Mn-2 and Mn-3 outcrops have kremydilites, although they do not constitute all of the ore mass from these layers. As previously described, kremydilites occur between the ore bands (Figs. 4A–J), which are massive or banded (and/or laminated), and are distributed in the layers in an apparently homogeneous manner. It is difficult to estimate the volume occupied by kremydilites owing to the fact that they are complicated to see in discontinuous outcrops. For those observed on the mining fronts, it is likely that they occupy more than about 50% of the ore layer by volume.

2.1. Forms and type of kremydilites

Kremydilites occur only between the laminations of the massive ore in the Mn-2 and Mn-3 layers, and are absent in banded- or massive ironstones. They are always contoured by the fine laminated ore with micronodular, microbialite micro-texture, in which the diameters of micro-nodules range from 0.2–0.8 mm (Fig. 4; SI 5-Fig, zones 1, 2, 3; and zones 20 to 24). Microbialite and micro-nodule rich layers are in turn contoured by wavy microbialite layers apparently composed by the amalgamation of nodules smaller than 10 μm. Its forms are oblate, centimeter-to-decimeter scale (Fig. 3) and concentrically zoned. Structures of what we interpret to be the different growth development stages also appear to occur together (Figs. 4 and 5), and each stage of growth is marked by the presence of pores, which delineate coarse concentric, sometimes incomplete envelopes (Fig. 4). Kremydilites on the other hand are porous structures absent of micro-nodules. They occur in varied forms as shown in Figures 4A to H.

Fig. 5.

The simplest kremydilite form consists of a bubble-filled nucleus (Fig. 4A), followed by those with a nucleus having diffuse borders (Figs. 4C). Other forms include a nucleus with one (Fig. 4E) or two (Fig.4G) diffuse concentric laminae (or shells). The more complex kremdylites, with a nucleus and many concentric shells delineated by millimeter to submillimeter pores, crosscut with lighter, massive, and metallic zones (Figs. 4I). In general, the various kremydilite forms contain many oblate structures (Figs. 4A, E, and G). These are less than 20 mm across distributed along the layer containing the kremydilite, and inside and/or near them. Mesoscopic inspections of sawn samples (Fig. 4K) as well as thin and polished sections, show that each layer contains disseminated pores. The quantity of pores increases toward the margin of the shell, and each lamina is surrounded and delimited by areas with high pore density (Biondi and Lopez 2017).

The pores are often lined by shiny acicular microcrystals of cryptomelane and/or contain organic matter (Biondi and Lopez 2017). Although kremydilites do not contain micro-nodules, and are instead inside the micronodular bands and contoured by microbialite layers, the outermost zones of kremydilite appear to have a composition similar to that of amalgamated micro-nodules. In these zones, the presence of ring-like structures of carbonate microcrystals are common (SI 5-Fig, zone 16 - detail image, Biondi and Lopez, 2017). The zones closer to the nucleus (zones 9, 10, and 11) contain mixed anhedral minerals with metallic luster, but with larger dimensions than the anterior zones. The nucleus of the kremydilites (zones 12 and 13) are microgranular and heterogeneous.

3. SAMPLES

Representative samples and the methods applied (number of photos and spectra) are summarized in Table 2 and Fig. 3–4. Localities of the sample collection are shown in Fig. 2.

258 The samples of Mn-1 are (Fig. 3, SI 3-Fig): COR-4B, a clast-bearing massive ironstone;
259 COR-6, a massive manganese ore; COR-7, a very fine-grained clast-bearing ore with braunite and
260 carbonate; COR-10, a sandy, detritic ore with braunite, quartz, and feldspar; COR-31, an arkosic
261 sandstone with hematite matrix; and COR-32, an amygdalite with cryptomelane massive nucleus
262 surrounded by arkosic sandstone with hematite matrix.
263 Samples of Mn-2 and Mn-3 are: COR-81, a sample of massive manganese ore; COR-78-
264 F3 (Fig. 4F), a nucleus of porous kremydilite with diffuse boundaries, surrounded by two zones
265 also with diffuse boundaries; COR-78-D1 (Fig. 4C), a kremydilite with a diffuse core enveloped
266 by two shells, also with diffuse boundaries; COR-75-B5 (Fig. 4E), a porous kremydilite nucleus;
267 COR-75-2 and COR-48 (Fig. 4J), complex kremydilites with porous core surrounded by many
268 concentric, porous shells; and COR-36-A1 (Fig. 4G), a kremydilite with a nucleus and at least two
269 shells (hereafter the samples are cited without COR).
270 **Table 2.**
271
272 **4. METHODS**
273 Thin section and polished section mineralogy was described and quantified using a ZEISS
274 Axio Imager A2m microscope (Federal University of Paraná State, Polytechnic Center, Geology
275 Department, Curitiba, Brazil).
276 Petrographic structural-textural studies by optical rock microscopy (OM) were also made
277 on 12 thin sections in transmitted and reflected light (NIKON ECLIPSE 600 rock microscope,
278 Institute for Geology and Geochemistry, Research Centre for Astronomy and Earth Sciences,
279 Hungarian Academy of Sciences - IGGR RCAES HAS, Budapest, Hungary).
280 Cathodoluminescence (CL) petrography was carried out on 7 thin sections using a
281 Reliotron cold cathode cathodoluminescence apparatus mounted on a BX-43 Olympus

282 polarization microscope (Szeged University, Hungary). The accelerating voltage was 7–7.7 keV
283 during the analysis. Cathodoluminescence spectra were recorded by using an Ocean Optics
284 USB2000+VIS-NIR spectrometer. Spectrometer specifications are a wavelength range of 350–
285 1000 nm and 1.5-nm (FWHM) optical resolution.

286 Mineralogical analyses were performed on three bulk samples using a Rigaku Miniflex-600
287 X-ray diffractometer (XRD), with carbon monochromator and Cu-Kα radiation, at 40 kV and 15
288 mA (IGGR RCAES HAS, Budapest, Hungary). Mineral composition was determined on randomly
289 oriented powdered samples. The diffraction patterns were processed using Siroquant V4 software,
290 and the modal contents determined by the Rietveld method.

291 *In situ* FTIR microspectrometry used for micro-mineralogy and organic material
292 identification on nine thin sections to determine the mineralogy and characterize the organic
293 material, as well as clarify the concentric structures (415 spectra, IGGR RCAES HAS, Budapest,
294 Hungary), using a Bruker FTIR VERTEX 70 equipped with a Bruker HYPERION 2000
295 microscope with a 20x ATR objective and MCT-A detector. During attenuated total reflectance
296 Fourier transform infrared spectroscopy (ATR) analysis, the samples were contacted with a Ge
297 crystal (0.5-µm) tip with 1 N pressure. The measurement was conducted for 32 s in the 600–4000
298 cm^{-1} range with 4-cm^{-1} resolution. Opus 5.5 software was used to evaluate the data. The equipment
299 inappropriate for most of Mn-oxide determinations because those peaks fall in the < 600 cm^{-1} range
300 (not equipped with that detector). Contamination by epoxy glue and glass was corrected for.

301 High-resolution *in situ* micro-Raman spectroscopy was used for micro-mineralogy and CM
302 identification and distribution on 9 thin sections (1 polished section) (Szeged University,
303 Hungary). A Thermo Scientific DXR Raman Microscope was used, with a 532-nm (green) diode
304 pumped solid-state (DPSS) Nd-YAG laser, using 1.5-mW laser power and 50x objective lens in
305 confocal mode (confocal aperture 25 µm slit). The acquisition time was 1 min, and the spectral

306 resolution was ~2 cm^{-1} for each measurement. The distance between each point was 10 μm, and
307 the measurement time was 10 min. A composite image of thin sections of Raman microscopy
308 measurements and a series of Raman spectra acquired along the vertical sections are provided in
309 the thin section photomicrographs (arrow points to measurement direction). Diagrams are
310 organized in terms of peak height versus analytical spot number for each of the phases along the
311 Raman-scanned section. Intensities were normalized to the highest peak for each spectrum.

312 Raman measurements were taken on 9 samples (4B, 7, 10, 31, 36-A, 75-2, 75-B5, 48-D1,
313 81). In the case of the homogeneous-like cases 400-500 and in the case of 75-2, 800 spectra were
314 taken along the line shown on section photos (4B, 7, 10, 31). These are systematic investigations
315 along the line profile. Spectra were obtained every 10 μm, providing a high-resolution sensitive
316 study. In samples 75-B5, 78-D1, and 81, the measurements were taken across whole thin sections.
317 The spectra were elaborated in two ways:
318 (1) Diagrams were organized in terms of peak height versus analytical spot number of each of the
319 phases along the Raman scanned section (main minerals and organic matter in general). (2) A
320 detailed determination of all spectra were also made. These results are summarized in tables (Excel
321 files, numbers 1, 2, and 3 indicate the intensity—1-weak, 2-moderate, 3-strong—reference data on
322 detection), in which the mineral composition can be followed from point to point, as well as the
323 type of organic matter. (Supporting Information)

324 Aside from the profile analyses, descriptions of the mineral phase transitions were also
325 constructed for clarification of aegirine (5 photos, 4 mineral spectra, and 1 profile), braunite (3
326 photos, 10 point analyses, and 1 profile across mineral transitional zones), cryptomelane (18
327 photos, 54 point analyses, and 2 profiles across spheres), and the composition of the oblate
328 structures (28 photos, 93 point analyses, and 1 profile).

329 The following Raman bands were used for normalization: rhodochrosite: ~1086 cm^{-1},
330 dolomite: ~1093-96 cm^{-1}, apatite: ~965 cm^{-1}, quartz: ~463 cm^{-1}; todorokite 633 cm^{-1}; manjiorite
331 641 cm^{-1}; ramsdellite: 650 cm^{-1}; cryptomelane: 183 cm^{-1} and 580 cm^{-1}; hollandite: 585 cm^{-1};
332 birnessite: 656 cm^{-1}; ferrihydrite: 707 and 1045 cm^{-1}; goethite: 297 and 385 cm^{-1}; celadonite: 545
333 cm^{-1}; barite: 446 and 985 cm^{-1}; johannite: 785 cm^{-1}; aegirine: 970 cm^{-1}; jacobsite: 620 cm^{-1};
334 hausmannite: 661 cm^{-1}; braunite: 210, 510, 685 cm^{-1}; and carbonaceous matter: ~1605 cm^{-1}. The
335 identification of minerals was made with the RRUFF Database (Database of Raman –
336 spectroscopy, X-ray diffraction, and chemistry of minerals: http://rruff.info/). Contamination by
337 epoxy glue was taken into consideration. Along with the profile analyses, a detailed determination
338 of all peaks was also made.
339 Comparing the two *in situ* methods, the AT-FTIR, which did not considerably modify the
340 mineral phases while using the lowest exciting energy, was used to investigate the upper 1–2 μm
341 of the samples. This is the also best method to determine organic matter (Polgári and Gyollai,
342 2019; Polgári et al., 2019). On the contrary, Raman spectroscopy, using higher excitation energy,
343 often caused the transformation of metastable minerals to more stable phases. This method yielded
344 information from the upper 3–4-μm depth of the sample surfaces and was the best method for
345 identifying Mn oxides and hydroxides. The Raman comparative spectra database is more extensive
346 than the AT-FTIR database.
347
348 **5. RESULTS**
349 **5.1. Optical (OM) and cathodoluminescence (CL) rock microscopy**
350 **5.1.1. Optical rock microscopy**
351 Thin sections represent mineralized biomats based on structural observations, which are
352 eminently visible on smaller magnification photos (40x) (Fig. 6, SI 6-, 7-Figs). In all thin sections,

353 adequately high-resolution optical rock microscopy (1000x) supports a series of mineralized
354 biomat microstructures, mineralized microbially produced textures (MMPT) as main constituents
355 (Fig. 6, SI 8-Fig). This microbial microtexture is a basic feature of all the samples, in transmitted
356 as well as reflective light. Well-preserved and mineralized remains of diverse filaments with pearl
357 necklace-like, vermiform inner signatures, and coccoid-like forms embedded in the Mn ore beds
358 are seen, and the whole samples appear densely woven. The minerals are very fine-grained (0.5-1
359 μm) except Mn-1, where clastic contribution occurs. The diameter of the mineralized filaments is
360 around 0.5–1 μm, with variable length (Fig. 6).
361 **Fig. 6.**
362 Samples 4B, 7, 10, 31, 32 (all from Mn-1) include debris-like components of variable size
363 (20–200 μm). In sample 4B, it seems that the darker gray mineral grains transform to lighter phase
364 (SI 8-Fig). The debris grains are mainly quartz with few fragments of jasper and hydrothermally
365 altered feldspar.
366 **5.1.2. Cathodoluminescence microscopy**
367 Cathodoluminescence revealed that a part of the debris-like grains (clastic components) is
368 probably composed of real clasts showing the bright, characteristic CL of the mineral (e.g., quartz-
369 blue, feldspar-yellowish) (Fig. 7AB, SI 9-Fig). Some other grains with sizes of some tens of μm
370 resemble clasts but do not show luminescence. These non-luminescent grains are most probably
371 secondary minerals formed via diagenesis (Marshall 1998; Hassouta et al. 1999).
372 Bright blue luminescence is characteristic of kaolinite group-dickite (supported by Raman
373 spectroscopy; Götze et al. 2002), which occurred frequently in our samples (samples 4B, 7, 10, 31,
374 Fig. 7A, B, G, H). The numerous small or larger bright yellow minerals are apatite grains, which
375 often have a lighter margin. These apatites occur along the ore lenses, minerals, and laminae in a
376 woven-like fine-grained biomat-type matrix which mark the borders as accompanying a series of

377 minerals that occurred frequently (Fig. 7, SI 9-Fig) (samples 4B, 7, 10). The fine-grained
378 rhodochrosite (mixed carbonate) show dull reddish (orange) luminescence (Fig. 7A, B) (samples
379 4B, 7, 10). Samples 75-2, 75-B5, and 78-D1 are non-luminescent.
380 **Fig. 7.**
381 **5.2. FTIR spectroscopy**
382 Measurements were performed in two ways: (i) randomly, in seven sections (6, 7, 10, 31,
383 32, 36-A1, 78-F3) and (ii) along profiles, in kremydilite sample 48B (Fig. 4K) and in oblate
384 structure (36-A2) (Fig. 4H).
385 **5.2.1. Local area analyses**
386 Mineral phases and types of organic matter for (i) are summarized in Table 3 and SI 10-
387 Table, according to the measuring area and frequency.
388 **Table 3.**
389 In summary, Fe-oxide-hydroxides (ferrihydrite, lepidocrocite, hematite) are common in all
390 the Mn ore beds, Fe-silicates (aegirine) are common in the Mn-1 ore bed, and Fe-sulphide (pyrite)
391 rarely occurs. Variable Mn oxides and hydroxides (todorokite, ramsdellite, pyrolusite,
392 cryptomelane), and oxide-silicates (braunite, serandite) are the main Mn ore minerals. Besides Fe
393 and Mn ore minerals, feldspar, chlorite, celadonite, kaolinite group-dickite, apatite, and quartz are
394 moderate or minor mineral components. Variable types of organic matter occur in all samples.
395 **5.2.2. Analyses of kremydilite**
396 Three profile analyses in kremydilite sample 48B were made (Fig. 4K and Fig. 8). Two
397 profiles crossed the concentric shells of the kremydilite structure on opposite sides (A and C), and
398 one profile crossed the inner part (B).
399 All concentric shells and the parts intersected between these shells are heterogenous and
400 very fine-grained. Considering that minerals represent the remnants of primary Mn and Fe

minerals, each measuring point in the concentric shells and intersected parts resulted in a mixture of minerals, with often poorly crystallized phases.

Fig. 8.

All shells and the inner part are heterogeneous and very fine-grained. Each measuring point resulted in a mixture of minerals, with often poorly crystallized phases like ferrihydrite. The shells —observed visually—often have the same mineralogy (cryptomelane, hollandite, hematite, rhodocrosite, and pores). The mineralogy of the two sides of the structure are asymmetric (Fig. 8D). *Profile A* (Fig. 8B), from the margin toward the inner part, contain rhodochrosite-goethite, manjiorite-todorokite, minor ferrihydrite-cryptomelane (6 shells), and in the vicinity of the inner part, cryptomelane-ferrihydrite. *Profile C*, from the margin toward the inner part, contain braunite-rhodochrosite, braunite-goethite-rhodochrosite (3 shells), braunite-cryptomelane-rhodochrosite, braunite-rhodochrosite, braunite, cryptomelane-ferrihydrite-rhodochrosite (2 shells), cryptomelane-ferrihydrite (2 shells), and cryptomelane-braunite, and in the vicinity of the inner part, cryptomelane-ferrihydrite. *Profile B*, representing the inner part from the shells to the center, contain cryptomelane-ferrihydrite, ramsdellite-rhodochrosite, birnessite-rhodochrosite (2 zones), cryptomelane-quartz-rhodochrosite, cryptomelane-birnessite-dolomite, cryptomelane-quartz-rhodochrosite, ferrihydrite-cryptomelane-dolomite-quartz, and cryptomelane-quartz-dolomite. Varying amounts of pores, with or without organic matter, are characteristic in all layers and in the central parts (Fig. 4).

In summary, mineralogical assemblages contain concentric zones (or "shells") of poorly crystallized, preserved Mn (birnessite, todorokite) and Fe minerals (ferrihydrite), and mainly more stable cryptomelane, hollandite, braunite, hematite, goethite, and rhodochrosite. *Profile C* mineral components are more stable. More stable minerals represent greater degree of crystallinity.

5.2.3. Analyses of oblate (bubble-like) structures

425 Based on OM of sample 36-A1, the outer and inner matrix and also the dark spots of the
426 oblate structures appear very similar, with only the reflective color differing slightly (SI 11-Fig).
427 FTIR analyses resulted in a similar mineralogy and variable organic matter composition, as the
428 sample is very fine-grained and heterogeneous (Fig. 9). The peaks of most of the minerals show
429 broad bands and low intensities, which are characteristic of disordered, poorly crystallized quartz,
430 carbonates, and feldspar.

431 **Fig. 9.**

432 Out of the oblate structures, the ore contains a matrix, micro-nodules, and dark spots. The
433 micro-nodules and the matrix consist of cryptomelane, ferrihydrite, minor goethite, rhodochrosite,
434 and variable organic matter. The analyzed dark spot in the outer part consists of pores,
435 cryptomelane, ferrihydrite, minor goethite, rhodochrosite, and organic matter.

436 There are no micro-nodules inside the oblate structure. The light part of the matrix inside
437 the oblate structure contains cryptomelane, ferrihydrite, quartz, minor dolomite, and organic
438 matter. The dark part comprises dolomite, ferrihydrite, cryptomelane, and organic matter. Inside,
439 the dark spot consists of ramsdellite, quartz, minor dolomite, and organic matter (SI 11-Table).

440 The oblate, rim structure, separating the outer and inner parts, consists of two phases: (1)
441 the fine-grained rim built up of ferrihydrite, minor goethite, and organic matter; and (2) the coarse-
442 grained phase, which is a mixture of cryptomelane, disordered quartz, rhodochrosite, dolomite,
443 traces of braunite, and variable organic matter. Comparing the outer and inner parts, differences in
444 mineralogy are reflected in the type of carbonate (rhodochrosite outside and dolomite inside), the
445 Mn oxides of the dark spots (cryptomelane outside and ramsdellite (γ-MnO_2) inside), and the
446 occurrence of quartz in the inner part and rim, and feldspar in the outer part. On the outside of the
447 oblate structure, the rock contains pores and the typical (micronodule-bearing) microtexture of

448 Mn-2 and 3, whereas inside, the micro-noduliferous textures do not exist, and pores are partially
449 filled by hollandite.

450 **5.3. Raman spectroscopy**

451 Nearly 11,000 spectra were taken for micro-mineralogical and organic matter composition
452 determinations as well as for the distribution of minerals according to the thin section profiles.
453 Representative analyzed profiles are shown in Fig. 10 and SI 12-Fig. The mineral distribution was
454 evaluated visually based on a series of Raman profiles at the 10-μm scale (Fig. 10, SI 12-Fig). The
455 determined minerals, including FTIR data, are summarized in Table 4. Variable Mn oxides and
456 hydroxides, Mn oxides-silicates, Mn carbonates, variable Fe oxides hydroxides, Fe silicates, Fe
457 sulfide, ore minerals, apatite, feldspar (albite and orthoclase), mica (muscovite, chlorite,
458 celadonite), kaolinite-dickite, barite, carbonates (strontianite, dolomite, ankerite), and quartz occur
459 in the Mn ore beds. Variable organic material is also an important constituent. Based on low
460 intensity and broad peaks, the minerals are poorly crystallized and cryptocrystalline. The
461 representative samples contain a mixture of poorly crystallized mineral phases and organic matter.

462 **Table 4.**
463

464 **5.3.1. Mineral distribution in profiles by Raman spectroscopy**

465 A distribution of minerals is evident in all samples, alternating micro-laminae (a few tens
466 of μm thick) along with the kremydilite inner part (Fig. 10, SI 12-Fig). This alternating micro-
467 lamination refer to mineralized microbial cycles in the sediment pile. The documented distribution
468 of minerals in the Mn ore beds is the following:

469 *Mn-1 from Figueirinha Mine*

470 - Sample 4B - Hematite (rarely aegirine)/rarely quartz alternation, starting with Mn
471 (braunite) alternation and random apatite, and K-feldspar.

- Sample 7 - Aegirine/braunite cycles with randomly occurring apatite, mica, and K-feldspar.
- Sample 10 - Aegirine-hematite/quartz alternation (Fe cycles) and Mn cycles superposed (braunite, serandite, hausmannite) occur with randomly occurring apatite, barite, feldspar (albite, K-feldspar), and strontianite.

Mn-1 from São Domingos Mine

- Sample 31 - Hematite (rarely kaolinite/dickite)/quartz alternation (Fe cycles), and Mn cycles superposed (braunite, manjiorite, jacobsite, todorokite, romanèchite).

Mn-2 from Urucum Mine

- Sample 75-2 - Only Mn minerals occur, but jacobsite and hollandite contain Fe. Jacobsite alternate with cryptomelane, ramsdellite, and hollandite. Ramsdellite is the most oxic phase. In the zone of kremydilite, the micro-lamination turns into random mineral distribution. Accessory minerals are: romanèchite (psilomelane), manganite, todorokite, pyrite, and pyrolusite.

- Sample 75-B5 - Goethite is frequent only in this sample. Representative Mn cycles are composed of cryptomelane, hollandite, and occasionally, braunite. Micro-lamination is disordered, and in those zones, random mineral distribution occurs, but locally micro-lamination is well visible. Accessory minerals are: jacobsite, manganite, ramsdellite, todorokite, hausmannite, romanèchite, pyrolusite, ferrihydrite, apatite, and mica.
- Sample 78-D1 - Hematite (Fe cycle) alternate with Mn oxide cycles (cryptomelane-hollandite) forming double microbial ore forming lamination. Cryptomelane and hollandite occur together. Hematite and braunite also occur together, but braunite occurs separately, too. Braunite binds to hematite. Locally, pyrolusite, birnessite, romanèchite, jacobsite,

494 manganite, ramsdellite, hausmannite, serandite, ferrihydrite, goethite, mica, and apatite
495 occur.
496 *Mn-3 from MCR Mine*
497 - Sample 81 - Hematite alternates with Mn oxide (cryptomelane-hollandite). Accessory
498 minerals are: todorokite, ramsdellite, jacobsite, rancieite, pyrolusite, birnessite, braunite,
499 ferrihydrite, magnetite, and mica.
500 **Fig. 10.**

501 **5.3.2. Mineral phase transitions by Raman spectroscopy**

502 Microscale mineral phase transitions offer very important information on syngenetic and
503 diagenetic formation processes. Mineral compositions of Urucum samples also provide
504 information on this aspect, which explains the focus on specific mineral transitions.

505 **5.3.2.1. Aegirine**

506 Aegirine is common in Mn-1, occurring as an alternating mineral with braunite. A detailed
507 study on the phase transition was made for sample 4B (Fig. 11). The microtexture of aegirine
508 resembles a vermiform network that intrudes into the quartz. The quartz occurs in the undulating
509 hematite network as a gel-like segregated silica. Aegirine is present at the contact of quartz, and
510 riebeckite seems to consume aegirine. This relationship shows that aegirine and riebeckite
511 consume quartz. At the contact of segregated quartz, hollandite/vernadite and apatite occur.
512 Braunite binds to hematite in the vicinity of quartz.
513
514 **Fig. 11.**

515 **5.3.2.2. Braunite**

516 Braunite also consumes segregated quartz similarly to aegirine, in a vermiform habit, and
517 is in close contact with the hematite network (Fig. 12) (sample 4B). Segregated quartz also contains
518 K-feldspar. Hematite occur as small clusters and contains an undulating network as mineralized
519 biomats.

Fig. 12.

5.3.2.3. Cryptomelane

All the spectra taken in the micro-nodules (cell colonies) and matrix material show dominant vernadite/hollandite-type Mn-oxides-hydroxide composition and a greater or less amount of cryptomelane and variable organic matter (sample 75-2). The minerals are in a cryptocrystalline mixture with variable amounts. The textural differences do not correspond to significant mineralogical differences (Fig. 13, SI 13-Fig). The central part of the micro-nodules consists of hollandite/vernadite and organic matter, around which cryptomelane, pyrolusite and ramsdellite occur.

Fig. 13.

5.3.3. Oblate structures

Detailed Raman measurements were elaborated on a representative oblate structure, used to compare the mineral composition and distribution inside the oblate structure, in its vicinity, and in the rim (sample 36-A1, Fig. 14, SI 14-Fig).

The dark spots in the outer matrix are mainly pores, except dark porous inner rims with variable thicknesses, which are composed of a hollandite-type Mn oxide phase (dominant phase), cryptomelane, and goethite. The matrix among the dark spots is built up by hollandite, cryptomelane, and goethite.

The non-porous rim of the oblate structure mainly consists of hollandite and cryptomelane in variable amounts. Rarely fine-grained clusters of goethite occur among the hollandite-cryptomelane flakes.

In comparing the mineral phases and distribution in the outer, inner, and rim areas of the measured oblate structure, we find that they are similar. The matrix of the inner part of the oblate structure is composed of very fine-grained goethite (ferrihydrite) and small particles of Mn oxides

544 (hollandite and cryptomelane in variable amounts); however, hollandite is dominant in the dark
545 spots. The mineral composition of the matrix and dark spots show a unified distribution, as any
546 difference or significant trend in the matrix or in the dark spots was not detected.

547 **Fig. 14**.

548 **5.3.4. Organic matter**

549 The organic matter of Mn-1 ores from Figueirinha (samples 4B, 7, and 10) and São
550 Domingos (sample 31) area are dominated by two bands near 1320 and 1610 cm^{-1}, which are D
551 and G bands of hydrogenated amorphous carbon (Chen et al. 2007). This ore bed contains also
552 traces of aromatic hydrocarbons (825 cm^{-1}), and skeletal stretching of C=C and C=O molecules.
553 Bands of aliphatic hydrocarbons occur at 1000–1280 cm^{-1} (Okolo et al. 2015) (samples 4B, 7, 10,
554 31), 1300–1390 cm^{-1} represents CH_3 (Jehlička et al. 2009), and 1487 cm^{-1} refer to CH_2/CH_3
555 vibrational mode (Jehlička et al. 2009) (samples 7, 10). The band at 1518 cm^{-1} refers to the C=C
556 stretching in polyenes (sample 31), while 1620–1820 cm^{-1} show the C=O vibration of oils (Orange
557 et al. 1996) (sample 4B).

558 The organic matter of ores of Mn-2 (Urucum West Mines) (samples 75-2, 78-D1, and 75-
559 B5), contain bands of aliphatic hydrocarbons (1104 cm^{-1}), CH_3, and the D and G band of
560 hydrogenated amorphous carbon based on bands near 1320 and 1610 cm^{-1}. The sample 75-2
561 contains only the D and G band of amorphous hydrocarbon, whereas sample 75-B5 contains the
562 aromatic hydrocarbon (825 cm^{-1}) bands of CH_2/CH_3 vibration (1386, 1469 cm^{-1}), and C=O
563 vibration of oils (1750–1800 cm^{-1}). The sample 78-D1 has bands D and G of hydrogenated
564 amorphous carbon and traces of CH_2/CH_3 vibrational mode of aliphatic hydrocarbon (1345, 1362
565 cm^{-1}). The sample of the Mn-3 ore bed (MCR Mine, sample 81) contains mostly hydrogenated
566 amorphous carbon (D and G bands at 1317 and 1600 cm^{-1}) and traces of aliphatic (1000–1200

567 cm^{-1}, 1469 cm^{-1}) and aromatic hydrocarbons (825 cm^{-1}). Only 60 of 1903 spectra contains organic
568 material.
569
570 **6. DISCUSSION**
571 **6.1. Sedimentation age and environments**
572 The presence of long chain oil type in manganese layers with kremydilite indicates that
573 temperatures were hardly larger than 90°C, which eliminates the possibility that the Jacadigo
574 Group' rocks have been metamorphosed. This find makes it likely that the $^{40}Ar/^{39}Ar$ age of the
575 Mn-1 layer is effectively 547 ± 3 to 513 ± 4 Ma, the ages of braunite and muscovite determined
576 by Piacentini et al. (2013). This age seems to be reinforced by that determined by Babinsky et al.
577 (2008), which dated detrital zircons (U – Pb SHRIMP) from a volcanic ash layer intercalated with
578 carbonate rocks of the Tamengo Formation at 543 ± 3 Ma.
579 Corumbella and stromatolite occurrences and field information published by Biondi and
580 Lopez (2017) indicate that the Santa Cruz Formation (BIFs) and the manganese layers sedimented
581 at the same time or after the Bocaina Formation; and that the ages of these rocks are about 550
582 Ma. The age of this fossil in the ironstones of the Santa Cruz Formations (Jacadigo Group) and
583 limestones of the Tamengo Formation (Corumbá Group) was estimated at ca. 550 Ma (Germs
584 1972; Grant 1990; Grotzinger et al. 1990; Hofmann and Mountjoy 2001; Bengtson 2002). Also,
585 the proposed age of this horizon was 555–542 Ma by ichnofossils, identified by Parry et al. (2017),
586 in the Bocaina Formation.
587 There is no diagnostic evidence that sedimentation occurred during some glacial period or
588 during some glaciation, as initially proposed by Urban et al. (1992). The only arguments of these
589 authors were: (a) the presence of the granite blocks they interpreted as dropstones, without even
590 observing whether any of these blocks have faceted, friction-sectioned sides, and/or have striated
591 faces, as is typical of dropstones. These characteristics were never observed in the Urucum
592 (Trompette et al., 1998; Freitas et al., 2011; Biondi and Lopez, 2017). (b) To consider the Santa
593 Cruz Formation, with at least 400 m thick BIFs, as similar to the Rapitan Formation, with less than
594 10 m thick BIFs (Young, 1976). As the Rapitan Formation would be Ediacaran and of glacial
595 origin (Young, 1976), Urban et al. (1992) inferred that the Santa Cruz would have the same origin;

596 and most subsequent authors adopted this idea. However, keeping in mind that this hypothesis is
597 traditionally defended by many authors (e.g. Angerer et al., 2016), it should be discussed.
598 The last glacier related to snowball earth, and the sedimentation of Rapitan-denominated
599 BIFs, was the Marinoan glaciation, which began at about 650 Ma and ended at about 635 Ma.
600 Considering all the information presented above, the Urucum's BIFs, ironstones and manganese
601 layers sedimented about 550 Ma ago, 85 Ma after the end of the Marinoan and the snowball
602 glaciations. The Gaskiers glaciation, which existed for 340,000 years (579.9 to 579.6 Ma), has
603 occurred about 29 Ma before the end of the Jacadigo Group sedimentation, and could hardly
604 influence its sedimentation. It remains, therefore, to relate the formation of the Jacadigo Group
605 with Baykonurian glaciation (547 to 545.5 Ma), so far recognized only in Asia and Africa
606 (Chumakov, 2009; and Chumakov, 2011; Germs and Gaucher, 2012). We therefore propose to
607 consider the possibility that the sedimentation of the BIFs and manganese layers of the Santa Cruz
608 Formation occurred during the Baykonurian glaciation, which would explain the existence of what
609 is interpreted by Urban et al. (1992), among other authors, as dropstones.
610 We hold the view that Mn-1 was most likely formed during the first inundation of the
611 ancient graben by the fluvial, oxidative sediments that gave rise to the Urucum Formation. Unit
612 Mn-1 contains predominantly siltic and sandy, ferruginous clastic rocks, cemented by microbially
613 mediated Fe minerals (e.g., aegirine), and Mn-oxide and silicate (braunite, serandite, and
614 hollandite). The areas of Figueirinha and São Domingos mines have a larger concentration of
615 manganese in Mn-1, which are contained in clast-bearing massive ores. The upper Mn-1 layers in
616 the Figueirinha and São Domingos mines, which include amygdalites, were probably deposited in
617 the basin depocenter, where the amygdalites formed from hydrodynamic flux. Layers Mn-2 and
618 Mn-3 formed in "offshore" (= greater depth) environments during periods of tectonic quiescence,
619 when fine, clastic quartz fragments and other detrital sedimentation ceased.
620 **6.2. Mineralogical interpretations**
621 Microtextural evidence in all the studied samples appears as dense features, and the mineral
622 types and embedded variable organic matter raise the microbially-mediated formation of the ore
623 beds, which we argue occur as microbialites (MMPT). Two microbial ore forming systems are
624 proposed as dual systems, characterized by Fe- and Mn-oxidizing metabolic processes (Fe-
625 oxidizing bacteria (FeOB) and Mn-oxidizing bacteria (MnOB)).

626 Several studies on the genesis and preservation of oil and natural gas have shown that long
627 chain hydrocarbons are decomposed at temperatures above 90ºC (Chilingar et al. 2005, p.138-
628 142). Preservation in Mn-2 and Mn-3 of aromatic and aliphatic hydrocarbons, C=C stretching in
629 polyenes, C=O vibration of oils, among others, indicates that temperatures during diagenesis were
630 low (<90ºC) and that syngenetic as well as diagenetic minerals were preserved, as identified by
631 the Raman and FTIR analyses. Along with hydrocarbons, these analyses identified minerals such
632 as birnessite and ferrhydrite, which we consider remnants of the original sedimentation, (i.e. they
633 were not entirely destroyed during diagenesis). Remnants of syngenetic and diagenetic minerals
634 interpreted as complex systems give a plausible series of processes and environmental formation
635 conditions during sedimentation and diagenesis (Table 4, Fig. 15, SI 15-Table). The frequency of
636 the minerals is different: the main minerals, such as cryptomelane, hollandite, hematite, and
637 braunite, form the ore beds, but the moderate and minor minerals have also genetic importance.
638 The Mn layers are the result of complex diagenetic processes and formation of diagenetic minerals,
639 which include the components of the decomposition of cells and extracellular polymeric substance
640 material (Fe and Mn bacteria, cyanobacteria, and other types; see Ewers 1983; Wignall 1994;
641 Konhauser 1998; Villalobos et al. 2003; Dupraz and Visscher 2005; Dupraz et al 2009; Chan et al.
642 2011; Gyollai et al. 2017).
643 Some syngenetic poorly crystallized minerals were preserved, and that serves as a starting
644 point. For a clear understanding, a short review on the most important mineral assemblages and
645 primary minerals is needed. Many types of minerals occur, and these can be grouped as follows.
646 **6.2.1. Remnants of syngenetic minerals – Syngenetic Fe- and Mn-rich biomat**
647 **formation**
648 Remnant syngenetic minerals are reported as microbially mediated minerals forming under
649 obligatory oxic (Mn) and suboxic (Fe) conditions, with neutral and semi-neutral pH. The

650 microbially mediated Mn and Fe oxidation have different oxygen demand, and the diagenetic
651 zones represent different oxygen conditions. The nomination “suboxic” has a double meaning
652 which can cause discrepancies. To avoid misunderstanding, definitions are listed in Table 5. In
653 general, Eh > 0 represent oxic conditions, but the concentration of oxygen can be different, as
654 shown in Table 5 and Fig. 15, and the microbially mediated processes occur at a given oxygen
655 content. Diagenetic zonation also separates the oxic, suboxic, and anoxic zones, and the oxidizing
656 agent is O_2 in the oxic zone, NO_3^-, MnO_2, and Fe_2O_3 in the suboxic zone, and SO_4^{2-} in the anoxic
657 zone (Berner 1980; Coleman 1985; Wignall 1994; Polgári et al. 2012ab).

658 **Table 5.**

659 Ferrihydrite and lepidocrocite on the Fe side, and vernadite, todorokite, birnessite, and
660 manganite on the Mn side, are regarded as syngenetic minerals (Ehrlich 2002). Accordingly, it is
661 obvious that ore formation started with microbial Fe oxidation. That is why interpretation starts
662 with a description of the Fe system.

663 **Syngenetic Fe system**

664 Understanding the biochemistry of the biomat formation is a key factor in determining the
665 type of Fe-rich biomat that may have been involved in the formation of the Urucum Mn layers,
666 and to define the environmental conditions. There are various types of microbial metabolisms that
667 can oxidize Fe^{2+} in nature, which occur under varying states of oxygen-deficient conditions. Three
668 types of Fe-rich biomats are considered for the Urucum; all are neutrophilic and consistent with
669 basin conditions (Fig. 15): (1) Microbial neutrophilic, micro-aerobic Fe(II) oxidizing bacteria (pH
670 ~8; Eh +0.3 V) (Hallbeck and Pedersen 1990; Ehrenreich and Widdel 1994; Konhauser 1998;
671 Ehrlich 2002) supported by mineral assemblage (ferrihydrite, goethite, hematite, celadonite); (2)
672 Nitrate-reducing Fe(II) oxidizers in suboxic/anaerobic conditions (lack of filaments; Straub et al.
673 1996); and (3) Photoferrotroph metabolism in anoxic/anaerobic light-demanding conditions,

674 which is not plausible based on mineral assemblage, which support suboxic-oxic conditions. The
675 fourth (4) type, strongly acidic, oxic metabolism is also not plausible in the Urucum basin, and
676 does not fit with the mineral assemblage. However, a further process we have to consider, is the
677 non–Fe-oxidizing microbes later overgrown by Fe oxides via microbial processes (Konhauser
678 1998). This cannot be excluded, but the homogenous Fe-precipitation on filamentous forms do not
679 support this scenario as a principal process.

680 The rhythmic developmental stages via microbial mediation is basic. Free-living Fe(II)
681 oxidizing bacteria exist in the lag and log phases (Novick 1955; Zwietering et al. 1990), and stalk
682 formation (Fe-rich biomat–mineralization) occurs during the stationary (abbrev.: stat) phase under
683 optimal conditions (pH > 6, aerobic, cell number > 6×10^5 mL^{-1}, low organic C content, 1–3 week
684 whole microbial population growth period; e.g., *Gallionella*-like freshwater types and
685 *Mariprofundus*-like marine types) (Hallbeck and Pedersen 1990; Chan et al. 2011; Polgári et al.
686 2012a).

687 Organic biomarkers were not directly associated with Fe-rich biomat structures. Raman
688 and FTIR data show organic matter in the biomat lacework but is not diagnostic as to its type.
689 Based on these data, the diagenesis developed more in rocks represented by sample 75-2, where
690 only amorphous carbon remained in traces, and other type of organic material was consumed.
691 Preservation of organic material was best in sample 75-B5, in which organic material occurs in
692 180 of 2447 spectra, and more complex organic material, like oils and aromatic hydrocarbons,
693 were detected. Sample 78-D1 (SI 3-Fig) is more altered, because only traces of complex organic
694 material were preserved, and organic material—mostly D and G bands—occur in only 60 of 3456
695 spectra. Biomarkers cannot be isolated because of multiphase microbial activity and extensive
696 diagenetic overprinting.

697 **Fig. 15.**

698 **Syngenetic Mn system**

699 Mn-oxide formation in Mn-1 ore bed can be explained by the oxide surface catalysis model
700 advocated by Morgan (2005). Metal-oxide surfaces are able to accelerate Mn(II) oxidation by
701 redox reactions (e.g., hematite, goethite, lepidocrocite, and manganese dioxide; Wilson 1980; Sung
702 and Morgan 1981; Davies and Morgan 1989). Raman spectroscopy detected vernadite as poorly
703 crystallized mineral phase in the vicinity of hematite biomat lacework (Fig. 11).

704 In the case of Mn-2 and Mn-3, during the development of the Mn-oxide proto-ore, the first
705 product of microbial enzymatic Mn(II) oxidation probably was a bio-oxide (e.g., vernadite,
706 todorokite, birnessite), similar to the experimental studies of Villalobos et al. (2003); Bargar et al.
707 (2005); and Bodeï et al. (2007). This enzymatic Mn oxidation can be referred to as Cycle I. The
708 demand of microbial (enzymatic) Mn(II) oxidation is obligatory oxic conditions (> 2 mL/L
709 dissolved oxygen). This bio-oxide is an X-ray amorphous oxide similar to δ-MnO_2 (vernadite,
710 todorokite, birnessite; all detected by Raman), which is thought to be a disordered
711 thermodynamically unstable 7-Å-vernadite (hexagonal phyllomanganate) containing Mn(IV)
712 vacancy defects, with very small particle sizes (< 20 nm lateral dimensions), and having only two
713 or three MnO_2 layers stacked along the c-axis (Villalobos et al. 2003). A decrease in the dissolved
714 Mn(II) appears to act as a reductant for the biogenic oxide and control the stability of secondary
715 abiotic reaction products (Mn^{2+} components in minerals of Urucum support this process). Cation
716 binding, like Mg, supports phyllomanganate transformation to stable tectomanganate (Bodeï et al.
717 2007). Experimental studies showed that extracellular polymers from bacteria catalyze the
718 adsorption of Mg on the surface of the cells (Mandernack et al. 1995). Thus, the bacterial cells not
719 only directly oxidize Mn(II) to Mn(IV), but also, in the early stages of oxidation, influence the
720 cation composition of the Mn-oxide mineral being produced. Mineralogical changes similar to
721 these are likely to be commonplace in natural settings where bacterial oxidation of Mn(II) occurs

and may liberate sorbed metal ions or alter the rates of Mn-oxide surface processes, such as the degradation of organic molecules. It is noteworthy that microbes may exploit such mineral transformation reactions to indirectly control chemical conditions in the vicinity of the cell (Mandernack et al. 1995).

A series of detailed mineralogy and micro-textures are shown in Fig. 13 (sample 75-2 from Mn-2 ore bed). The studied part is representative for syngenetic microbial Mn oxidation. The distribution of vernadite/hollandite and very early diagenetic cryptomelane and nsutite show micro-nodules with mineralized microbial colonies with embedded organic matter, which appear to support this scenario. Recent results also comport with the study of Piacentini et al. (2013) who, based on petrographic evidence, reported that cryptomelane may not be the primary Mn mineral precipitated in the Neoproterozoic ocean floor.

6.2.2. Diagenetic minerals

Diagenetic Fe system

According to the diagenesis of Fe-rich biomats, the microbes produce poorly ordered ferrihydrite (lepidocrocite) as a primary mineral, which transforms to more ordered minerals, such as goethite or hematite (reduced form as magnetite), within a few months or years via dissolution-dehydration processes, as mentioned before (Konhauser 1998; Schwertmann and Cornell 2007; Gyollai et al. 2015). The main Fe oxide mineral in the filaments of our samples is hematite, but Raman analyses indicate that goethite also occurs (sample 75-B5, SI 12-Fig). In Mn-1, aegirine, and in Mn-2, rare jacobsite can represent mineralized Fe-biomats. In other rare occurrences, pyrite also occurs reflecting that locally anoxic conditions existed but did not become dominant. The fossilized Fe-rich biomats were rapidly and extensively encrusted by minerals, such as dolomite and silica, similar to what has been reported by Baele et al. (2008). Amorphous silica segregation

745 is derived by either the destruction of organic complexes or the transformation of ferrihydrite
746 (Baele et al. 2008).

747 Aegirine, occurring in cyclic microlaminae alternating with braunite in Mn-1, is the
748 diagenetic mineral form of FeOB (Fig. 10). Aegirine forms via early diagenesis from the
749 syngenetic Fe-oxi-hydroxides (ferrihydrite) and segregated silica, and represents a more stable
750 mineral phase. Aegirine micro-laminae represent the Fe-oxidizing microbial cycles, and braunite
751 represents the Mn cycle in silicified and stable form, also reported by Johnson et al. (2016). This
752 aegirine-braunite microbialite represents oxic/suboxic conditions (Listova, 1961). High-resolution
753 Raman investigations show that aegirine consumes segregated silica from hematitic biomat toward
754 the segregated silica via the transitional mineral riebeckite (Fig. 11). Riebeckite is also a common
755 constituent in BIF with aegirine reported by Savko (2006), who proposed metamorphic formation,
756 which does not fit with our observations. In Mn-1, aegirine forms a woven network (Fig. 11), the
757 hematitic proforma of biomat with the segregated silica. At the contact between hematite and silica,
758 apatite, vernadite/hollandite, and braunite occur. Similar to aegirine, braunite also consumes the
759 segregated silica. Our results fail to fit with the hydrothermal origin of aegirine proposed for
760 Paleoproterozoic Hotazel iron-formation, South Africa (Tsikos and Moore 2005); the cyclic
761 occurrence, worm-like consuming behavior, and also the mineral assemblage contradicts with that
762 scenario. Comparison with other natural aegirine occurrences, however, such as authigenic
763 aegirine in the lacustrine Green River Formation of Wyoming, U.S.A. (Fortey and Michie 1978),
764 shows a close similarity. In short, the reported authigenic formation of aegirine fits well with our
765 results, but the source of Na instead of volcanic activity was more probably the decomposition of
766 cell and extracellular polymeric substance organic material.

767 As the depth of the basin is not known, fragments of slightly lithified and re-sedimented
768 and cemented biomats occur, a shallow marine condition cannot be excluded. In such

769 environments, evaporitic alkaline sodium-rich conditions cannot be ruled out and indeed, are
770 preferred for aegirine formation. The high silica concentration favors aegirine formation instead
771 of clay minerals (Decarreau et al. 2004, 2008), which only sporadically occur in the samples
772 studied here (celadonite, chamosite).

773 Celadonite, a dominant mineral phase in the Mesozoic Úrkút Mn-deposit (Polgári et al.
774 2012b; 2016ab), is an Fe-mica reflecting suboxic neutral conditions. It is rare in Urucum
775 presumably because of high silica content.

776 Chamosite formation is favored by seawater solutions at low temperatures with a relatively
777 reduced pH, a low amount of SiO_2, high content of Fe^{2+} and Fe^{3+}, and a relatively high amount of
778 Al and Mg. Aluminum may be donated to the system by organic matter as reported by Maliva et
779 al. (1999) who showed that the aluminum content is greatly increased by complexation with
780 organic acids. Low silica concentration in solution is the most important condition for low-
781 temperature synthesis of clay minerals, as high silica concentration in solution inhibits their
782 formation (Harder 1976).

783 **Diagenetic Mn system**

784 In diagenesis, the stabilization of the syngenetic Mn oxide hydroxides proceeded and pure
785 forms, such as pyrolusite, ramsdellite, nsutite, hausmannite, manganite, and variable-cation-bound
786 forms (e.g., Na, K, Ca, Mg, Ba, Fe) such as cryptomelane, jacobsite, romanèchite, and manjiorite
787 grew (Giovanoli 1980; Mandernack et al. 1995; Villalobos et al. 2003; Bargar et al. 2005; Bodeï
788 et al. 2007; Johnson et al. 2016). Of note, as described by Polgári et al. (2012b), Maynard (2014),
789 and Johnson et al. (2016), rhodochrosite can result from the sporadic activity of heterotrophic
790 microbes during the early stages of diagenesis. Rhodochrosite is, however, only frequent in the
791 only fully analyzed kremydilite sample shown in Fig. 8. Otherwise, these poorly mineralized
792 cryptocrystalline mineral phases mix in a variable amount in the microlaminae as a manifestation

793 of mineralized Mn cycles. Similarly, pyrolusite, ramsdellite, and romanèchite indicate Mn
794 precipitation via diagenesis from low-temperature pore fluids as reported by Rajabzadeh et al.
795 (2017).

796 **6.3. Combined diagenesis of the two ore-forming microbial systems and other**
797 **microbial forms**

798 Harder (1978) noted that "…the silica content of sedimentary iron ores is found in quartz
799 and different iron-containing clay minerals. Chamosite, greenalite, cronstedtite, nontronite,
800 glauconite, and thuringite are common minerals in sedimentary iron ores. In general, all these
801 minerals are extremely fine-grained." We find that the formation of Mn-1 manganese ore in
802 Urucum influenced and changed this general protocol, despite the observation of quartz, local Fe
803 mica, and Fe clay. Highly alkaline pore water conditions in diagenesis (accompanied by elevated
804 Na content) caused aegirine precipitation instead of smectite (Decarreau et al. 2004, 2008). Low
805 silica content and Si/Fe ratio lead to chamosite formation under reduced pH and Eh conditions.
806 The high silica content probably influenced silica uptake of variable Mn oxide-hydroxide minerals.
807 Through stabilization caused by diagenetic processes, the Mn oxide hydroxide bound not only Fe^{2+}
808 and Fe^{3+} (e.g., jacobsite, hollandite minerals), but also silica (braunite, serandite), to form a highly
809 variable content of oxide-silicate mixed minerals. These are characterized by highly variable
810 composition. Texturally, mineral habits are strongly modulated (and perhaps templated) by
811 extracellular polymeric substances that form a network of pore spaces.

812 Braunite alternates with aegirine in Mn-1 and also occurs in Mn-2 representing the
813 mineralized Mn cycle (Fig. 10). The principal reasons for this viewpoint is that the system acts as
814 a diagenetic cycle owing to the fact that in Mn-1 an active oxide surface catalyst is likely
815 responsible for the mineral assemblage, as opposed to enzymatic Mn oxidation. The interpretation
816 is that braunite formation is due to combined diagenesis, as the segregated silica needed for

braunite is typical of Fe system diagenesis. The most likely formation of braunite is sedimentary or early diagenetic via biogeochemically mediated processes, as proposed by Serdyuchenko (1980) and Johnson et al. (2016). These studies report scenarios that are broadly similarly to our Urucum samples. Micro-textural evidence (Fig. 11–12) clearly shows the formation of braunite in the vicinity of hematite biomat, vernadite/hollandite, and apatite, via the consumption of segregated silica. While syngenetic mineralization took place under oxic neutrophilic conditions, slightly alkaline and oxic conditions were also reported for braunite formation (pH 9.5–9.9; Eh +0.43 V; Listova 1961); this comports well with our scenario.

Serandite, as an oxide-silicate mineral, also belong to this process (empirical composition of hollandite also can contain Si). The relationship between serandite and braunite is documented by our Raman profiles (Fig. 10). Jacobsite can be interpreted as the transitional form between Mn and Fe oxides.

6.4. Diagenesis of other minerals

After cell death and decomposition, as well as breakdown of extracellular polymeric substance, ions that were previously bound on their surfaces release Ca, Mg, Na, K, P, S, Si, Co, Zn, Ba, Sr, and rare earth elements. These are bioactive elements in accordance with Takahashi et al. (2007), Heim (2010), Meyer et al. (2012), Gyollai et al. (2017), and Yu et al. (2019). Formation of CO_3^{2-}, PO_4^{2-}, SiO_4^{4-}, and SO_4^{2-} anions commences and a complex transforming mineralization begins to take place, which (depending on local geochemical conditions) can result in clay mineral formation, mixed carbonates, feldspar, silica, and apatite. These poorly crystallized minerals can transform into more stable minerals over time (Konhauser 1998; Dupraz and Visscher 2005). The various geochemical features of Mn ores are modulated by such syngenetic and diagenetic processes. These include increased Co content compared with crustal abundance, a characteristic for Urucum ores as well as the Úrkút locality (Polgári et al. 2012b; Biondi and Lopez 2017).

841 Reaction of FeOB with Co proceeds easily, and MnOB can also oxidize Cobalt (Moffett 1990).
842 The liberalization of the cell surface-bound elements provides sources of elements e.g., in the case
843 of K in the formation of hollandite or Si in the case of braunite and other elements (Piacentini et
844 al. 2013).

845 Abundant quartz is common in Mn-1, which in part is attributable to the contribution of
846 detrital debris, but also represents the dominant segregated reactive silica phase (Cole and Shaw
847 1983; Fisk et al. 2006). In laboratory experiments, FeOB requires protection against concentration
848 and other types of stress, and silica is used for protection by microbes (Młoszewska et al 2018).
849 The amorphous silica can easily transform into more stable minerals, such as quartz (Herdianita et
850 al. 2000).

851 In unit Mn-1, a part of the segregated silica is stabilized as quartz, but the formation of
852 aegirine and braunite also consumed considerable amounts. Through combined diagenesis in Mn-2
853 and Mn-3, braunite and serandite formed, which consumed (and thus, reduced) the segregated
854 silica content.

855 Feldspar and kaolinite/dickite also formed, and rarely, cancrinite occurs. Kaolinite minerals
856 can form under acidic condition (pH 2-7) and within a wide temperature range. In our Urucum
857 samples, only kaolinite and dickite were detected in this class of minerals. Kaolinite can form at
858 low temperatures 25 °C (Dekoninck et al. 2018). Dickite typically forms under low pH conditions.
859 that forms in the temperature range between 120 and 280 °C (Eberl and Hower 1975; Inoue 1995),
860 and its presence is not supported by our results, which favor low-temperature conditions. On the
861 other hand, the reported important role of organic matter in the formation of dickite fits with our
862 results (Maliva et al. 1999). Similar to the Al demand of chamosite mentioned above, the mobility
863 of aluminum is enhanced by complexation with organic acids. In such systems, aluminum is

released and hence available for clay-mineral precipitation when the organo-aluminum complexes are destabilized (Maliva et al. 1999).

Cancrinite is a mixed silicate-carbonate-sulfate transitional mineral, which only sporadically occurs in Urucum, but nevertheless reflects the variability of diagenetic conditions. Apatite can precipitate at pH of 7–8 and occurs in micrometer-sized crystals in the silica-rich part of BIFs. Similar apatite occurrences were noted in our samples, based on Raman and CL analyses. Muscovite (hydromuscovite) is common in the studied samples and was most likely formed by the diagenesis of cyanobacteria filaments in Fe-rich microbialites by the leaching of biofilm alkali elements (Na, Ka, Al, Mg) (Ewers 1983; Gyollai et al. 2015, 2017).

Among carbonates, the occurrence of dolomite (ankerite) in Mn-1 can be considerable, and strontianite is present but scarce. Barite, gypsum, and johannite belong to the sulfates that form from marine sulfate and/or organic constituents. Barite, a mineral precipitating under typical oxic conditions (Eh > +0.2) at low temperature, is considered here as oxygen supply indicator, because barite occurring with hematite indicates conditions that are more oxic than occurring without hematite (Hanor 2000).

Considering the mineral assemblage, it is clear that the initially high segregated silica content did not support clay formation via early diagenesis, and silica-consuming minerals are numerous, which finally resulted in a decrease in silica content, which did not support quartz formation. In Mn-1, the quartz content is considerable compared with Mn-2 and Mn-3, which can be interpreted by the lower amount of Mn oxyhydroxides in Mn-1. Some quartz is probably of clastic origin as well as feldspar and mica, but authigenic formation of these minerals is also common in microbially mediated diagenetic processes, and non-luminescent minerals belong to this group (Marshall 1998; Hassouta et al. 1999) (Fig. 7).

887 The Mn-2 and Mn-3 beds represent real enzymatic Mn(II) oxidation with extremely high
888 amounts of Mn oxides and hydroxides, which overwhelm microbial Fe oxidation.
889 Most of the minerals detected here have well characterized formation conditions, as
890 summarized in Table 4. Based on mineralogy, proto-ore sedimentation and diagenesis occurred
891 under suboxic-obligatory to oxic and semi-neutral to alkaline conditions.
892 **6.5. Formation of kremydilites and oblate structures**
893 Kremydilites occur in varied forms shown in Figures 4A, C, E, G, I and K, which probably
894 correspond to different stages of development or growth. The presence of oblate structures and
895 pores inside and outside the kremydilites indicate that they and the sediments in which they formed
896 were a highly soft, porous, and permeable aqueous mud, within which pore fluids and gases could
897 form and migrate out (Figs. 4A-B, E-F, G-H and Fig. 16). Gas bubbles are common accompanying
898 phases of microbial mediation, which are trapped after burial, which is also characteristic of our
899 Urucum samples (Figs. 4A-B, E-F, and G-H). Different stages of the formation of a kremydilite,
900 including oblate structures, are shown in Fig. 4. The beginning of the microbial activity inside the
901 aqueous mud deposited in the marginal basin floor, composed mainly of birnessite, ferrihydrite,
902 organic matter, and Mn and Fe oxides (Fig. 8). Organic matter becomes oxidized (Fig. 4)
903 generating CO_2 and/or CH_4 and/or H_2, which forms intergranular bubbles (Figs. 4A-B, E-F, and
904 G-H) that migrate towards the surface (Fig. 16B). After the first oxidation stage of organic matter,
905 a cluster of pores remains, constituting the nucleus zone of the kremydilite structures (Fig. 4A-B
906 and C-D). The reactivation of microbial oxidation of organic matter generates the first concentric
907 layer of pores (= shell) around the previously formed nucleus (Fig. 4E-F). The repetition of this
908 process can generate multiple concentric layers of pores (shells) (Fig. 4G-H), and evolve to form
909 a complex kremydilite (Fig 4 I-J) with many layers, marked by the accumulation of pores
910 concentrically organized around the nucleus, as in the kremydilite sample 48 (Figs. 4K and 8A-

911 B). The reactivation process of microbial oxidation can cease at any time, forming kremydilites
912 with one or two concentric layers around the nucleus or repeating at different times, forming
913 complex structures with multiple concentric layers (Figs. 4I-J and K). The oblate structures, now
914 preserved in the Urucum ores, did not reach the basin floor and were preserved during diagenesis.
915 The cryptomelane needle mesh structure, the prismatic cryptomelane crystallites, and the micro-
916 nodules were microbialites or organominerals (Dupraz et al. 2009), and the cylindrical holes are
917 likely tube escape structures through which gas bubbles migrated from the zone of microbial
918 activity (organic matter oxidation).

919 The mineralogy of the kremydilite from sample 48 (Fig.8C-E) seems to reflect the changes
920 caused by the diagenesis of the original sediment while it was buried (Fig. 16), as defined by
921 Raiswell (1987). Burial initiated the diagenesis and ore formation (Figs. 8C-D and 16B)
922 simultaneously with successive cycles of heterotrophic microbial activity, which formed the
923 kremydilite concentric layers of cryptomelane, birnessite, ferrihydrite, rhodochrosite crystallized
924 in the nucleus zone, braunite, rhodochrosite, cryptomelane crystallized in the bottom part, and
925 ferrihydrite and cryptomelane in the upper part (Figs. 8C-D, and Fig. 16B). The complete oxidation
926 of the layer and of all the kremydilites contained therein, forming the massive Mn-2 and 3 ore
927 type, is a process that began during early diagenesis and was extended after lithification through
928 microbial mediation. The origin of the oblate form of kremydilites, with concentric layers around
929 a nucleus, is a consequence only of the oxidation of the organic matter (biomass) during diagenesis
930 and the subsequent formation of pores. This process is independent of the chemical and/or mineral
931 composition of the original sediment (but Mn reduction occurs). The original and present chemical
932 and mineral composition of kremydilites arises from: (a) the abundant sedimentation of Mn
933 oxyhydroxides via enzymatic oxidation and, to a lesser extent, of Fe oxyhydroxides and (b) the
934 changes caused by diagenesis, which transforms the sediment into different minerals, as

935 manganese (Fe-)-rich biomass becomes manganese-rich sediment, then Mn(Fe)-rich sedimentary
936 rock. This is the origin of an economical Mn ore deposit. The absence of iron kremydilites in the
937 jaspilites, similar to the Mn ore beds, shows that the formation of kremydilites was a unique
938 process that only occurred in the Mn-rich sediments, forming a new type of manganese ore.
939 **Fig. 16.**
940 It was previously proposed that kremydilite formed by photoferrotroph microbial processes
941 (photosynthetic) under anoxic conditions (Biondi and Lopez 2017), which is not in accordance
942 with the interpretation of recent results on the mineral assemblage. Our new interpretation is that
943 these formed in suboxic-oxic conditions and slightly alkaline pH. To reach a plausible
944 interpretation, as a first step, it is important to determine the formation processes of kremydilite.
945 The mineral assemblage of the studied sample supports an early diagenetic origin, rather than
946 syngenesis (Fig. 8). The kremydilite structure resembles both nodules and concretions; thus, to
947 compare these structures, definitions are necessary. Nodules and concretions are very similar, and
948 sometimes, these terms are used interchangeably. However, while concretions incorporate material
949 of the host sediment, nodules contain solely authigenic phases (Raiswell and Fisher 2000; Jackson
950 2005; Baumann et al. 2016; and references therein). In our case, there are only authigenic minerals
951 based on mineral assemblage in kremydilite and in oblate structures. Consequently, based on
952 definition, these cannot be concretions but instead are most probably better termed nodules. The
953 definition of a nodule is also contradictory in our case, however, as in sedimentology and geology
954 terminology a nodule is usually defined as a small, irregularly rounded knot, mass, or lump of a
955 mineral or mineral aggregate that typically has a contrasting composition from the enclosing
956 sediment or sedimentary rock (Jackson 2005). This is not the case in Urucum. In general, the
957 objects we dub “nodules” lack any internal structure except for the preserved remnants of original
958 bedding or fossils, which is also not the case here, as kremydilite is a concentric structure

(structured pore system forming “pore shells” without cement infilling, which is also a difference). A further aspect is mineralogy, which differs from the typical ones occurring in nodules and concretions including most commonly calcite, siderite, chert, apatite (phosphorite), anhydrite, and pyrite. In Urucum, kremydilite occurs as high-quality Mn oxide ore.

Hence, based on the above definitions and features, kremydilite could be considered as a unique concretion-like structure, which lacks the background sediment, and the accumulated sediment is the result of successive phases of oxidation of organic matter (Fig. 4) during diagenesis (Fig. 8). Authigenic mineral formation occurs during syngenesis and early diagenesis. In this sense, kremydilite, the most characteristic structure in Mn-2 and Mn-3 ore beds, can be interpreted as a unique type of syngenetic and diagenetic structure and represent a unique type of ore (also taking into consideration Maynard (2010) and Kuleshov (2011), on ore types). This interpretation is further in accordance with the main features of kremydilites, like variable-preserved porous content, signs of gas production and migration, concentric structures, and the multiple stages of development. Then again, differences, such as lack of cementation and incorporation of material of the host sediment, are consequential. All things considered, this is a rare ore-type, as reported by Biondi and Lopez (2017).

Yet, how did these kremydilite structures form *en masse*? The interpretation that we favor is that heterotrophic cell colonies randomly activated in the microbialite sediment after burial in suboxic neutral/alkaline conditions, side-by-side with lithification and stabilization of minerals (Mn reduction (MnR) and reactive organic matter decomposition via heterotrophic microbial mediation can be referred to as Cycle II). Rhodochrosite is a common (dominant) component in the kremydilite structure in the core zone and also in the shells, from the core to the margin (Fig. 8). The process probably continues only along the poorly crystallized reactive vernadite and todorokite. Cryptomelane and braunite are more stable. They do not take part in the process, nor

983 does ferrihydrite, as the system does not reach the Fe reduction zone (FeR) because of the high
984 Mn concentration and relatively low organic matter content.

985 Why is Urucum (Neoproterozoic, Brazil) concretionary and not laminated like in Úrkút
986 (Mesozoic, Hungary)? Much less organic matter was buried, and this fact did not lead to the
987 formation of a horizontally continuous MnR zone realizing rhodochrosite laminae. Instead, local
988 heterotrophic cell colony centers caused the formation of kremydilite in the biomat system,
989 overprinting the syngenetic lamination, causing a nodular, concretional appearance. The
990 kremydilites are most probably diagenetic and not syngenetic, as rhodochrosite is diagenetic, as
991 referred to in Polgári et al. (2012b), Maynard (2014), and Johnson et al. (2016).

992 Both FTIR and RAMAN analyses show that substances inside and outside the oblate
993 structures evolved in different ways. This is exemplified by the presence of pores in each
994 kremydilite shell, the absence of pores inside the bubbles, and the absence of micro-nodules inside
995 the oblate structures. At the contact zone of the "more" oxic outer part and "suboxic" inner part,
996 spherical enrichment of cryptomelane occurred, forming a dense margin (rim). The micro-texture
997 of this rim (and also the outer and inner part) is microbial and contain "diffusional channels" (SI
998 11-Fig).

999 **6.6. Basin development**

1000 As mentioned, unit Mn-1 follows the basin floor relief, while Mn-2 and Mn-3 occur as
1001 horizontal beds in the ironstone. This can be viewed as a special series produced by syngenetic
1002 processes via authigenic mineral accumulation, summarized according to chronology of
1003 syngenetic and diagenetic processes in Fig. 17. The ore formation commenced with flooding on
1004 porous fluvial sediments, and the ore forming fluids (Fe^{2+} and Mn^{2+}) infiltrated and microbially
1005 colonized the pores in a woven form, and around the clastic particles in the sediment to the depth
1006 where diffusion was active (supported by microbially mediated micro-texture, which is

1007 syngenetic). Initially, biomass, composed of Mn and Fe hydroxides, organic matter, manganoan
1008 and ferroan carbonate and amorphous silica, deposited on the basin floor. In the extracellular
1009 polymeric substance network, diagenetic minerals along with clastic material dominated (based on
1010 CL). The ore formation started with enzymatic Fe oxidation, as the Raman profiles of Mn-1
1011 samples prove, resulting in a well-developed biomat system. This offered oxide surface catalysis
1012 for Mn oxidation, which was not enzymatic during Mn-1 because the level of oxygen supply did
1013 not reach the obligatory oxic level (Morgan 2005). The dynamic processes affected the top zone
1014 of sediments up to the diffusion depth, which moved upward in time, forming the Mn-1 ore bed.
1015 The effect of fluvial contribution decreased via marine flooding, and the clastic
1016 contribution ceased gradually, offering excellent calm conditions for undisturbed Fe- and Mn-
1017 biomat formation, resulting in fine cyclic mineral lamination (mineralized biomats, microbialite)
1018 (Fig. 10, SI 12-Fig). The FeOB continued forming ironstone (Biondi and Lopez 2017), under
1019 suboxic conditions, in which oxygen supply was not favorable for MnOB.
1020 Enzymatic Mn oxidation starting as chemical nutrients (Mn^{2+}) were in the system, and the
1021 Mn-2 and later Mn-3 layers suddenly occurred in the Fe sediments. This made conditions more
1022 oxic and obligatory oxic. The sudden change is caused simply by the turning of oxygen supply
1023 from suboxic (dissolved oxygen-DO 0.2-2.0 mL/L) to obligatory oxic (DO > 2.0 mL/L) conditions,
1024 which is the *criterion* of enzymatic Mn(II) oxidation. In the background of formation of Mn-2 and
1025 Mn-3, the microbial Fe oxidation continued, as supported by the well detectable micro-lamination
1026 (cyclicity) of microminerals. The sharp contact in the field representing that horizon where Fe is
1027 forced back to local suboxic parts. The Fe^{2+} ascending fluid does not reach the obligatory oxic
1028 zone as a dominant contribution, because microbes oxidize it in the suboxic zone (Fig. 15). The
1029 Raman profiles clearly show that the Fe biomat system existed via all Mn ore beds, but with
1030 different intensity. Fe and Mn occurred together in an intimate form similar to Úrkút (Polgári et

al. 2012b). A similar sharp boundary (contact zone) occurs between gray (black) shale and Mn carbonate ore in Úrkút, which is also the result of change in the oxygen supply becoming obligatory oxic. This was a sensitive redox system for enzymatic Mn oxidation (Polgári et al. 2016a).

Summarizing the ore formation, Fig. 17 shows our model for the process that generated the massive manganese ore with kremydilites, found in the Mn-2 and Mn-3 layers of Urucum. After the formation of the ferrihydrite, birnessite, organic matter, and rhodochrosite mud-like biomass (Fig. 17A), the microbial reduction generates micro-nodules with the minerals of the original sediment in the nucleus involved by ferrihydrite (Fig. 17B), then by rhodochrosite and braunite. Late diagenetic and post-diagenetic oxidation generates Mn-2 and Mn-3 ore layers, composed of massive and/or zoned, concentric, spherical nodules, and/or zoned nodules with an eye shape (Fig. 17C). The formation of kremydilites begins simultaneously or immediately after the formation of micro-nodules, in places where a cluster of microbes begins to oxidize organic matter, generating pores and producing methane, CO_2, and/or H_2 bubbles. This activity forms a small structure with a homogeneous and porous nucleus bound by a porous layer, which may involve the nucleus totally or partially, formed at the edge of the zone of microbial activity. The resumption of microbial activity around the same nucleus will cause greater oxidation where a greater amount of non-oxidized organic matter is available, generally near and on the outside of the last formed layer.

Fig. 17.

Late and post-diagenetic processes cause complete oxidation of the micro-nodules and kremydilites (Fig. 17D). Raman analyses of spherical nodules of sample 75-B2 show that central parts of micro-nodules were transformed to hollandite/vernadite and organic matter, around which cryptomelane and nsutite (pyrolusite and ramsdellite) crystallize (Fig. 17F). The minerals of the kremydilites are entirely oxidized during post-diagenetic conditions and transformed mainly into

1055 cryptomelane, hollandite, braunite, with little organic matter, hematite and goethite, generating the
1056 massive manganese ore of the Urucum and Mn-2 and Mn-3 layers (Fig. 17G). From time to time,
1057 coarse detrital influx disturbed the calm formation of microbial mats, resulting in turbiditic
1058 accumulation. It has been proposed that these turbidites were caused by earthquakes from rifting
1059 activity (Biondi and Lopez 2017). The most probable source of ore was hydrothermal, exhalative
1060 in submarine environment (Biondi and Lopez 2017 and references therein).
1061

1062 **7. CONCLUSIONS**

1063 High-resolution Raman and AT-FTIR spectroscopy used on Mn ore samples of Mn-1, Mn-2, and
1064 Mn-3 ore beds in the ca. 550 Ma Urucum deposit yields information used to construct a self-
1065 consistent model for the formation of these ores. This approach was used to document numerous
1066 metastable, poorly crystallized mineral phases and organic matter that represent the remnants of
1067 primary microbially mediated Mn and Fe minerals.

1068 1. Based on mineralogy, the proto-ore sedimentation and the diagenesis of the Urucum Mn
1069 ore deposit occurred under suboxic-obligatory oxic and semi-neutral to alkaline conditions, where
1070 microbial Mn^{2+} enzymatic oxidation (with reactive organic matter) resulted in fine-grained
1071 accumulation of Mn oxides (Cycle I).

1072 2. The sharp contact between the manganese and iron layers represents that horizon, where
1073 the obligatory oxic conditions facilitated the start of enzymatic Mn oxidation (Mn engine), which
1074 overwhelmed microbial Fe oxidation. The Fe biomat system existed via all Mn ore beds, but with
1075 different intensity. Fe and Mn occurred together in an intimate form.

1076 3. Heterotrophic microbially mediated Mn reduction (Cycle II) developed only locally
1077 embedded in the form of oxide kremydilite structure, which represents a unique, new ore type.
1078 Among the kremydilite structures, regular double-microbial mineralogical cycles formed with

alternating mineralized Fe- and Mn-oxidizing bacterial activity (microbialite). Detailed study raised that kremydilite and oblate structures formed on the effect of heterotrophic cell colonies, whose activity overprinted the original lamination. The Mn reduction resulted in rhodochrosite (Cycle II) a characteristic constituent in these structures. The reason that rhodochrosite formation did not become dominant in the form of laminae is the smaller amount of organic matter accumulation, which allowed for Mn reduction via diagenesis only in random centers, resulting in diagenetic kremydilite. That is why oxic-suboxic mineral stabilization and diagenetic mineral formation became dominant.

4. Mn-1 follows the basin floor relief, whereas Mn-2 and Mn-3 occur as horizontal beds in the ironstone pile. The ore formation started with flooding on porous fluvial sediments, and the ore forming fluids (Fe^{2+} and Mn^{2+}) infiltrated and microbially colonized the pores in a woven form, and around the clastic particles on chemical (Fe^{2+}, Mn^{2+}) nutrients, in the sediment to the depth where diffusion was active. In the extracellular polymeric substance network, diagenetic minerals along with clastic material became dominant.

5. The Fe-oxidizing bacteria continued forming ironstone, under suboxic conditions, in which oxygen supply was not favorable for Mn-oxidizing bacteria.

6. From time to time, coarse detrital influx disturbed the calm biomat formation, resulting in clast accumulation, which interrupted the fine microbial lamination. These turbidites may have been caused by earthquakes (due to rifting activity).

8. REFERENCES

Almeida, F.F.M., 1946. Origem dos minérios de ferro e manganês de Urucum (Corumbá, Estado do Mato Grosso): Boletim da Divisão de Geologia e Mineralogia do Departamento Nacional da Produção Mineral (DNPM, Rio de Janeiro), 119, 58p.

1103 Angerer, T., Hagemann, S.G., Walde, D.H.G., Halverson, G.P., Boyce, A.J., 2016. Multiple metal
1104 source in glaciomarine facies of the Neoproterozoic Jacadigo iron formation in the "Santa
1105 Cruz deposit", Corumbá, Brazil. Precambrian Research 275, p. 369-393.
1106 Babinski, M., Boggiani, P.C., Fanning, C.M., Fairchild, T.R., Simo, C.M., Sial, A.N., 2008. U-Pb
1107 SHRIMP geochronology and isotope chemostratigraphy (C, O, S) of the Tamengo
1108 formation, Southern Paraguay Belt, Brazil. South American Symposyum on Isotope
1109 Geology, 6th, San Carlos de Bariloche (Argentina), p. 160.
1110 Baele, J.M., Bouvain, F., De Jong, J., Matielli, N., Papier, S., Préat, A., 2008. Iron microbial mats
1111 in Modern and Phanerozoic environments. In Instruments, Methods, and Missions for
1112 Astrobiology XI (Vol. 7097, p. 70970N 12p.). International Society for Optics and
1113 Photonics.
1114 Banfield J.F. and Nealson K.H. (eds), 1997. Geomicrobiology: Interactions between Microbes and
1115 Minerals. Reviews in Mineralogy 35, Mineralogical Society of America, Washington, D.C.
1116 Bargar, J.R., Tebo, B. M., Bergmann, U., Webb, S.M., Glatzel, P., Chiu, V.Q., Villalobos, M.,
1117 2005. Biotic and abiotic products of Mn (II) oxidation by spores of the marine Bacillus sp.
1118 strain SG-1. American Mineralogist 90(1):143-154.
1119 Baumann, L.M., Birgel, D., Wagreich, M., Peckmann, J., 2016. Microbially-driven formation of
1120 Cenozoic siderite and calcite concretions from eastern Austria. Austrian Journal of Earth
1121 Sciences 109(2):211-232.
1122 Bazylinski, D.A., Frankel, R.B., 2003. Biologically controlled mineralization in prokaryotes. In:
1123 Biomineralization (Dove P.M., De Yoreo J.J. and Weiner S. eds). Reviews in Mineralogy
1124 and Geochemistry 54, Mineralogical Society of America and the Geochemical Society,
1125 Washington, D.C.
1126 Bengtson, S., 2002. Origins and early evolution of predation. Paleontological Society papers 8:
1127 289-317.
1128 Berner, R.A., 1980. Early diagenesis: a theoretical approach, 250 pp., Princeton University Press,
1129 Princeton.
1130 Biagioni, C., Capalbo, C, Lezzerini, M., Pasero, M., 2014. Ferrihollandite, $BaMn^{4+}_{6}Fe^{3+}_{2}O_{16}$, from
1131 Apuan Alps, Tuscany, Italy: description and crystal structure. Eur. J. Mineral. 26, 171–178.

1132 Biondi, J.C.; Lopez, M., 2017. Urucum Neoproterozoic–Cambrian manganese deposits (MS,
1133 Brazil): Biogenic participation in the ore genesis, geology, geochemistry, and depositional
1134 environment. Ore Geology Reviews 91:335-386.
1135 Bodeï, S., Manceau, A., Geoffroy, N., Baronnet, A., Buatier, M., 2007. Formation of todorokite
1136 from vernadite in Ni-rich hemipelagic sediments. Geochimica et Cosmochimica Acta
1137 71(23):5698-5716.
1138 Chan, C.S., Fakra, S.C., Emerson, D., Fleming, E.J., Edwards, K.J., 2011. Lithotrophic iron-
1139 oxidizing bacteria produce organic stalks to control mineral growth: implications for
1140 biosignature formation. Multidisciplinary Journal of International Society for Microbial
1141 Ecology 5:717-727.
1142 Chen, J.Y., Schopf, J.W., Bottjer, D.J., Zhang, C.Y., Kudryavtsev, A.B., Tripathi, A.B., Wang,
1143 X.Q., Yang, Y.H., Gao, X. and Yang, Y., 2007. Raman spectra of a Lower Cambrian
1144 ctenophore embryo from southwestern Shaanxi, China. Proceedings of the National
1145 Academy of Sciences 104(15):6289-6292.
1146 Chilingar, G.V., Buryakovsky, L.A., Eremenko, N.A and Gorfunkel, M.V., 2005. Geology and
1147 Geochemistry of Oil and Gas: Developments in Petroleum Science 52, 138-142.
1148 Chumakov, N. M., 2009. The Baykonurian glacio-horizon of the Late Vendian. Stratigraphy and
1149 Geological Correlation 17 (4): 373–381. doi:10.1134/S0869593809040029
1150 Chumakov, N. M., 2011. Glacial deposits of the Baykonur Formation, Kazakhstan and
1151 Kyrgyzstan. Geological Society, London, Memoirs Chapter 26, 36(1): 303-
1152 307.doi:10.1144/M36.26.
1153 Cole, T.G., Shaw, H.F., 1983. The nature and origin of authigenic smectites in some recent marine
1154 sediments. Clay Miner. 18:239-252.
1155 Coleman, M.L., 1985. Geochemistry of diagenetic non-silicate minerals: kinetic considerations.
1156 Philos. Trans. R. Soc. Lond. A315:39–56.
1157 Costa, M.L., Fernandez, O.J.C., Ribeiro, P.A., Silva, N.C., Poellmann, H., 2005. Contribuições
1158 mineralógicas e geoquímicas sobre a origem do minério de manganês do Morro do Urucum
1159 (Corumbá, Brasil): Simpósio Brasileiro de Metalogenia, 1th, Gramado (RS, Brasil),
1160 Abstracts, CDROM.

1161 Dardenne, M.A., 1998. Modelo hidrotermal exalativo para os depósitos de Fe-Mn da região de
1162 corumbá, Mato Grosso do Sul: Congresso Brasileiro de Geologia, 40th, São Paulo, Brasil,
1163 Abstracts, p. 158.
1164 Davies, S.H., Morgan, J.J., 1989. Manganese (II) oxidation kinetics on metal oxide surfaces.
1165 Journal of Colloid and Interface Science 129(1): 63-77.
1166 Decarreau, A., Petit, S., Martin, F., Farges, F., Vieillard, P., Joussein, E., 2008. Hydrothermal
1167 synthesis, between 75 and 150ºC, of high-charge, ferric nontronites. Clays and Clay
1168 Minerals 56(3):322-337.
1169 Decarreau, A., Petit, S., Vieillard, P., Dabert, N., 2004. Hydrothermal synthesis of aegirine at 200
1170 C. European Journal of Mineralogy 16(1):85-90.
1171 Dekoninck, A., Moussi, B., Vennemann, T., Jamoussi, F., Mattielli, N., Decrée, S., Chaftar, H.-
1172 R., Hatira, N., Yans, J., 2018. Mixed hydrothermal and meteoric fluids evidenced by
1173 unusual H- and O-isotope compositions of kaolinite-halloysite in the Fe(-Mn) Tamra
1174 deposit (Nefza district, NW Tunisia). Applied Clay Science 163, 33–45.
1175 https://doi.org/10.1016/j.clay.2018.07.007
1176 Dorr, J.V.N., 1945. Manganese and iron deposits of Morro do Urucum, Mato Grosso, Brazil:
1177 United States Geological Survey Bulletin 946A, 47p.
1178 Dupraz, C., Visscher, P.T., 2005. Microbial lithification in marine stromatolites and hypersaline
1179 mats. Trends Microbiol. 13:429-438.
1180 Dupraz, S., Parmentier, M., Ménez, B., Guyot, F., 2009. Experimental and numerical modeling of
1181 bacterially induced pH increase and calcite precipitation in saline aquifers. Chemical
1182 Geology 265:44-53.
1183 Eberl, D., Hower, J. O. H. N., 1975. Kaolinite synthesis: The role of the Si/A1 and (alkali)/(H+)
1184 ratio in hydrothermal systems. Clays and Clay Minerals 23:301-309.
1185 Ehrenreich, A., Widdel, F., 1994. Anaerobic oxidation of ferrous iron by purple bacteria, a new
1186 type of phototrophic metabolism. Applied and Environmental Microbiology 60(12):4517-
1187 4526.
1188 Ehrlich, H.L., 2002. Geomicrobiology. (4th edition). Marcell Dekker Inc., 183 – 274.
1189 Ewers, W.E., 1983. Chemical Factors in the Deposition and Diagenesis of Banded Iron-Formation,
1190 in: A.F. Trendall and R.C. Morris (Eds.): Developments in Precambrian Geology 6, Iron
1191 formation: Facts and Problems. Elsevier, pp. 491-512.

1192 Fisk, M.R., Popa, R., Mason, O.U., Storrie-Lombardi, M.C., Vicenzi, E.P., 2006. Iron-magnesium
1193 silicate bioweathering on Earth (and Mars?). Astrobiol. 6(1):48-69.
1194 Fortey, N.J., Michie, U.M., 1978. Aegirine of possible authigenic origin in Middle Devonian
1195 sediments in Caithness, Scotland. Mineralogical Magazine 42(324):439-442.
1196 Frei, R., Døssing, L.N., Gaucher, C., Boggiani, P.C., Frei, K.M., Bech Árting T., Crowe, S.A.,
1197 Freitas, B.T., 2017. Extensive oxidative weathering in the aftermath of a late
1198 Neoproterozoic glaciation – Evidence from trace element and chromium isotope records in
1199 the Urucum district (Jacadigo Group) and Puga iron formations (Mato Grosso do Sul,
1200 Brazil). Gondwana Research 49, 1-20.
1201 Freitas, B.T., Warren, L.V., Boggiani, P.C., Paes de Almeida, R., Piacentini, T., 2011. Tectono-
1202 sedimentary evolution of the Neoproterozoic BIF-bearing Jacadigo Group, SW Brazil:
1203 Sedimentary Geology, 238, p. 48-70.
1204 Garrels, R.M., MacKenzie, F.T., 1971. Evolution of Sedimentary Rocks. Ed. Nortom, New York.
1205 Germs, G.J.B., 1972. New y fossil from Nama Group, South West Africa. American Journal of
1206 Sciences 272:752-761.
1207 Germs, G.J.B.; Gaucher, C., 2012. Nature and extent of a late Ediacaran (ca. 547 Ma) glaciogenic
1208 erosion surface in southern Africa. South African Journal of Geology 115, 91-
1209 102.doi:10.2113/gssajg.115.91.
1210 Giovanoli, R., 1980. On natural and synthetic manganese nodules. In: Varentsov I.M. and
1211 Grasselly Gy. (Eds.) Geology and Geochemistry of Manganese. 1. Akadémiai Publishing
1212 House, Budapest, 159-203.
1213 Götze, J., Plötze, M., Götte, T., Neuser, R.D., Richter, D.K., 2002. Cathodoluminescence (CL) and
1214 electron paramagnetic resonance (EPR) studies of clay minerals. Mineralogy and Petrology
1215 76(3-4):195-212.
1216 Graf, J.L., O'Connor, E.A., Leeuwen, P.V., 1994. Rare earth element evidence of origin and
1217 depositional environment of late Proterozoic ironstone beds and manganese ore deposits,
1218 SW Brazil and SE Bolivia: Journal of South American Earth Sciences 7, p. 115-133.
1219 Grant, S.W.F., 1990. Shell structure and distribution of Cloudina, a potential index fossil for the
1220 terminal Proterozoic. American Journal of Sciences 290:261-294.
1221 Grotzinzer, J.P., Bowring, S.A., Saylo, B.Z., Kaufman, A.J., 1990., Biostratigraphic and
1222 geochronology constraints on early animal evolution. Science 270:598-604.

1223 Gyollai, I., Polgári, M. P., Fintor, K., Popp, F., Mader, D., Pál-Molnár, E., 2015. Microbially
1224 mediated deposition of postglacial transition layers from the Neoproterozoic Otavi Group,
1225 Namibia: evidence of rapid deglaciation after the Sturtian cryogenic period. Carpathian
1226 Journal of Earth and Environmental Sciences 10(1):63-76.
1227 Gyollai, I., Polgári, M., Fintor, K., Pál-Molnár, E., Popp, F., Koeberl, C., 2017. Microbial activity
1228 records in Marinoan Snowball Earth postglacial transition layers connecting diamictite
1229 with cap carbonate (Otavi Group, NW-Namibia). Austrian Journal of Earth Sciences
1230 110(1): 2-18.
1231 Hallbeck, L., Pedersen, K., 1990. Culture parameters regulating stalk formation and growth rate
1232 of Gallionella ferruginea. Microbiology 136(9):1675-1680.
1233 Hanor, J.S., 2000. Barite-celestine geochemistry and environments of formation. Reviews in
1234 Mineralogy and Geochemistry 40:193-275.
1235 Haralyi, N.L.E., Walde, D.H.G., 1986. Os minerais de ferro e manganês da região de Urucum,
1236 Mato Grosso do Sul, in Schobenhaus, C., and Coelho, C.E.S., ed., Principais Depósitos
1237 Minerais do Brasil. Departamento Nacional da Produção Mineral (Brasilia, Brazil), v.2,
1238 p.127-144.
1239 Harder, H., 1976. Nontronite synthesis at low temperatures. Chemical Geology 18(3):169-180.
1240 Harder, H., 1978. Synthesis of iron layer silicate minerals under natural conditions. Clays and Clay
1241 Minerals 26(1):65-72.
1242 Hassouta, L., Buatier, M.D., Potdevin, J.L., Liewig, N., 1999. Clay diagenesis in the sandstone
1243 reservoir of the Ellon Field (Alwyn, North Sea). Clays and Clay Minerals 47(3):269-285.
1244 Hasui, Y., Almeida, F.F.M., 1970. Geocronologia do Centro-Oeste brasileiro. Boletim da
1245 Sociedade Brasileira de Geologia (São Paulo), 19:5-26.
1246 Heim, C.N., 2010. An integrated approach to the study of biosignatures in mineralizing biofilms
1247 and microbial mats. PhD thesis, Georg-August-University of Göttingen, Germany. p. 183
1248 Herdianita, N.R., Browne, P.R.L., Rodgers, K.A., Campbell, K.A., 2000. Mineralogical and
1249 textural changes accompanying ageing of silica sinter. Mineralium Deposita 35:48-62.
1250 Hofmann, H.J., Mountjoy, E.W., 2001. Namacalathus-Cloudina assemblage in Neoproterozoic
1251 Miette Group (Byng Formation), British Columbia – Canada oldest shelly fossil. Geology
1252 29:1091-1094.
1253 Inoue, A., 1995. Determination of aspect ratios of clay-sized particle. Clay Science 9(5):259-274.

1254 Jackson, J.A., 2005. Glossary of geology. 5th revised and enlarged ed. ISBN 3-540-27951-2.
1255 Berlin: Springer, 900 p.
1256 Jehlička, J., Šťastná, A., Přikryl, R., 2009. Raman spectral characterization of dispersed
1257 carbonicaceous matter in decorative crystalline limestones. Spectrochimica Acta Part A:
1258 Molecular and Biomolecular Spectroscopy 73(3):404-409.
1259 Johnson, J.E., Webb, S.M., Ma, C., Fischer, W.W., 2016. Manganese mineralogy and diagenesis
1260 in the sedimentary rock record. Geochim. et Cosmochim. Acta 173, 210-231.
1261 Klein, C., Ladeira, E.A., 2004. Geochemistry and mineralogy of Neoproterozoic banded iron-
1262 formations and some selected, siliceous manganese formations form the Urucum district,
1263 Mato Grosso do Sul, Brazil.Economic Geology 99, p. 1233-1244.
1264 Konhauser, K.O., 1998. Diversity of bacterial iron mineralization: Earth-Science Revs. 43:91–121.
1265 Kuleshov, V.N., 2011. Manganese deposits: Communication 1. Genetic models of manganese ore
1266 formation. Lithology and Mineral Resources 46, 473–493.
1267 https://doi.org/10.1134/S0024490211050038
1268 Leeuwen, P. van, Graaf, J.L., 1987. The Urucum-Mutum iron and manganese deposits, Mato
1269 Grosso do Sul, Brazil, and Santa Cruz, Bolivia. Part 1-The region's potential as an economic
1270 source of iron and manganese: Geologie en Mijnbouw 65, p. 317-325.
1271 Leonardos, O.H., Walde, D.H.G., 1982. Sobre a estratigrafia e a gênese dos depósitos de manganês
1272 a luz do vulcanismo Jacadigo: Congresso da Sociedade Brasileira de Geociências, 27th,
1273 Salvador, Abstracts, p. 203.
1274 Listova, L.P., 1961. Experimental studies of physic-chemical conditions of sedimentation of
1275 manganese oxides and carbonate. Ocherki Metallogen. Osadochn. Porod. Publication of
1276 the AN USSR, Moscow, 319-351.
1277 Maliva, R.G., Dickson, J.A.D., Fallick, A.E., 1999. Kaolin cements in limestones; potential
1278 indicators of organic-rich pore waters during diagenesis. Journal of Sedimentary Research
1279 69(1):158-163.
1280 Mandernack, K.W., Post, J., Tebo, B.M., 1995. Manganese mineral formation by bacterial spores
1281 of the marine Bacillus, strain SG-1: evidence for the direct oxidation of Mn (II) to Mn (IV).
1282 Geochimica et Cosmochimica Acta 59(21):4393-4408.
1283 Marshall, D.J., 1998. Cathodoluminescence of Geological Materials. Unwin Hyman, Boston, 146
1284 pp.

1285 Maynard, J.B., 1983. Geochemistry of Sedimentary Ore Deposits. Ed. Springer Verlag, New York
1286 Maynard, J.B., 2010. The chemistry of manganese ores through time: a signal of increasing
1287 diversity of earth-surface environments. Economic Geology 105, 535–552.
1288 https://doi.org/10.2113/gsecongeo.105.3.535
1289 Maynard, J.B., 2014. Manganiferous sediments, rocks, and ores, in: Treatise on Geochemistry.
1290 Elsevier, pp. 327–349.
1291 Meyer, E.E., Quicksall, A.N., Landis, J.D., Link, P.K., Bostick, B.C., 2012. Trace and rare earth
1292 elemental investigation of a Sturtian cap carbonate, Pocatello, Idaho: Evidence for ocean
1293 redox conditions before and during carbonate deposition. Precambrian Research 192-195,
1294 89-106.
1295 Młoszewska, A.M., Cole, D.B., Planavsky, N.J., Kappler, A., Whitford, D.S., Owttrim, G.W.,
1296 Konhauser, K.O., 2018. UV radiation limited the expansion of cyanobacteria in early
1297 marine photic environments. Nature Communications 9, 3088.
1298 Moffett, J.W., 1990. Microbially meddiated cerium oxidation in sea-water. Nature 345 (6274):421-
1299 423.
1300 Morgan, J.J., 2005. Kinetics of reaction between O_2 and Mn (II) species in aqueous solutions.
1301 Geochimica et Cosmochimica Acta 69(1):35-48.
1302 Novick, A., 1955. Growth of Bacteria. Ann. Rev. Microbiol. 9: 97-110.
1303 O'Connor, E.A., Walde, D.H.G., 1985. Recognition of an Eocambrian orogenic cycle in SW
1304 Brazil and Bolivia: Zbl. Geologie Paläontologie 1, p. 1441-1456.
1305 Okolo, G.N., Neomagus, H.W., Everson, R.C., Roberts, M.J., Bunt, J.R., Sakurovs, R., Mathews,
1306 J.P., 2015. Chemical–structural properties of South African bituminous coals: Insights
1307 from wide angle XRD–carbon fraction analysis, ATR–FTIR, solid state 13C NMR, and
1308 HRTEM techniques. Fuel *158*, pp.779-792.
1309 Orange, D., Knittle, E., Farber, D., Williams, Q., 1996. Raman spectroscopy of crude oils and
1310 hydrocarbonic fluid inclusions: A feasibility study. The Geochemical Society, Special
1311 Publication 5:65-81.
1312 Parry, L.A., Boggiani, P.C., Condon, D.J., Garwood, R.J., Leme, J.M., McIlroy, D., Brasier, M.D.,
1313 Trindade, R., Campanha, G.A.C., Pacheco, M.L.A.F., Cleber Q. C. Diniz, C.Q.D.,
1314 Alexander, G., Liu, A.G., 2017. Ichnological evidence for meiofaunal bilaterians from the

terminal Ediacaran and earliest Cambrian of Brazil: Nature (Ecology and Evolution), v. 1(10), p. 1455-1464. DOI: 10.1038/s41559-017-0301-9.

Piacentini, T., Vasconcelos, P.M., Farley, K.A., 2013. $^{40}Ar/^{39}Ar$ constraints on the age and thermal history of the Urucum Neoproterozoic banded-iron formation, Brazil. Precambrian Research 228:48-62.

Polgári, M., Gyollai, I., 2019 Connection between biomineralization and the evolution of Earth. Frontiers in Microbiology (in press)

Polgári, M., Gyollai, I., Fintor, K., Horváth, H., Pál-Molnár, E., Biondi, J.C., 2019. Microbially mediated ore forming processes and the cell mineralization. Frontiers in Microbiology (in press)

Polgári, M., Hein, J. R., Tóth, A.L., Pál-Molnár, E., Vigh, T., Bíró, L., Fintor, K., 2012a. Microbial action formed Jurassic Mn-carbonate ore deposit in only a few hundred years (Úrkút, Hungary). Geology 4(10):903-906.

Polgári, M., Hein, J.R., Bíró, L., Gyollai, I., Németh, T., Sajgó, C., Fekete, J., Schwark, L., Pál-Molnár, E., Hámor-Vidó, M., Vigh, T., 2016a. Mineral and chemostratigraphy of a Toarcian black shale hosting Mn-carbonate microbialites (Úrkút, Hungary). Palaeogeography, Palaeoclimatology, Palaeoecology 459:99-120.

Polgári, M., Hein, J.R., Németh, T., Pál-Molnár, E., Vigh, T., 2013. Celadonite and smectite formation in the Úrkút Mn-carbonate ore deposit (Hungary). Sedimentary Geology 294, 157-163.

Polgári, M., Hein, J.R., Vigh, T., Szabó-Drubina, M., Fórizs, I., Bíró, L., Müller, A., Tóth, A.L., 2012b. Microbial processes and the origin of the Úrkút manganese deposit, Hungary. Ore Geology Reviews 47:87-109.

Polgári M, Németh T, Pál-Molnár E, Futó I, Vigh T, Mojzsis S.J., 2016b. Correlated chemostratigraphy of Mn-carbonate microbialites (Úrkút, Hungary). Gondwana Research 29, 1, 278-289. DOI: 10.1016/j.gr.2014.12.002.

Putzer, H., 1958. Die Kryptomelan- und Jaspelit-Lagerstätten von Corumbá im Staate Mato Grosso, Brasilien: Erzmet all, v. 11, p. 527-538.

Raiswell, R., 1987 Non-steady state microbial diagenesis and the origin of carbonate concretions and nodular limestones. In: Marshall J D. eds. of “Diagenesis of sedimentary sequences”. London: Geological Society Spec Pub 36:41-54.

1346 Raiswell, R., Fisher, Q.J., 2000. Mudrock-hosted carbonate concretions: a review of growth
1347 mechanisms and their influence on chemical and isotopic composition. Journal of the
1348 Geological Society 157(1):239-251.
1349 Rajabzadeh, M. A., Haddad, F., Polgári, M., Fintor, K., Walter, H., Molnár, Z., Gyollai, I., 2017.
1350 Investigation on the role of microorganisms in manganese mineralization from Abadeh-
1351 Tashk area, Fars Province, southwestern Iran by using petrographic and geochemical data.
1352 Ore Geology Reviews 80:229-249.
1353 Savko, K.A., 2006. Phase equilibria in rocks of the paleoproterozoic banded iron formation (BIF)
1354 of the Lebedinskoe deposit, Kursk Magnetic Anomaly, and the petrogenesis of BIF with
1355 alkali amphiboles. Petrology 14(6):567-587.
1356 Schneider, G., 1984. Zur Mineralogie and Lagerstättenbildung der Mangan- und
1357 Eisenerzvorkommen de Urucum Distriktes (Mato Grosso, Brasilien): Frankfurter Geowiss.
1358 Arb. Serie C 1, (Frankfurt), 205 p.
1359 Schreck, P., 1984. Geochemische Klassifikation und Petrogenese der Manganerze des Urucum
1360 Distriktes bei Corumbá (Mato Grosso do Sul, Brasilien): Frankfurter Geowiss. Arb. Serie C
1361 1, (Frankfurt), 206 p.
1362 Schwertmann, U., Cornell, R.M., 2007. Iron Oxides in the Laboratory: Preparation and
1363 Characterization. Wiley-VCH, 188 pp.
1364 Serdyuchenko, D.P., 1980. Precambrian biogenic-sedimentary manganese deposits. In Geology
1365 and Geochemistry of Manganese, Vol. 2 (ed. I. M. Varentsov and G. Grasselly), Stuttgart,
1366 61-88.
1367 Skinner, H.C.W., 1993. A review of apatites, iron and manganese minerals and their roles as
1368 indicators of biological-activity in black shales. Precambrian Research 61, 3-4, 209-229.
1369 Straub, K.L., Benz, M., Schink, B.,Widdel, F., 1996. Anaerobic, nitrate-dependent microbial
1370 oxidation of ferrous iron. Applied and environmental microbiology 62(4):1458-1460.
1371 Sung, W., Morgan, J.J., 1981. Oxidative removal of Mn (II) from solution catalysed by the γ-
1372 FeOOH (lepidocrocite) surface. Geochimica et Cosmochimica Acta 45(12):2377-2383.
1373 Takahashi, Y., Hirata, T., Shimizu, H., Ozaki, T., Fortin, D., 2007. A rare earth element signature
1374 of bacteria in natural waters? Chemical Geology 244(3–4):569-583.

1375 Trompette, R., Alvarenga, C.J.S., Walde, D.H.G., 1998. Geological evolution of the
1376 Neoproterozoic Corumbá graben system (Brazil) – Depositional context of the stratified Fe
1377 and Mn of the Jacadigo Group: Journal of south American Earth Sciences 11, 587-597.
1378 Trudinger, P.A., Swaine, D.J. eds., 1979. Biogeochemical cycling of mineral-forming elements
1379 (Vol. 3). Elsevier. pp. 1-672.
1380 http://oriasmail.citromail.hu/dl3/?tid=7aab706ea32020b3008ea46a063058758
1381 Tsikos, H., Moore, J.M., 2005. Sodic metasomatism in the Palaeoproterozoic Hotazel
1382 iron-formation, Transvaal Supergroup, South Africa: implications for fluid–rock
1383 interaction in the Kalahari manganese field. Geofluids 5(4):264-271.
1384 Urban, H., Stribrny, B., Lippolt, H., 1992. Iron and manganese deposits of the Urucum district,
1385 Mato Grosso do Sul, Brazil. Economic Geology 87:1375-1392.
1386 Villalobos, M., Toner, B., Bargar, J., Sposito, G., 2003 Characterization of the manganese oxide
1387 produced by Pseudomonas putida strain MnB1. Geochimica et Cosmochimica Acta
1388 67(14):2649-2662.
1389 Walde, D.H.G., 1981. Die Mangan- und Eisenvorkommen von Urucum, Mato Grosso, Brasilien:
1390 Erste Ergebnisse und ein weiteres Program, Zbl. Geol. Paläontologie 1, p. 505-513.
1391 Walde, D.H.G., 1988. Das proterozoische Paraguay-Araguaia Orogen in West-Brasilien,
1392 Ausgehend von Untersuchungen im Raum Corumbá: Habilitationsscrift, Albert Ludwigs
1393 Universität, Freiburg, 122 p. (umpublished).
1394 Walde, D.H.G., Gierth, E., Leonardos, O.H., 1981. Stratigraph and mineralogy of the manganese
1395 ores of Urucum, Mato Grosso, Brazil: Geologie Rundschau 70, p. 1077-1085.
1396 Whitney, D.L., Evans, B.W., 2010. Abbreviaations for names of rock-forming minerals. American
1397 Mineralogist 95, 1, 185-187. DOI: 10.2138/am.2010.3371.
1398 Wignall, P.B., 1994. Black shales: Oxford, UK, Clarendon Press, 124 p.
1399 Wilson, D.E., 1980. Surface and complexation effects on the rate of Mn (II) oxidation in natural
1400 waters. Geochimica et Cosmochimica Acta 44(9):1311-1317.
1401 Young, G.M., 1976. Iron-formation and galciogenic rocks of the Rapitan Group, Northwest
1402 Territories, Canada. Precambrian Research 3, 137-158.
1403 Yu, W., Polgári, M., Gyollai, I., Fintor, K., Szabó, M., Kovács, I., Fekete, J., Yuansheng, Du.Y.,
1404 Zhou, Q., 2019. Microbial metallogenesis of the Cryogenian manganese ore deposits in
1405 South China on micrometer scale. Precambrian Research 322, 122-135.

Zwietering, M.H., Jongenburger I, Rombouts F.M, van Riet T.K., 1990. Modeling of the bacterial growth curve. Appl. Envir. Microbiol. 56:1875-1881.

ACKNOWLEDGMENTS

The authors thank the support of National Research, Development and Innovation Office, National Scientific Research Found No. 125060. We also thank the Companies VALE URUCUM and MCR URUCUM, for allowing us access to their mines and allowing the collection of samples of their ores. S.J.M. thanks the University of Lorraine (France) for a visiting professorship appointment during the writing phase of this paper. Comments by anonymous reviewers, as well as editorial handling by Wilson Teixeira and Eric Tohver are appreciated.

FIGURE CAPTION

Fig. 1. (A) Map showing the positions of manganese layers Mn-1 to Mn-3 and the mines of the central Urucum region (modified after Urban et al. 1992, Biondi and Lopez 2017) and, (B) S – S' regional geological section. The thicknesses of layers Mn-1 to Mn-3 are exaggerated by a factor of approximately ten. UTM coordinates referenced to Datum WGS 84.

Fig. 2. Stratigraphic columns made in the region of manganese and iron mines of Urucum, and sample locations. Note that the Mn-1 layer is not flat, and its shape is adapted to the basin floor while Mn-2 and Mn-3 are plane-parallel (modified after Urban et al. 1992, Biondi and Lopez 2017).

Fig. 3. Representative samples of Mn-1 (A-C), Mn-2, and Mn-3 (D-F). (A) Sample of silt, massive Mn-1 (fragments of quartz, altered feldspar, apatite, chert). (B) Clast-bearing, massive-, arkosean-, Fe-rich sample from Lower Mn-1. (C) Oblate amygdalite-bearing massive, fine-grained manganese ore, with arkosean Fe-rich bands. (D-F) Kremydilite in its most developed form after diagenesis, sawed according to orthogonal planes, showing its oblate form. (D) Kremydilite sawn according to orthogonal planes, showing its oblate form. (E) The concentric organization of the several layers that constitute complex kremydilite, each concentric layer with limits marked by pores. (F) Schematic drawing of a cut kremydilite, illustrating its shape and its interior. For more representative samples see SI-3-Fig.

1436 Fig. 4. Different stages of development or growth of kremydilites. The text in the figure explains
1437 each stage. Bubbles: oblate structures. (A-I): photos of polished surfaces, (K)
1438 photomicrograph.
1439 Fig. 5. Photomicrographs (reflected light) of the micro-nodules that constitute the massive parts of
1440 the Mn-2 and Mn-3 ore beds. (A-B) The larger nodules, less than 0.8 mm (3A) at present
1441 are formed mainly by cryptomelane and hollandite, and the matrix is hematite (Biondi and
1442 Lopez 2017). (C-D) Most micro-nodules are zoned, with a dark, porous nucleus. A, C, D
1443 photos are photomicrographs made by optical rock microscope, reflective mode, (B) is
1444 back scattered electron image by EPMA.
1445 Fig. 6. Micro-textural features of samples (photomicrographs). Mineralized microbial
1446 biosignatures. (A) biomat (arrow, sample 36-A); (B) clastic particles (arrow, reflected light
1447 1 N, sample 4B); (C) mineralized microbial biosignatures (arrows, reflected light 1 N,
1448 sample 75-2, rectangle shows enlarged area); (D) mineralized microbial biosignatures
1449 (arrows, reflected light 1 N, sample 75-2, enlarged area on C); (E) mineralized microbial
1450 biosignatures (arrows, 1N, transmitted light, sample 7); (F) mineralized microbial
1451 biosignatures (arrows, reflected light 1 N, sample 10); (G, H) mineralized microbial
1452 biosignatures (arrows, 1N, transmitted light, samples 32 and 36-A1). On (G) putative
1453 cyanobacteria are shown by arrow (based on similarity published by Gyollai et al., 2015
1454 on Namibian Neoproterozoic sample).
1455 Fig. 7. Mineralogy observed under cathodoluminescence microscopy. (A, B) Typical CL image of
1456 Mn-1 samples. Bright blue luminescence is characteristic of kaolinite group-dickite
1457 (supported by Raman spectroscopy, Götze et al. 2002); bright yellow minerals are apatite
1458 grains; the fine-grained rhodochrosite (mixed carbonate) show dull reddish (orange)
1459 luminescence color. (C, E, G) transmitted light photos by 1N, crossed N, and CL images
1460 of the same area of sample 7. (D, F, H) transmitted light photos by 1N, crossed N, and CL
1461 images of the same area of sample 10. Circles show the clastic-like but non-luminescent
1462 mineral grains.
1463 Fig. 8. Results of the FTIR analyses of the kremydilite sample 48-B and interpretation of the
1464 results. (A-B) Image of sample (A), its concentric shells (layers) and location of the
1465 analyzed points (B). (C) Simplified proposed syngenetic minerals that build up each layer.
1466 (D) Interpretation of early diagenetic minerals detected by FTIR. Abbrev.: fehy-

1467 ferrihydrite; Mnox-Mn oxide and hydroxide; manji-manjiorite; todor-todorokite; cryp-
1468 cryptomelane; birn-birnessite; qz-quartz; rhod-rhodochrosite; Mndol-Mn-bearing
1469 dolomite; brau-braunite; goeth-goethite; spherical micro-nodules border: fluffy
1470 micronoduliferous host material.
1471 Fig. 9. Representative part of oblate structure, sample 36-A (A-B) and mineral distribution
1472 (FTIR)(C). (A-B) Microtexture of a part of oblate structure, OM, reflective mode (1 and
1473 xN), arrows show mineralized microbial signatures and diffusion channels. Abbrev: Ferri-
1474 ferrihydrite; Goe-goethite; Rhod-rhodochrosite; Cryp-cryptomelane; C org-organic matter;
1475 Q-quartz; Dol-dolomite; Brau-braunite; Ramsd-ramsdellite; Mx-matrix material; inhom-
1476 inhomogenous, italic-the component is poorly crystallized, minor.
1477 Fig. 10. Raman profiles. Representative alternating (cyclic) mineral micro-lamination in sample 7
1478 (Mn-1) (for detailed section see SI 12-Fig).
1479 Fig. 11. Distribution of minerals in sample 4B (A-B) by Raman spectroscopy. Aegirine, riebeckite,
1480 braunite, quartz, hematite, apatite, hollandite/vernadite identified by Raman (A-B). Mineral
1481 abbreviations are after Whitney and Evans (2010) except bra = braunite, ver = vernadite,
1482 hol = hollandite.
1483 Fig. 12. Distribution of minerals in sample 4B (A-B) by Raman spectroscopy. Braunite, hematite,
1484 apatite, quartz, and K-feldspar were identified by Raman (A-B). Mineral abbreviations are
1485 after Whitney and Evans (2010); except bra = braunite.
1486 Fig. 13. Distribution of minerals in sample 75-2 by Raman spectroscopy. Cryptomelane,
1487 hollandite/vernadite and nsutite (pyrolusite+ramsdellite) were identified in a micronodule,
1488 as shown in Fig. 5C-D.
1489 Fig. 14. Composite map from the investigated oblate structure sample 36-A by Raman
1490 spectroscopy—measured areas are indicated on the picture (those places which are detailed
1491 in SI 14-Fig are in yellow color). Abbrev.: M-matrix area, 001 line-rim area.
1492 Fig. 15. Physico-chemical vs bacterial Fe and Mn oxidation (modified after Garrels and
1493 MacKenzie 1971; Maynard 1983). Eh in Volt. Concerning NR, FeR, MnR, and SR see
1494 Table 5 and note that “suboxic” zone is used for these diagenetic zones in the sense of an
1495 oxidant agent. Sharp-turning contact between Fe and Mn mineralization as transformation
1496 to obligatory oxic conditions is estimated at Eh = 0.4 V (DO > 2mL/L).

Fig. 16. Kremydilite formation environment on the floor of the Urucum basin. (A) General environment schematically showing the formation of a layer such as Mn-2 or Mn-3. (B) Detail of "mud" or silica-clayey biomass sedimented on the basin floor (left side), showing the evolutionary stages that occur from sedimentation to late diagenesis (right side).

Fig. 17. Cartoon showing the processes of formation of the micro-nodules, oblate structures, kremydilites, and the massive manganese ore of the Mn-2 and Mn-3 layers of Urucum. Abbrev.: CM-organic matter. Read text for details.

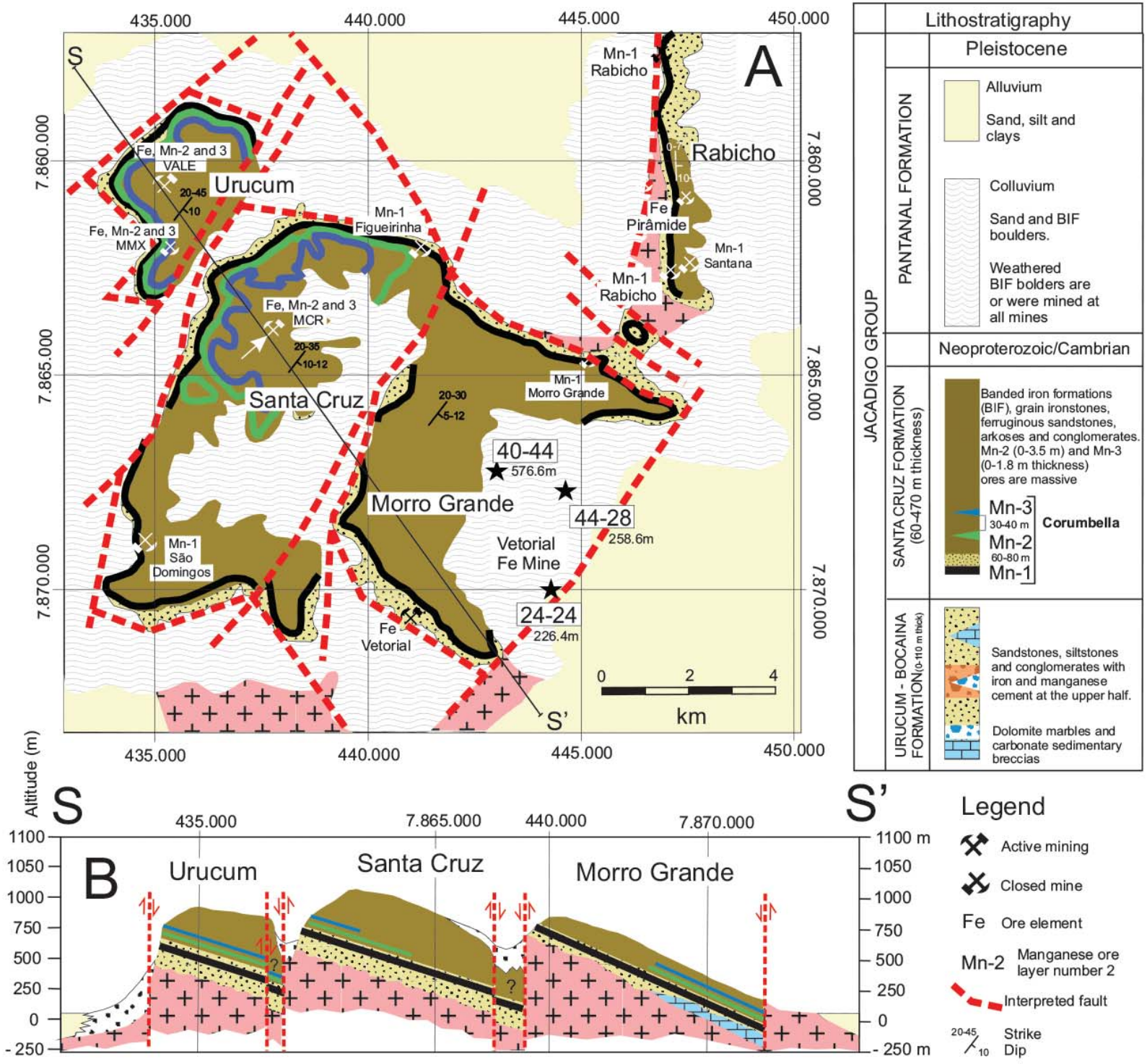
A
435.000
440.000
445.000
450.000
7.860.000
7.865.000
7.870.000
S
S'
Urucum
Santa Cruz
Morro Grande
Rabicho
Fe, Mn-2 and 3
VALE
Fe, Mn-2 and 3
MMX
Fe, Mn-2 and 3
MCR
Mn-1
Figueirinha
Mn-1
Rabicho
Fe
Pirâmide
Mn-1
Santana
Mn-1
Rabicho
Mn-1
Morro Grande
Mn-1
São
Domingos
Fe
Vetorial
Vetorial
Fe Mine
20-45
10
20-35
10-12
20-30
5-12
40-44
576.6m
44-28
258.6m
24-24
226.4m
0
2
4
km
Lithostratigraphy
Pleistocene
PANTANAL FORMATION
Alluvium
Sand, silt and clays
Colluvium
Sand and BIF boulders.
Weathered BIF bolders are or were mined at all mines
Neoproterozoic/Cambrian
JACADIGO GROUP
SANTA CRUZ FORMATION (60-470 m thickness)
Banded iron formations (BIF), grain ironstones, ferruginous sandstones, arkoses and conglomerates. Mn-2 (0-3.5 m) and Mn-3 (0-1.8 m thickness) ores are massive
Mn-3
30-40 m
Mn-2
60-80 m
Mn-1
Corumbella
URUCUM - BOCAINA FORMATION(0-110 m thick)
Sandstones, siltstones and conglomerates with iron and manganese cement at the upper half.
Dolomite marbles and carbonate sedimentary breccias
B
S
S'
Altitude (m)
435.000
7.865.000
440.000
7.870.000
1100
1050
1000
750
500
250
0
- 250
1100 m
1050
1000
750
500
250
0
- 250 m
Urucum
Santa Cruz
Morro Grande
Legend
Active mining
Closed mine
Fe Ore element
Mn-2 Manganese ore layer number 2
Interpreted fault
20-45/10 Strike Dip

Figure 1.

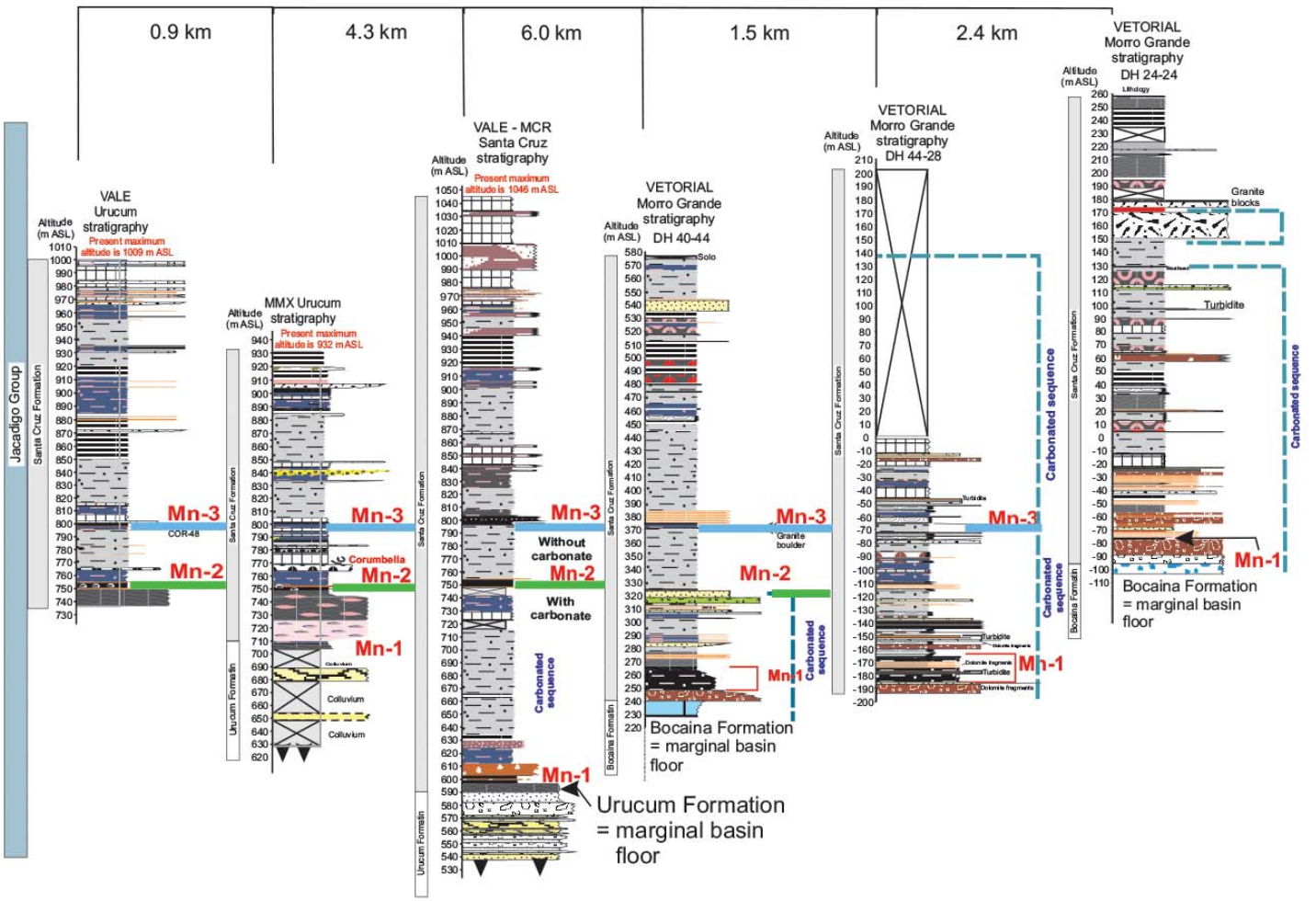

Legend

- Massive jaspilite
- Nodular jaspilite
- Banded jaspilite - Banded BIF - Interstratification of bands of massive hematite and chert with narrow carbonate lens
- Laminated jaspilite - Banded hematite intercalated with banded chert, sometimes peloidal.
- Laminated and nodular jaspilite - Laminated and peloidal stratified BIF with chert and ferroan carbonate intercalations
- Banded and nodular jaspilite - Peloidal stratified BIF - Massive peloidal BIF, with chert and ferroan carbonate intercalations
- Nodular and laminated jaspilite
- Jaspilite with embedded jasper nodules
- Disorganized jaspilite
- Massive hematite, gray in color, with ferruginous chert and some nodules (COR-117)
- Massive hematite with minor nodules
- Massive hematite with black nodules and jasper lenses
- Massive manganese ore layer
- Mn-1 clastic-chemical manganese ore, with qz + fK fragments cemented by manganese minerals
- Mn-1 clastic-chemical manganese-rich rock, with qz (+fK) fragments cemented by manganese minerals
- Jaspilite with arkosic, micro-conglomerate or sandstone layers (channels)
- Ferruginous coarse/mediu/fine grained sandstone
- Banded, coarse ferruginous sandstone
- Grain ironstone with intercalations or chert lenses, reddish in color
- Banded-, arkosian sandstone or micro-conglomerate with parallel lamination
- Turbidite or avalanche (channels)
- Intraclastic float ironstone
- Polimitic conglomerate/microconglomerate with sandy hematite matrix
- Polimitic conglomerate/microconglomerate with sandy hematite matrix and altered fragments
- Polimitic, non ferruginous conglomerate
- Polimitic, non ferruginous conglomerate, with dolomit2 blocks
- Ferruginous-, channeled-, arkosean sandstone
- Jaspilite with bioturbation
- Laminated BIF with worm tracks
- Sedimentary breccia with hematite pebbles
- Talus breccia with jaspilite boulders
- Oolitic grain ironstone
- Cherty-, grain ironstone
- Massive, quartz poor arkose, pinksh in color, with some jaspilite lens
- Grain ironstone
- Grain ironstone
- Sandstone with low angle crossed stratification
- Sandstone with crossed lamination
- Whitish and greensh dolomite with interbeded dolomite breccia

Figure 2.

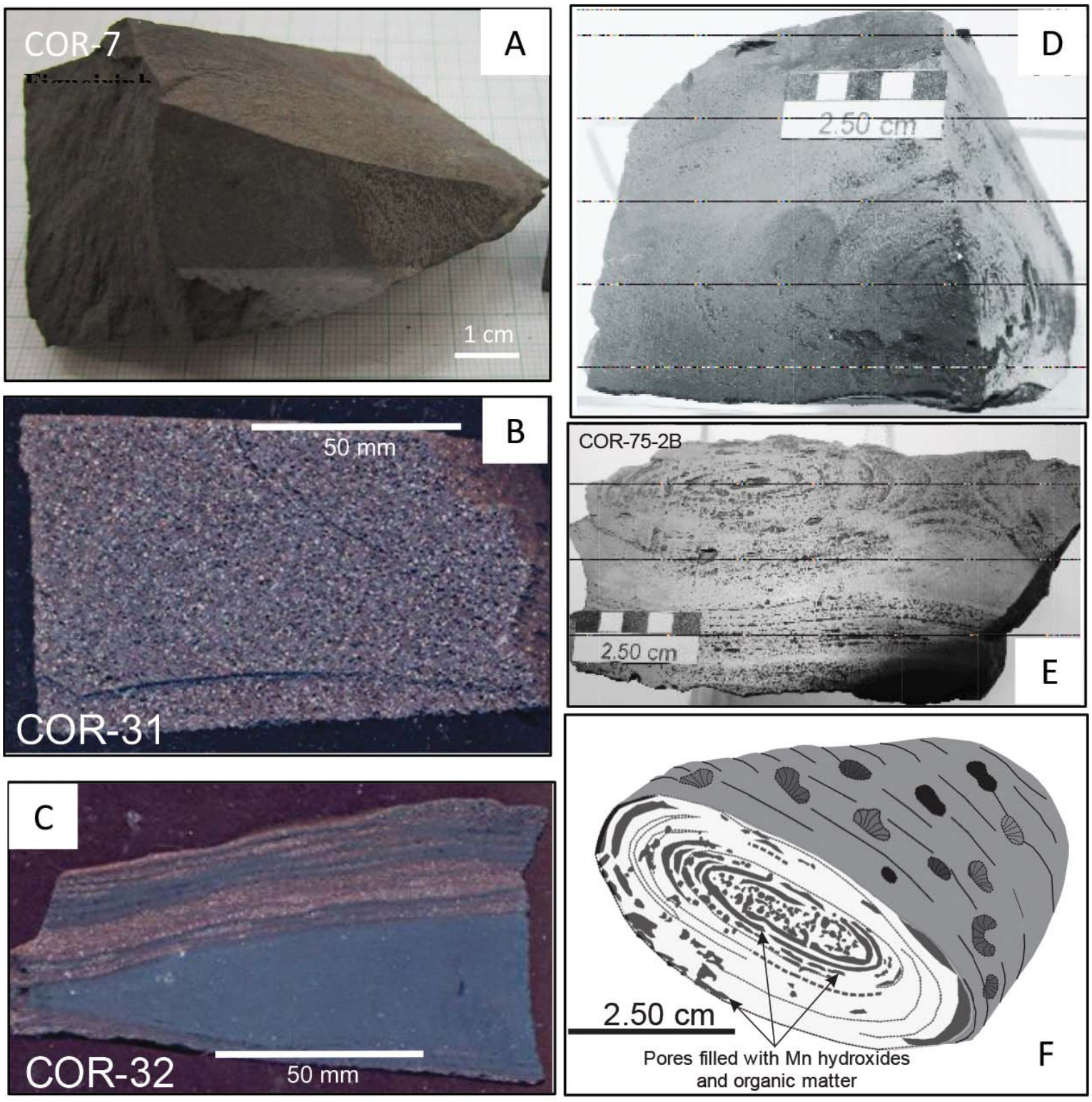
COR-7
A
1 cm
B
50 mm
COR-31
C
COR-32
50 mm
D
2.50 cm
COR-75-2B
2.50 cm
E
2.50 cm
Pores filled with Mn hydroxides
and organic matter
F

Figure 3.

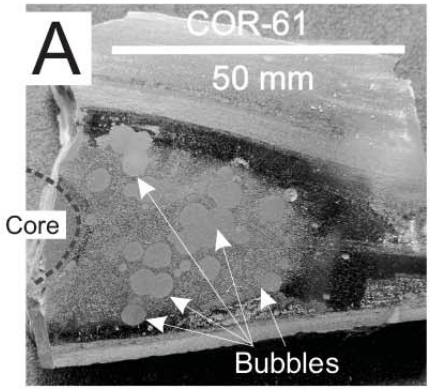

The onset of microbial activity at a site of the manganese sediment layer oxidizes organic matter and generates gas bubbles.

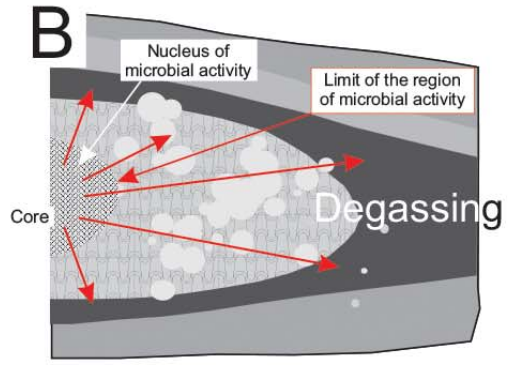

After the oxidation of the organic matter, there remains a nucleus constituted by pores formed where organic matter was oxydized.

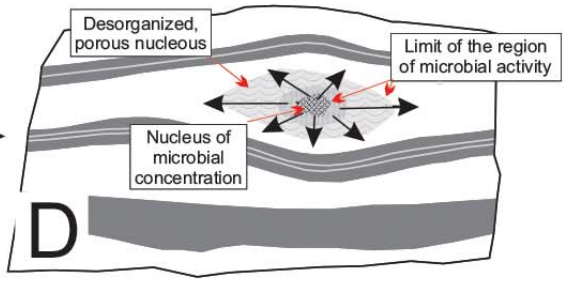

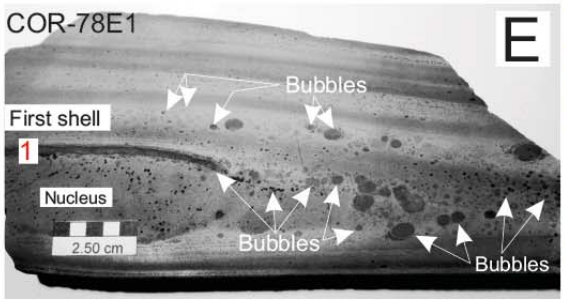

The first reactivation of the microbial activity oxidizes the organic matter existing around the nucleus generating a first layer (shell) of pores around the nucleus.

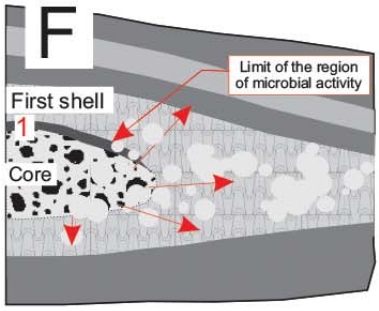

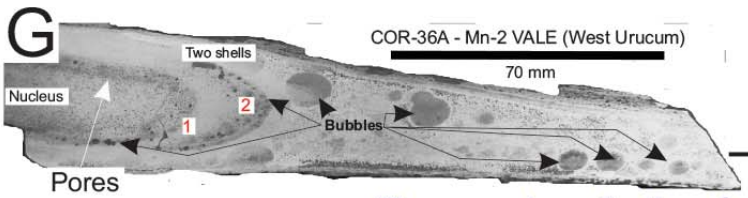

The second reactivation of microbial activity forms the second pore layer (second shell)

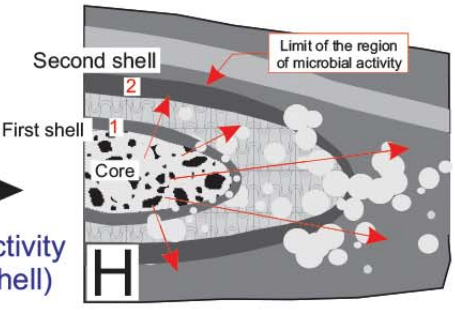

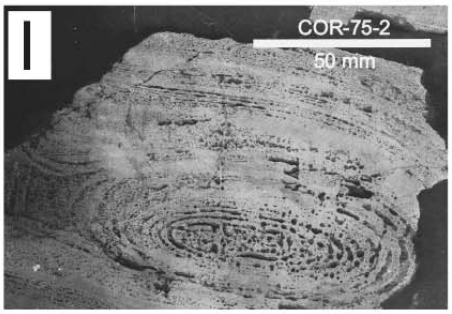

In a well-developed kremydilite, the amount of concentric layers of pores (shells) indicates how many times there was reactivation of microbial activity in that location

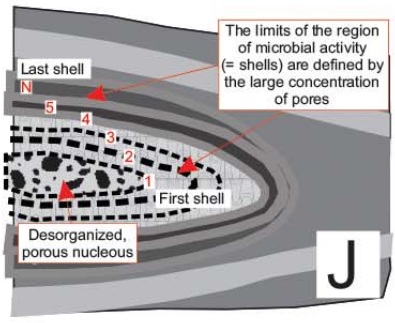

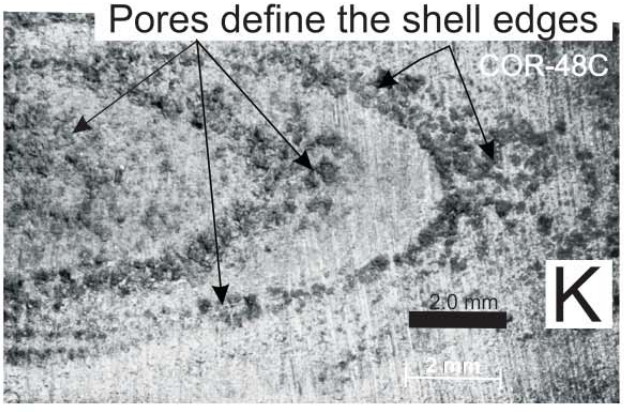

Figure 4.

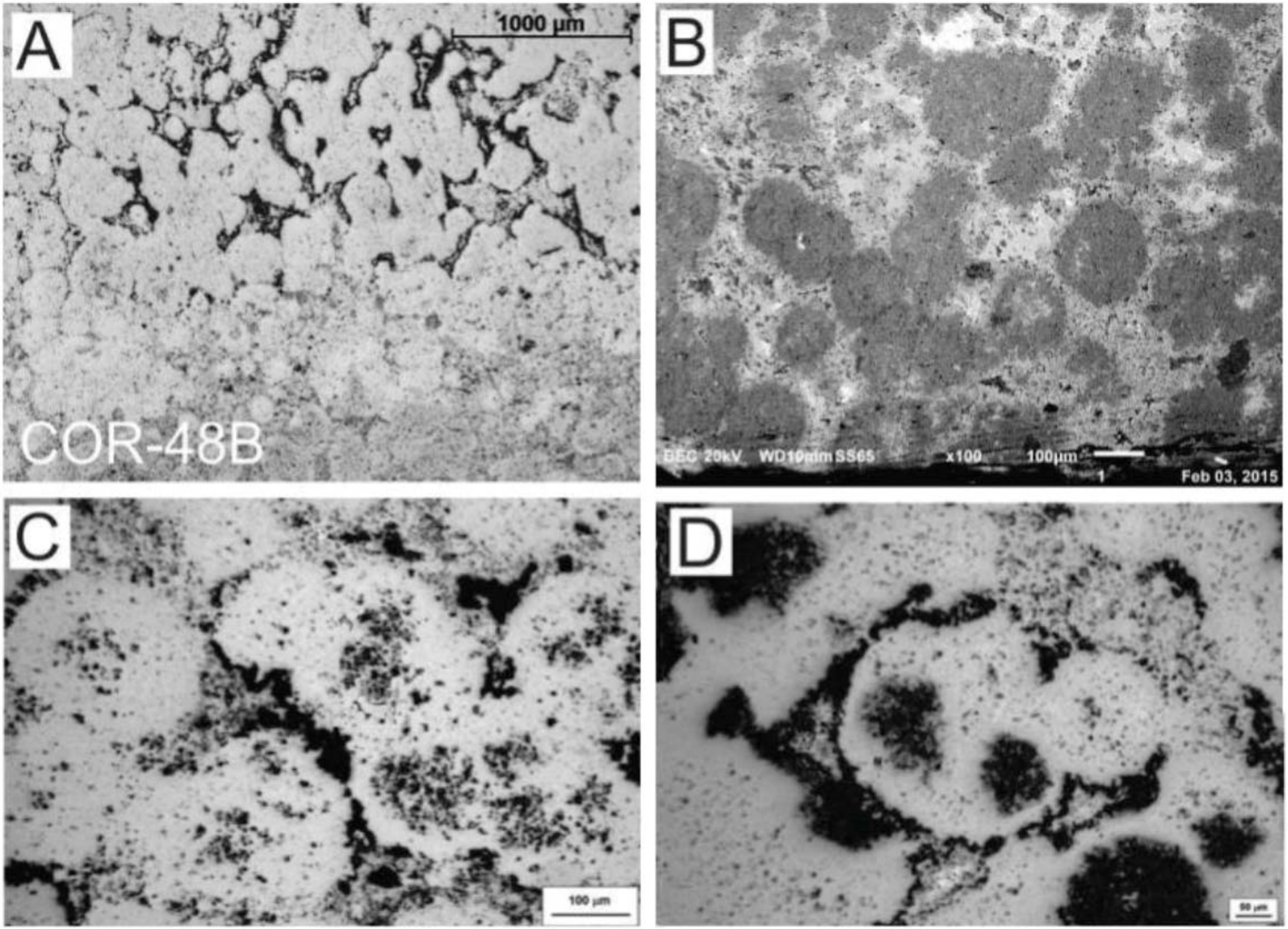
A
1000 µm
COR-48B
B
DEC 20kV WD10mm SS65 x100 100µm 1 Feb 03, 2015
C
100 µm
D

Figure 5.

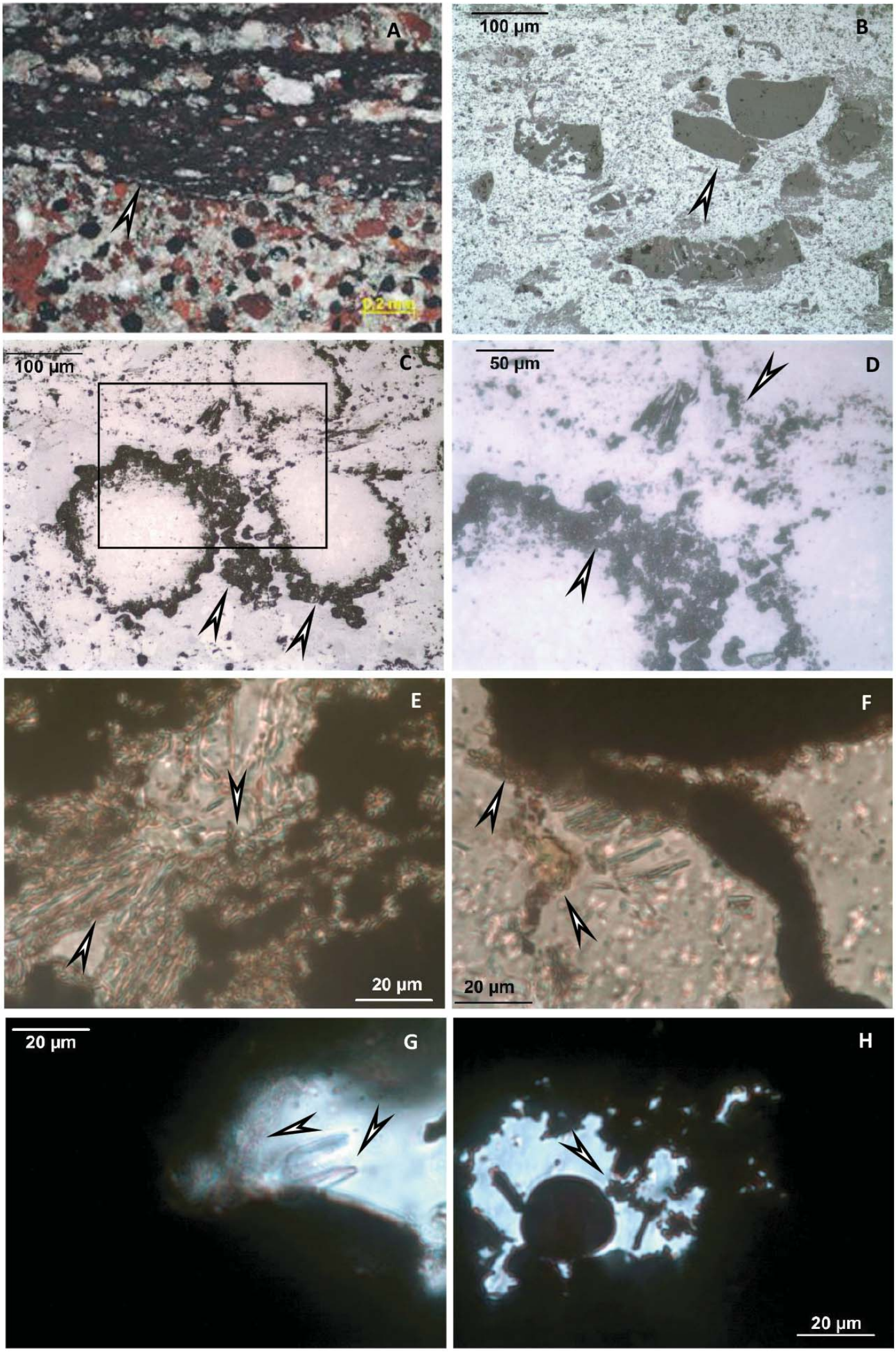

Figure 6.

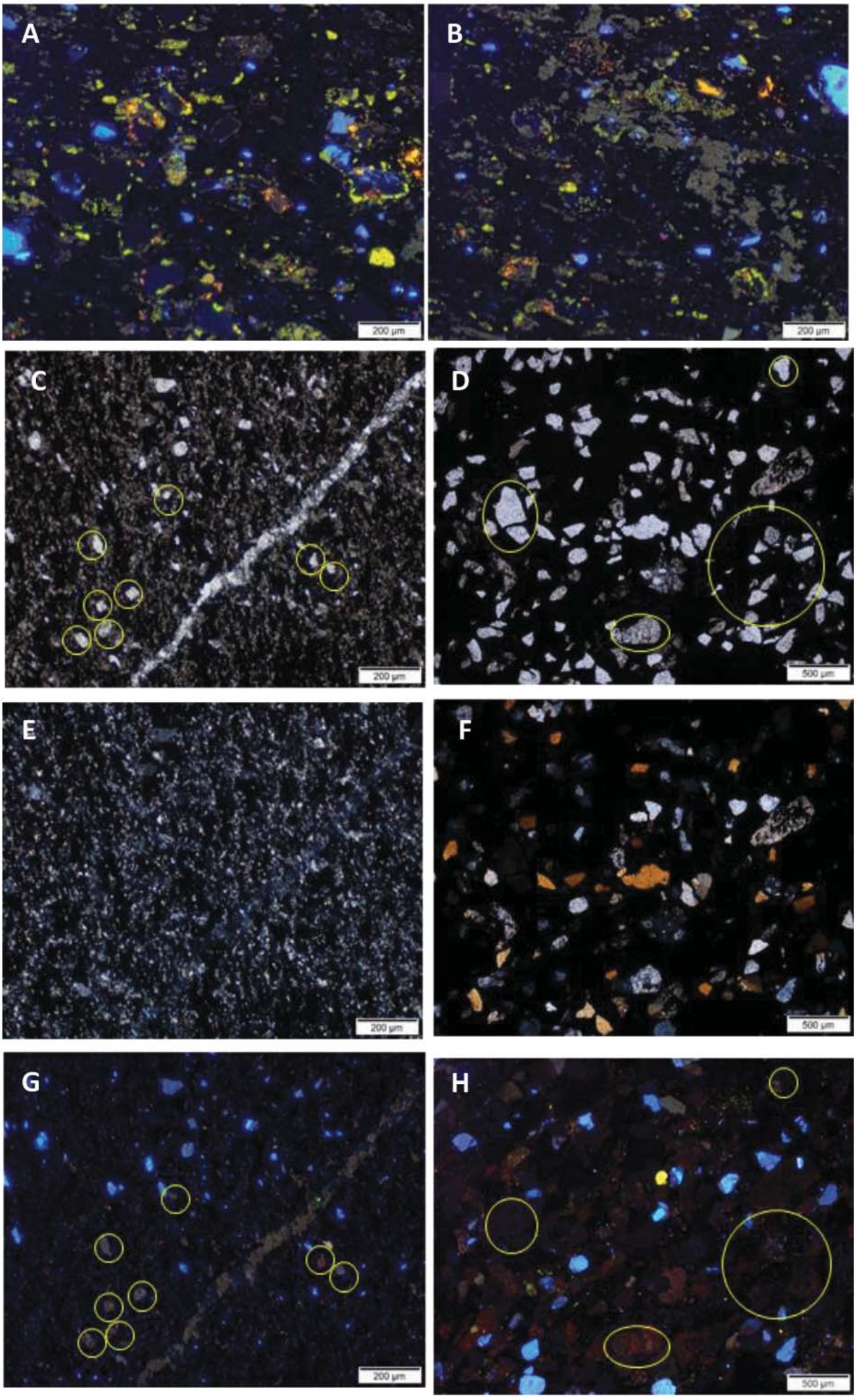

Figure 7.

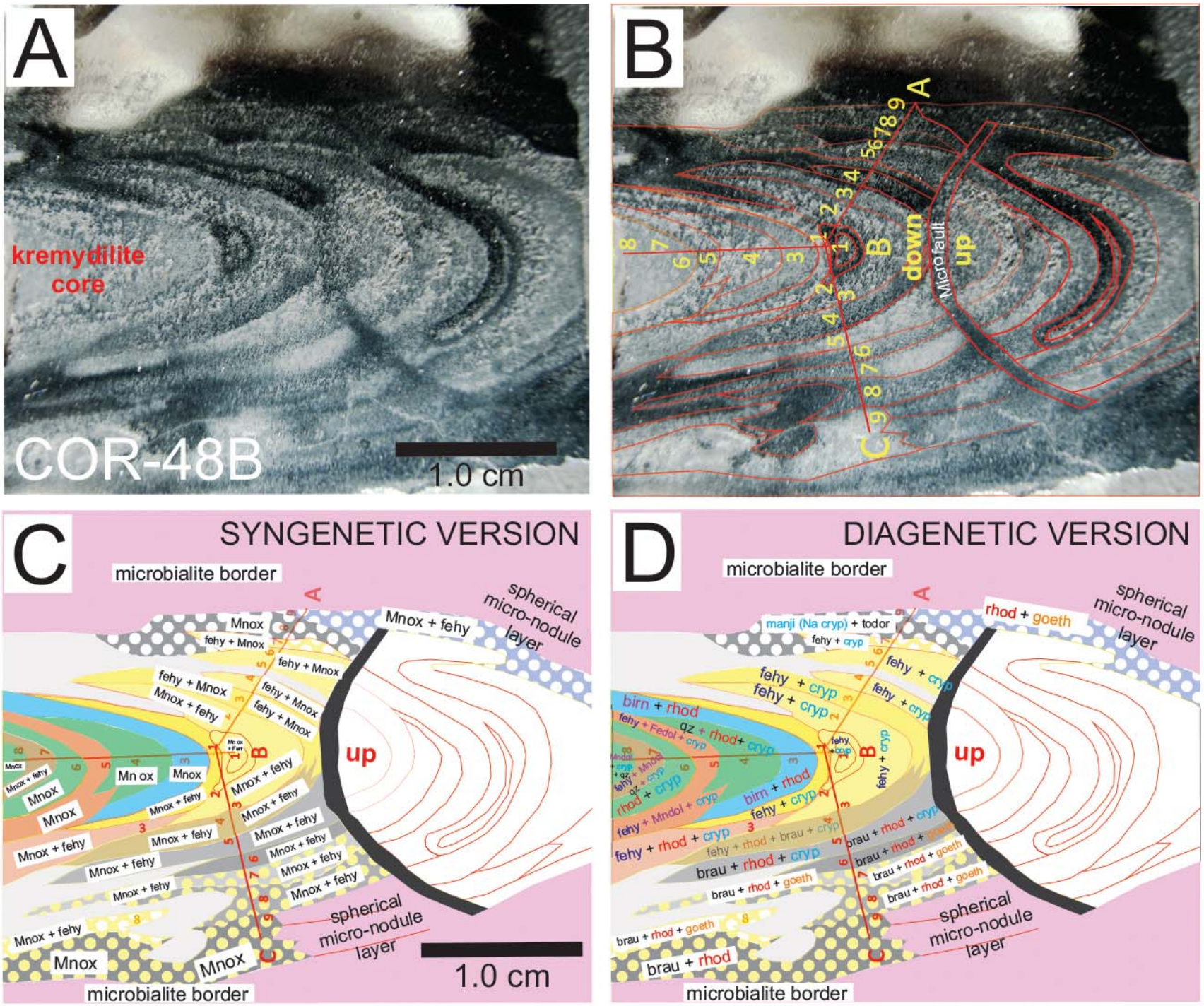
A
kremydilite
core
COR-48B
1.0 cm
B
down
up
Microfault
C
SYNGENETIC VERSION
microbialite border
spherical
micro-nodule
layer
Mnox
Mnox + fehy
fehy + Mnox
Mn ox
up
1.0 cm
microbialite border
D
DIAGENETIC VERSION
microbialite border
rhod + goeth
manji (Na cryp) + todor
fehy + cryp
birn + rhod
fehy + Fedol + cryp
qz + rhod + cryp
fehy + Mndol + cryp
fehy + rhod + cryp
brau + rhod + cryp
brau + rhod + goeth
brau + rhod
up
spherical
micro-nodule
layer
microbialite border

Figure 8.

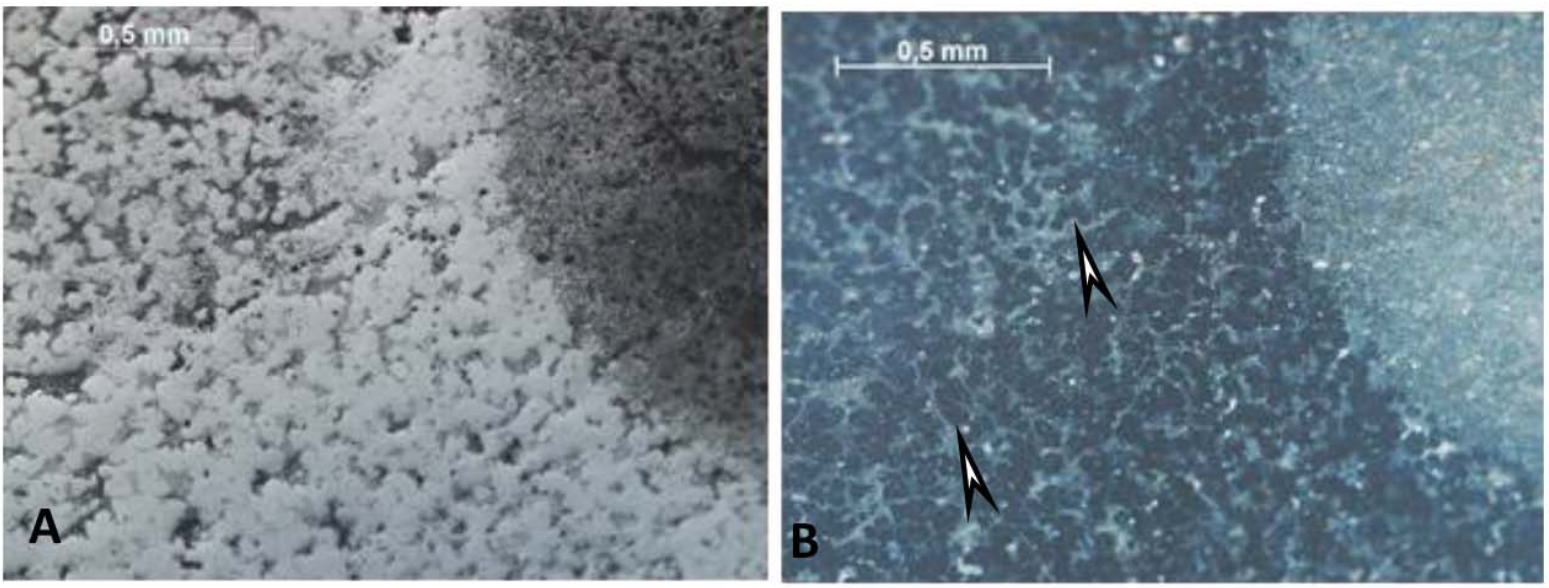
0,5 mm
A
0,5 mm
B

C

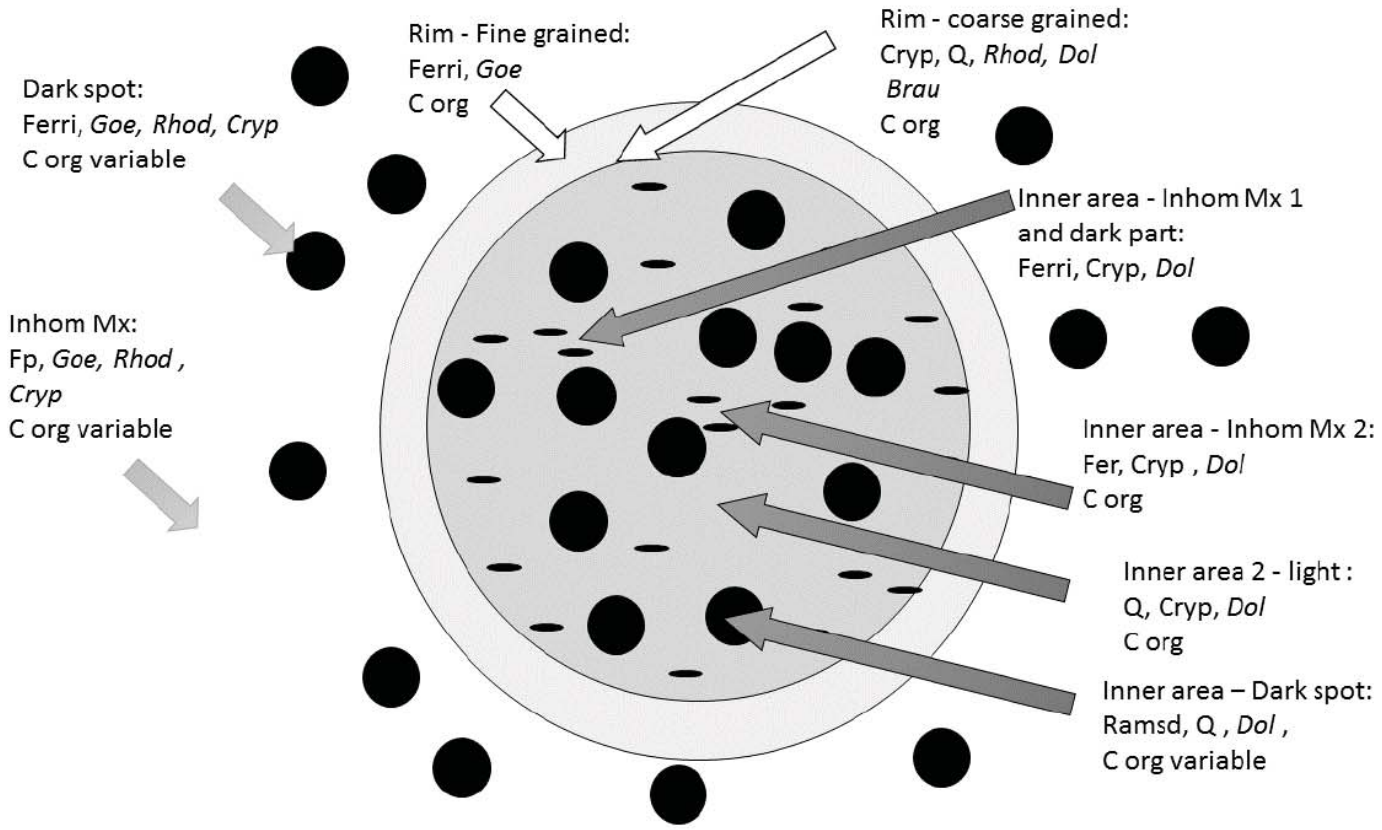
Dark spot:
Ferri, Goe, Rhod, Cryp
C org variable
Rim - Fine grained:
Ferri, Goe
C org
Rim - coarse grained:
Cryp, Q, Rhod, Dol
Brau
C org
Inner area - Inhom Mx 1
and dark part:
Ferri, Cryp, Dol
Inhom Mx:
Fp, Goe, Rhod ,
Cryp
C org variable
Inner area - Inhom Mx 2:
Fer, Cryp , Dol
C org
Inner area 2 - light :
Q, Cryp, Dol
C org
Inner area – Dark spot:
Ramsd, Q , Dol ,
C org variable

Figure 9.

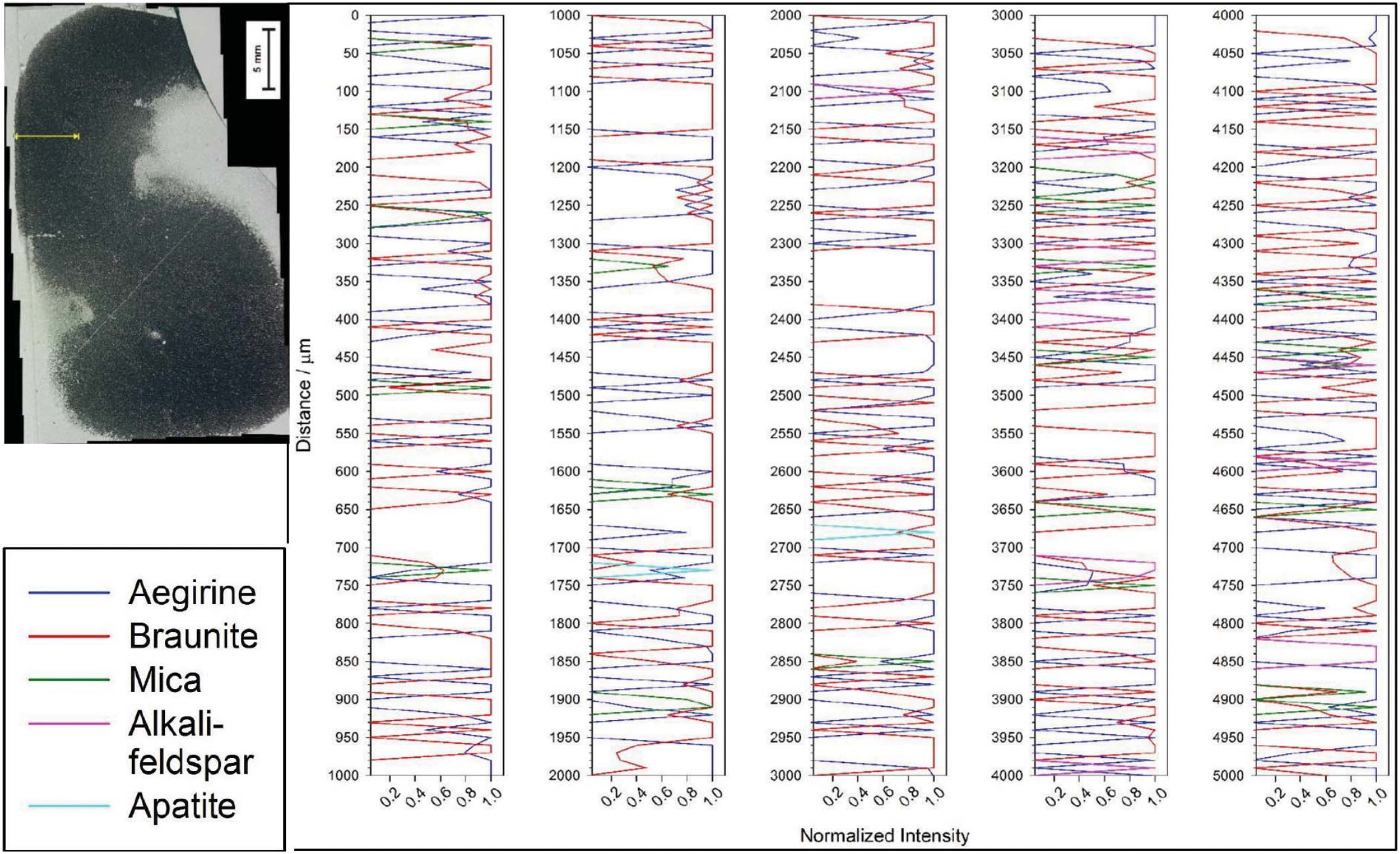
5 mm
Distance / µm
Normalized Intensity
Aegirine
Braunite
Mica
Alkali-feldspar
Apatite

Figure 10.

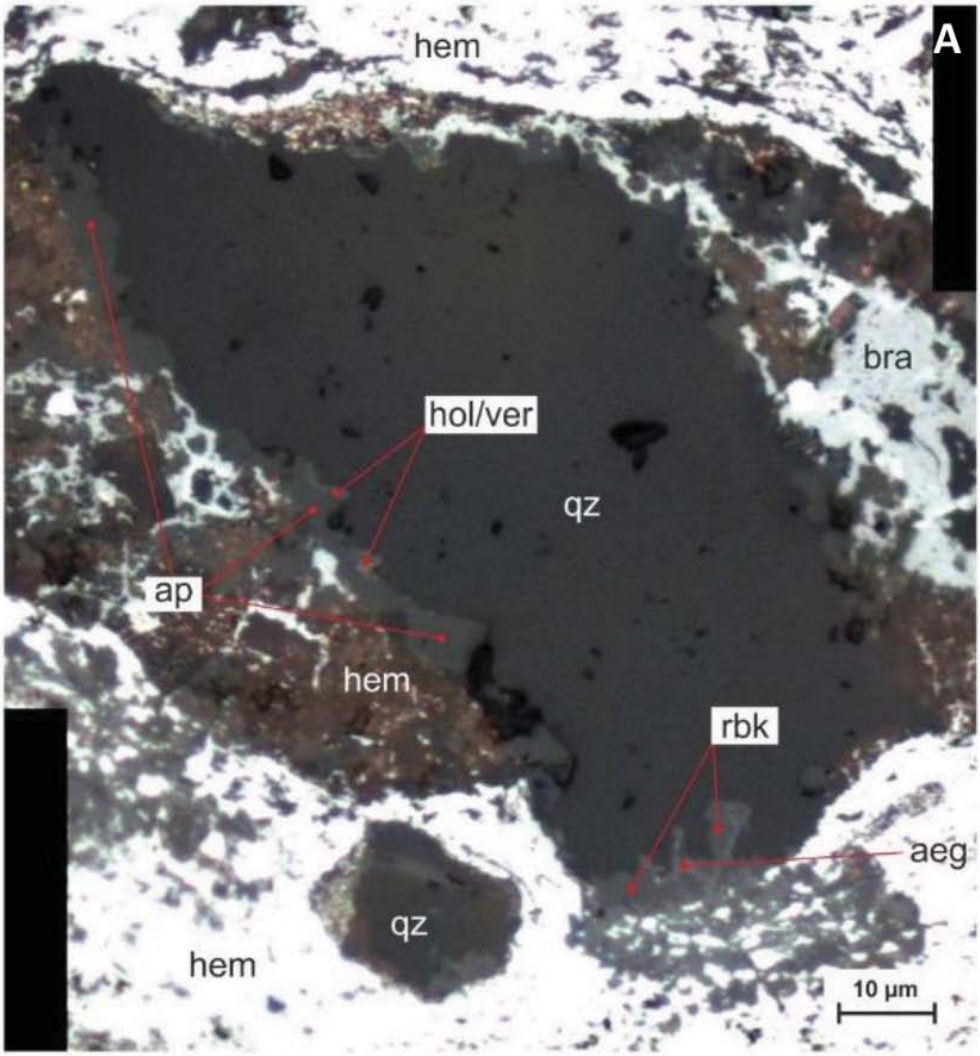

Mineral abbreviations are after Whitney & Evans (2010), except ver: vernadite; hol: hollandite
bra: braunite

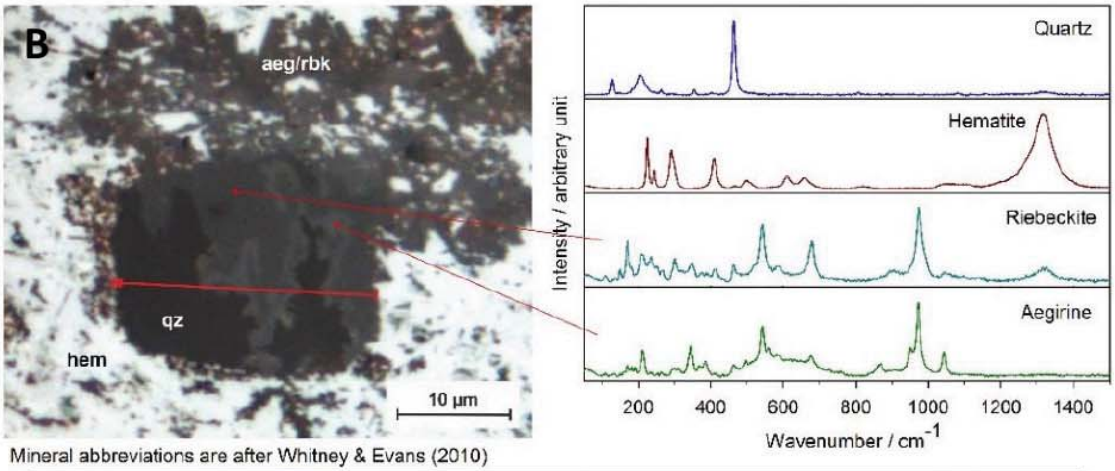

Mineral abbreviations are after Whitney & Evans (2010)

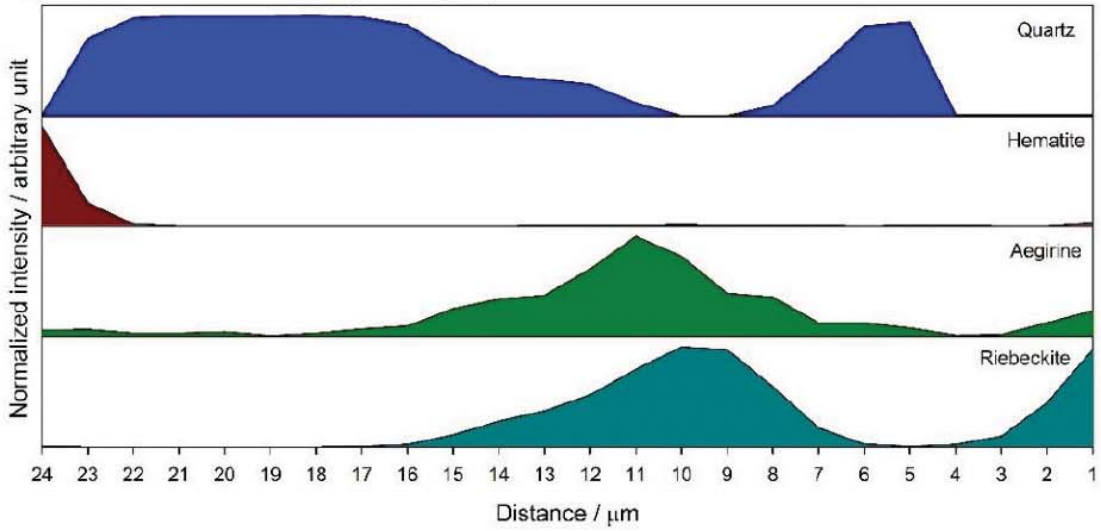

Figure 11.

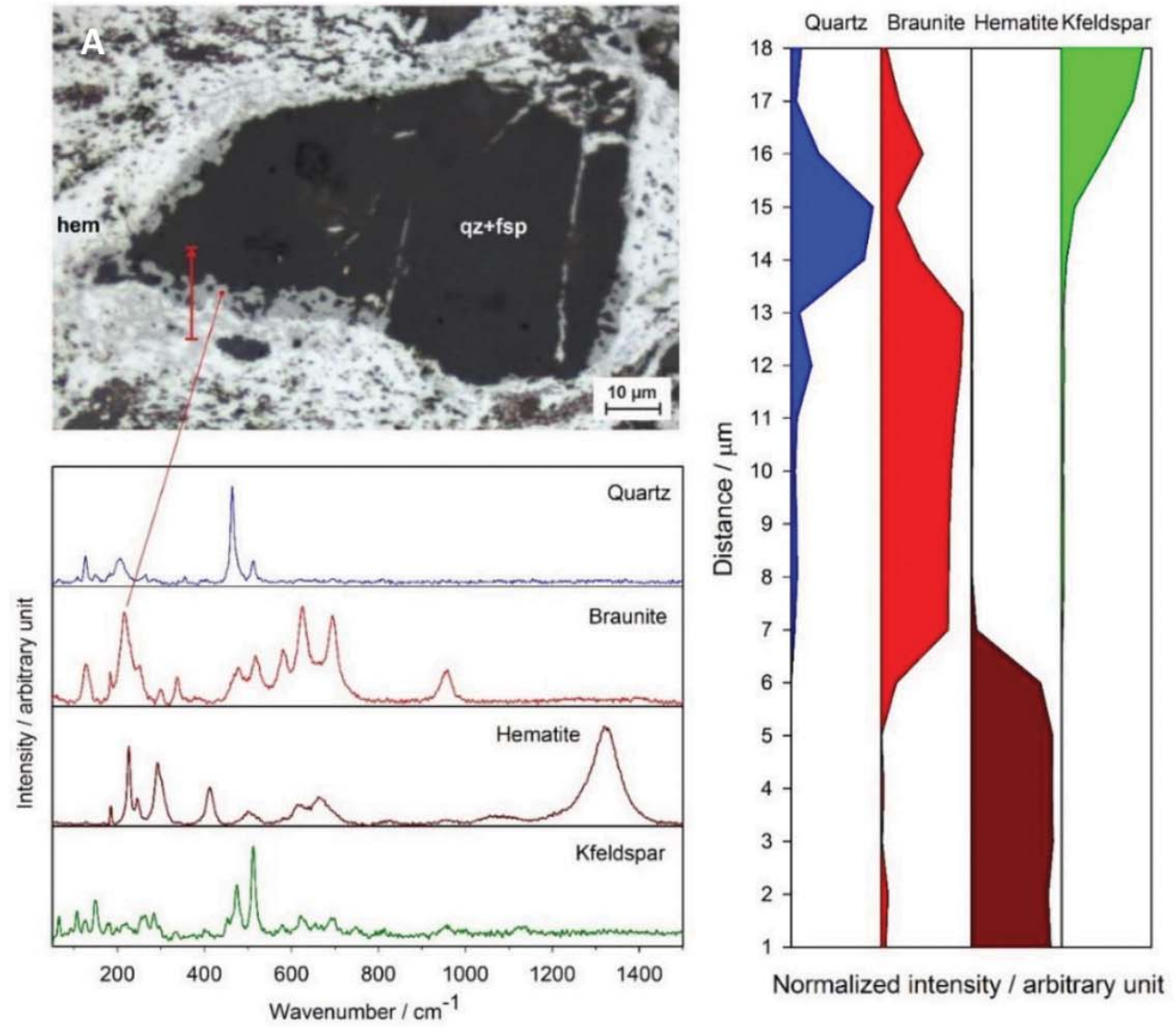
A
hem
qz+fsp
10 µm
Quartz
Braunite
Hematite
Kfeldspar
Intensity / arbitrary unit
200
400
600
800
1000
1200
1400
Wavenumber / cm-1
Quartz
Braunite
Hematite
Kfeldspar
Distance / µm
Normalized intensity / arbitrary unit

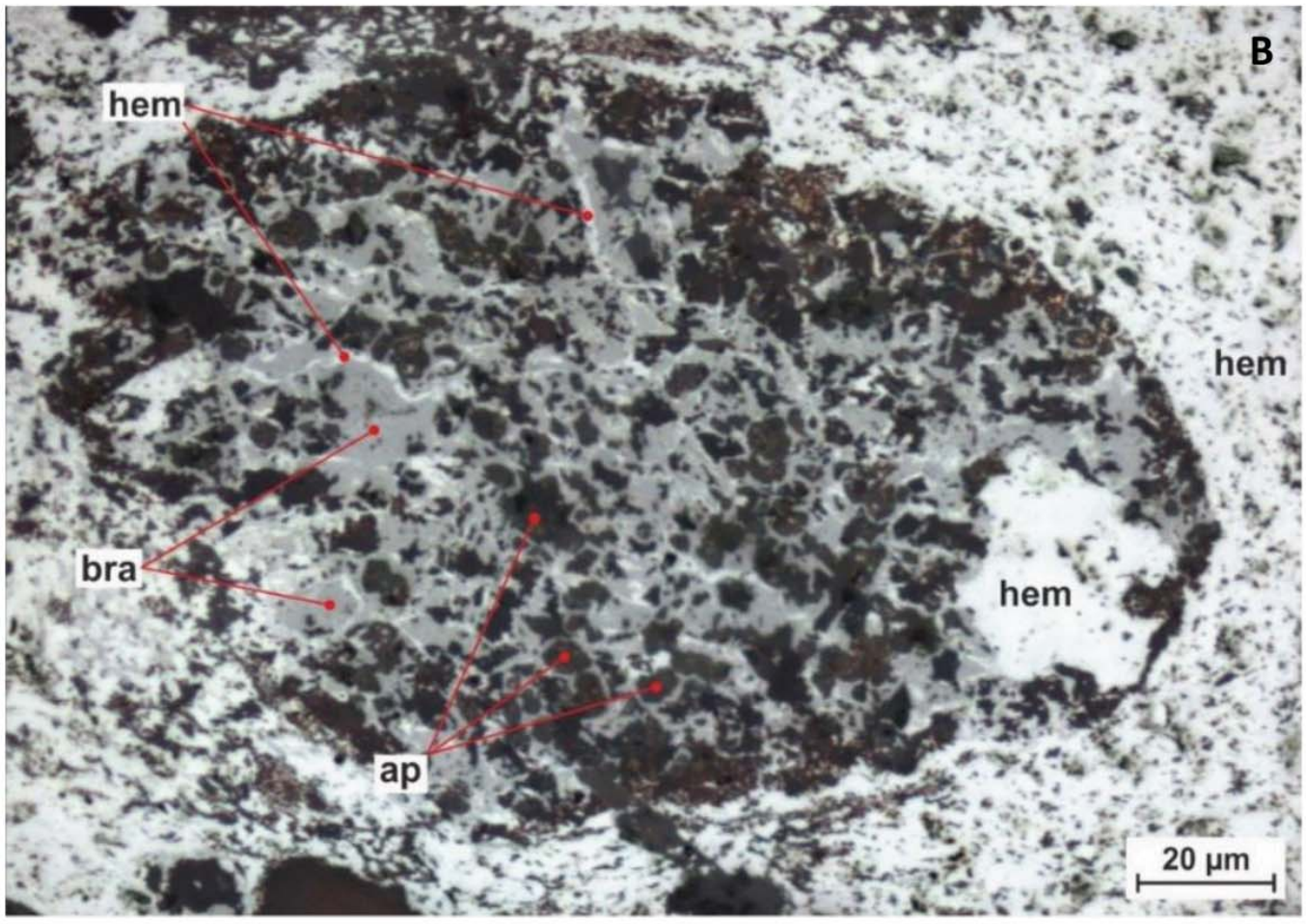
B
hem
hem
hem
bra
ap
20 µm

Figure 12.

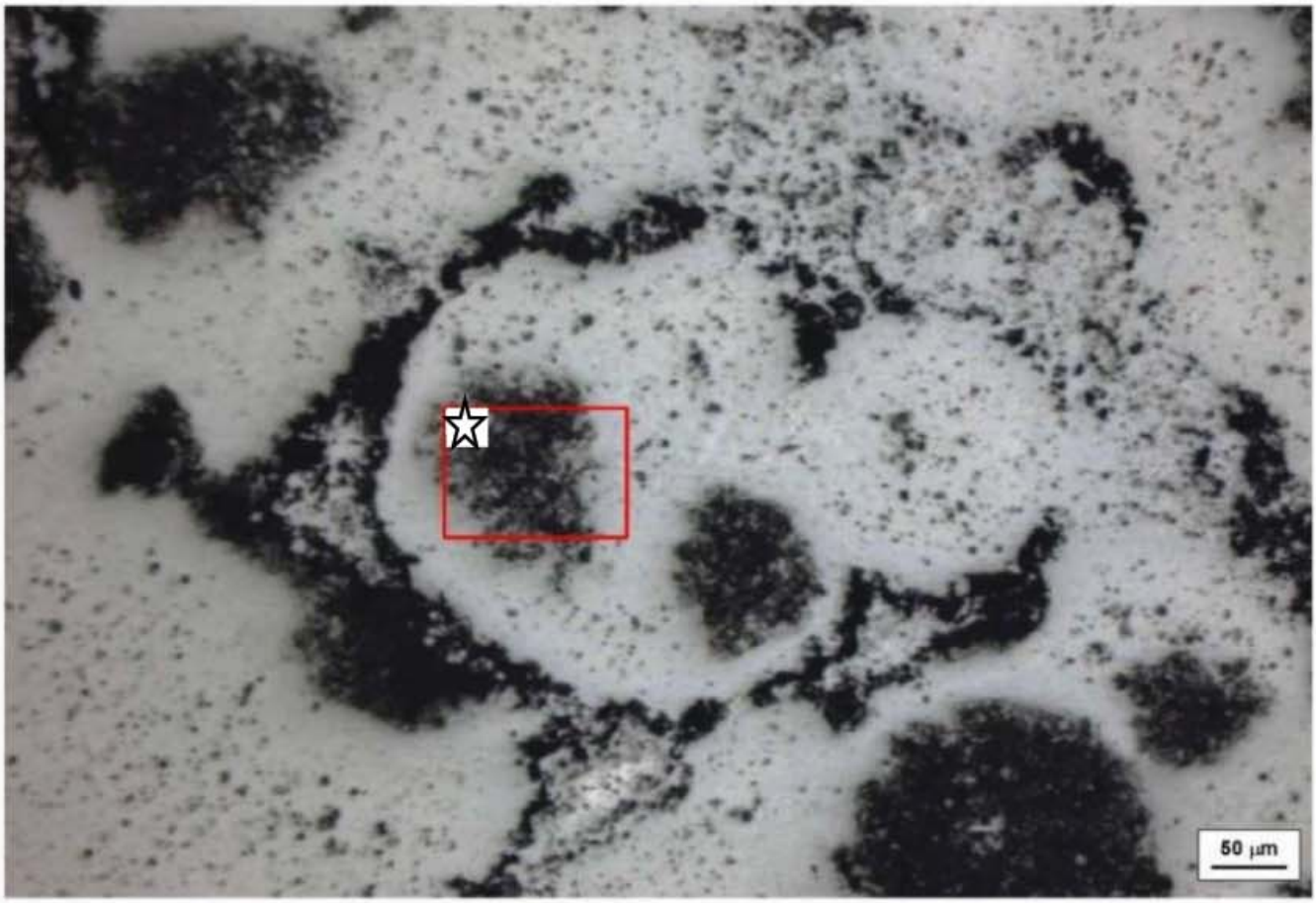
50 μm

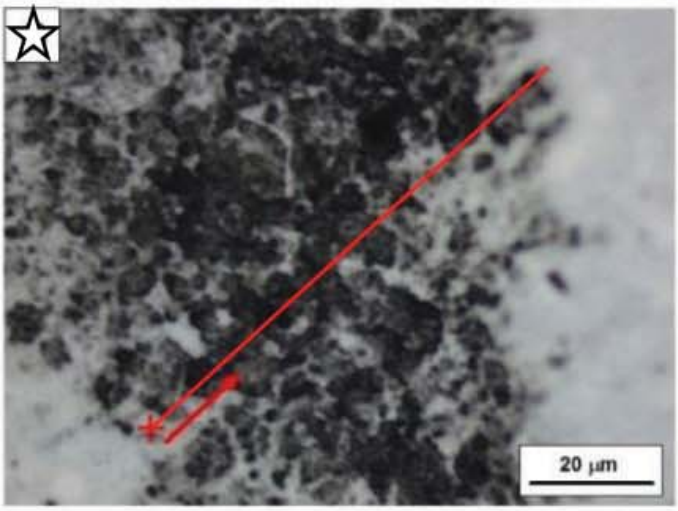
20 μm

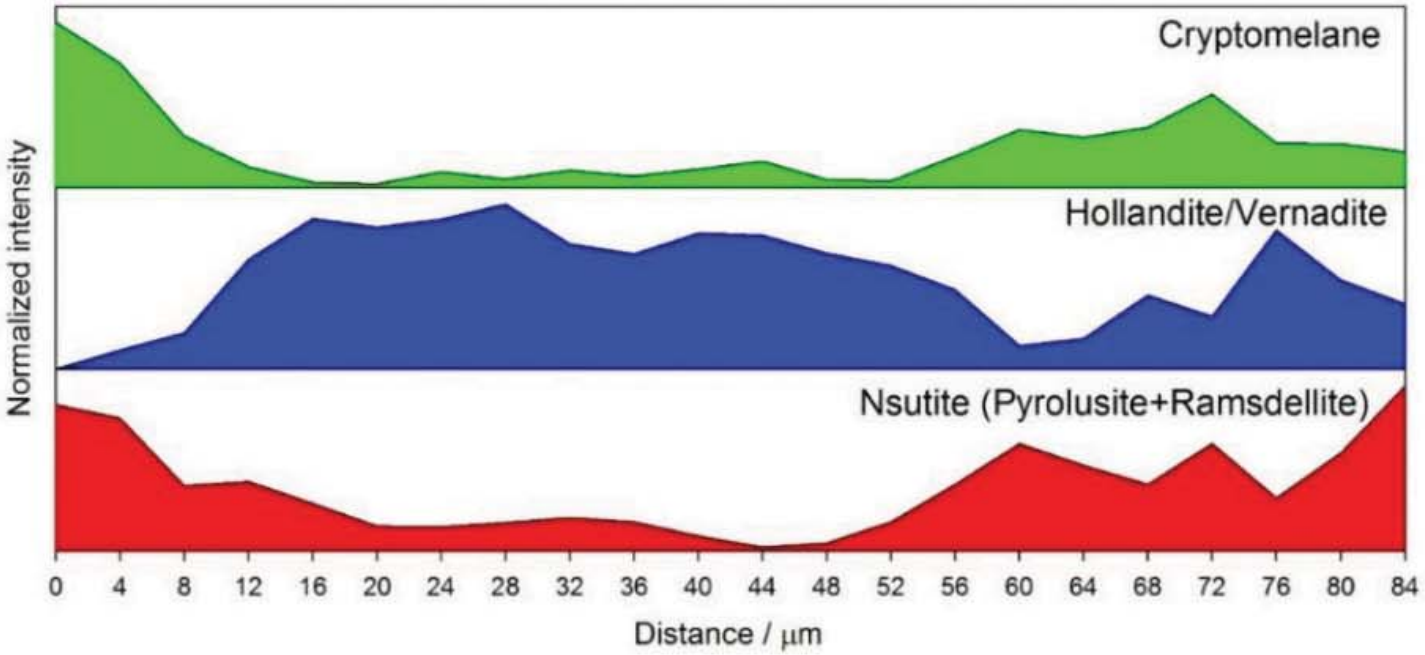
Cryptomelane
Hollandite/Vernadite
Nsutite (Pyrolusite+Ramsdellite)
Normalized intensity
0
4
8
12
16
20
24
28
32
36
40
44
48
52
56
60
64
68
72
76
80
84
Distance / μm

Figure 13.

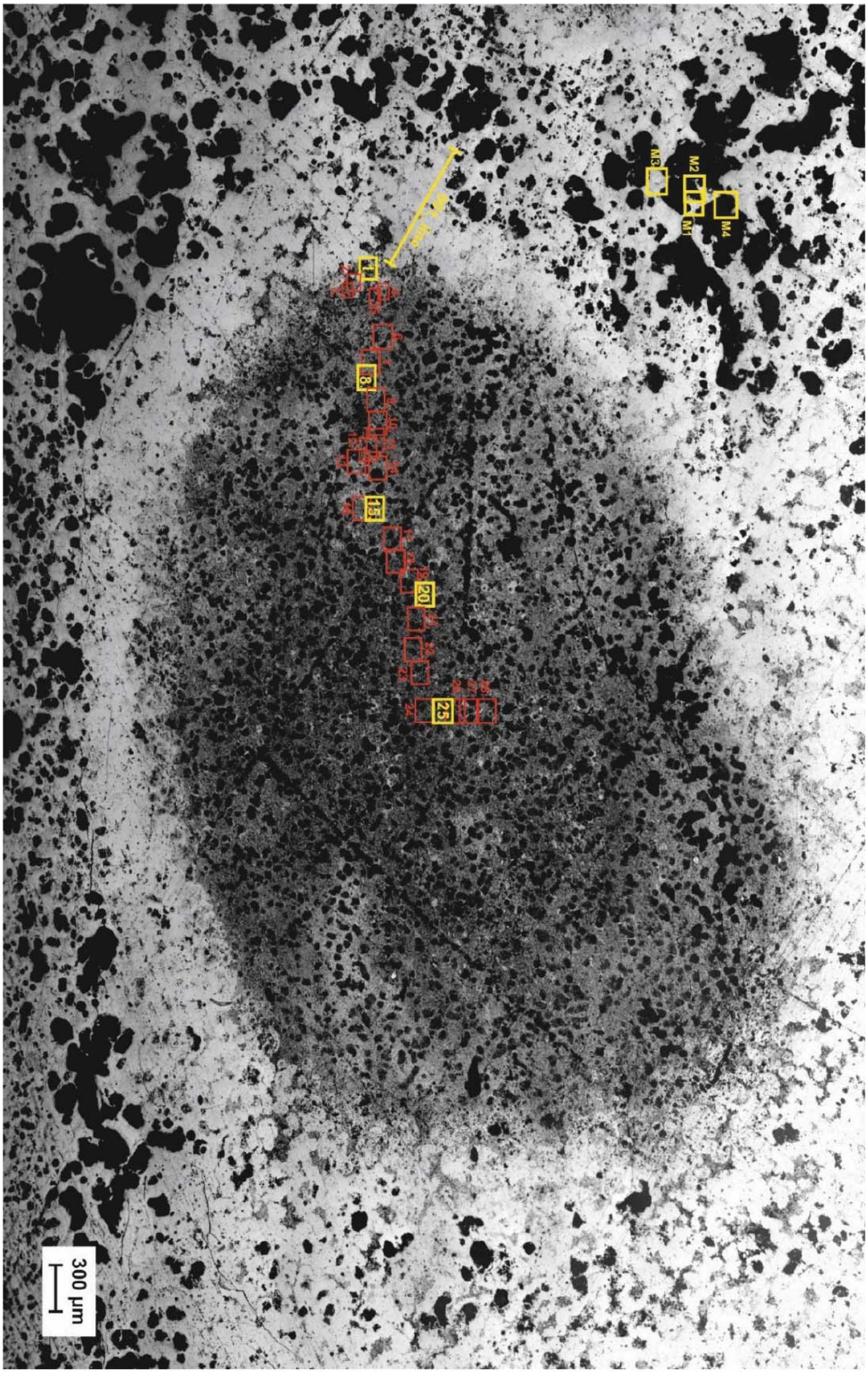

Figure 14.

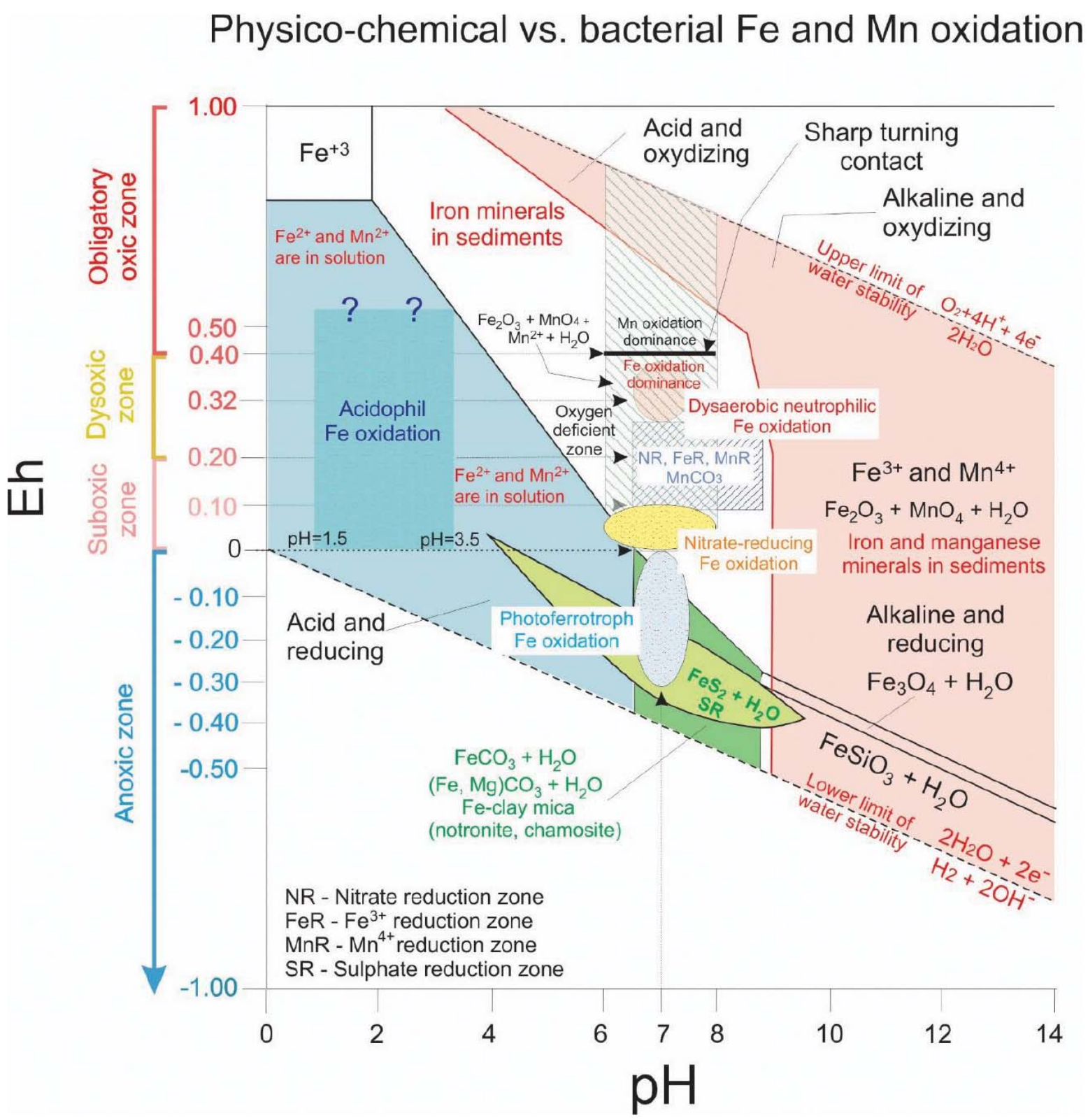
Physico-chemical vs. bacterial Fe and Mn oxidation
Eh
pH
Obligatory oxic zone
Dysoxic zone
Suboxic zone
Anoxic zone
1.00
0.50
0.40
0.32
0.20
0.10
0
- 0.10
- 0.20
- 0.30
- 0.40
-0.50
-1.00
0
2
4
6
7
8
10
12
14
Fe+3
Acid and oxydizing
Sharp turning contact
Alkaline and oxydizing
Iron minerals in sediments
Fe2+ and Mn2+ are in solution
? ?
Fe2O3 + MnO4 + Mn2+ + H2O
Mn oxidation dominance
Fe oxidation dominance
Upper limit of water stability
O2+4H+ + 4e- 2H2O
Acidophil Fe oxidation
Oxygen deficient zone
Dysaerobic neutrophilic Fe oxidation
NR, FeR, MnR MnCO3
Fe2+ and Mn2+ are in solution
Fe3+ and Mn4+
Fe2O3 + MnO4 + H2O
Iron and manganese minerals in sediments
pH=1.5
pH=3.5
Nitrate-reducing Fe oxidation
Acid and reducing
Photoferrotroph Fe oxidation
FeS2 + H2O SR
Alkaline and reducing
Fe3O4 + H2O
FeCO3 + H2O
(Fe, Mg)CO3 + H2O
Fe-clay mica
(notronite, chamosite)
FeSiO3 + H2O
Lower limit of water stability
2H2O + 2e- H2 + 2OH-
NR - Nitrate reduction zone
FeR - Fe3+ reduction zone
MnR - Mn4+ reduction zone
SR - Sulphate reduction zone

Figure 15.

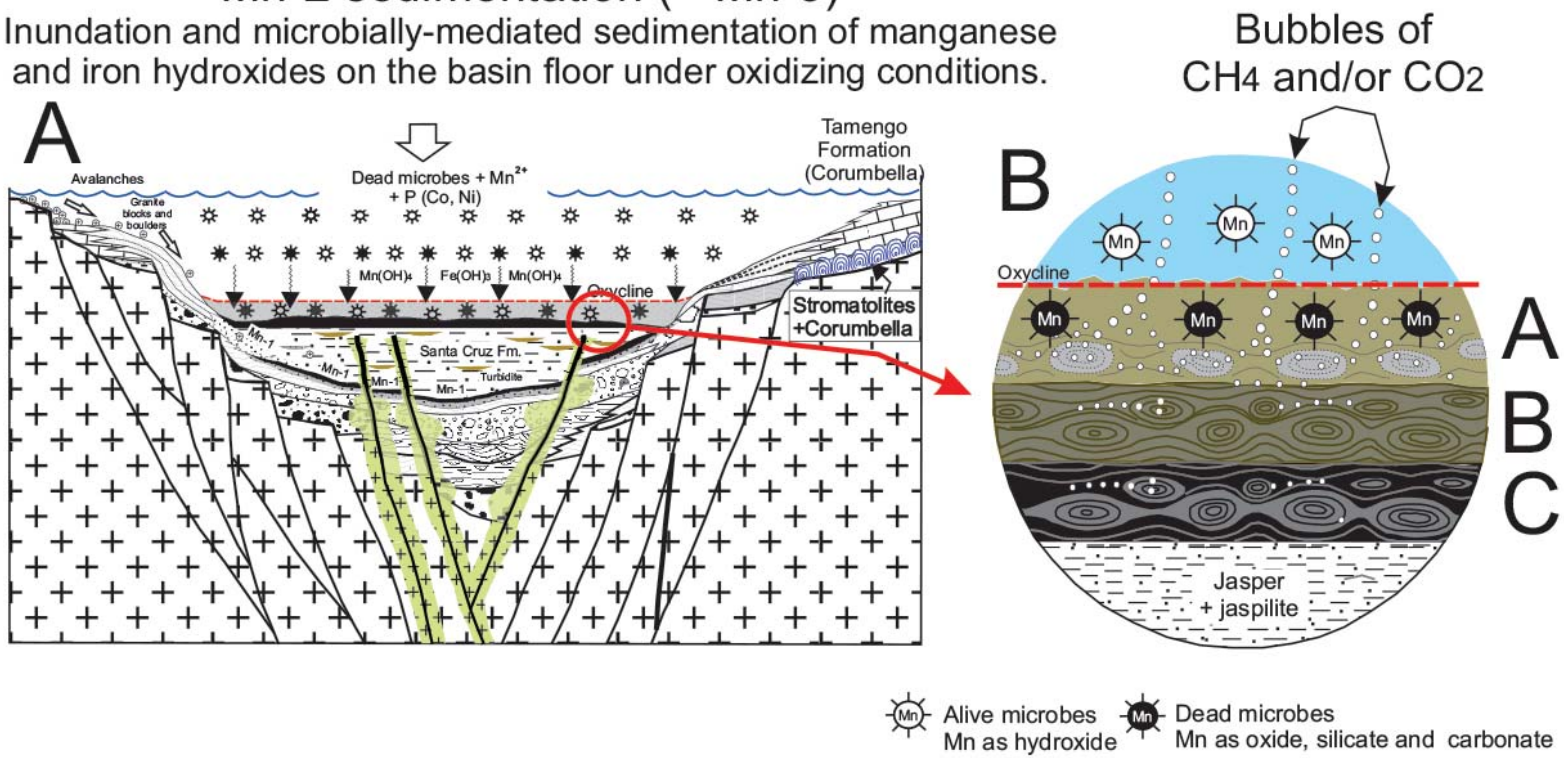

Zone	Sediment zones	Diagenetic product	Kremydilite growth
A	**Biomass sedimentation** Aqueous biomass mud with dead microbes. Mn reduction and carbonate nucleation	Microbial oxidation of buried organic matter under suboxic conditions	Birnesite and ferrihydrite nucleation, CM decay and formation of CH_4 and/or CO_2 bubbles
B	**Biomass early diagenesis** Biomass with Mn and Fe hydroxides + manganoan carbonate	Birnesite, ferrihydrite, manganoan carbonate	Nucleous, ferrihydrite and braunite + rhodochrosite zones formation, Ch_4 + CO_2 bubbles
C	**Biomass late diagenesis** **= Ore formation** Mn and Fe oxidation and carbonate precipitation	Transformation to cryptomelane, braunite and minor rhodochrosite	Transformation to cryptomelane, braunite and minor rhodochrosite

Figure 16.

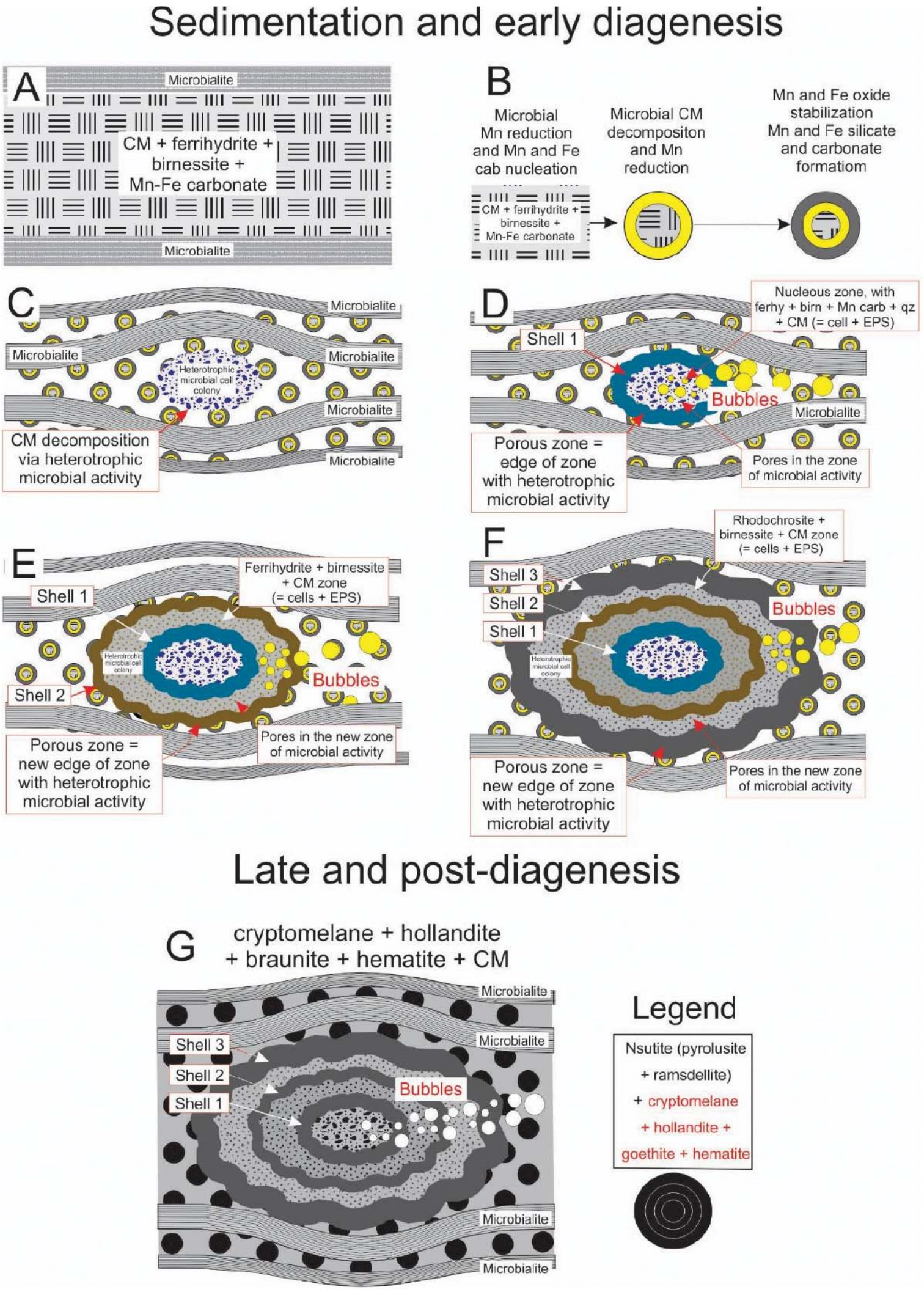
Sedimentation and early diagenesis
A
Microbialite
CM + ferrihydrite + birnessite + Mn-Fe carbonate
Microbialite
B
Microbial Mn reduction and Mn and Fe cab nucleation
Microbial CM decompositon and Mn reduction
Mn and Fe oxide stabilization Mn and Fe silicate and carbonate formatiom
CM + ferrihydrite + birnessite + Mn-Fe carbonate
C
Microbialite
Microbialite
Microbialite
Heterotrophic microbial cell colony
Microbialite
Microbialite
CM decomposition via heterotrophic microbial activity
D
Nucleous zone, with ferhy + birn + Mn carb + qz + CM (= cell + EPS)
Shell 1
Bubbles
Microbialite
Porous zone = edge of zone with heterotrophic microbial activity
Pores in the zone of microbial activity
E
Shell 1
Ferrihydrite + birnessite + CM zone (= cells + EPS)
Heterotrophic microbial cell colony
Bubbles
Shell 2
Porous zone = new edge of zone with heterotrophic microbial activity
Pores in the new zone of microbial activity
F
Rhodochrosite + birnessite + CM zone (= cells + EPS)
Shell 3
Shell 2
Shell 1
Bubbles
Heterotrophic microbial cell colony
Porous zone = new edge of zone with heterotrophic microbial activity
Pores in the new zone of microbial activity
Late and post-diagenesis
G
cryptomelane + hollandite + braunite + hematite + CM
Microbialite
Microbialite
Shell 3
Shell 2
Shell 1
Bubbles
Microbialite
Microbialite
Legend
Nsutite (pyrolusite + ramsdellite) + cryptomelane + hollandite + goethite + hematite

Figure 17.

Table 1. Main features, mineralogical and selective element composition of ore beds (12 samples)(Biondi and Lopez 2017)

Ore bed	Mn-1	Mn-2-3
Main features	Sandy (fragments of quartz, altered feldspar, apatite, chert), laminated, amygdalite-bearing	Kremydilite
Mineralogy	**Figueirinha-Upper Mn-1** 30-75 v% braunite <0.5 vol% aegirine 3-15 vol% quartz 5-15 vol% feldspar 1-5 vol% clay minerals, apatite, chlorite locally 10-30 vol%Fe-dolomite or siderite, Mn-dolomite **São Domingos-Upper Mn-1** (laminated, amygdalite-bearing) 40-75 vol% cryptomelane-hollandite 10-30 vol% quartz 10-15 vol% hematite, apatite, clay minerals *Composition of amygdalite cores* 60-90 vol% cryptomelane (hollandite?) 0-10 vol% quartz 5-15 vol% hematite, clay minerals **Santa Cruz-Mn-1** arkozic sandstone cemented by hollandite (cryptomelane, pyrolusite), quartz, feldspar, hematite *Composition of ferruginous sandstone* 30-40 vol% hematite 60-70 vol% quartz 1-5 vol% clay minerals	77-98 vol% cryptomelane 0-23 vol% hollandite 9-19 vol% braunite 7-21 vol% hematite 0-5 vol% clay minerals and CM
Average chemical composition of selective elements (wt. %)		
Mn	Mn-1 contains a Lower and an Upper part, whose compositions vary locally, which is the reason why it is not possible to determine the average chemical composition of this unit.	50.06 (SD-2.73%)
Fe		8.58 (SD-2.59%)
K		1.82 (SD-0.75%)
Ba		0.29 (SD-0.30%)
LOI		10.80 (SD-0.88%)

Samples COR-16P, 16M, 17, 36A, 42, 43, 48L, 48P, 61L, 61P, 75 and 78 published in Biondi and Lopez (2017)

Table 2. Samples and used methods

Sample ID	Layer	Locality (Fig. 1)	TS*	OM	CL	FTIR	Raman	XRD
COR-81	Mn-3	MCR-VALE mine, Sta Cruz Plateau	x	x(34)			x(1,903)	
COR-78-F3	Mn-2	Urucum-VALE mine, Urucum W plateau	x	x(65)		x(60)		
COR-78-D1	Mn-2	Urucum-VALE mine, Urucum W plateau	x	x(59)	x(11)		x(3,456)	
COR-75-B5	Mn-2	Urucum-VALE mine, Urucum W plateau	x	x(63)	x(6)		x(2,449)	
COR-75-2	Mn-2	Urucum-VALE mine, Urucum W plateau	x	x(56)	x(9)		x(1,209)	
COR-48B	Mn-2		x			x(178)		
COR-36-A1-A2	Mn-2	MMX mine, Urucum E plateau	x	x(56)		x(50)		
COR-10	Mn-1	Figueirinha mine, Sta Cruz N plateau	x	x(95)	x(23)	x(14)	x(504)	x
COR-7	Mn-1	Figueirinha mine, Sta Cruz N plateau	x	x(38)	x(27)	x(12)	x(504)	x
COR-6	Mn-1	Figueirinha mine, Sta Cruz N plateau	x	x(46)		x(37)		
COR-4B	Mn-1	Figueirinha mine, Sta Cruz N plateau	x	x(43)	x(10)		x(400)	
COR-32	Mn-1	Sao Domingos mine, Sta Cruz SW plateau	x	x(79)		x(32)		
COR-31	Mn-1	Sao Domingos mine, Sta Cruz SW plateau	x	x(56)	x(27)	x(32)	x(504)	x
Total 14 samples (photos, spectra)				690	113	415	10,997	3

Abbrev.: TS-thin section; OM-optical rock microscopy; CL-cathodoluminescence microscopy; FTIR-ATR-infra red spectroscopy; Raman-Raman spectroscopy; XRD-X-ray powder diffraction
gray background: samples from Mn-2 and 3 beds (Fig. 3-4 and SI 3-Fig)
number of analyses in brackets.

Table 3. Mineral composition

Samples → Minerals ↓	COR-6	COR-7	COR-10	COR-31	COR-32	COR-36A1	COR-78F3
Mn minerals							
todorokite	*						
ramsdellite	*						
cryptomelane	*				*	*	*
pyrolusite					*		
romanéchite						*	
serandite	*						
braunite	*		*				
Fe minerals							
ferrihydrite	*			*	*	*	*
lepidocrocite		*					
hematite				*	*		*
aegirine	*						
pyrite				*			
Other minerals							
apatite		*		*	*		
feldspar (albite, anortite)		*	*		*		
chlorite	*		*				
quartz				*	*		
kaolinite/dickite				*			
celadonite				*			
Organic matter	*	*	*	*	*	*	*

Table 4: Mineral assemblage in Mn ore beds and typical minerals indicative of Eh-pH ranges in Urucum based on environmental mineralogy

Minerals/Processes Mn mineral assemblage	Chemical formula	Mn-1	Mn-2	Mn-3	Eh			pH		Microbiallly mediated
					ox-subox	anox	acidic	neutral-slightly alkaline	alkaline	
Oxides and hydroxide										
Pyrolusite	$Mn^{4+}O_2$	*	*	*	*					
Ramsdellite	$Mn^{4+}O_2$	*	*	*	*					
Nsutite	$(Mn^{4+}Mn^{2+})(O,OH)_2$		*		*				*	
Hausmannite	$Mn^{3+}{}_3O_4$	*	*							
Cryptomelane	$KMn^{4+}{}_6Mn^{2+}{}_2O_{16}$	*	*	*						
Jacobsite	$Mn^{2+}{}_{0.6}Fe^{2+}{}_{0.3}Mg_{0.1}Fe^{3+}{}_{1.5}Mn^{3+}{}_{0.5}O_4$	*	*	*						
Manganite	$Mn^{3+}OOH$	*	*							
Vernadite δMnO_2 (wad)	$(Mn^{4+}Fe^{3+}CaNa)(OOH)_2{*}nH_2O$	*	*							*
Todorokite	$Na_{0.2}Ca_{0.05}K_{0.02}Mn^{4+}{}_4Mn^{3+}{}_2O_{12}{\bullet}3(H_2O)$	*	*	*	*			*		*
Birnessite	$Na_{0.7}Ca_{0.3}(Mn^{3+}\ Mn^{4+})_7O_{14}.2.8H_2O$	*	*	*	*			*		*
Romanèchite (psilomelane)	$[(Ba,H_2O,Mn_5O_{10},\ Ba(Mn^{4+},\ Mn^{3+})O_{10}.1.4H_2O)]$	*	*	*						
Hollandite*	$Ba(Mn^{4+},Mn^{2+})_8O_{16}$	*	*	*						
Manjiroite	$Na(Mn^{4+}{}_7Mn^{3+})O_{16}$	*								
Manganite	$Mn^{3+}OOH$	*			*					*
Carbonates										
Rhodochrosite	$MnCO_3$	*						*		*
Oxides-silcates										
Serandite	$NaMn^{2+}{}_{1.5}Ca_{0.5}Si_3O_8(OH)$	*	*							
Braunite	$Mn^{2+}Mn^{3+}{}_6SiO_{12}$	*	*	*	*				*	*
Fe mineral asssemblage										
Oxides and hydroxides										
Ferrihydrite	FeOOH	*	*	*	*			*		*
Lepidocrocite	$Fe^{3+}O(OH)$	*						*		*
Hematite	Fe_2O_3	*	*	*	*					
Goethite	FeOOH	*	*		*					
Magnetite	Fe_2O_3		*	*		*				
Sulfides										
Pyrite	FeS_2	*	*			*				*
Silicates										
Aegirine	$Ca_{0.75}Na_{0.25}Mg_{0.5}Fe^{2+}{}_{0.25}Fe^{3+}{}_{0.25}(Si_2O_6)$	*			*				*	
Riebeckite	$Na_2(Fe^{2+}{}_3Fe^{3+}{}_2)Si_8O_{22}(OH)_2$	*								
Celadonite	$KMg_{0.8}Fe^{2+}{}_{0.2}Fe^{3+}{}_{0.9}Al_{0.1}Si_4O_{10}(OH)_2$	*			*			*		*
Chlorite	$Mg_{3.75}Fe^{2+}{}_{1.25}Si_3Al_2O_{10}(OH)_8$	*								
Chamosite	$(Fe^{2+}Mg)_5Al(AlSi_3O_{10})(OH)_8$	*				*				
Others										
Oxides - hyydroxides										
Quartz	SiO_2	*					*			*
Carbonates										
Dolomite	$CaMg(CO_3)_2$	*			*			*		*
Strontianite	$Sr(CO_3)$	*			*			*		
Ankerite	$Ca(Fe^{2+},Mg)(CO_3)_2$	*								

Silicates											
Orthoclase	$KAlSi_3O_8$	*						*			
Albite	$NaAlSi_3O_8$	*						*			
Kaolinite/dickite	$Al_2Si_2O_5(OH)_4$	*			?	?	*				
Muscovite	$KAl_3Si_3O_{10}(OH)_{1.8}F_{0.2}$	*	*	*							
Silicate-carbonate-sulphate											
Cancrinite	$(NaCa…)(Al_6Si_6O_{24})(CO_3,SO_4)_2*2H_2O$	*									
Phosphates											
Apatite	$[(Ca_{10}(PO_4)_6(OH, F, Cl)_2]$	*	*		*			*	*	*	
Sulphates											
Barite	$Ba(SO_4)$	*			*			*			
Gypsum (anhidrite)	$CaSO_4.2H_2O$		*								
Johannite	$Cu(UO_2)_2(SO_4)_2(OH)_2\ 8H_2O$	*	*								
Organic material		*	*	*							

Mineral assemblage is based on Raman and FTIR spectroscopy analyses

Eh-pH ranges and microbially mediated mineralogy is based on: Listova (1961); Harder (1976, 1978); Trudinger& Swaine eds. (1979); Berner (1980); Giovanoli (1980); Sung & Morgan (1981); Cole & Shaw (1983); Ewers (1983); Maynard (1983); Coleman (1985); Skinner (1993); Ehrenreich & Widdel (1994); Wignall (1994); Mandernack et al. (1995); Straub et al. (1996); Banfield & Nealson (1997); Konhauser (1998); Herdianita et al. (2000); Ehrlich (2002); Bazylinski & Frankel (2003); Villalobos et al.(2003); Bargar et al. (2005); Dupraz & Visscher (2005); Morgan (2005); Bodeï et al. (2007); Schwertmann & Cornell (2007); Dupraz et al. (2009); Chan et al. (2011); Polgári,et al. (2012ab, 2013, 2016); Biagioni et al. (2014); Johnson et al. (2016); Gyollai et al. (2017); Mloszewska et al. (2018)

* Hollandite *(empirical)* $Ba_{0.8}Pb_{0.2}Na_{0.1}Mn^{4+}_{6.1}Fe^{3+}_{1.3}Mn^{2+}_{0.5}Al_{0.2}Si_{0.1}O_{16}$

Table 5. Environmental oxygen levels

Environmental oxygen levels	Eh (V)	Dissolved oxygen (DO)	FeOB demand*	MnOB demand
obligatory oxic	0.4<Eh<1.0	DO > 2 mL/L		x
dysoxic	0.2-0.4	DO 0.2–2.0 mL/L	≈ 0.3	
suboxic	0-0.2	DO 0–0.2 mL/L		
anoxic	<0			

*: FeOB demand is around the dysoxic-suboxic zone, and suboxic is the generally used as simplified form; abbrev: FeOB-Fe oxidizing bacteria; MnOB-Mn oxidizing bacteria (Berner 1980; Coleman 1985; Wignall 1994)

Conflict of interest

The authors declare no competing financial interests on this research. The research in this manuscript has not been previously published nor is under consideration elsewhere. All authors have approved submission of this manuscript to *Precambrian Research*.

SUPPORTING INFORMATION

BIOGENESIS OF THE NEOPROTEROZOIC KREMYDILITE MANGANESE ORES FROM URUCUM (BRAZIL) – A NEW MANGANESE ORE TYPE

Running title: Biogenesis of a Neoproterozoic manganese ore

João Carlos Biondi[1+], Márta Polgári[2,3*+], Ildikó Gyollai[2], Krisztián Fintor[4], Ivett Kovács[2], József Fekete[2], Stephen Mojzsis[2,5]

[1]*Federal University of Paraná State, Polytechnic Center, Geology Department, 81531-980 Curitiba, Brazil, e-mail: biondiufpr@gmail.com*

[2]*Institute for Geological and Geochemical Research, RCAES, Hungarian Academy of Sciences, 1112 Budapest, Budaörsi u. 45, Hungary, e-mail: rodokrozit@gmail.com, gyildi@gmail.com, iv.kovacs@gmail.com, fekete.jozsef@csfk.mta.hu*

[3]*Eszterházy Károly University, Dept. of Natural Geography and Geoinformatics, 3300 Eger, Leányka u. 6, Hungary*

[4]*Szeged University, Dept. of Mineralogy, Geochemistry and Petrology, 6722 Szeged, Egyetem u. 2-6, Hungary, e-mail: efkrisz@gmail.com*

[5]*University of Colorado, Department of Geological Sciences, 2200 Colorado Avenue, UCB 399, Boulder, Colorado 80309-0399, United States of America*

**corresponding author:*
rodokrozit@gmail.com
[+] The first two authors have contributed equally to this work

Content

SI 1-Fig. Map and geological section of Urucum

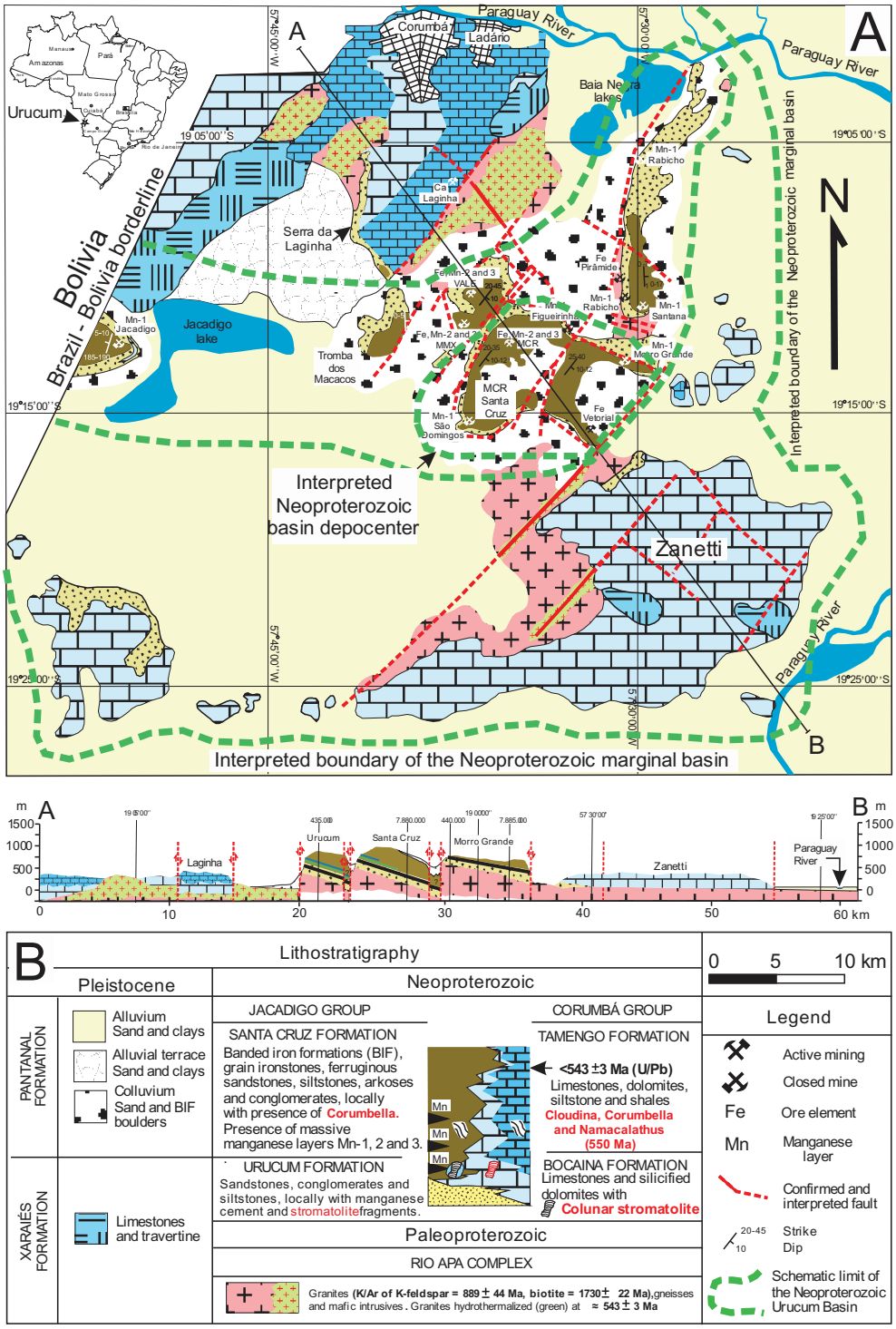

SI 1-Fig. (A) Geological map (modified after Urban et al. 1992) and geological cross-section. Lines with an interpretation of the probable relative depth of the depocenter of the Urucum marginal basin, and the regional distribution of hydrothermalized granites were added to the map. (B) Lithostratigraphy of the Urucum mining region (modified after Biondi and Lopez 2017).

SI 2-Fig. Stratigraphic columns of the Jacadigo Group

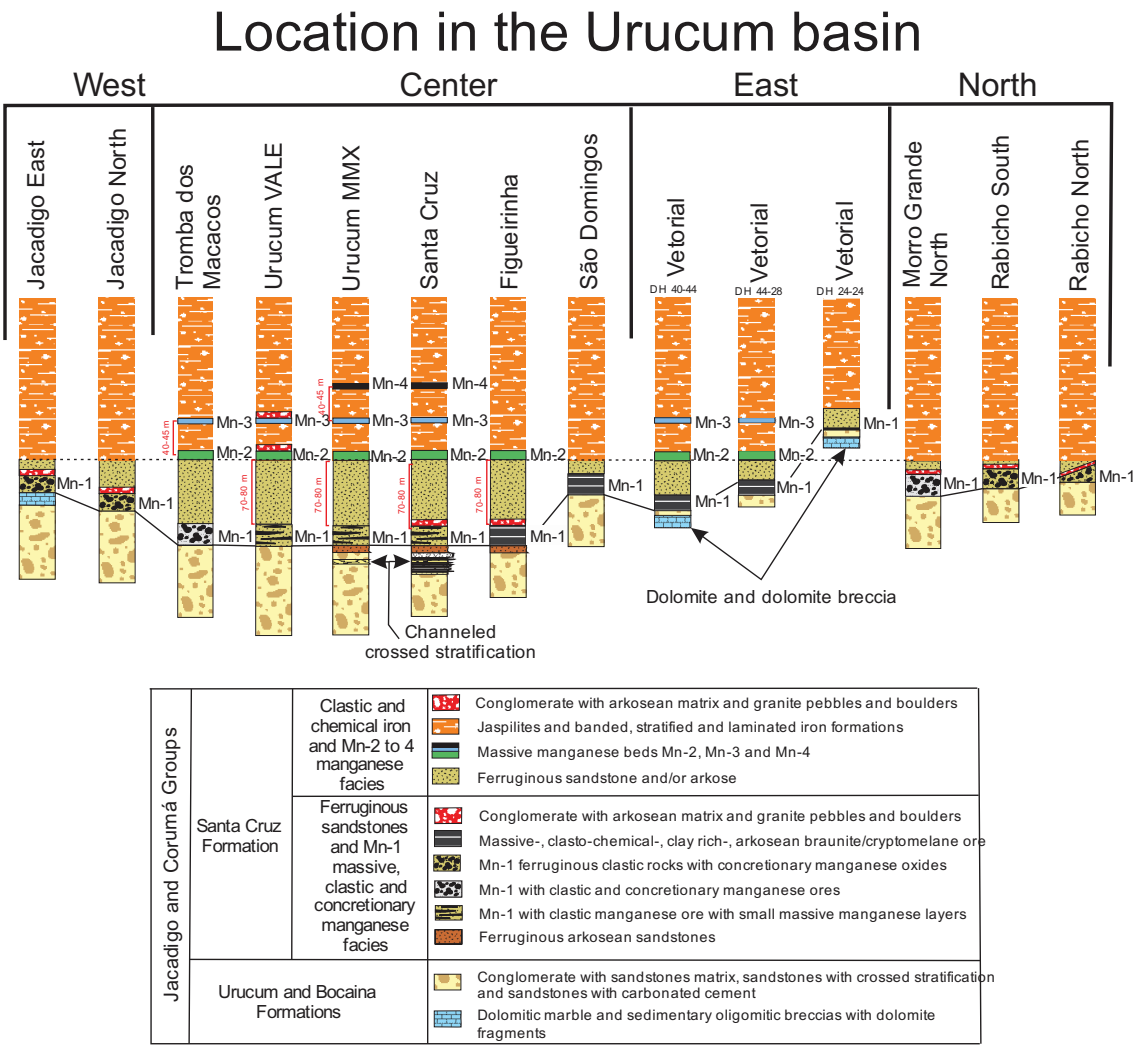

Stratigraphic columns of the Jacadigo Group, arranged from west to east passing through the basin depocenter. The stratigraphic columns of the Morro Grande Norte and Rabicho plateaus, located to the north of the basin, were positioned in the right part of the figure (modified after Urban et al. 1992, Biondi and Lopez 2017). The column elevations are normalized to the stratigraphic position of layer Mn-2 or, where this layer is absent, to the IF base.

SI 3-Fig. Representative samples of Mn-1, Mn-2 and Mn-3

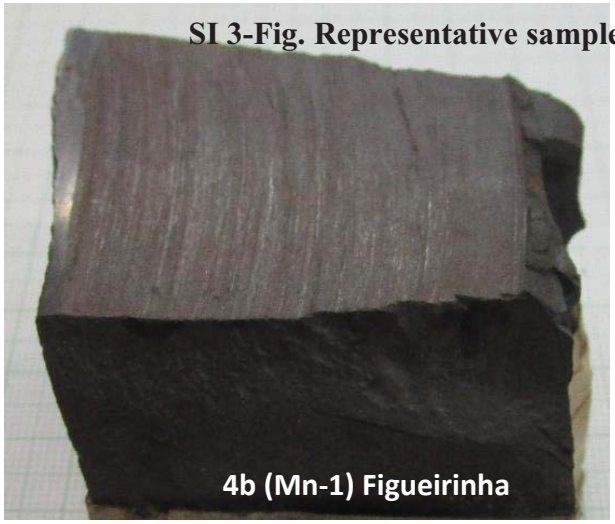

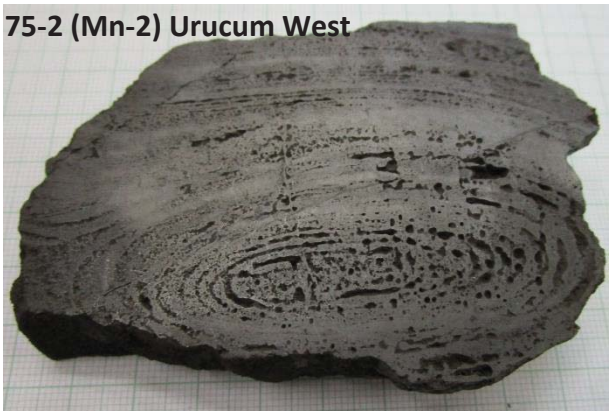

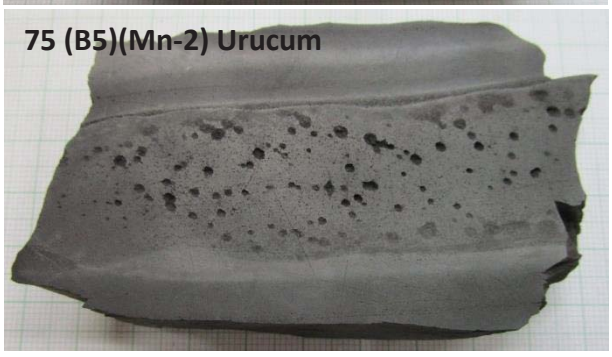

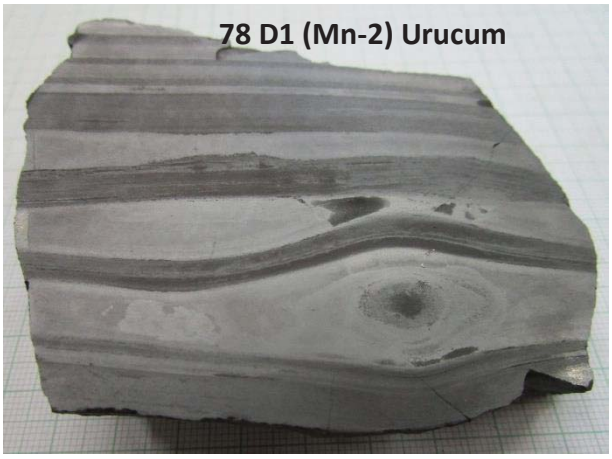

Cut samples

For details see Fig. 1-3 and Table 2.

Scale: 1 cm

SI 4-Fig. Pores and micro-channels in kremydilites

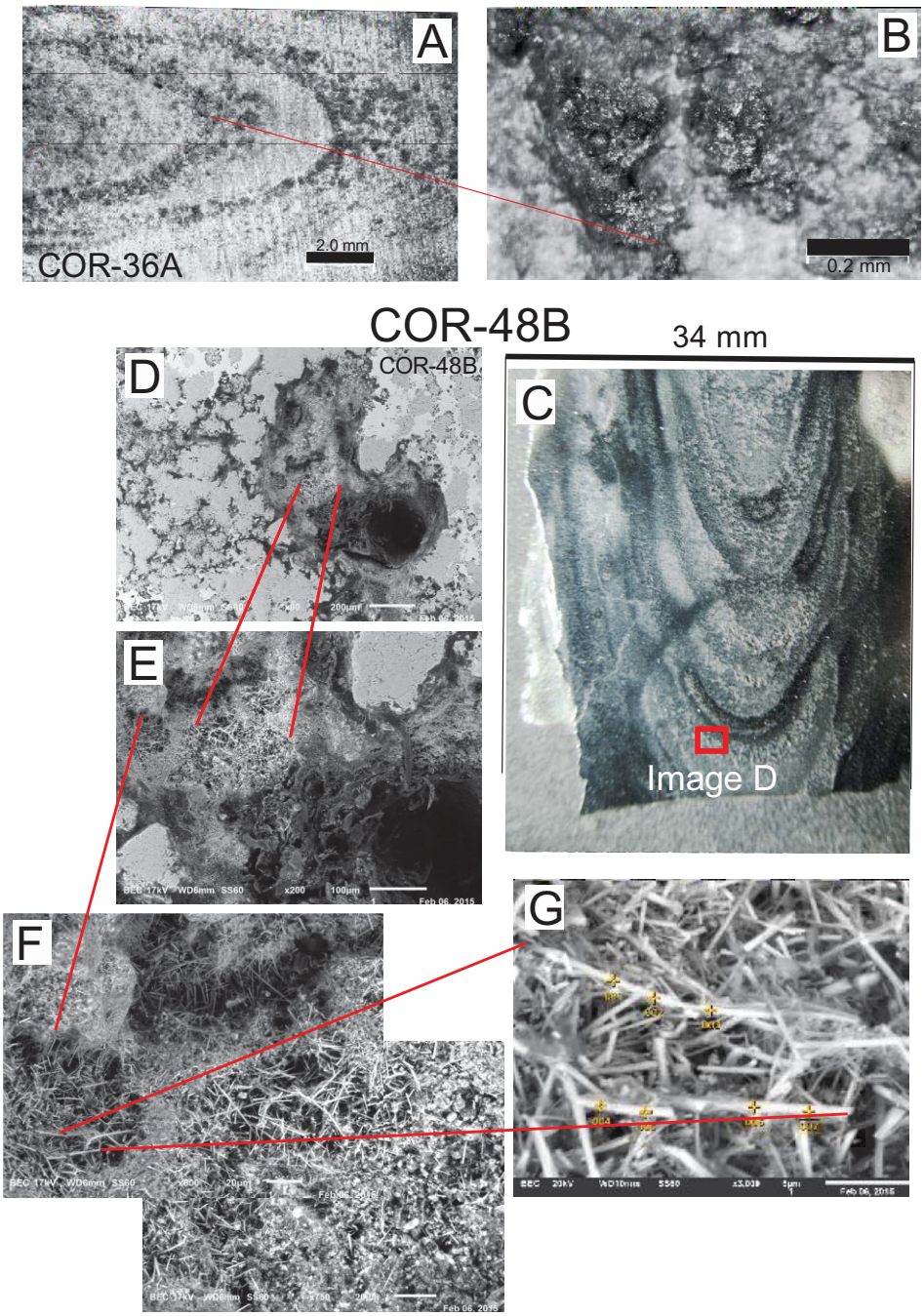

Pores and micro-channels in kremydilites. (A) A set of pores that delineate the micro-layers that surround the nucleus. (B) Pores covered by acicular microcrystals of cryptomelane. (C-G) Micro-channels enveloped by acicular microcrystals of cryptomelane (image C = polished section; images D to G obtained with SEM - Scanning Electron Microscopy)(Biondi and Lopez 2017)

SI 5-Fig. Structure of kremydilite

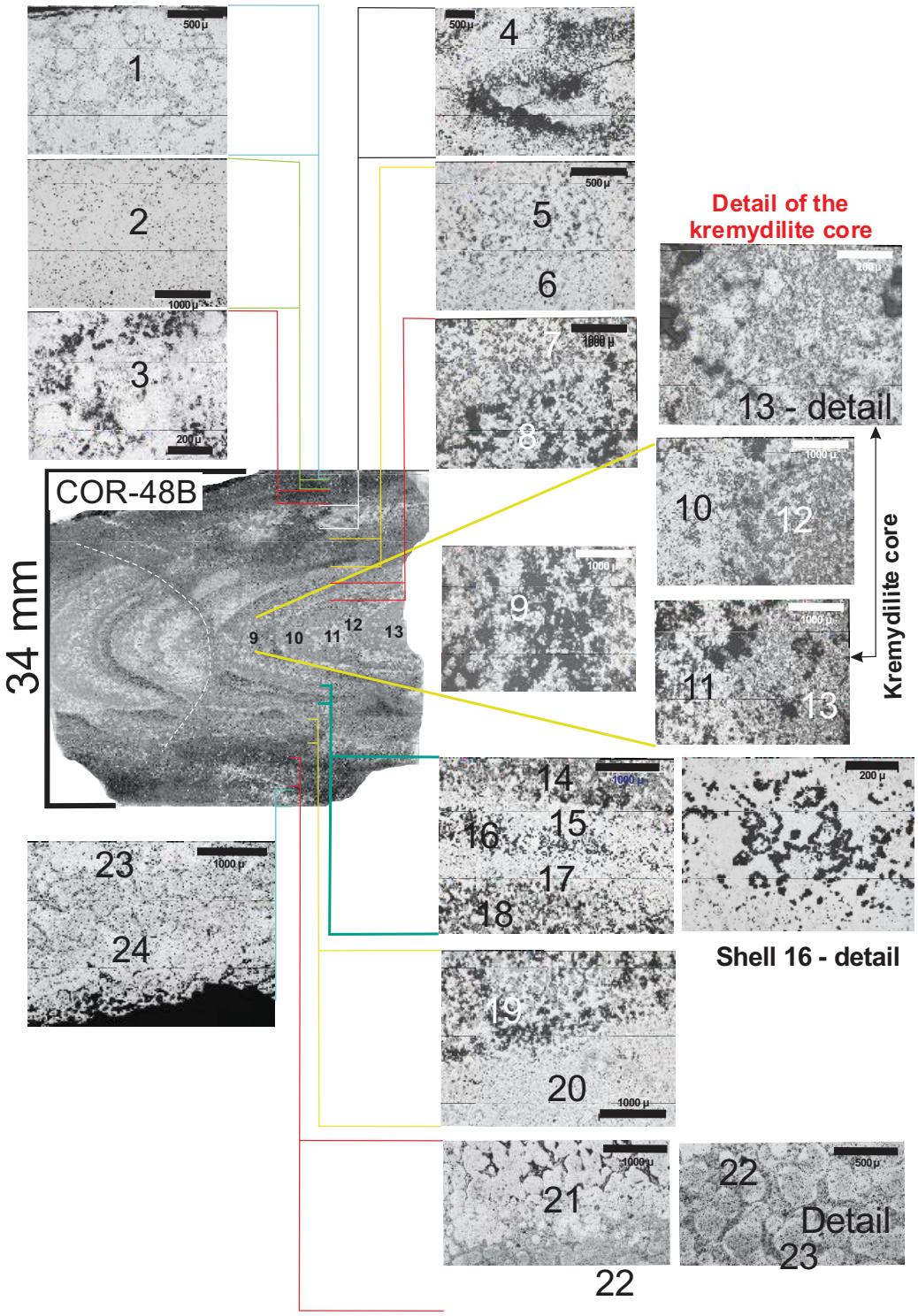

Polished section of the sample 48B showing the bands or sheets of Mn-3 layer in between kremydilite formed (zones 1, 2, 3, and 20 up to 24). Surrounding the core are the most distant concentric micro-layers, shells (shells 4, 5, 6 and 14 to 18) and the nearest ones (shells 9, 10 and 11). Shells 12 and 13 are in the core of the structure. See text for details (Biondi and Lopez 2017).

The curved and undulating layers (bands) in which kremydilite formed are composed of flakes whose diameters ranged from 0.8 to 0.2 mm (SI 5-Fig, zones 1, 2, 3; and zones 20 to 24), apparently composed by the amalgamation of flakes, micronodules smaller than 10 μm (Fig. 4K). The outermost zones (shells) of kremydilite (SI 5-Fig, shells 4, 5, 6, and 14 to 18) consist of anhedral and irregularly shaped minerals, looking like amalgamated flakes. In these shells the presence of ring-like structures, composed of dark carbonate microcrystals are common (SI 5-Fig, shell 16 - detail image). The shells closer to the nucleus (9, 10 and 11) are also composed of mixed anhedral, metallic minerals, but with larger dimensions than the anterior shells. The nucleus of the kremydilites (zones 12 and 13) are microgranular and with homogeneous appearances.

SI 6-Fig. Panorama images of the analyzed samples

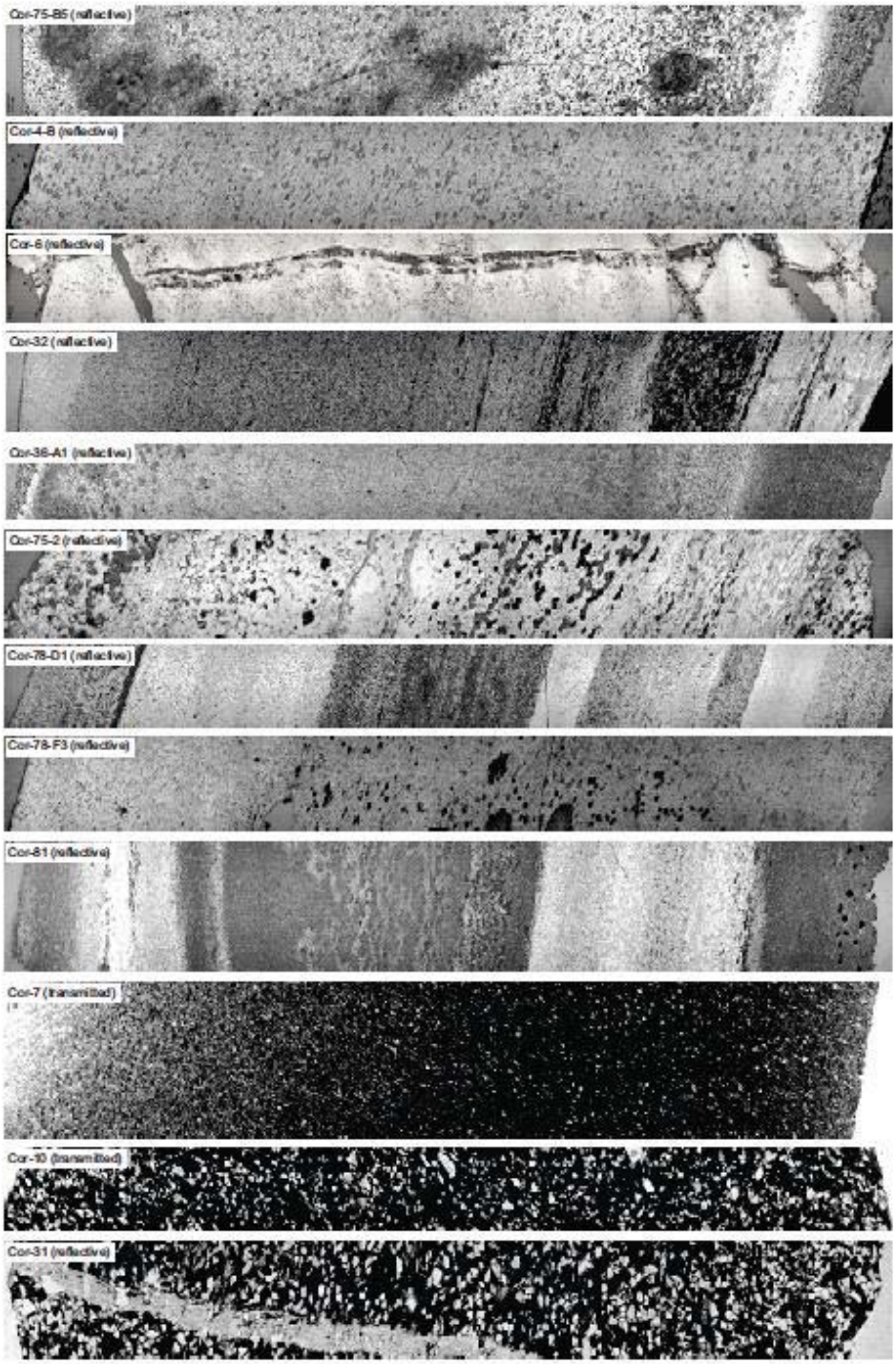

SI 7-Fig. Biomat structures of representative samples (arrows)

Optical rock microscopy, reflected light, 1 Nicol (left side) and crossed Nicols (right side)

Sample 32

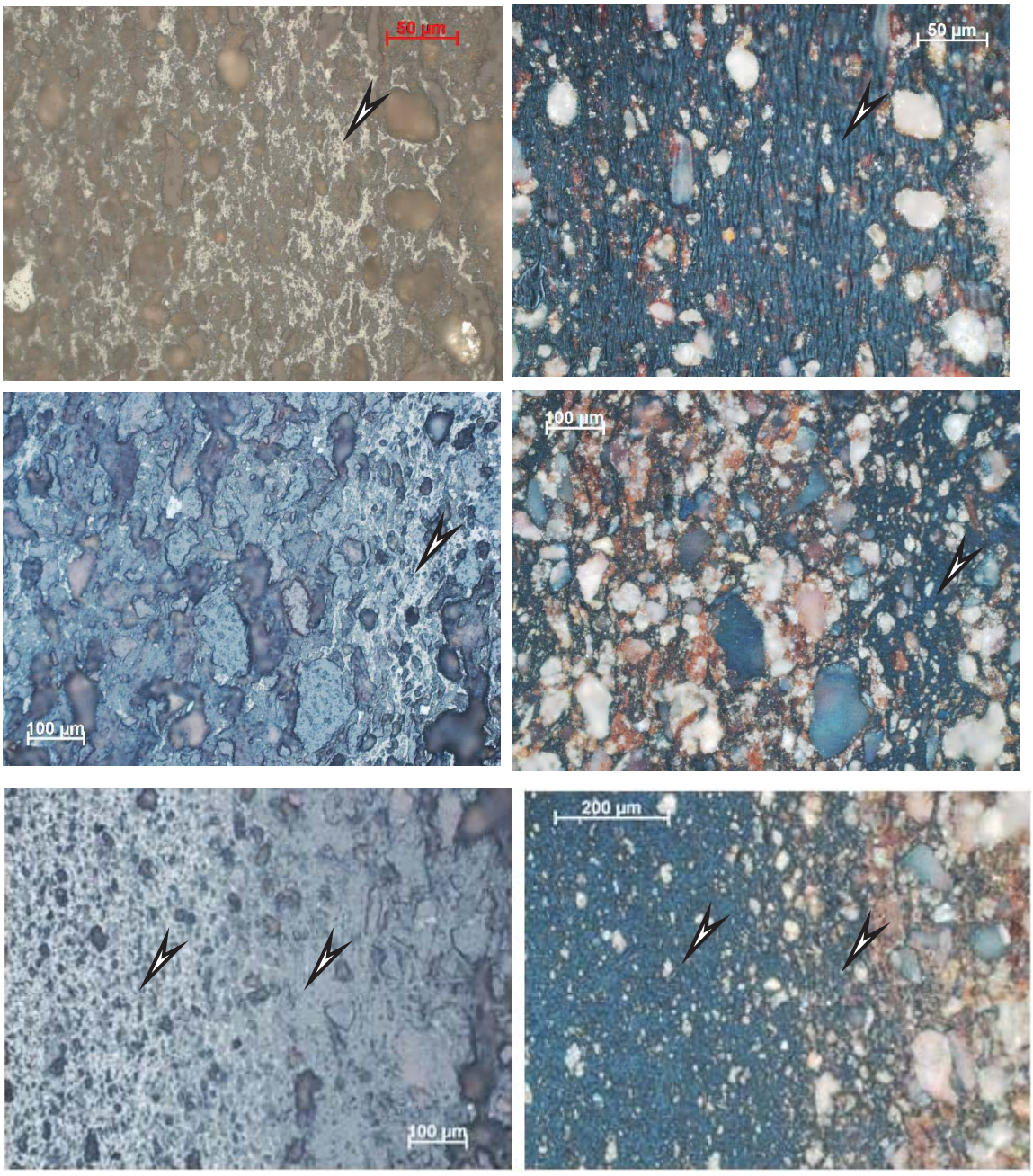

SI 8-Fig. Microtexture of samples by optical rock microscopy

Sample 4B

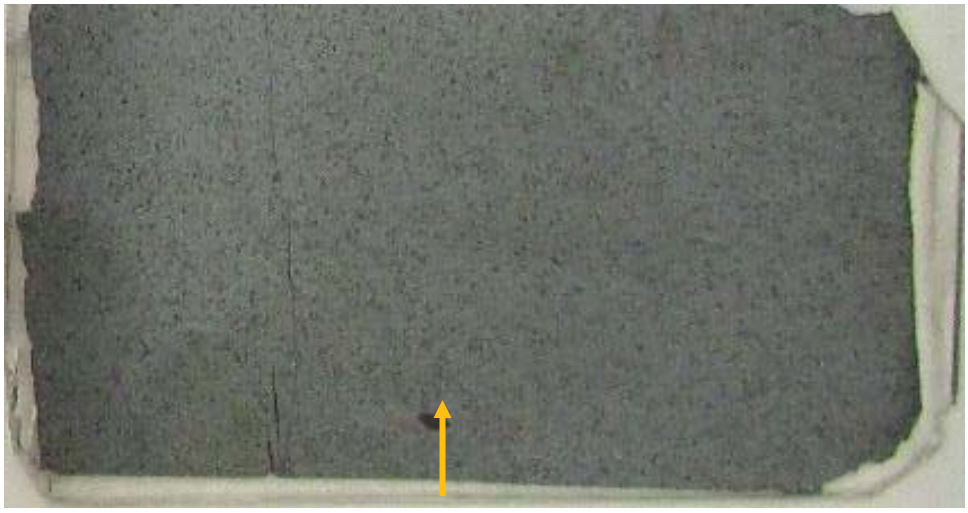

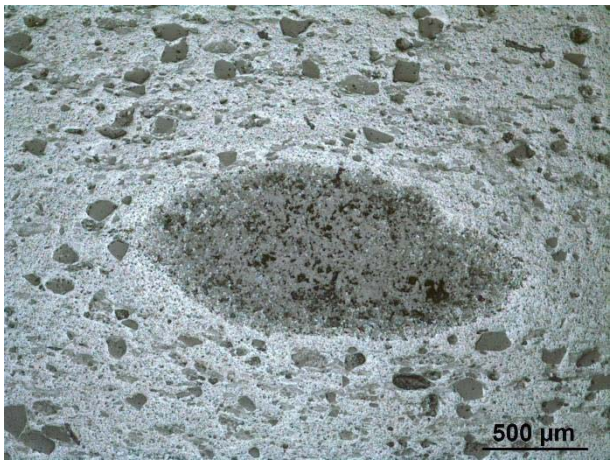

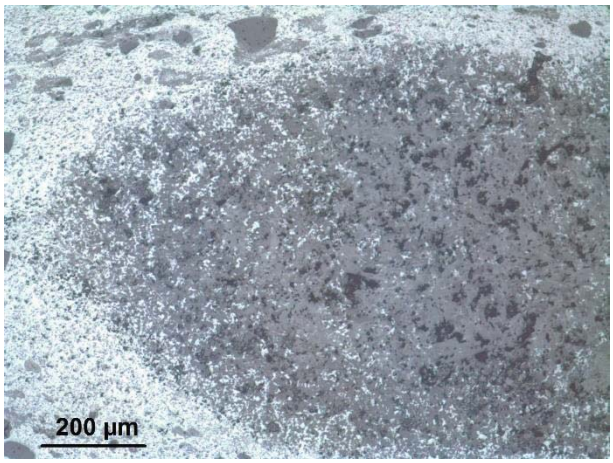

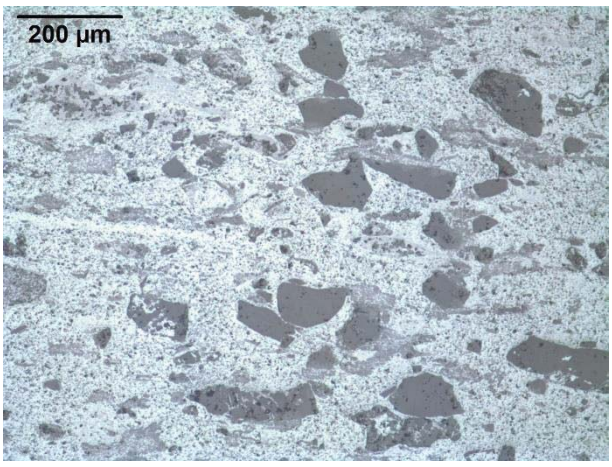

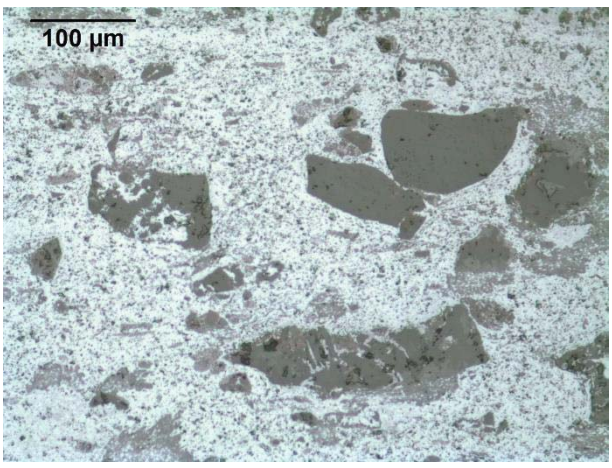

Sample 7

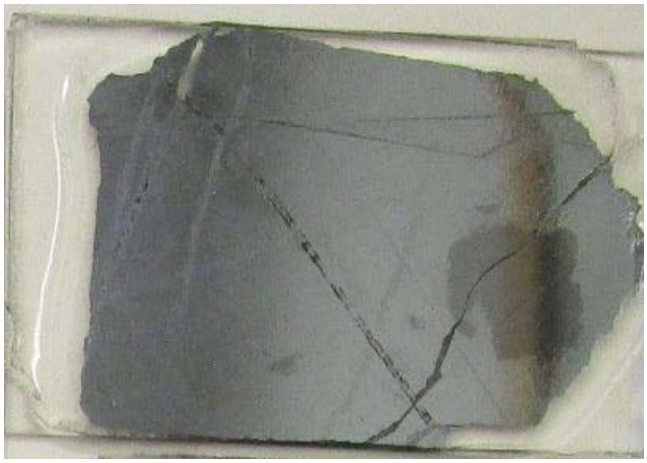

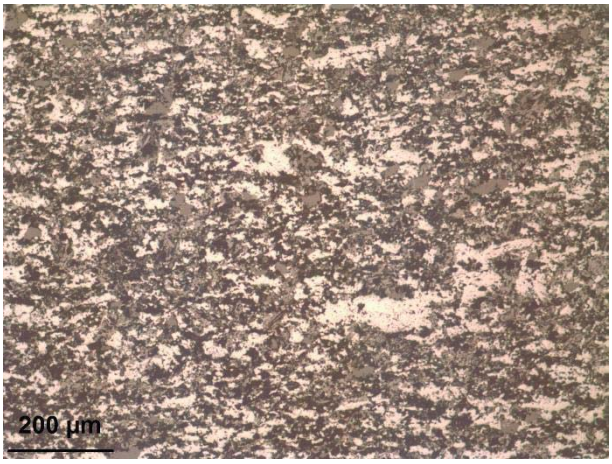

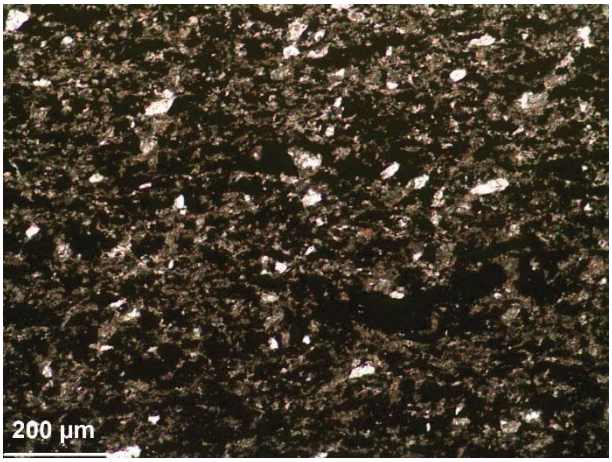

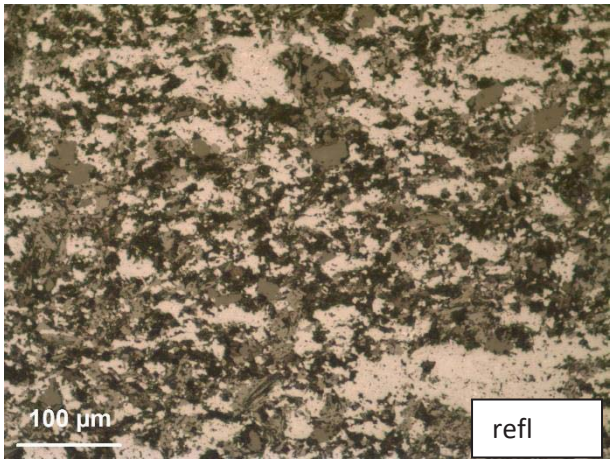

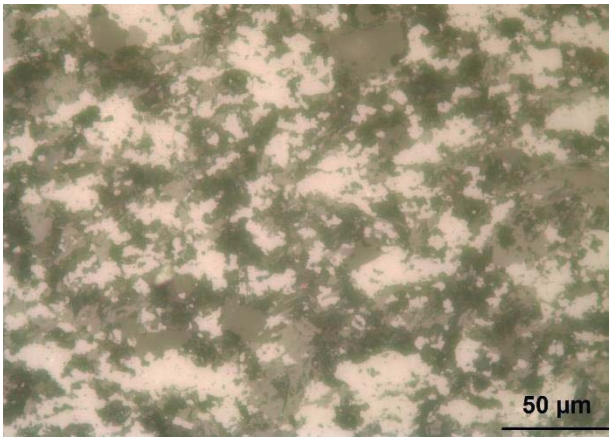

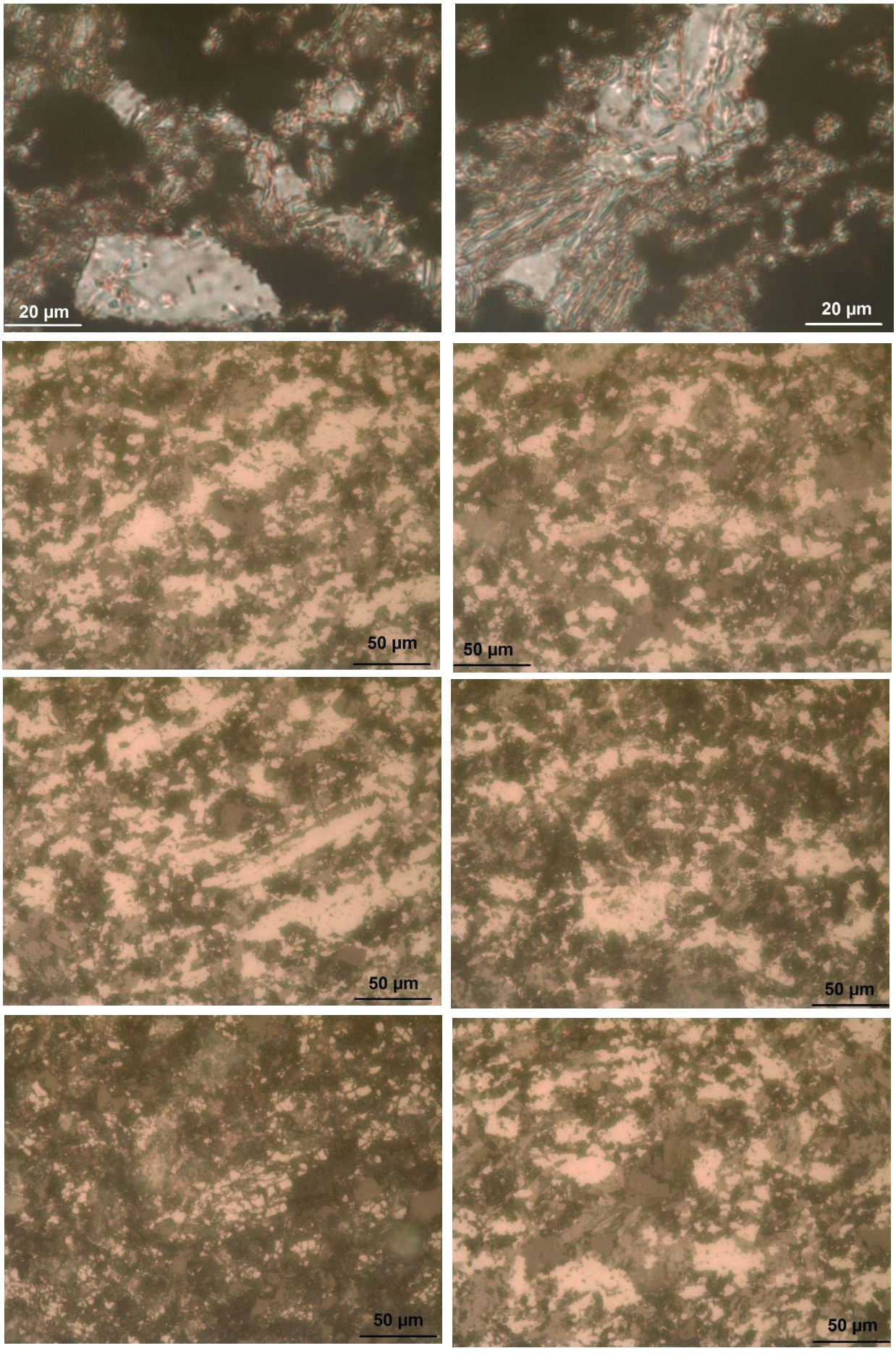
20 µm
20 µm
50 µm
50 µm
50 µm
50 µm
50 µm
50 µm

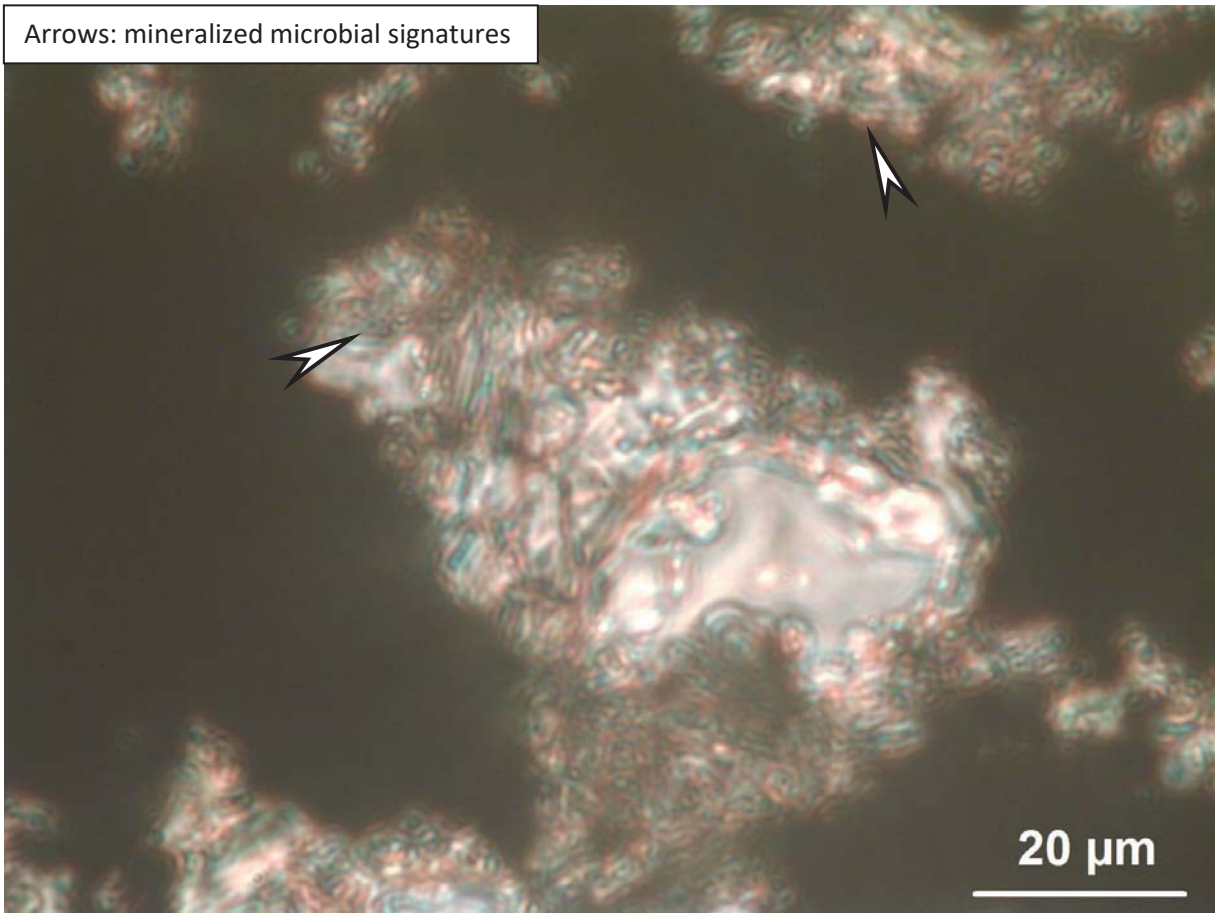
Arrows: mineralized microbial signatures
20 µm

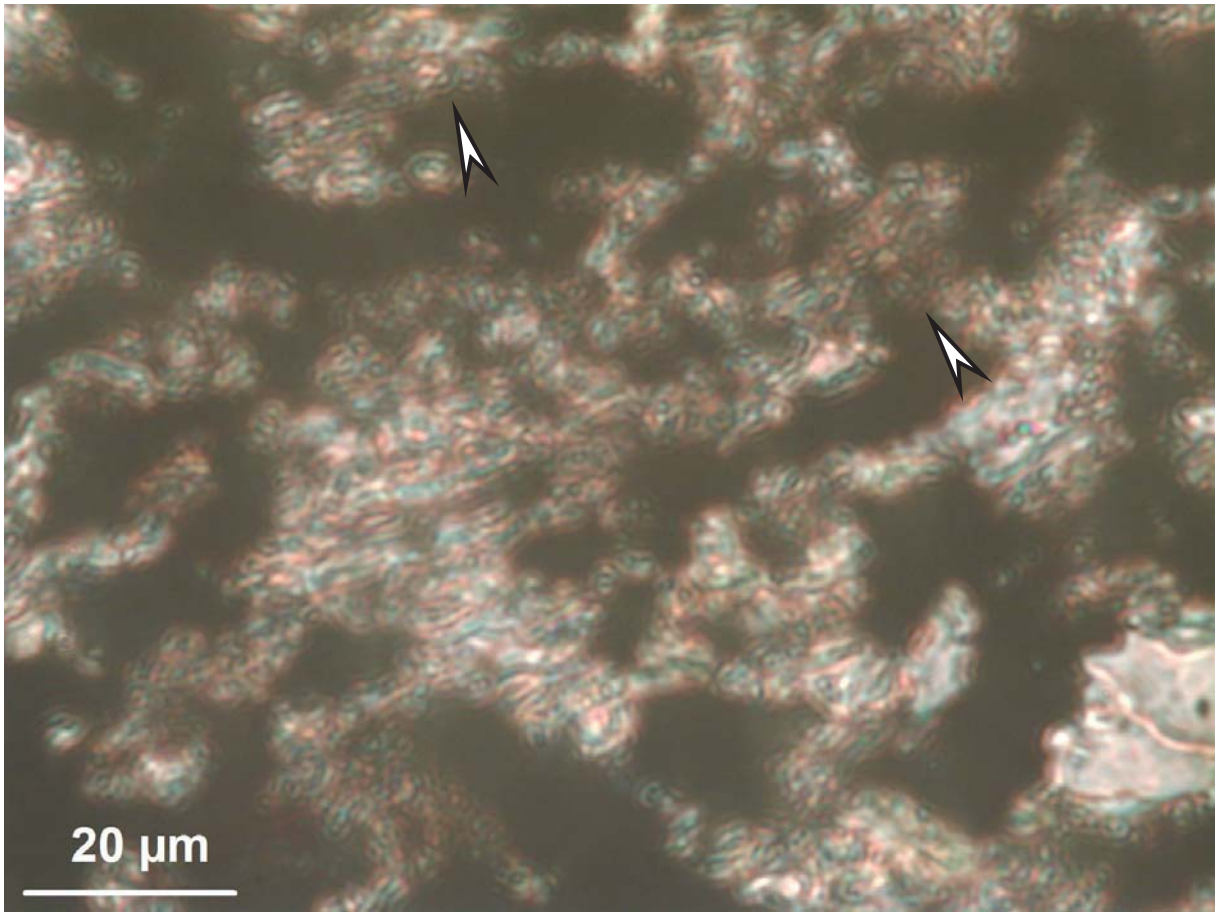
20 µm

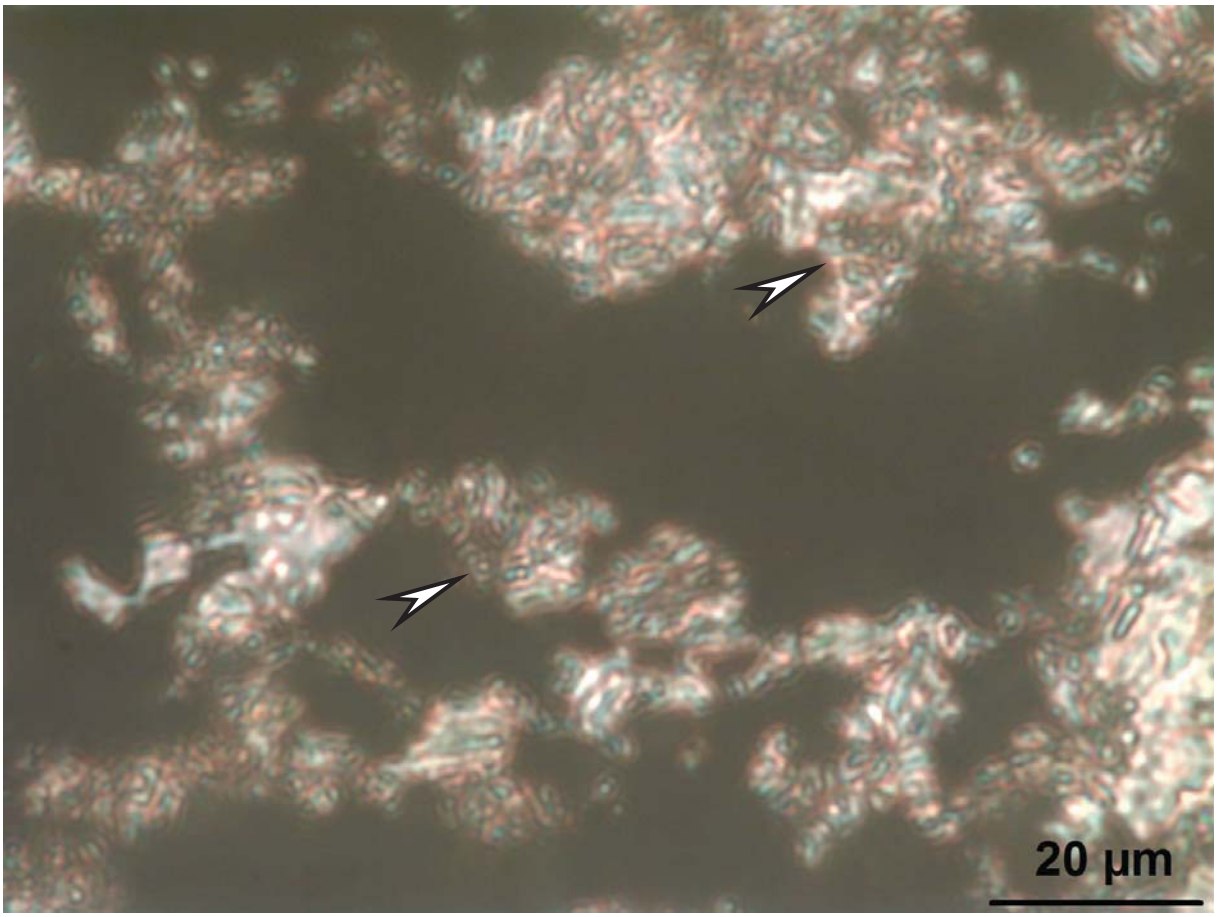
20 µm

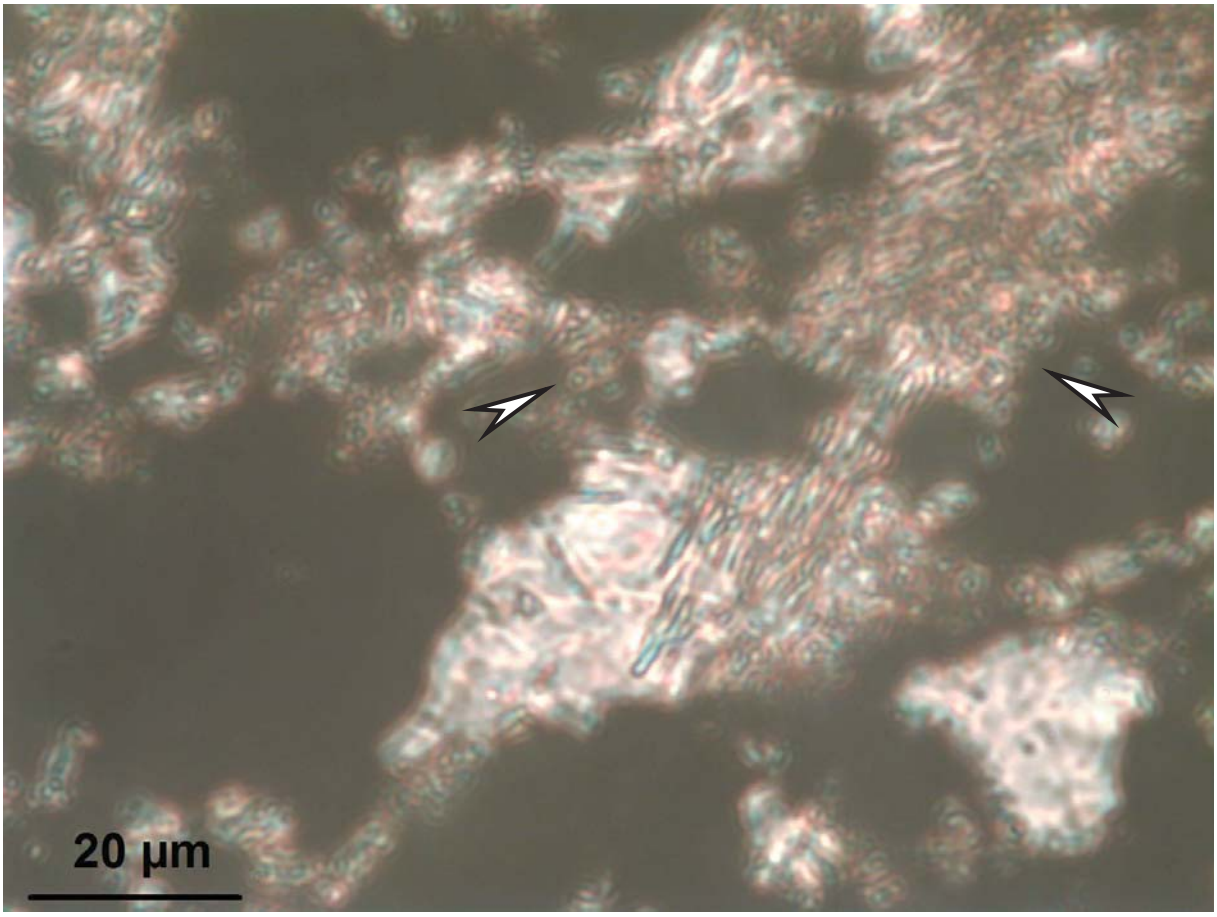
20 µm

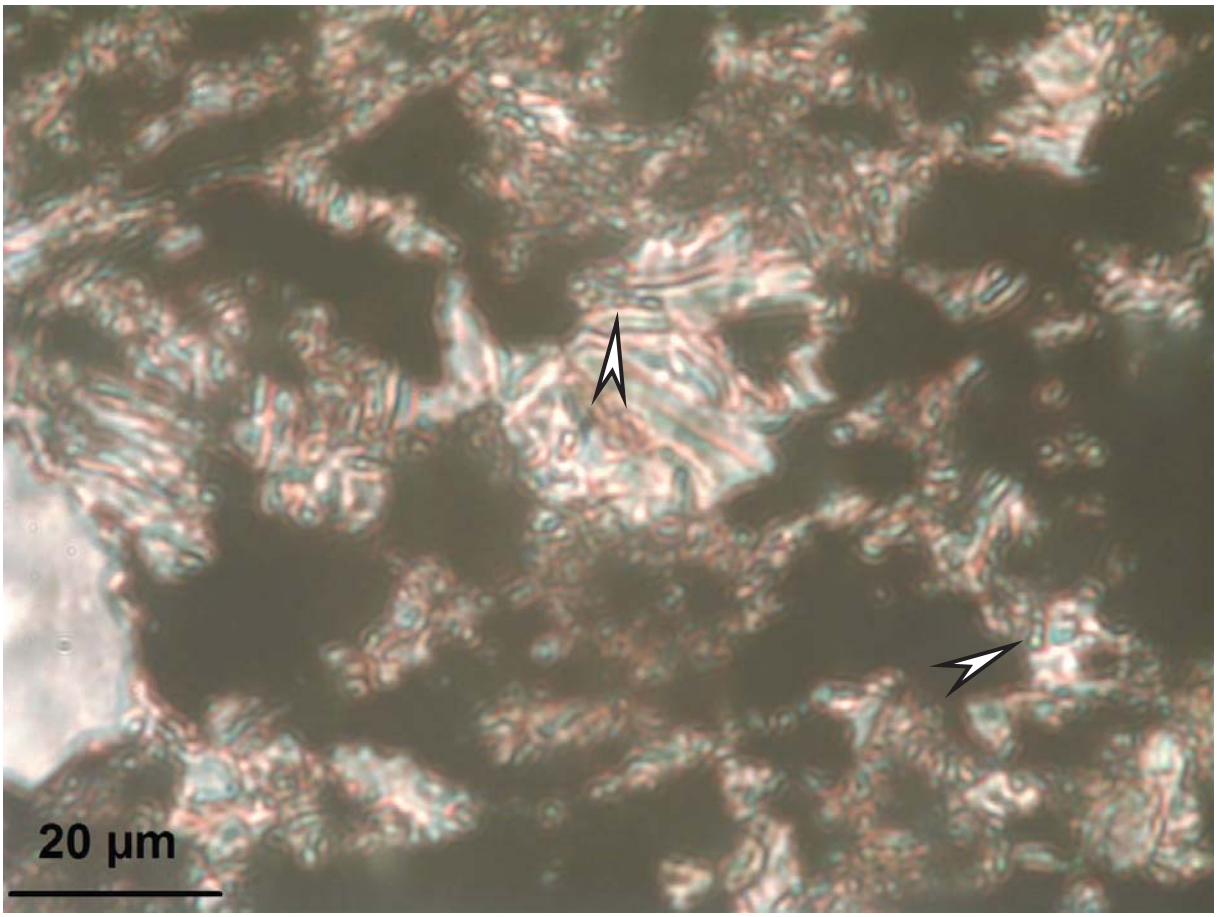
20 µm

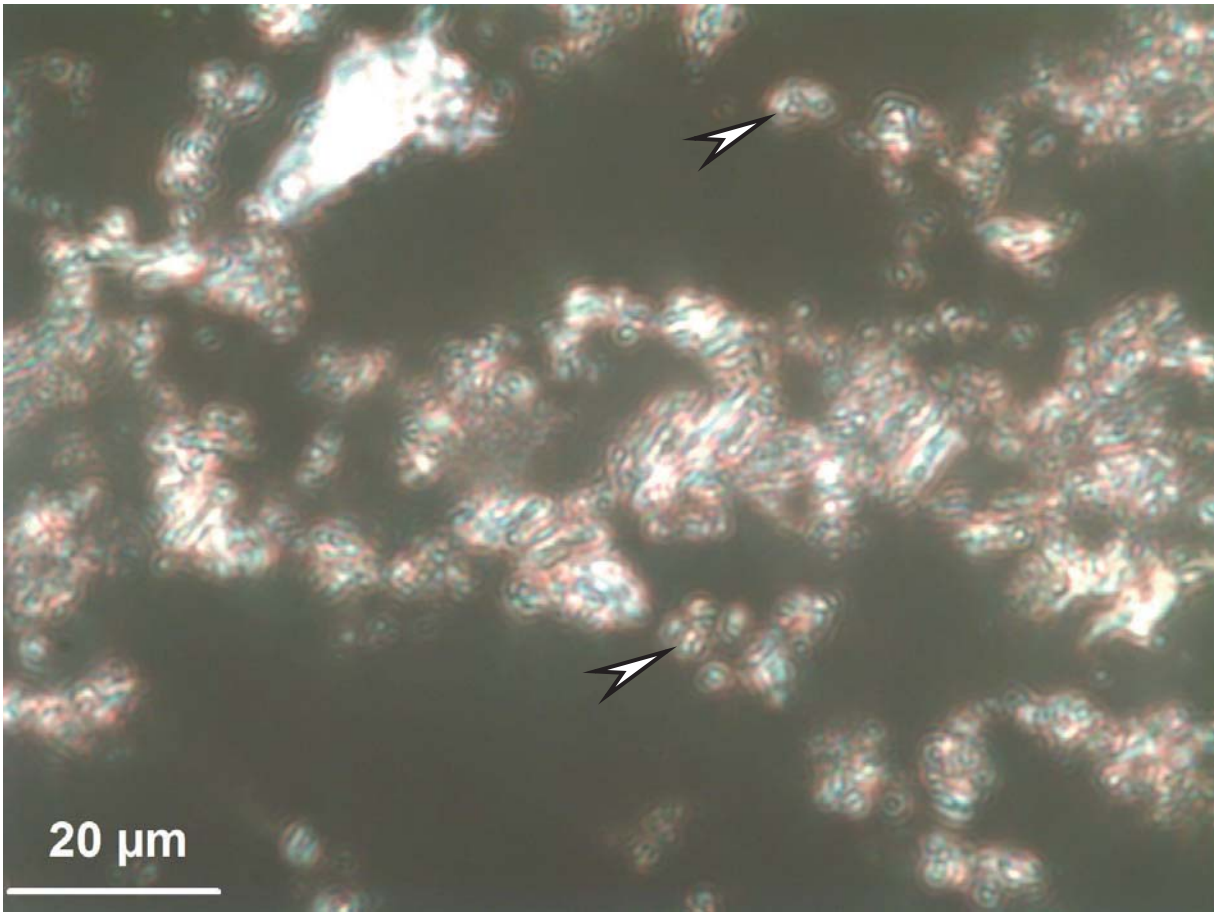
20 µm

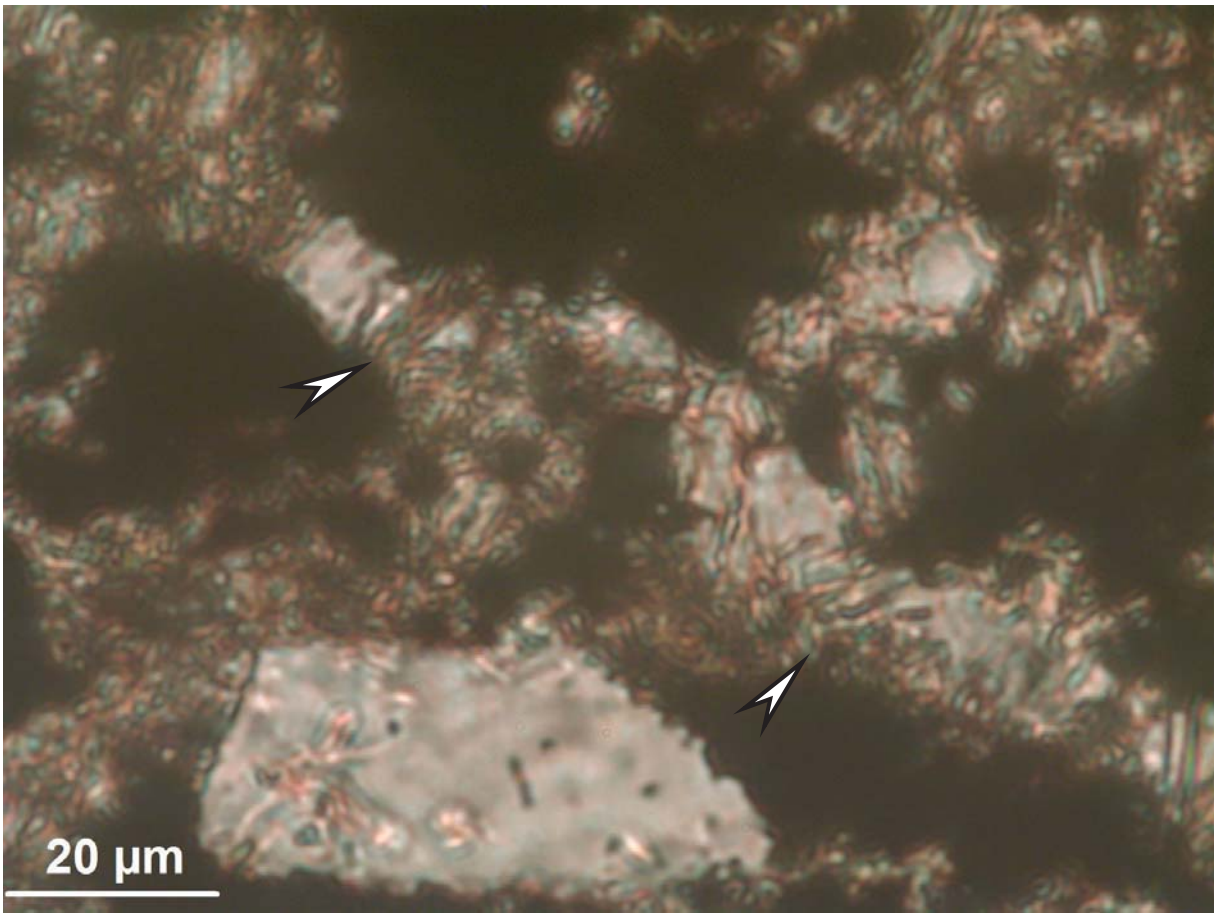
20 µm

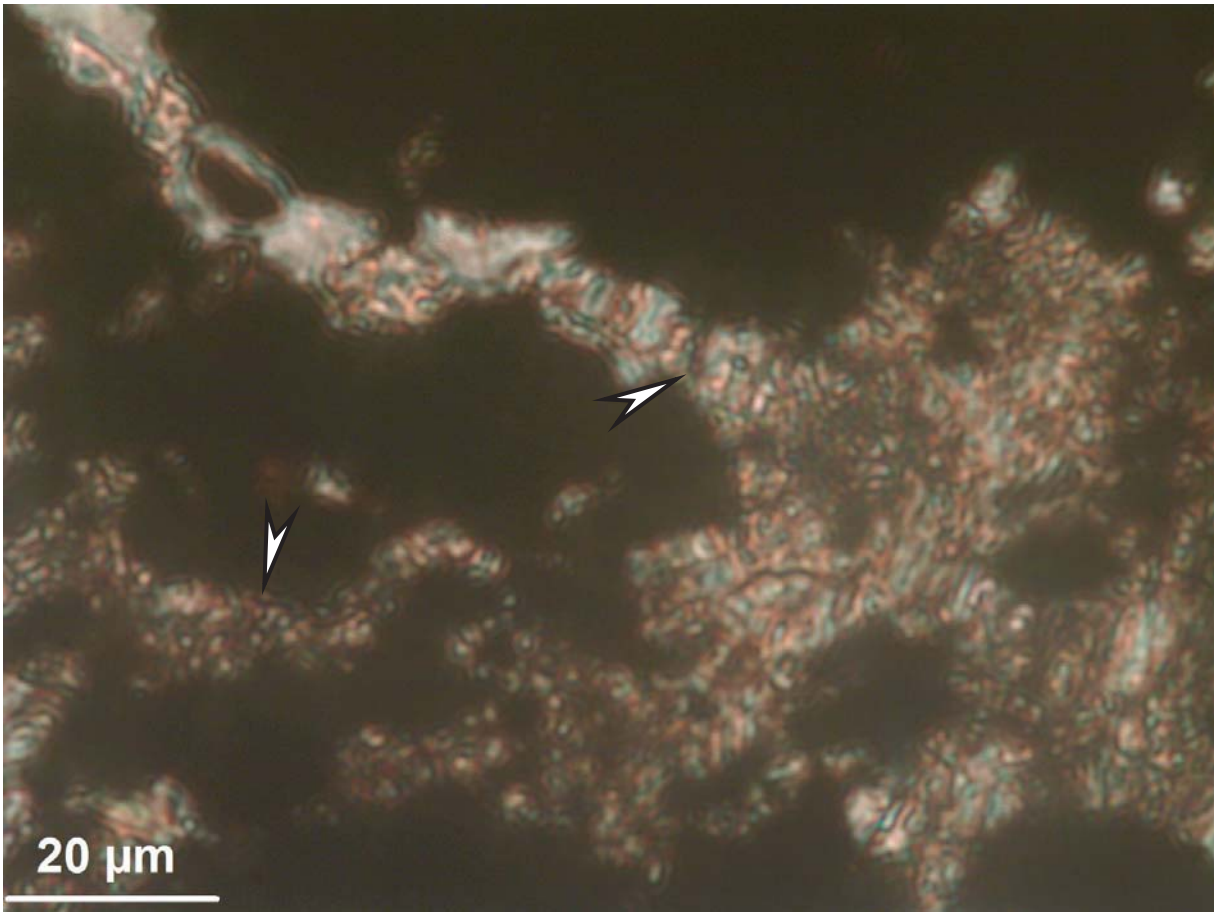
20 µm

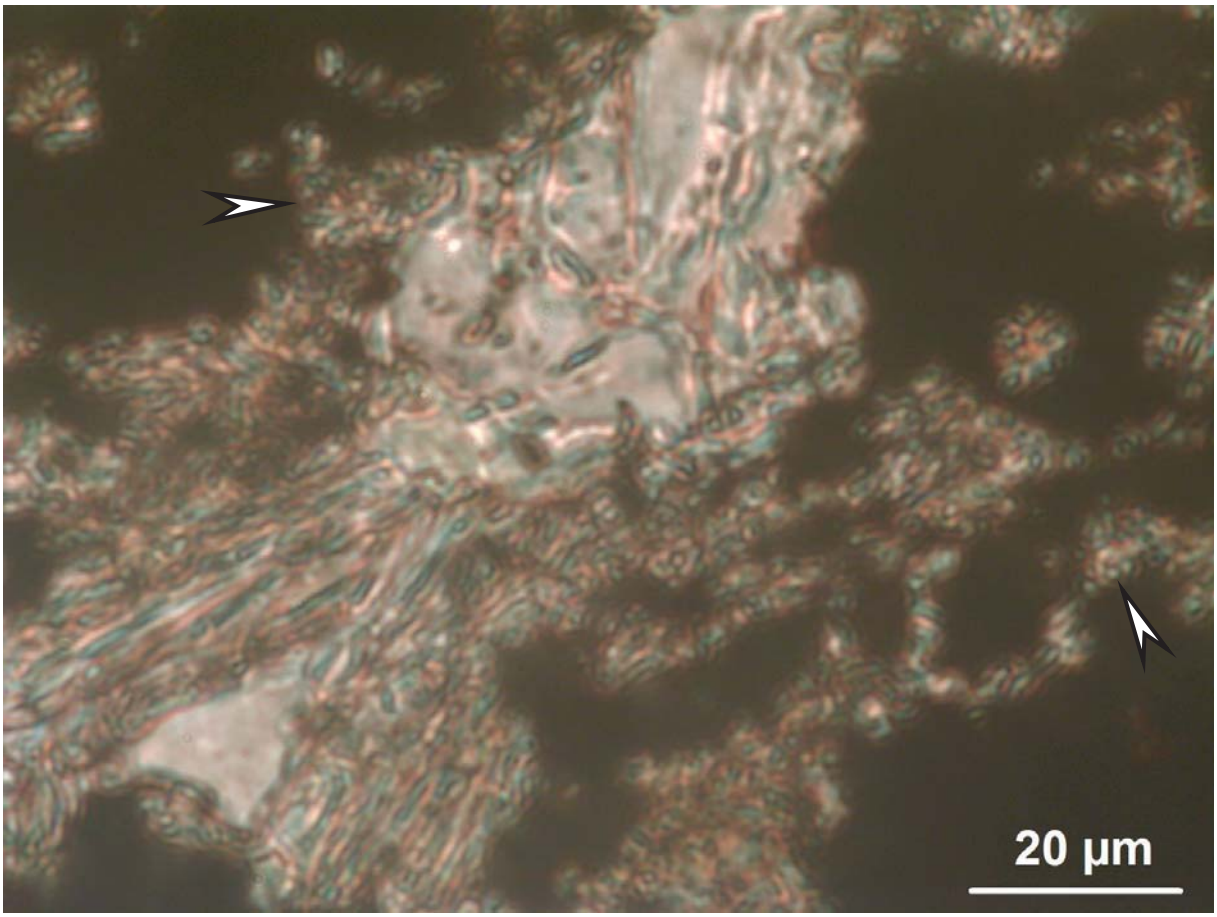
20 µm

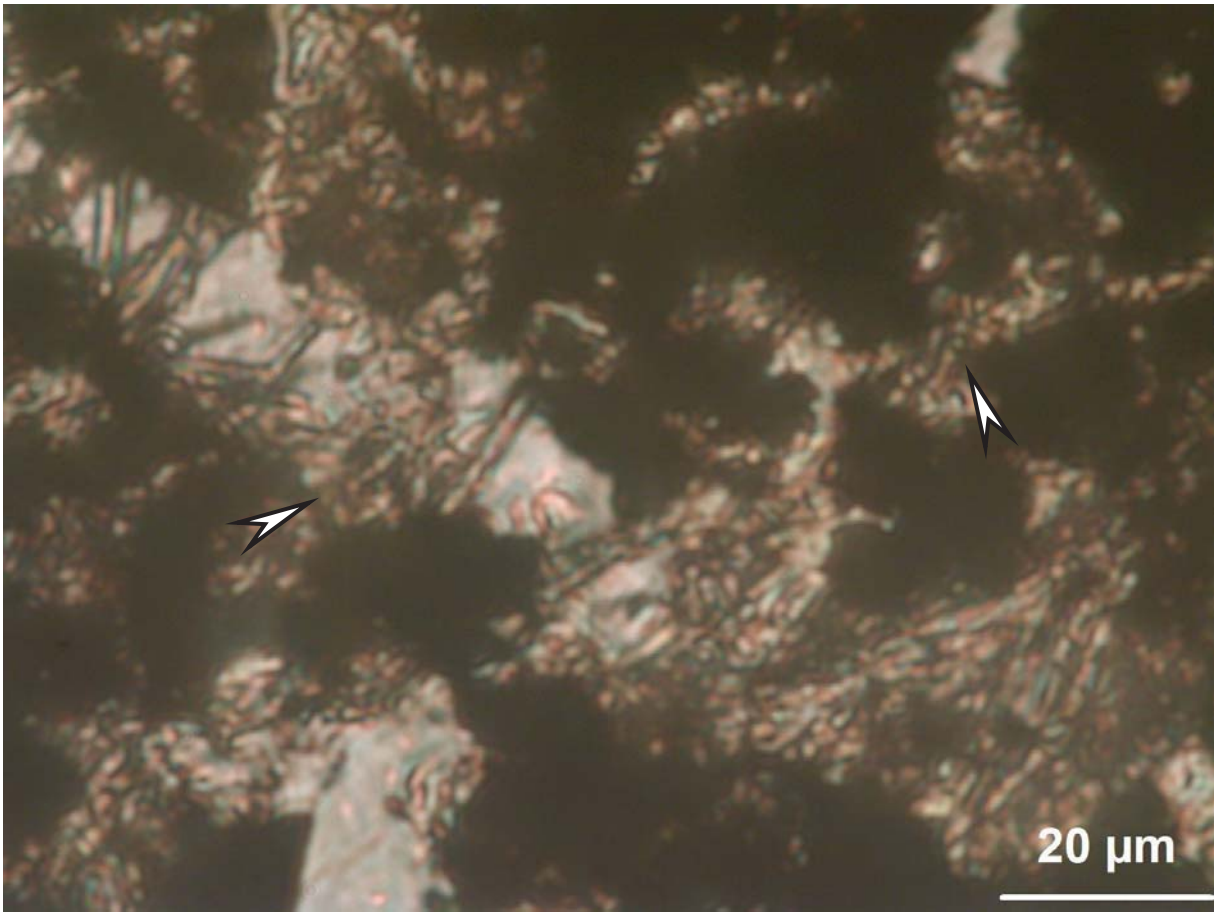
20 µm

Sample 10

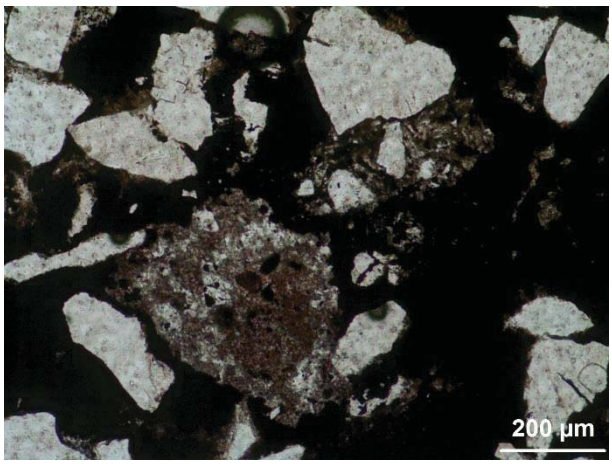

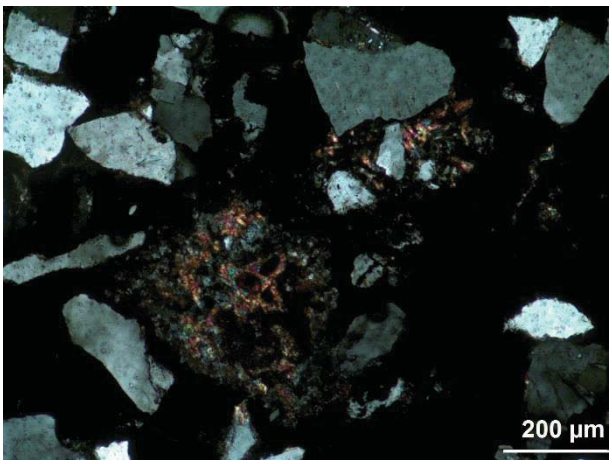

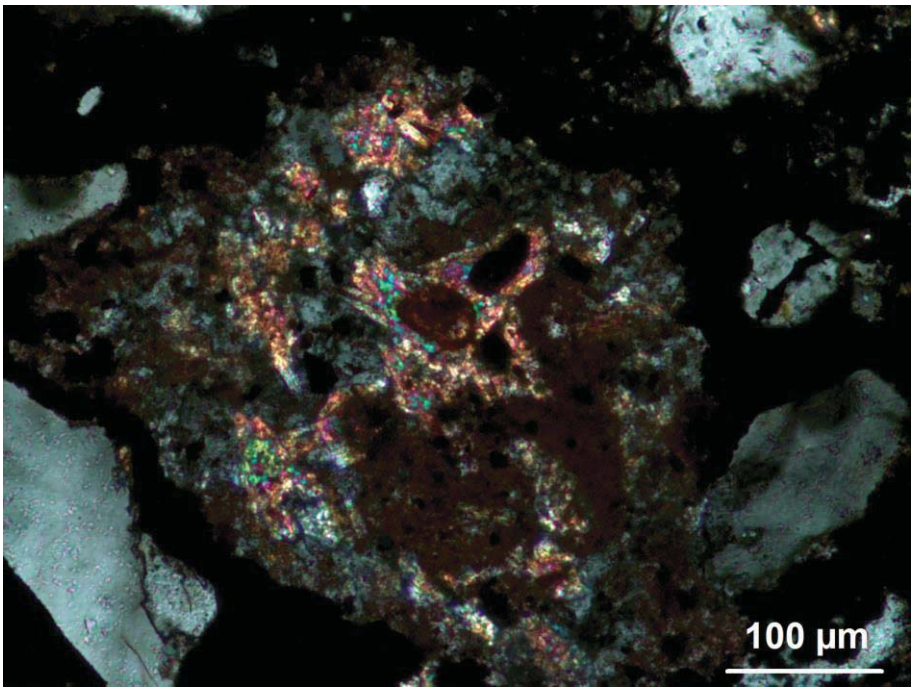

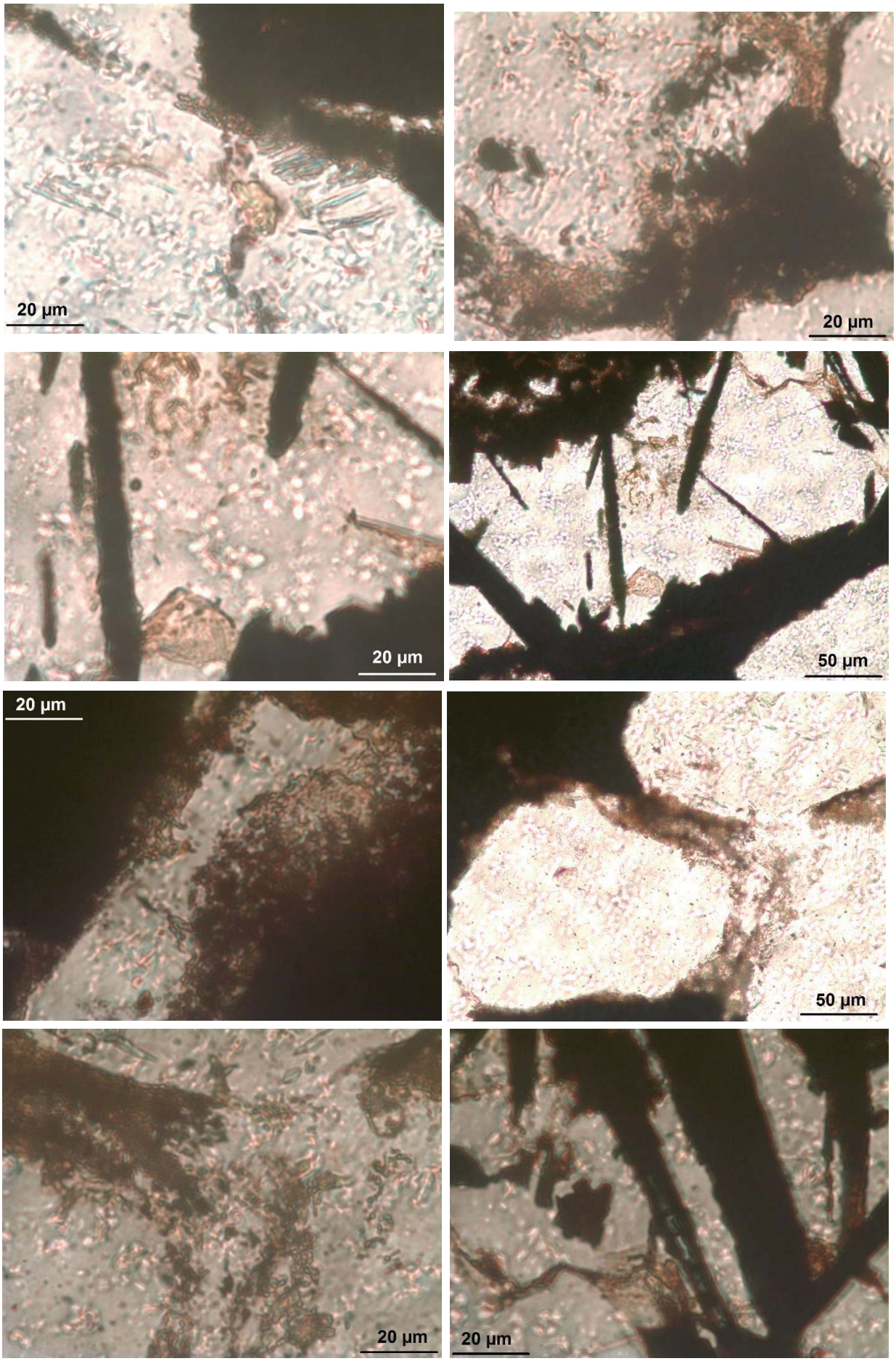
20 µm
20 µm
20 µm
50 µm
20 µm
50 µm
20 µm
20 µm

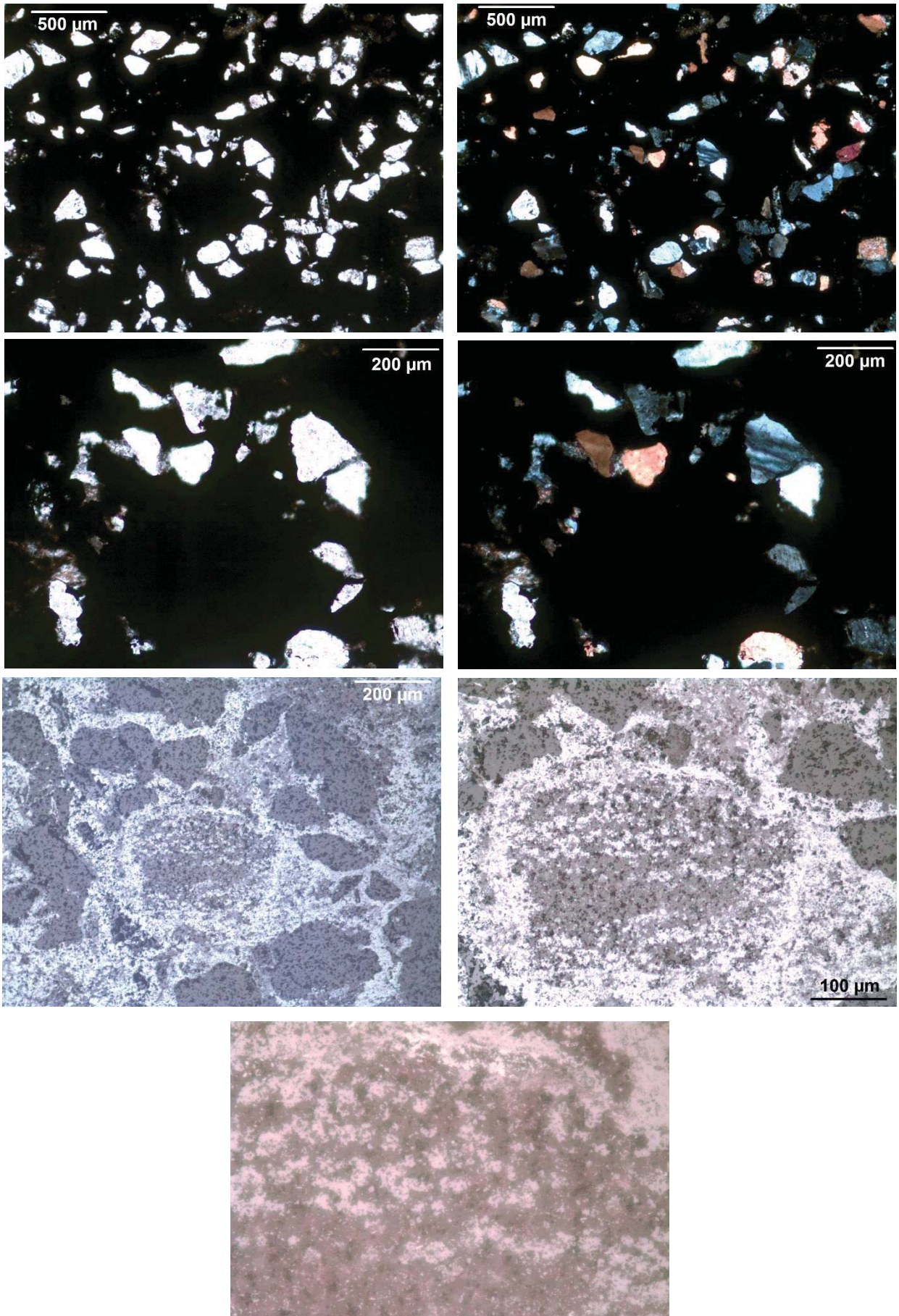
500 µm
500 µm
200 µm
200 µm
200 µm
100 µm
50 µm

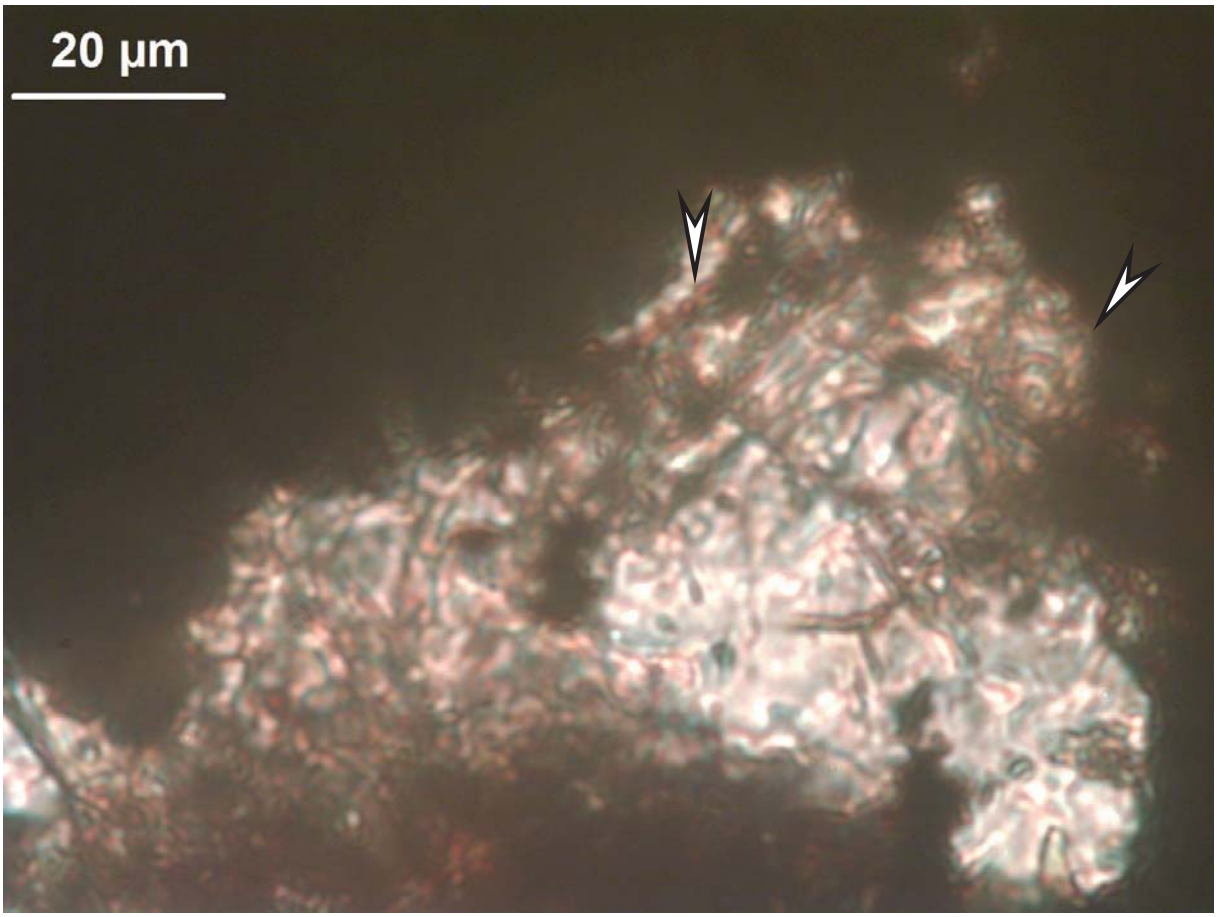
20 µm


20 µm

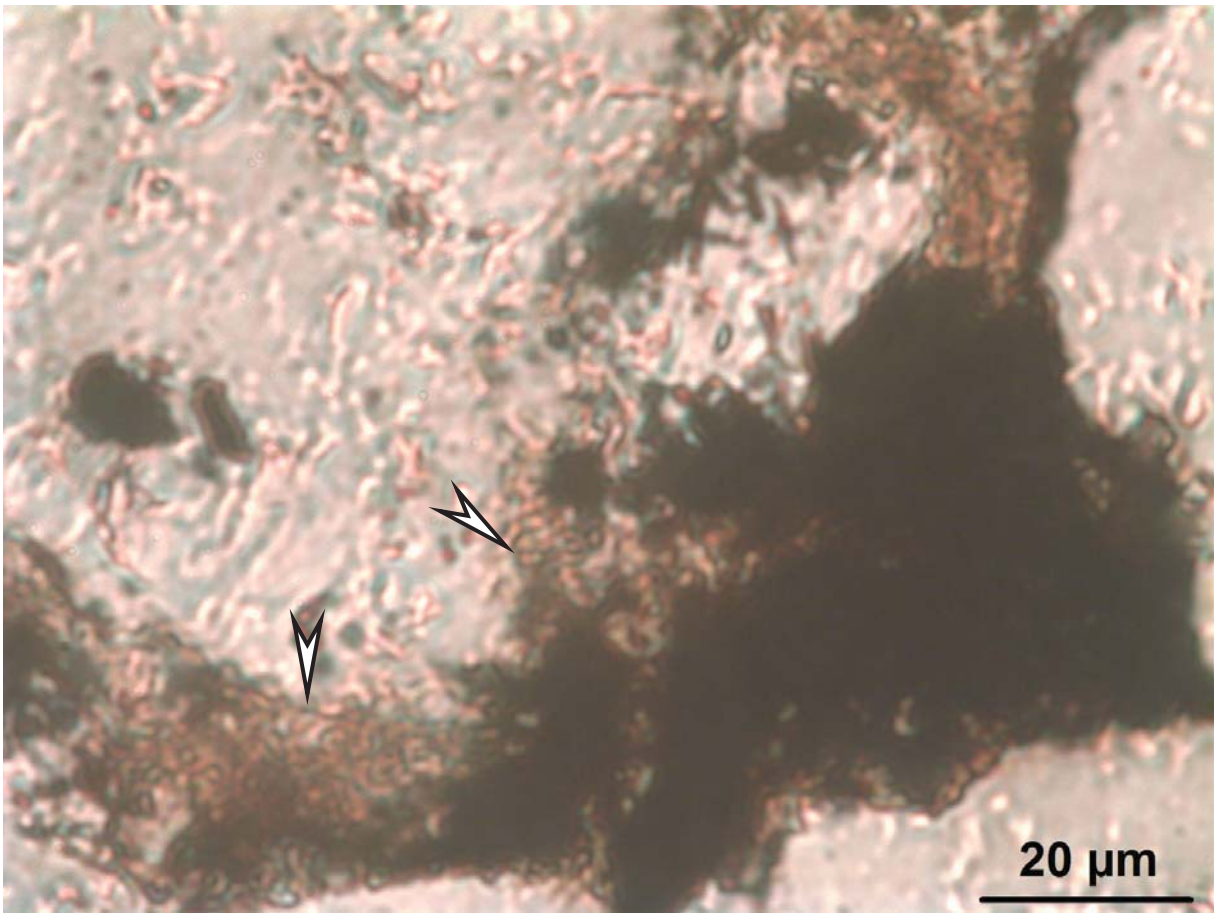
20 µm

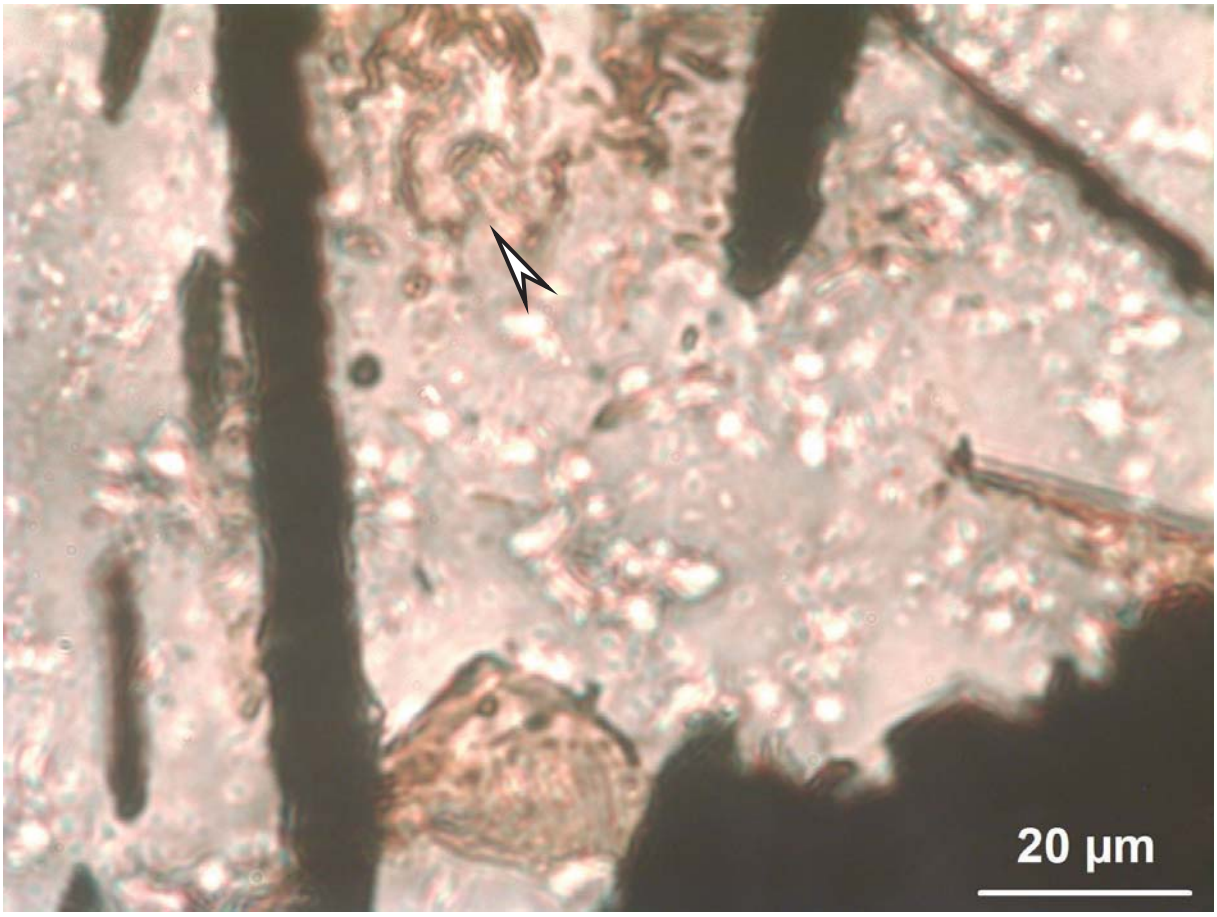
20 µm

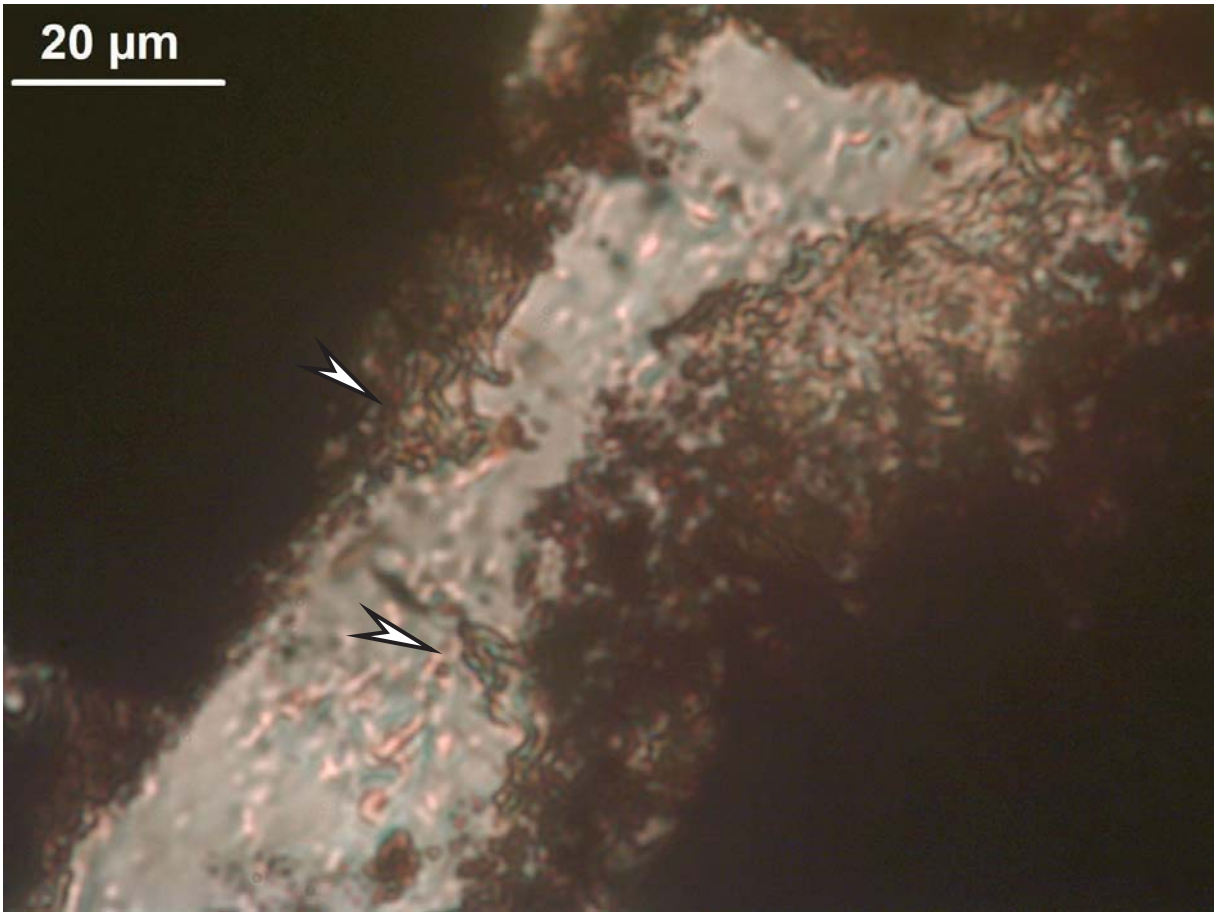
20 µm

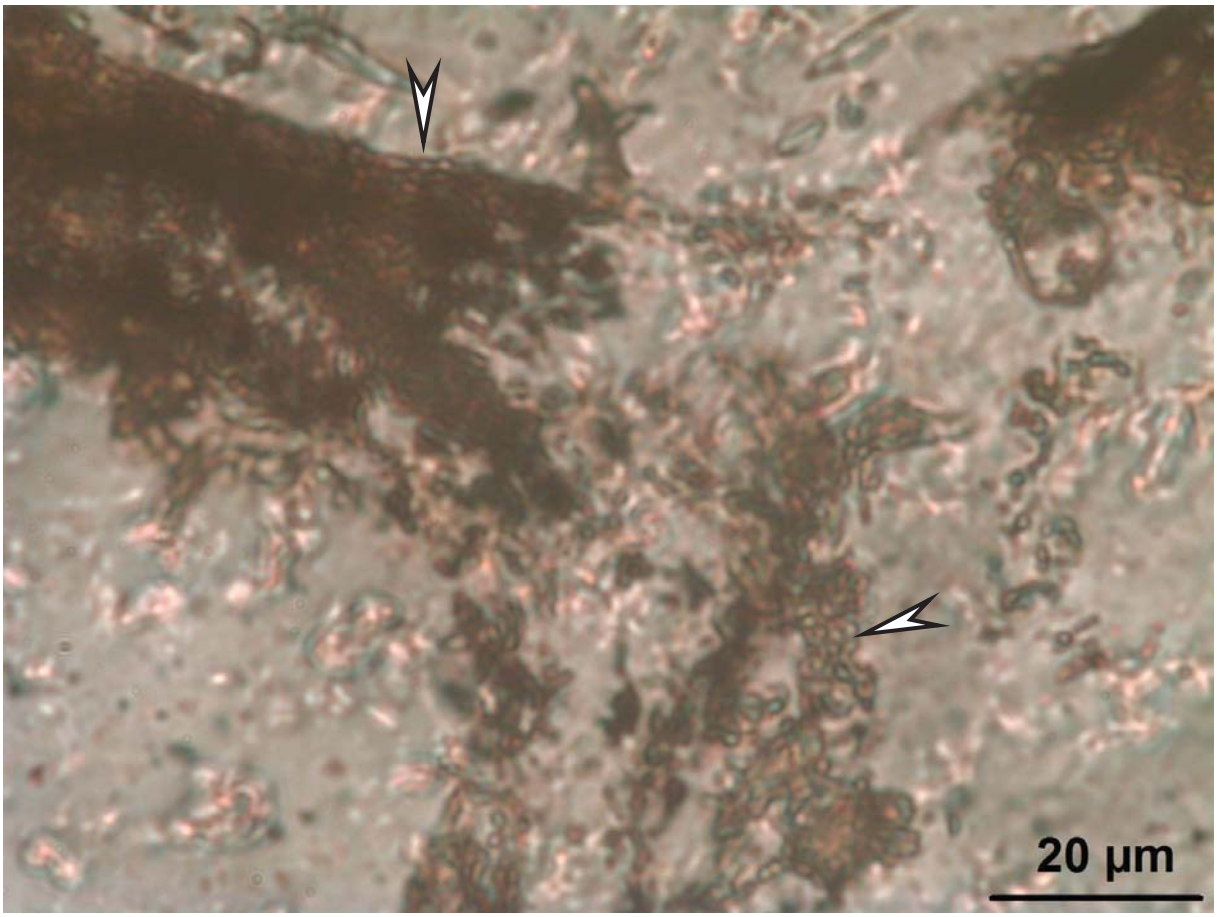
20 µm

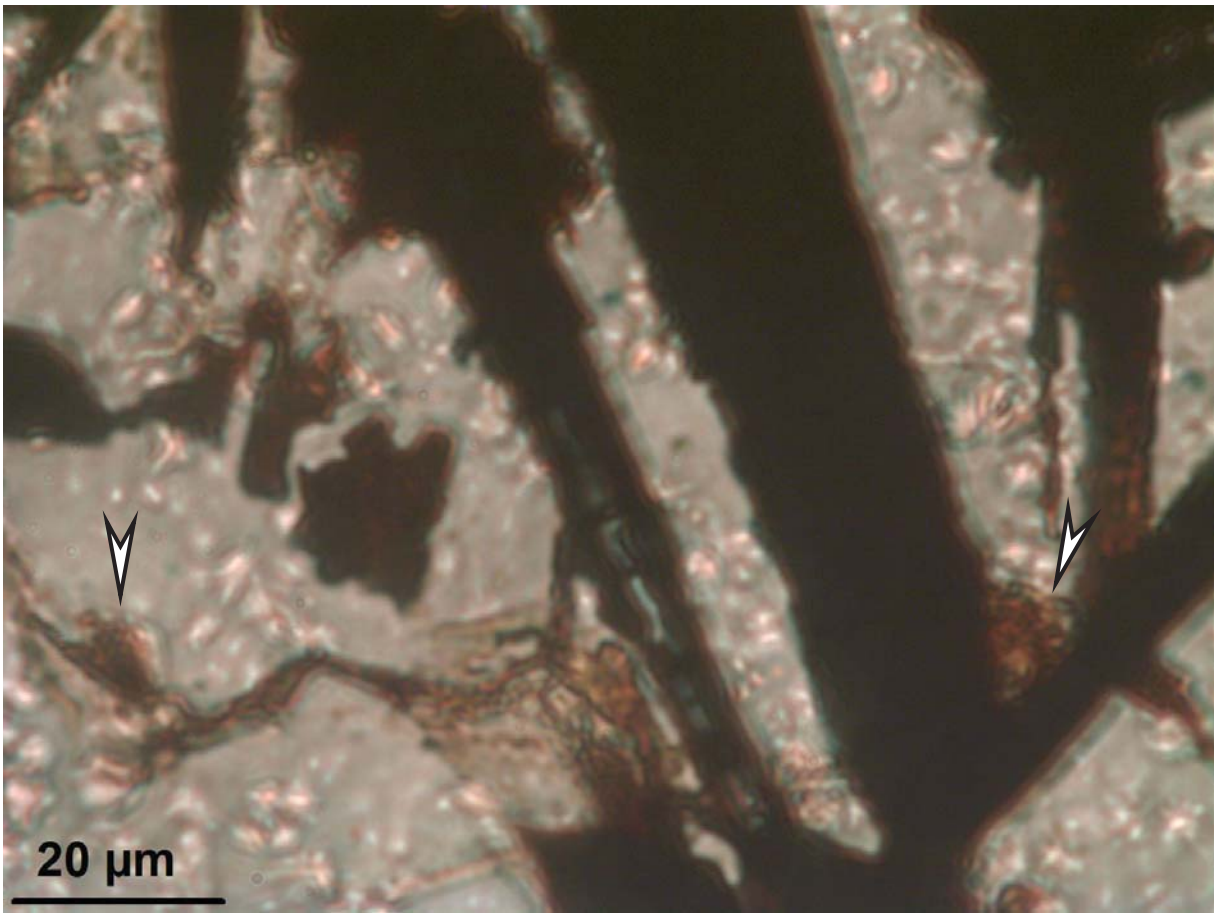
20 µm

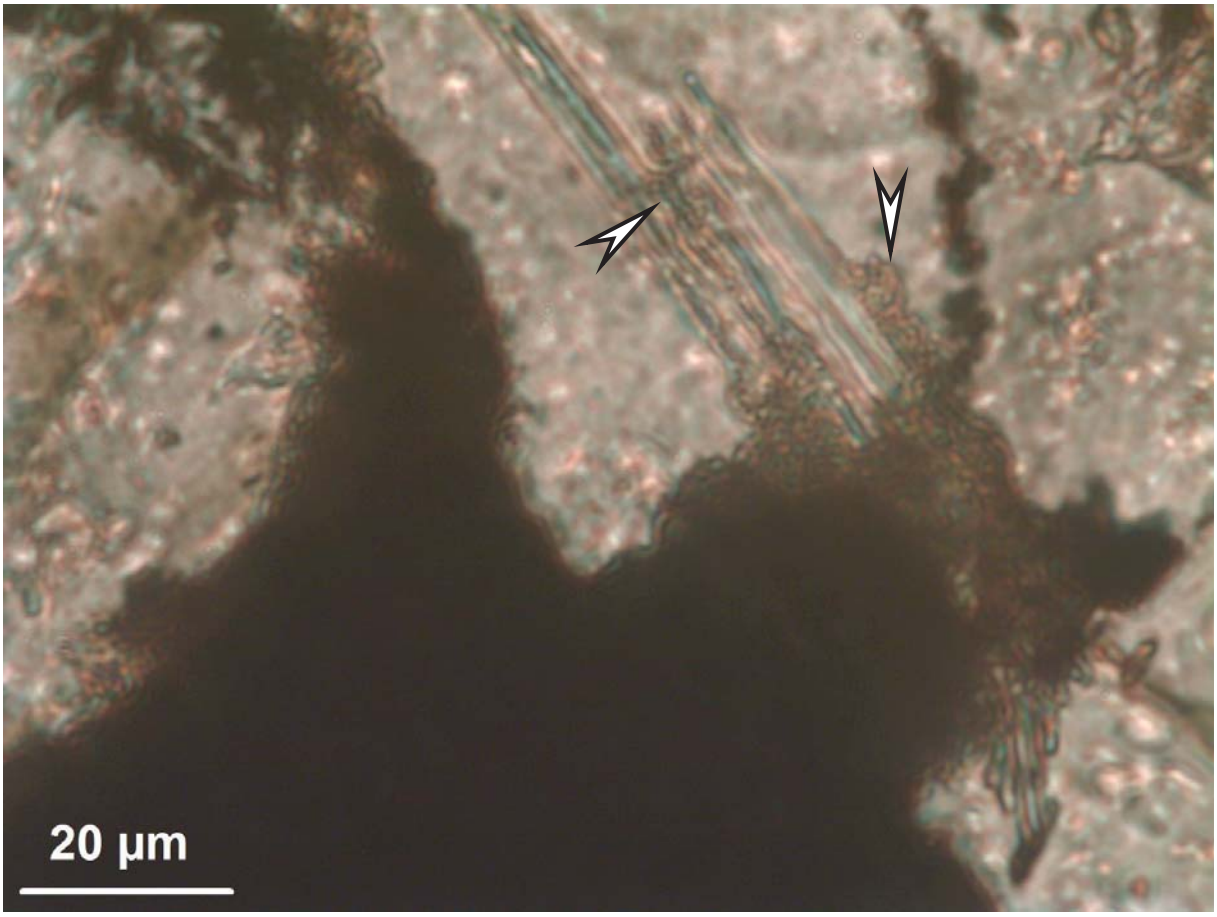
20 µm

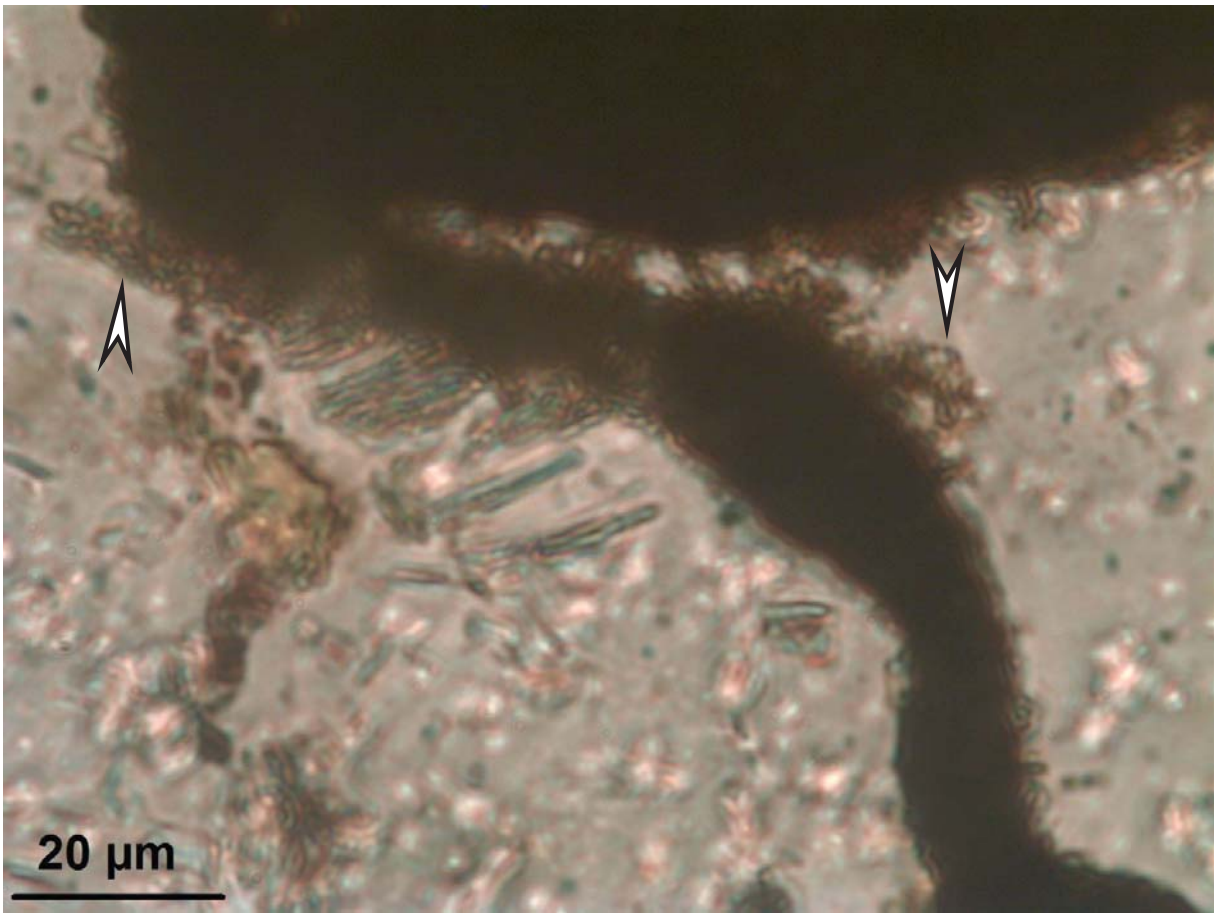
20 µm

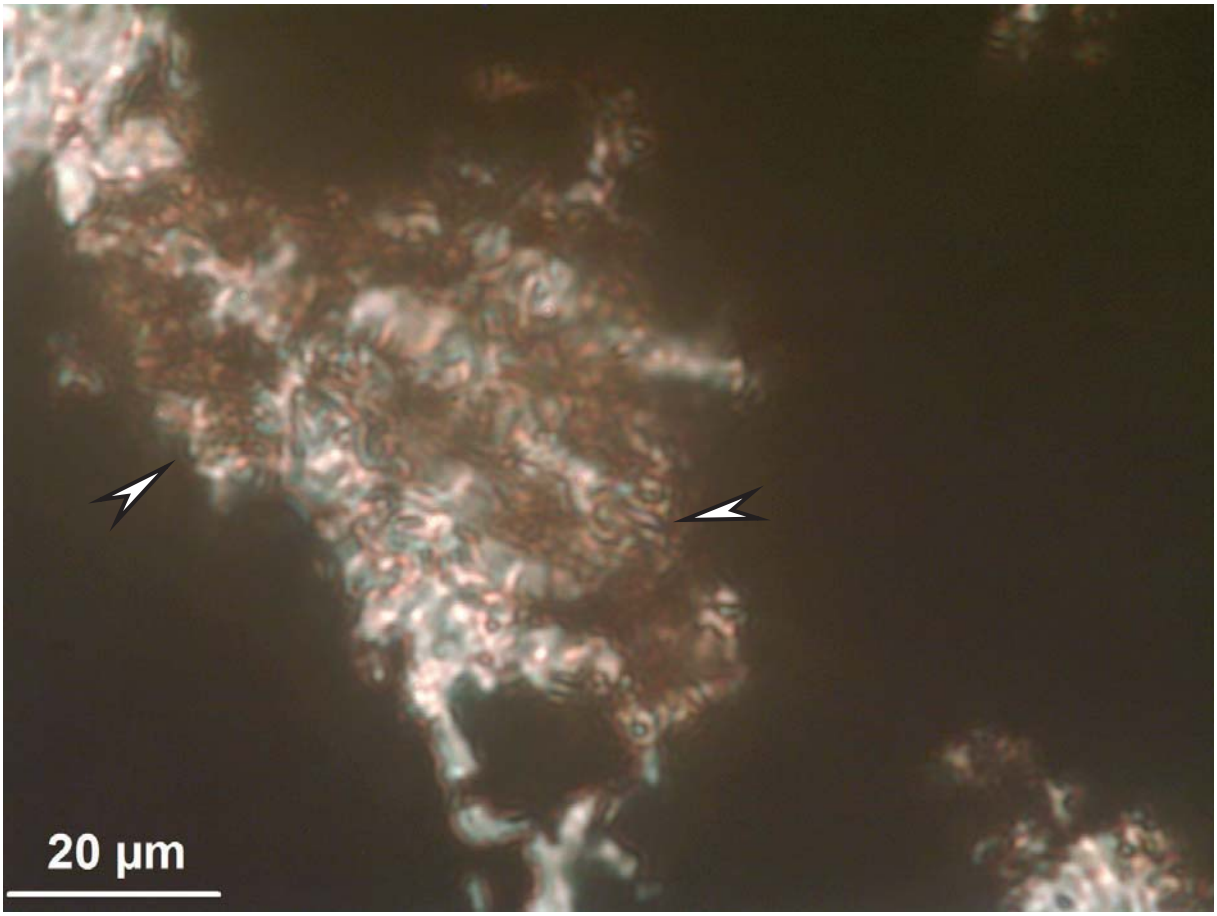
20 µm

Sample-32

The sample is opaque, but at some places we can look into the material, and microbial signatures are well visible. The reflective photos also show dense microbial mediation. Also, cyanobacteria-like forms are visible. The opaque part is a very dense microbially mineralized material.

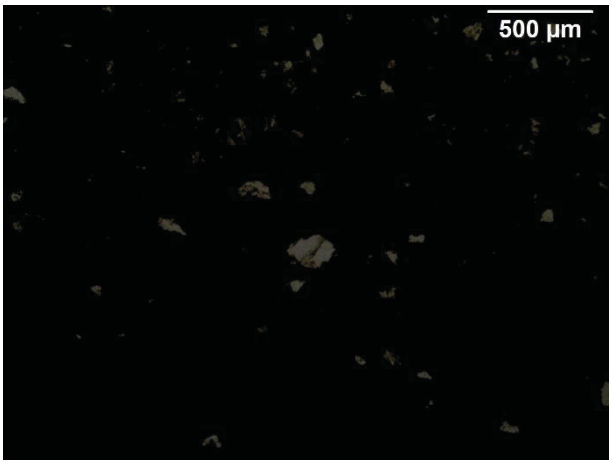

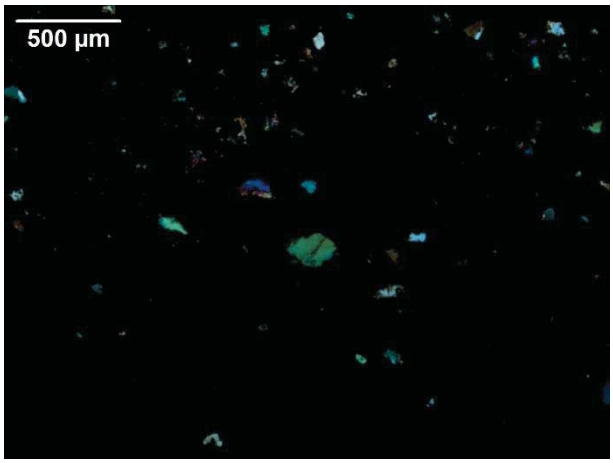

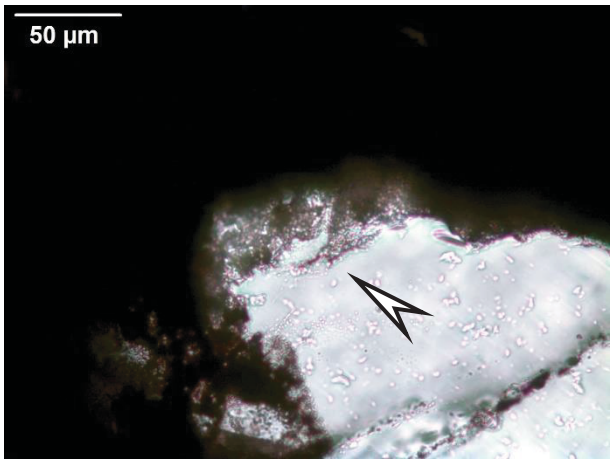

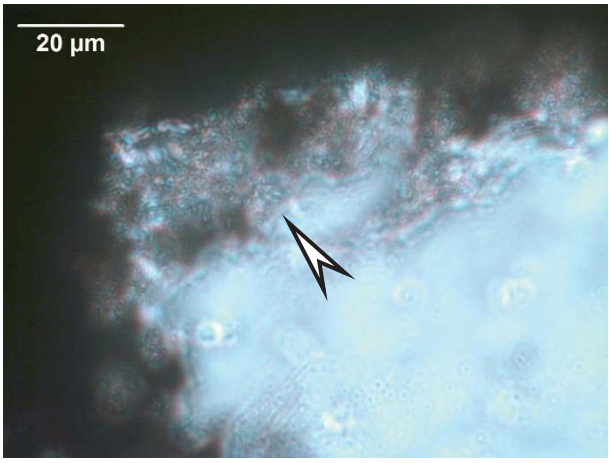

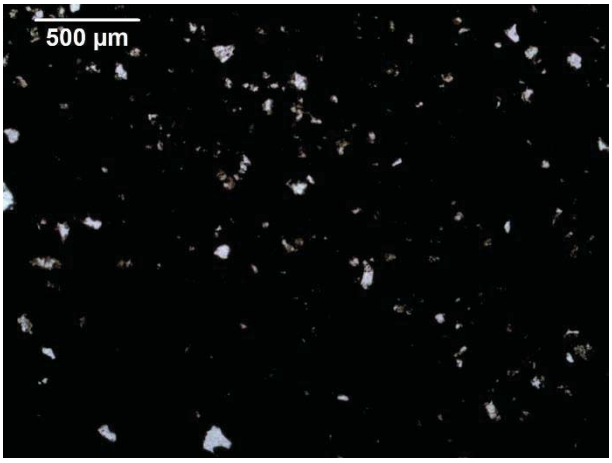

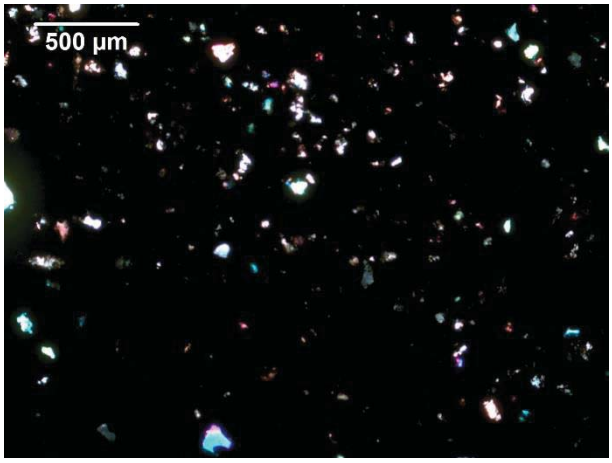

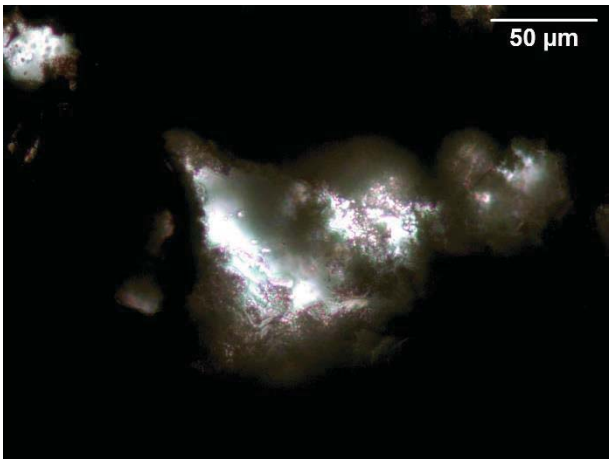
50 µm

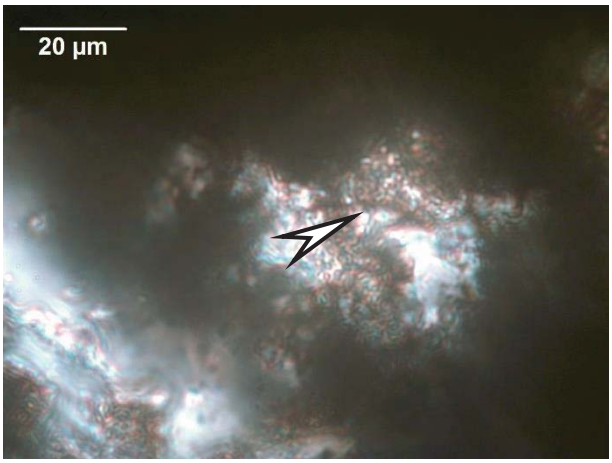
20 µm

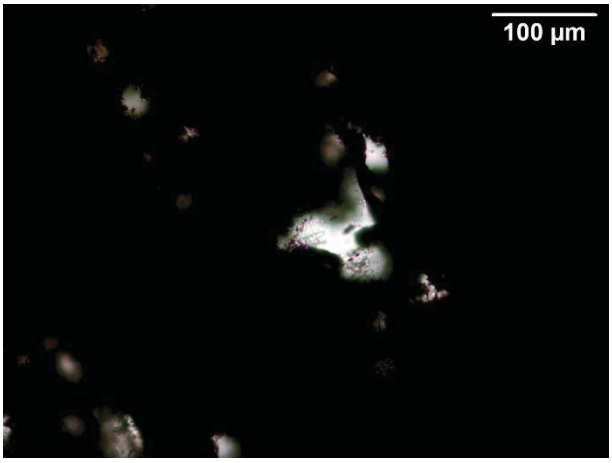
100 µm

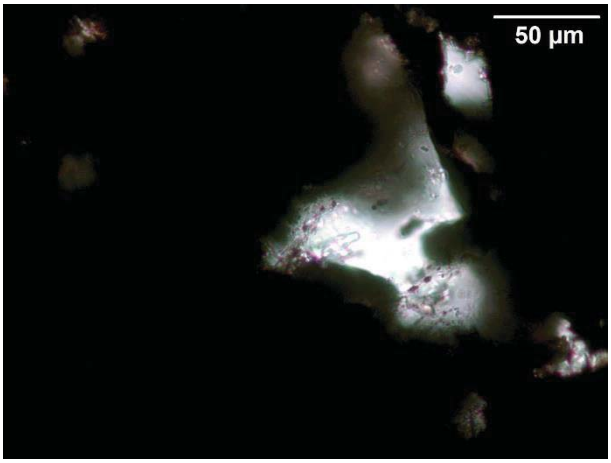
50 µm

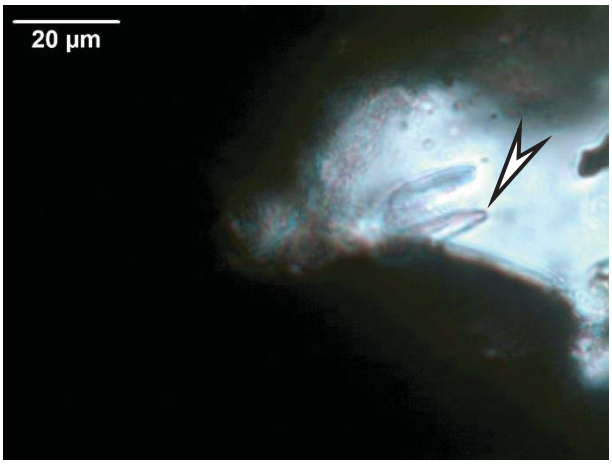
20 µm

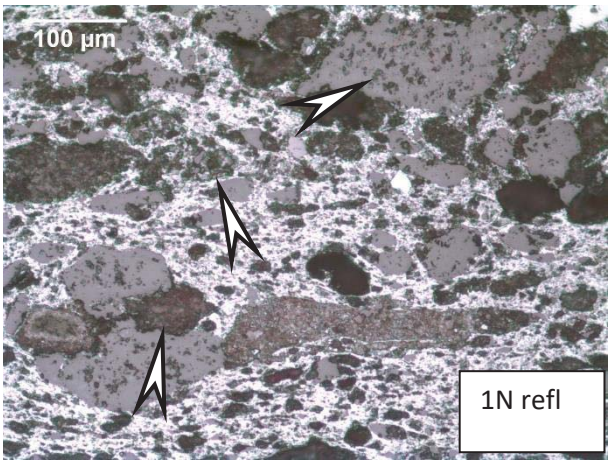
100 µm
1N refl

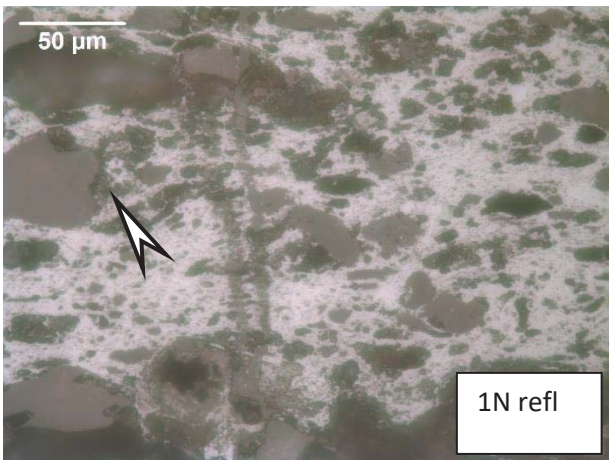
50 µm
1N refl

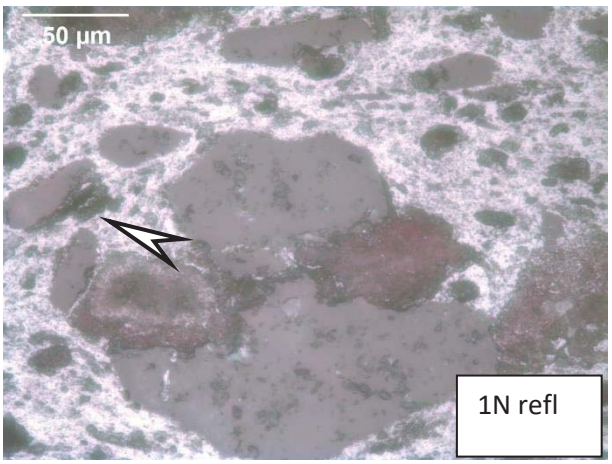
50 µm
1N refl

SI 9-Fig. CL images of samples

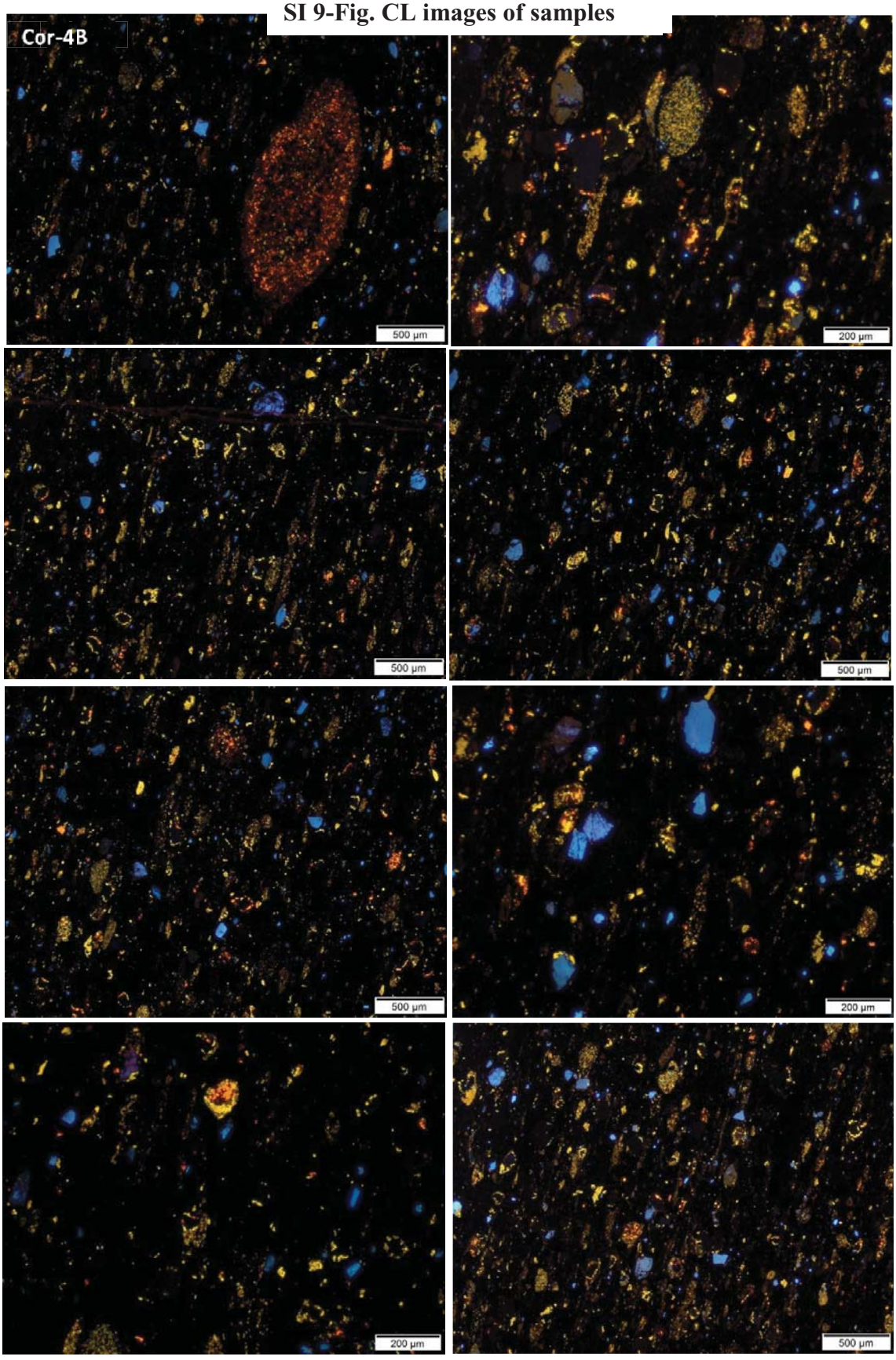

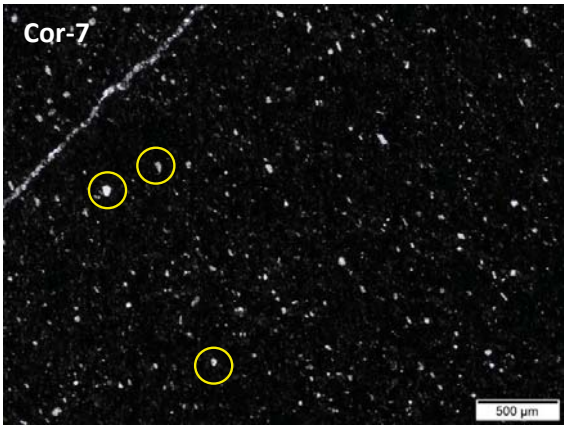

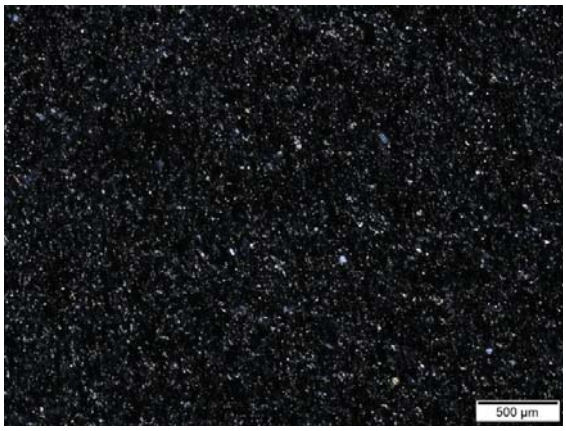

dull: non lumin.

yellow: apatite

blue: „dickite”

orange: carbonate

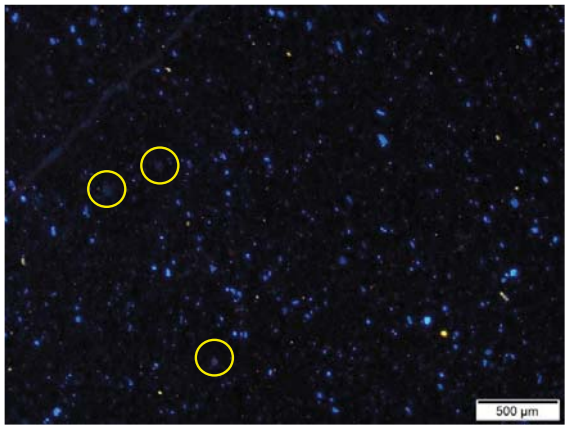

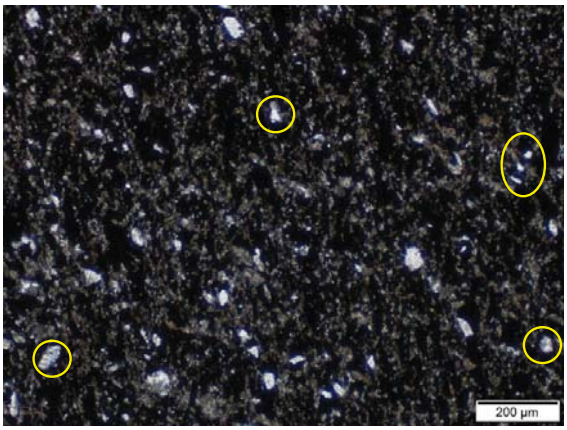

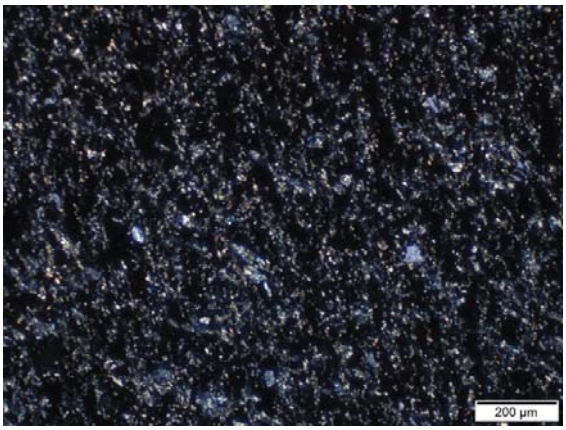

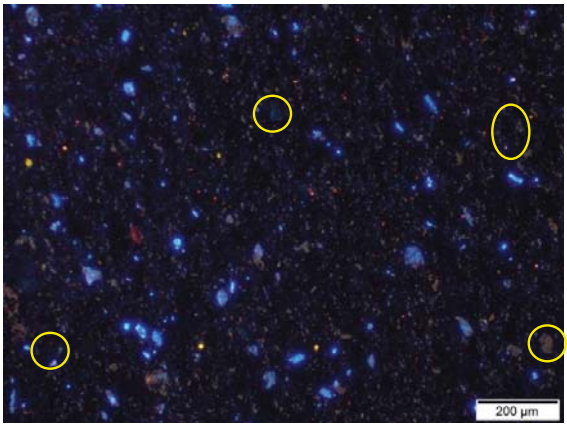

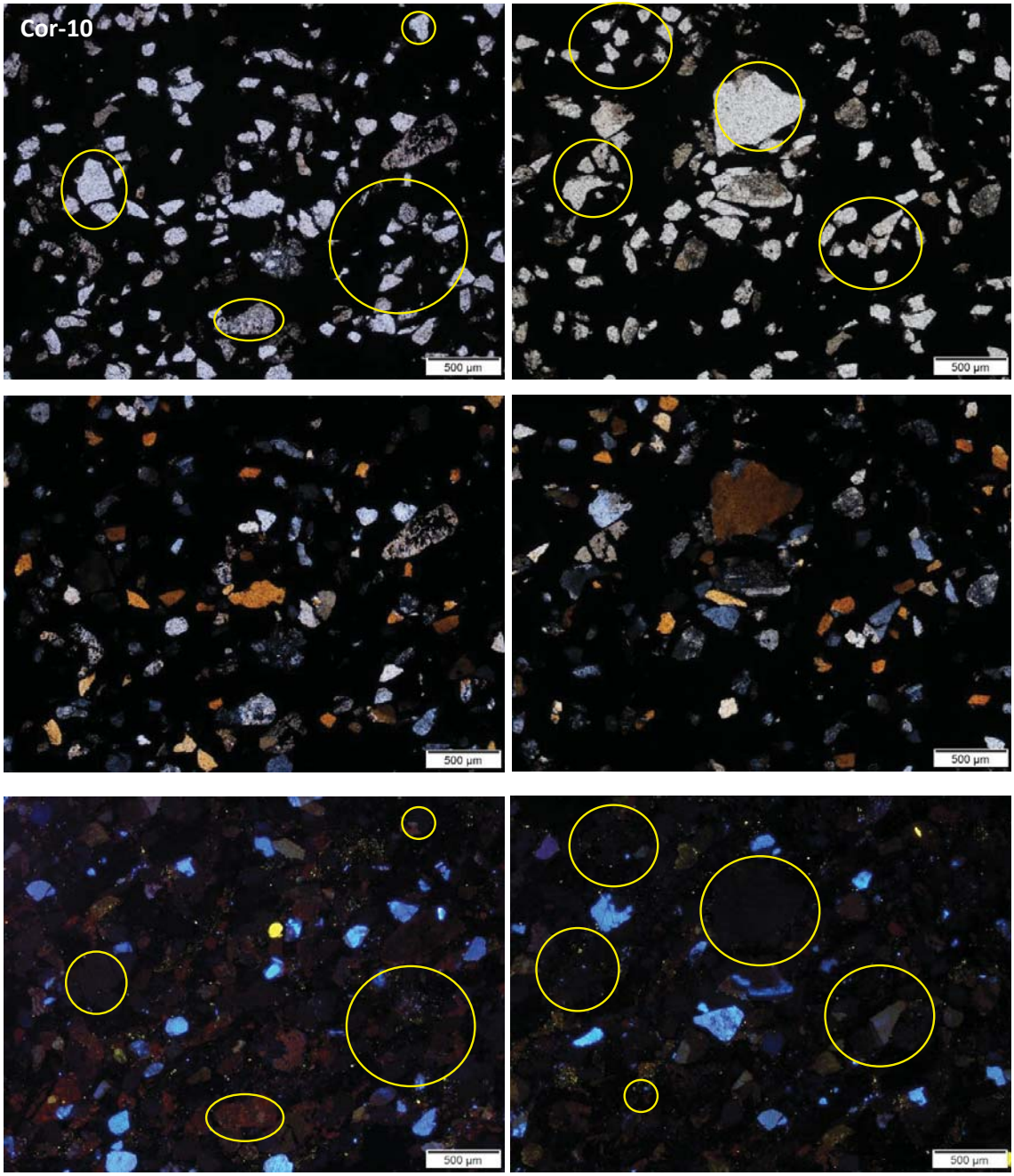
Cor-10
500 µm
500 µm
500 µm
500 µm
500 µm
500 µm

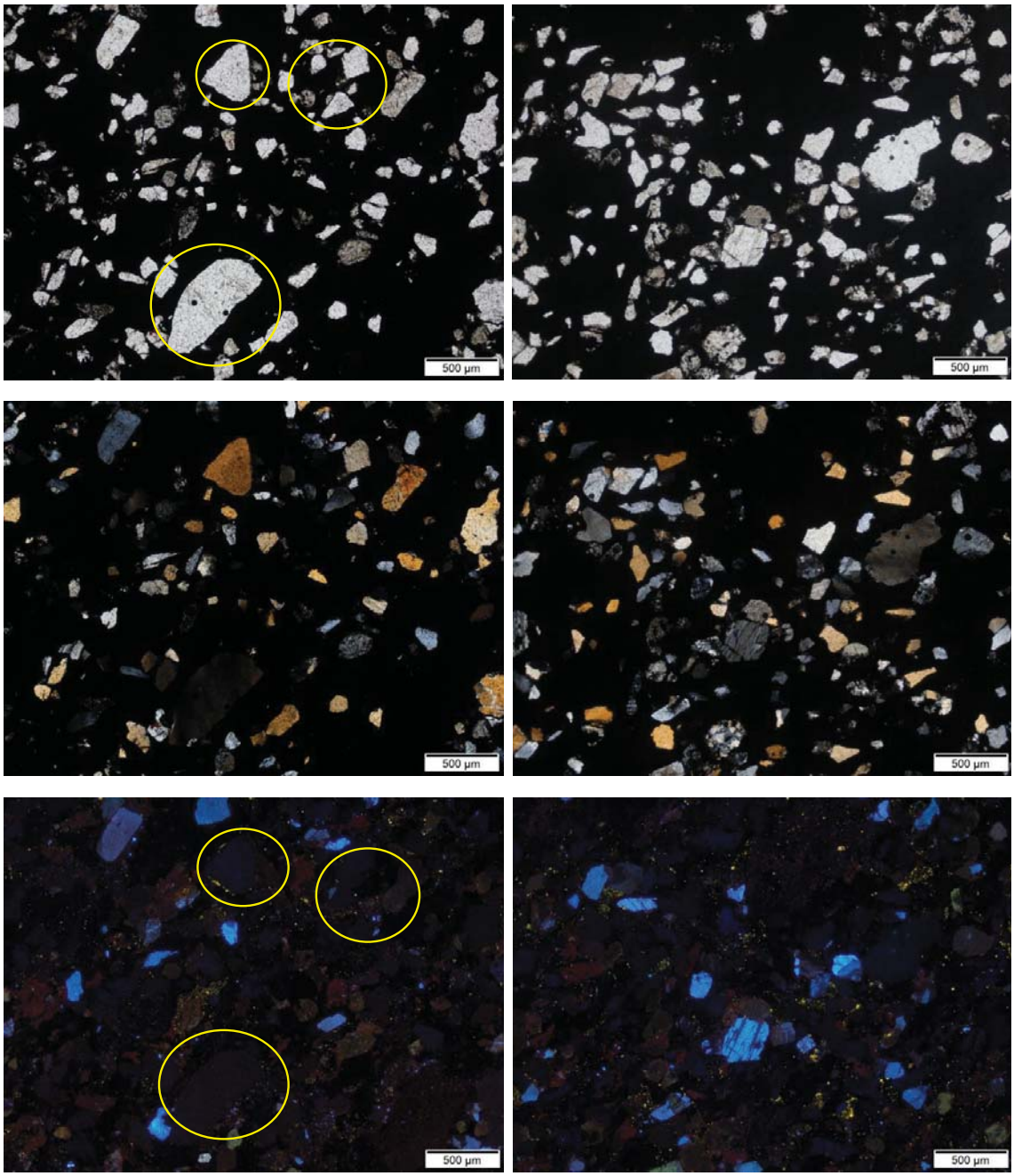
500 µm
500 µm
500 µm
500 µm
500 µm
500 µm

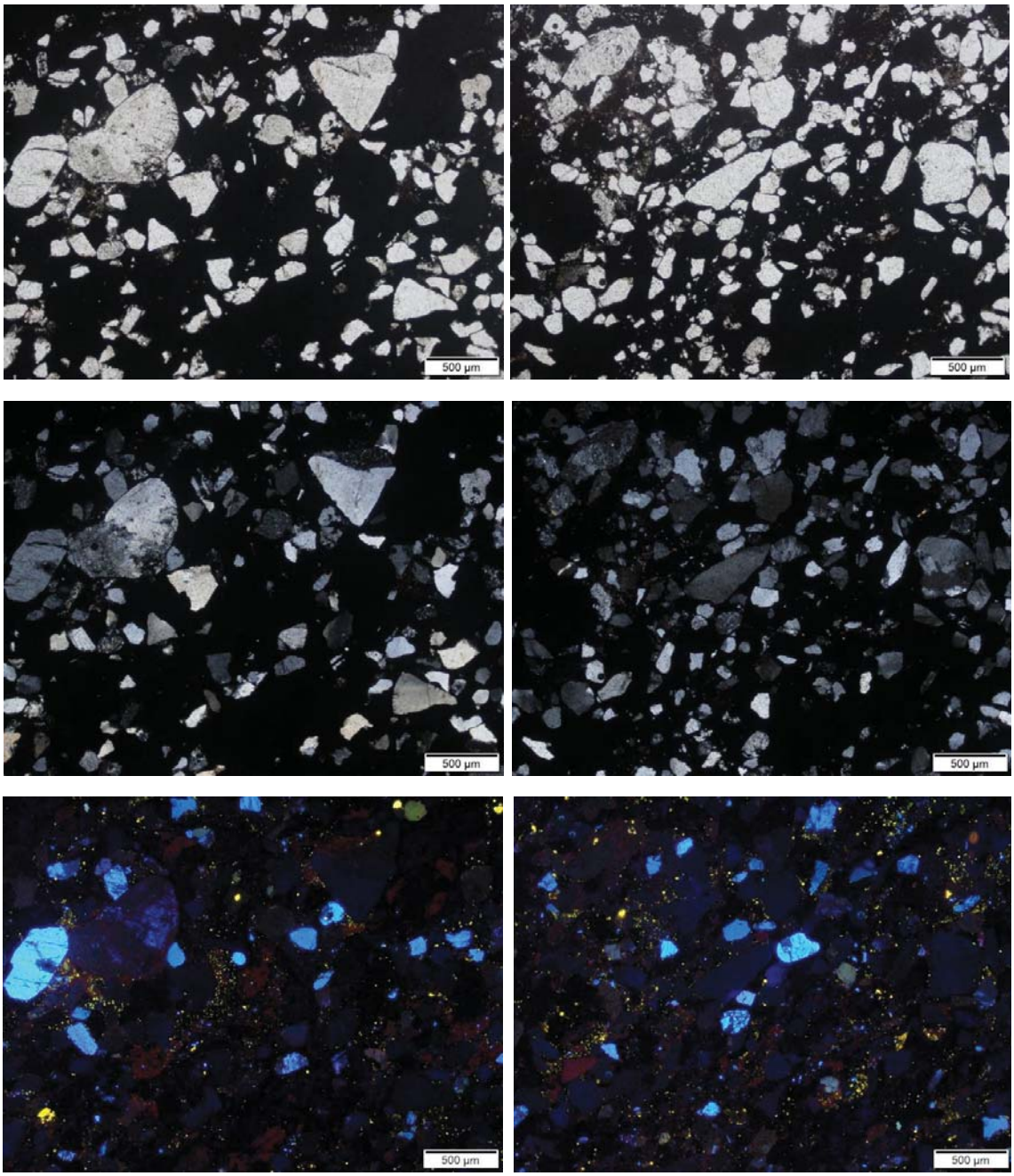

yellow (apatite) grains follow biomat texture

most of the grains looking like debris clasts are non luminescent.

SI 10-Table.

Table A: FTIR measurement of samples (6, 7, 10)

Sample ID			6									7		10		
measuring area			1	2	3	4	5	6	7	8	9	1	2	1	2	3
Total No. of spectra→			4	4	4	4	4	4	5	4	4	5	7	4	4	6
Mineral phase	**Ref**	**Wavelength [cm^{-1}]**														
aegirine	1	630, 856, 928	2		1											
albite	2	798, 950, 1000											3	4	2	2
orthoclase	2	700, 987, 1107sh														
apatite	3	790, 1012, 1093										4	2			
celadonite	4	675, 800, 953s, 973s, 1074, 1113, 3641														
kaolinite	5	641, 684, 750, 789, 912, 935, 1004, 1028, 1114, 3619, 3650, 3691														
dickite	1	742, 794, 906, 1003, 1027, 1115														
chlorite	6	978, 3400	2												2	
ferrihydrite	7	692, 878, 3400					4									
lepidocrocite	7	734, 1019										1	2			
ramsdellite	8	740, 880, 3420									4					
romanèchite	8	600s, 680														
serandite	1	912, 987							4							
todorokite	8	630, 760								4						
cryptomelane	8	600, 760							2	4	4					
pyrolusite	8	600, 720sh			4	4	4									
braunite	1	699, 940		4	2	4		4								4
quartz	2	701, 776, 1059														
hematite	7	600, 1019														
pyrite	1	662, 818														
Organic compounds																

v C=C/C-O	9	1070-1240		4					5			1	1	4	4	6
vs CO	9	1360-1450	4	4									1	4		6
d CH2	9	1454-1482	4	4									1	4	4	6
C-N, CH deformation	9	1526		4	4	4	4	4					1	4		6
C-N N-H amide II	9	1540-1550	4	4	4											
C=C asym. Stretch	9	1598														
amide I C=O, C-N, N_H	9	1632-1652		4	4	4	4	4								
v as COOH	9	1720-29													4	
C-O	9	1799														
CO	9	2343	4	4	4	4	4	4	5	4	4	5	7	4	4	6
CO	9	2365	4	4	4	4	4	4	5	4	4	5	7	4	4	6
C-H sym. Stretch CH2	9	2853												4	4	6
C-H asym. Stretch CH2	9	2926												4	4	6
CH2 /C=C	9	3130										5	7	4	4	6
OH	5	3230-3700	4	4	4	4	4	4		4	4	5	7	4	4	6

References are marked by numbers, details in reference list. The number of spectra for minerals and organic materials in measuring area is added in columns.

SI 10-Table - Table B: FTIR measurement of samples (31, 32, 36-A1, 78-F3)

Sample ID			31						32							36-A1					78-F3							
measuring area			1	2	3	4	5	6	1	2	3	4	5	6	7	1	2	3	4	5	1	2_6	7	8	9	10_11	12_13	14_15
Total No. of spectra→			5	6	4	6	6	5	6	6	4	4	4	4	4	4	4	4	4	4	4	20	4	4	4	8		
Mineral phase	**Reference**	**Wavelength [cm^{-1}]**																										
aegirine	1	630, 856, 928																										
albite	2	798, 950, 1000							6	5	1	1	4	1	2													
orthoclase	2	700, 987, 1107sh												3	2													
apatite	3	790, 1012, 1093	1	3		2		5		1																		
celadonite	4	675, 800, 953s, 973s, 1074, 1113, 3641		1																								
kaolinite	5	641, 684, 750, 789, 912, 935, 1004, 1028, 1114, 3619, 3650, 3691				1	4																					
dickite	1	742, 794, 906, 1003, 1027, 1115				2	2																					
chlorite	6	978, 3400																										
ferrihydrite	7	692, 878, 3400	4			1					3							1	4	4		20	4		4			8
lepidocrocite	7	734, 1019																										

ramsdellite	8	740, 880, 3420																										
romanèchite	8	600s, 680	4													4												
serandite	1	912, 987																										
todorokite	8	630, 760																										
cryptomelane	8	600, 760											4					4	4	4	4	20	4	3	4		8	8
pyrolusite	8	600, 720sh												2														
braunite	1	699, 940																										
quartz	2	701, 776, 1059		2					6	6																		
hematite	7	600, 1019			2	1						3									2					8	8	8
pyrite	1	662, 818			2																							
Organic compounds																												
v C=C/C-O	9	1070-1240	5	6	1	3	4	1		1													4			8	8	8
vs CO	9	1360-1450			1	3	3	1		1													4			8	8	8
d CH2	9	1454-1482	5	5	1	3	3	1		1													4			8	8	8

C-N, CH deformation	9	1526	5	5	1	3	3	1		1													4			8	8	8
C-N N-H amide II	9	1540-1550																					4			8	8	8
C=C asym. Stretch	9	1598						1																				
amide I C=O, C-N, N_H	9	1632-1652																					4			8	8	8
v as COOH	9	1720-29																					4			8	8	8
C-O	9	1799																										
CO	9	2343	5	6	4	6	6	5	6	6	4	4	4	4	4	4	4	4	4	4	4	20	4			8	8	8
CO	9	2365	5	6	4	6	6	5	6	6	4	4	4	4	4	4	4	4	4	4	4	20	4			8	8	8
C-H sym. Stretch CH2	9	2853	5	6				5																				
C-H asym. Stretch CH2	9	2926	5	6				5		1																		
CH2 /C=C	9	3130		6	4	6	6	5		1									4							8		
OH	5	3230-3700		6	4	6	6	5					4						4							8		

References are marked by numbers, details in reference list. The number of spectra for minerals and organic materials in measuring area is added in columns.

SI 10-Table - Table C: Summa of detected mineral phases, organic matter and measuring areas in studied samples

		Sample ID	6	7	10	31	32	36-A1	78-F3
		Summa measuring areas	*9*	*2*	*3*	*6*	*7*	*5*	*15*
		Total No. of spectra→	*37*	*12*	*14*	*32*	*32*	*20*	*60*
Mineral phase	Reference	Wavelength [cm^{-1}]		0	0	0	0	0	0
aegirine	1	630, 856, 928	3	0	0	0	0	0	0
albite	2	798, 950, 1000	0	3	8	0	20	0	0
orthoclase	2	700, 987, 1107sh	0	0	0	0	5	0	0
apatite	3	790, 1012, 1093	0	6	0	11	1	0	0
celadonite	4	675, 800, 953s, 973s, 1074, 1113, 3641	0	0	0	1	0	0	0
kaolinite	5	641, 684, 750, 789, 912, 935, 1004, 1028, 1114, 3619, 3650, 3691	0	0	0	5	0	0	0
dickite	1	742, 794, 906, 1003, 1027, 1115	0	0	0	4	0	0	0
chlorite	6	978, 3400	2	0	2	0	0	0	0
ferrihydrite	7	692, 878, 3400	4	0	0	5	3	9	36
lepidocrocite	7	734, 1019	0	3	0	0	0	0	0
ramsdellite	8	740, 880, 3420	4	0	0	0	0	0	0
romanèchite	8	600s, 680	0	0	0	4	0	4	0
serandite	1	912, 987	4	0	0	0	0	0	0
todorokite	8	630, 760	4	0	0	0	0	0	0
cryptomelane	8	600, 760	10	0	0	0	4	12	51
pyrolusite	8	600, 720sh	12	0	0	0	2	0	0
braunite	1	699, 940	14	0	4	0	0	0	0
quartz	2	701, 776, 1059	0	0	0	2	12	0	0

hematite	7	600, 1019	0	0	0	3	3	0	26
pyrite	1	662, 818	0	0	0	2	0	0	0
Organic compounds			0	0	0	0	0	0	0
v C=C/C-O	9	1070-1240	9	2	14	20	1	0	28
vs CO	9	1360-1450	8	1	10	8	1	0	28
d CH2	9	1454-1482	8	1	14	18	1	0	28
C-N, CH deformation	9	1526	20	1	10	18	1	0	28
C-N N-H amide II	9	1540-1550	12	0	0	0	0	0	28
C=C asym. Stretch	9	1598	0	0	0	1	0	0	0
amide I C=O, C-N, N_H	9	1632-1652	20	0	0	0	0	0	28
v as COOH	9	1720-29	0	0	4	0	0	0	28
C-O	9	1799	0	0	0	0	0	0	0
CO	9	2343	37	12	14	32	32	20	52
CO	9	2365	37	12	14	32	32	20	52
C-H sym. Stretch CH2	9	2853	0	0	14	16	0	0	0
C-H asym. Stretch CH2	9	2926	0	0	14	16	1	0	0
CH2 /C=C	9	3130	0	12	14	27	1	4	8
OH	5	3230-3700	32	12	14	27	4	4	8

References are marked by numbers, details in reference list. The number of spectra for minerals and organic materials in measuring area is added in columns.

References:

[1] RRUFF Database

[2] Müller, C. M., Pejcic, B., Esteban, L., Delle Piane, C., Raven, M. & Mizaikoff, B. (2014). Infrared attenuated total reflectance spectroscopy: an innovative strategy for analyzing mineral components in energy relevant systems. *Scientific reports*, *4*, 6764.

[3] Beasley, M. M., Bartelink, E. J., Taylor, L. & Miller, R. M. (2014). Comparison of transmission FTIR, ATR, and DRIFT spectra: implications for assessment of bone bioapatite diagenesis. *Journal of Archaeological Science*, *46*, 16-22.

[4] Moretto, L. M., Orsega, E. F. & Mazzocchin, G. A. (2011). Spectroscopic methods for the analysis of celadonite and glauconite in Roman green wall paintings. *Journal of Cultural Heritage*, *12*(4), 384-391.

[5] Madejova, J. & Komadel, P. (2001). Baseline studies of the clay minerals society source clays: infrared methods. *Clays and clay minerals*, *49*(5), 410-432.

[6] Udvardi, B., Kovács, I.J., Kónya, P., Földvári, M., Füri, J., Budai, F., Falus, G., Fancsik, T., Szabó, C., Szalai, Z. and Mihály, J. 2014. Application of attenuated total reflectance Fourier transform infrared spectroscopy in the mineralogical study of a landslide area, Hungary. *Sedimentary Geology*, *313*, pp.1-14.

[7] Glotch, T. D. & Rossman, G. R. (2009). Mid-infrared reflectance spectra and optical constants of six iron oxide/oxyhydroxide phases. *Icarus*, *204*(2), 663-671.

[8] Potter, R. M. & Rossman, G. R. (1979). The tetravalent manganese oxides: identification, hydration, and structural relationships by infrared spectroscopy. *American Mineralogist*, *64*, I199-1218.

[9] Parikh, S. J. & Chorover, J. (2006). ATR-FTIR spectroscopy reveals bond formation during bacterial adhesion to iron oxide. *Langmuir*, *22*(20), 8492-8500.

SI 11-Fig. Interpretation of mineral composition and distribution of spherical (bubble-like) structure of sample 36-A based on FTIR

Outer area

This area is inhomogeneous, consist of dark spots and bright inhomogenous area.

Matrix
This inhomogenic matrix area was investigated in „outer area 1" This part is mixed by goethite, feldspar, disordered rhodochrosite, traces of cryptomelane. The organic material contains immaturated hydrocarbons - CH-CCN bonds of amid I-amid II (1520-1660 cm^{-1}).

Dark spots
This parts contain ferrihydrite (with traces of goethite), disordered rhodochrosite, traces of cryptomelane, organic material and maturated, long-chain hydrocarbon (bands 2900-3100 cm^{-1}), and ketons (C=O)

Rim area

This is inhomogenous, composed of a fine-grained area, and coarser crystallized area.
The coarser area is mixture of cryptomelane and broad bands of disordered quartz, rhodochrosite and dolomite, and traces of braunite. The dolomite has CO3 vibration at 1425 cm^{-1}, the rhodocrosite has near 1390 cm^{-1}. This area contains variable organic material, which contain long chain hydrocarbons (CH2 symmetric and asymmetric stretching modes 2853-3130 cm^{-1}), and C-O vibration of ketons (2343-2365 cm^{-1})
The fine-grained porous part is composed of ferrihydrite, traces of goethite. This area contain bands of C-O vibration of ketons at 2343 and 2365 cm^{-1}.

Inner area

It was measured by 3 FTIR area (inner area 1-3).

Matrix
The inhomogeneous matrix, which composed of porous, laminated parts, which was measured by lighter part, darker part, and average inhomogeneous part:

The lighter part (area2) is mixture of cryptomelane, quartz, and dolomite, and organic material with CH2 bonds (1452-1482 cm^{-1}) and ketons (C=O).
Inhomogenous matrix (area1) dark parts contains dolomite, ferrihydrite, cryptomelane.
Porous inhomogenous matrix (area2) is also mixed material, which contain cyptomelane, ferrihydrite, dolomite (traces) and organic material with CH2 bonds (1452-1482 cm^{-1}) and ketons (C=O).

Dark spot

The inner area 3 focused on dark spots, which are composed of mixture of ramsdellite, quartz and dolomite, and contains organic material of long-chain hydrocarbons (2900-3100 cm^{-1}), ketons, and CN-CH bonds of PAHs.

36-A FTIR vibrations

		Part of spherical structure	Outer area		Rim		Inner area				
		Component	Matrix	Dark spot			Matrix				Dark spot
		Measuring area	1	2	1		1		2		3
		Texture	inhom. mx	dark	fine-grained	coarse	inhom. 1	darkparts	inhom. 2	lightpart	dark
		Total No. of spectra→	5	5	2	2	2	3	4	1	5
Mineral phase	**Ref**	**Wavelength [cm^{-1}]**									
dol	1	720, 888, 1425,				(1)	2	3	(1)	1	5
rhod	1	729, 860, 1394	5	5		(2)					
goe		798, 910, 3400	5	(5)	(2 trace)						
ferri	7	692, 878, 3400		5	2		2	3	4		
ramsdellite	8	740, 880, 3420									5
feldspar (albite)	2	798, 950, 1000	5								
cryptom	8	600, 760	(5)	(5)		2	2	3	4	1	
braunite	1	699, 940				(2)					
quartz	2	701, 776, 1059				2				1	5
Organic compounds											
vs CO	9	1360-1450	5								
d CH2	9	1454-1482	5						4	1	
C-N, CH deformation	9	1526	5	5							5
C-N N-H amide II	9	1540-1550	5	5							5
amide I C=O, C-N, N_H	9	1632-1652	5	5							5
CO	9	2343			2	2			4	1	5
CO	9	2365			2	2			4	1	5
C-H sym. Stretch CH2	9	2853	5	5		2					5
C-H asym. Stretch CH2	9	2926	5	5		2					5
CH2 /C=C	9	3130	5	5		2					
OH	5	3230-3700	5	5							

Summary table of mineral phases (References see in SI 10-Table).

Outer area		Rim		Inner area				
inhom. matrix	dark spot	coarse	fine-grained	inhom. matrix1	inhom. matrix2	dark part	light part	dark spot
goe feldsp rhod cryptom	ferri goe rhod cryptom	cryptom quartz rhod dol brau	ferri goe	ferri cryptom dol	ferri cryptom dol	ferri cryptom dol	cryptom quartz dol	ramsdellite quartz dol

Abbrev: goe-goethite, ferri-ferrihydrite, feldsp-feldspar, rhod-rhodochrosite, cryptom-cryptomelane, dol-dolomite, brau-braunite

36-A – Microtexture of spherical (bubble-like) structure,OM, reflective mode, arrows show mineralized microbial signatures and diffusion channels.

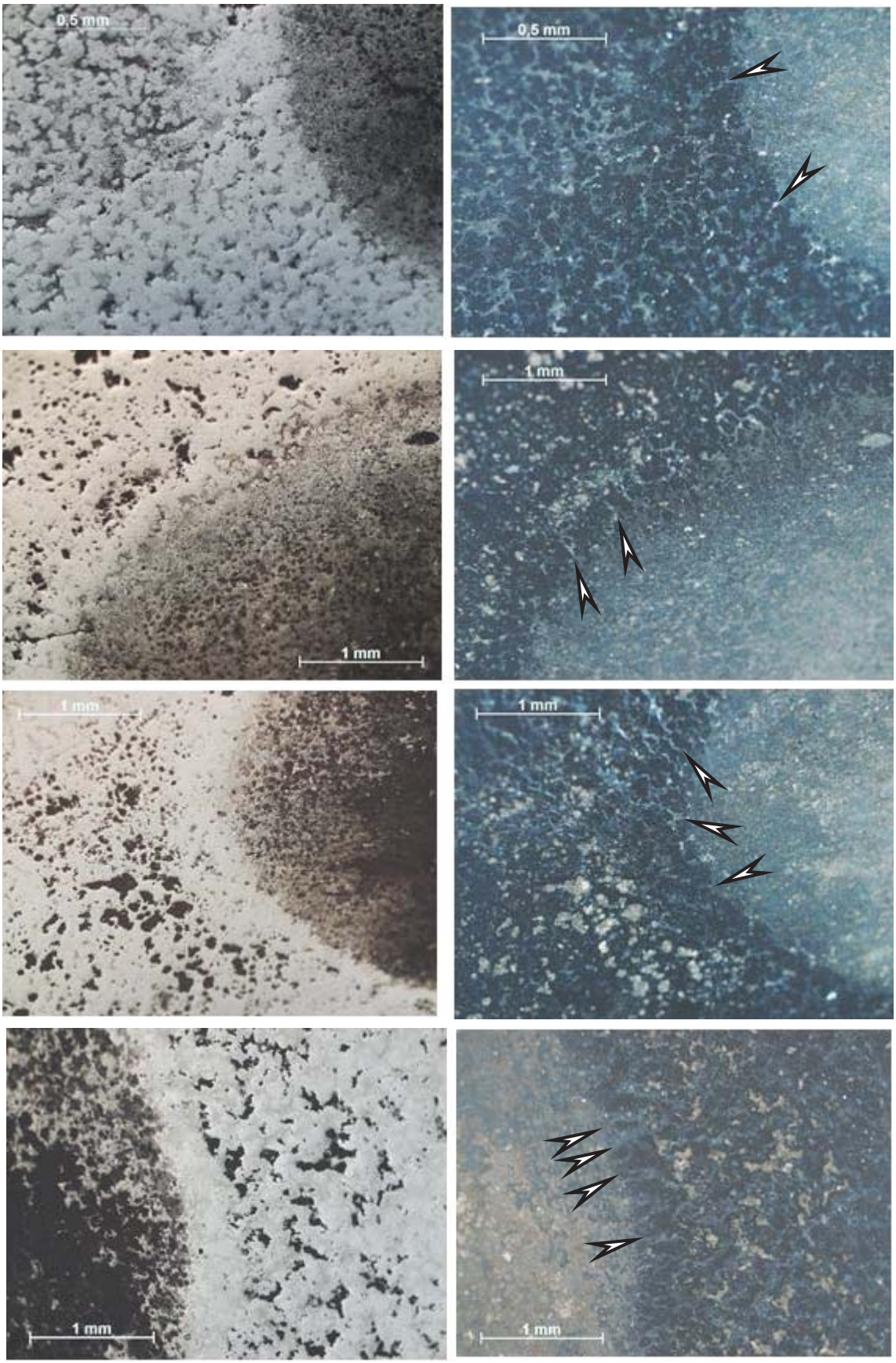

SI 12-Fig. Mineral distribution in profiles by Raman spectroscopy

Abbrev: Plg+Kfs-plagioclase+F-feldspar; CM-carbonaceous material (organic matter)

4B (Mn-1)

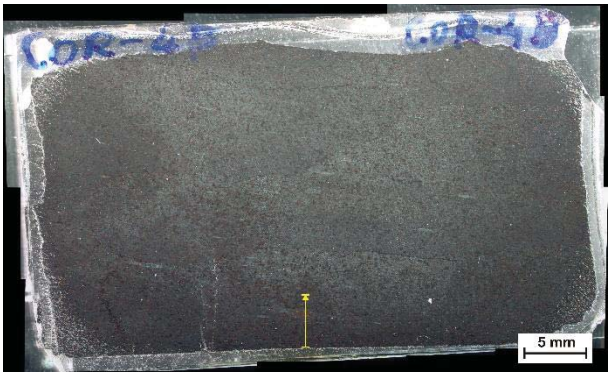

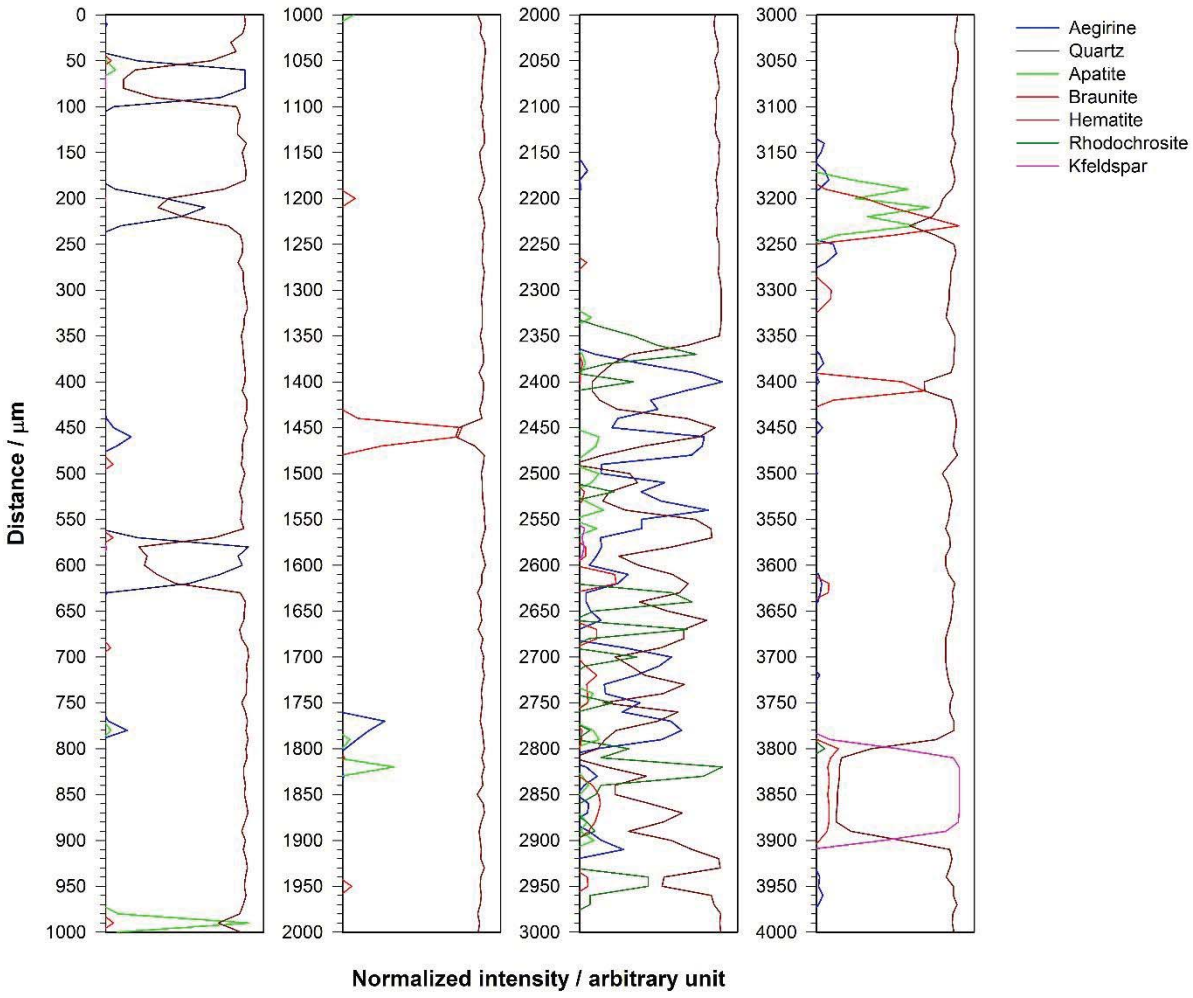

10 (Mn-1)

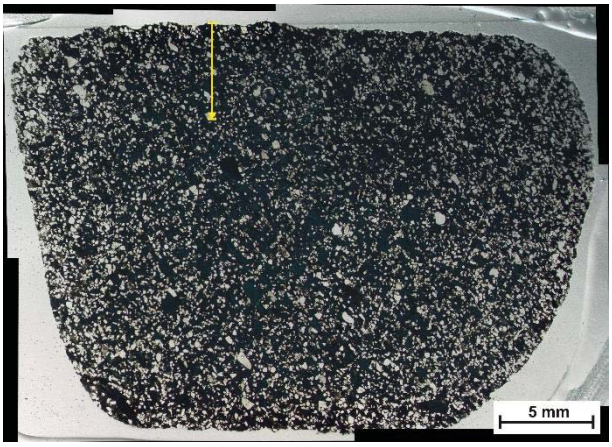
5 mm

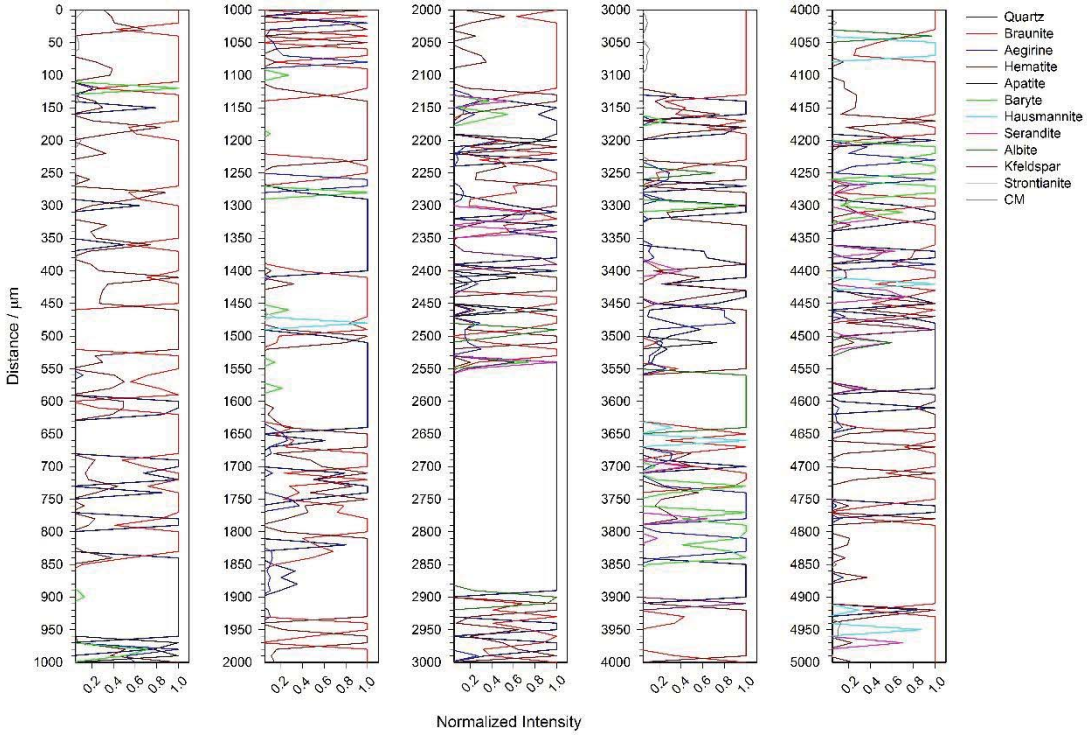
Distance / µm
Normalized Intensity
Quartz
Braunite
Aegirine
Hematite
Apatite
Baryte
Hausmannite
Serandite
Albite
Kfeldspar
Strontianite
CM

31 (Mn-1)

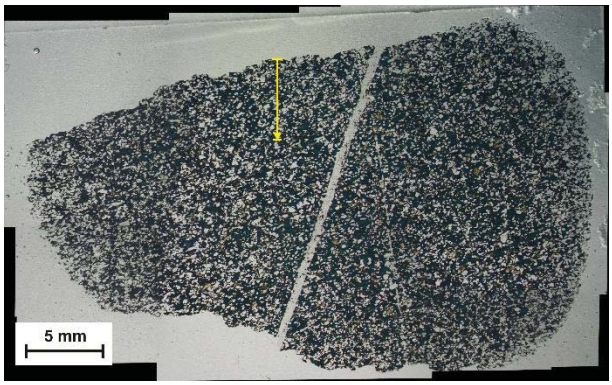
5 mm

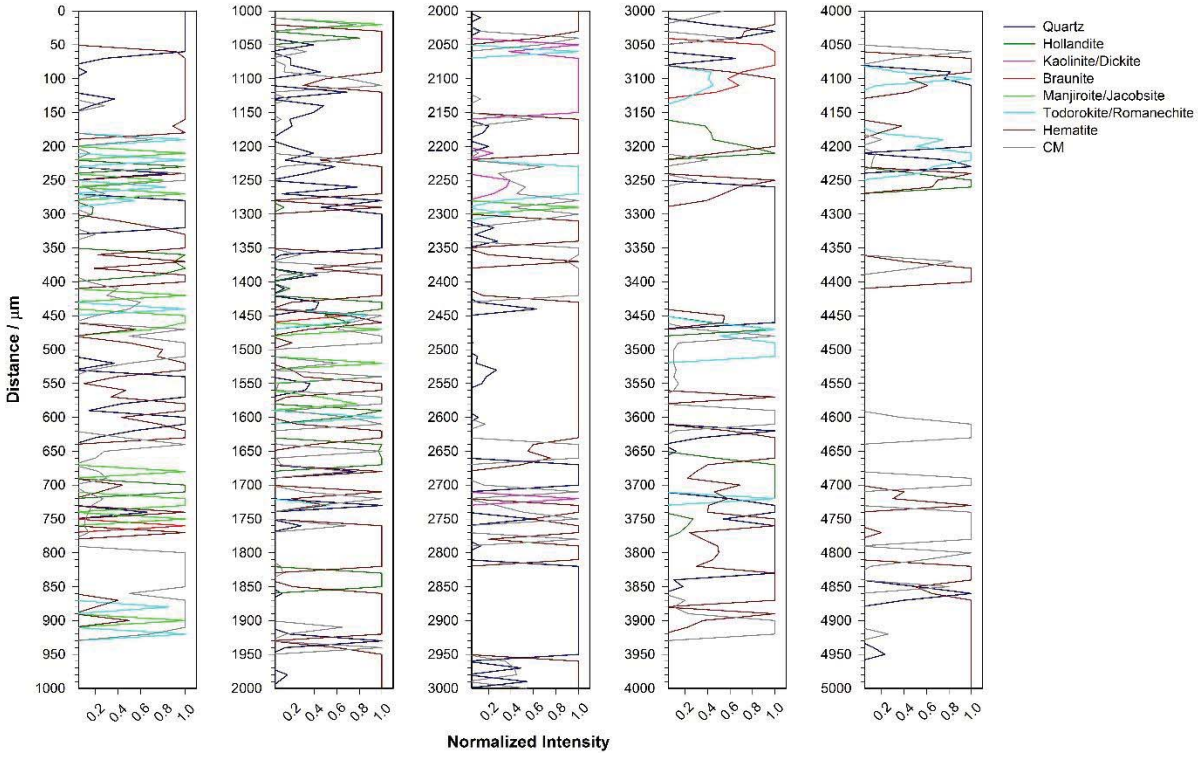
Distance / µm
Normalized Intensity
Quartz
Hollandite
Kaolinite/Dickite
Braunite
Manjiroite/Jacobsite
Todorokite/Romanechite
Hematite
CM

75-2 (Mn-2)

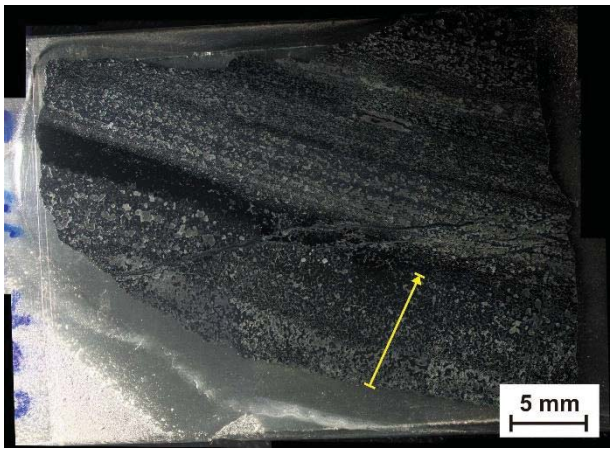
5 mm

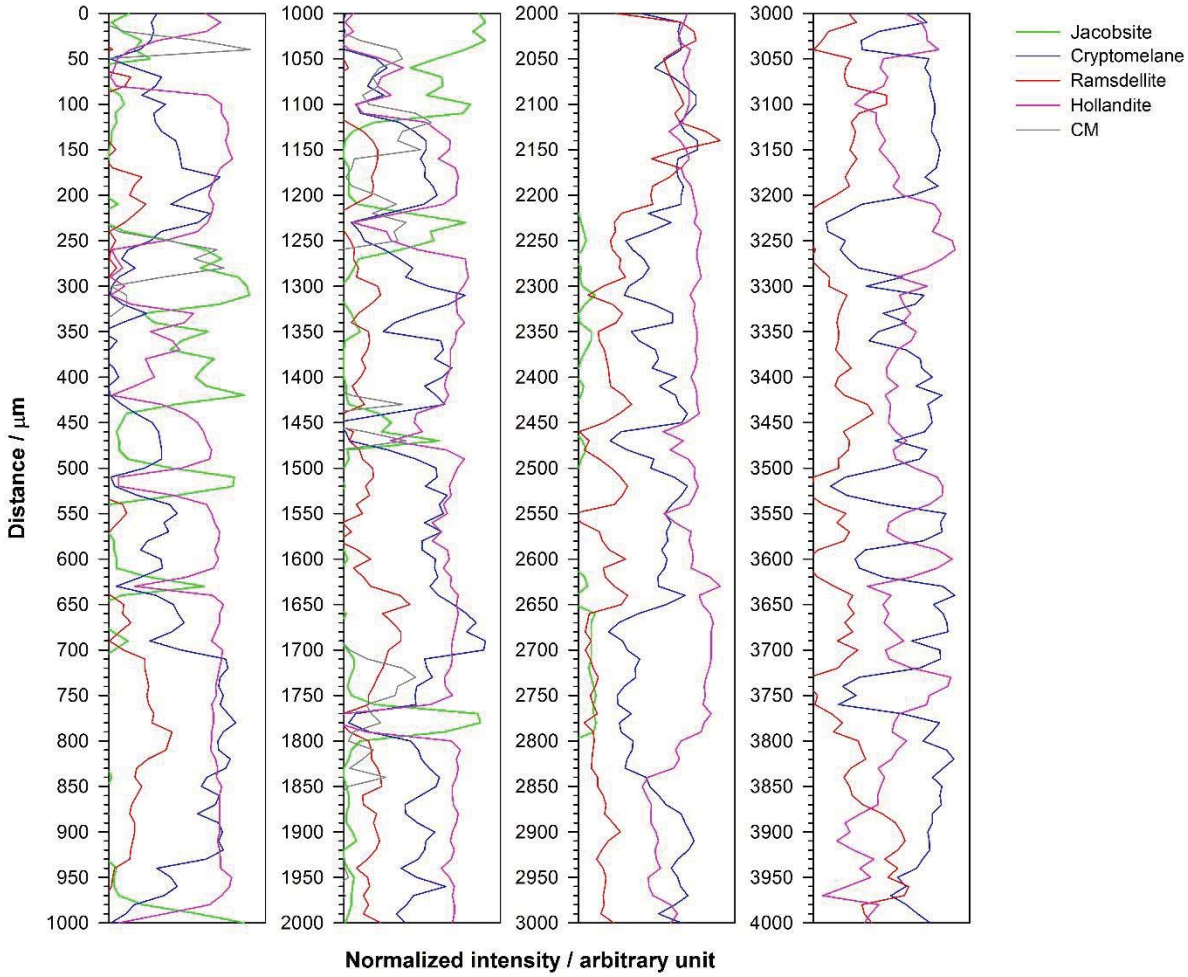
Distance / μm
Normalized intensity / arbitrary unit
Jacobsite
Cryptomelane
Ramsdellite
Hollandite
CM

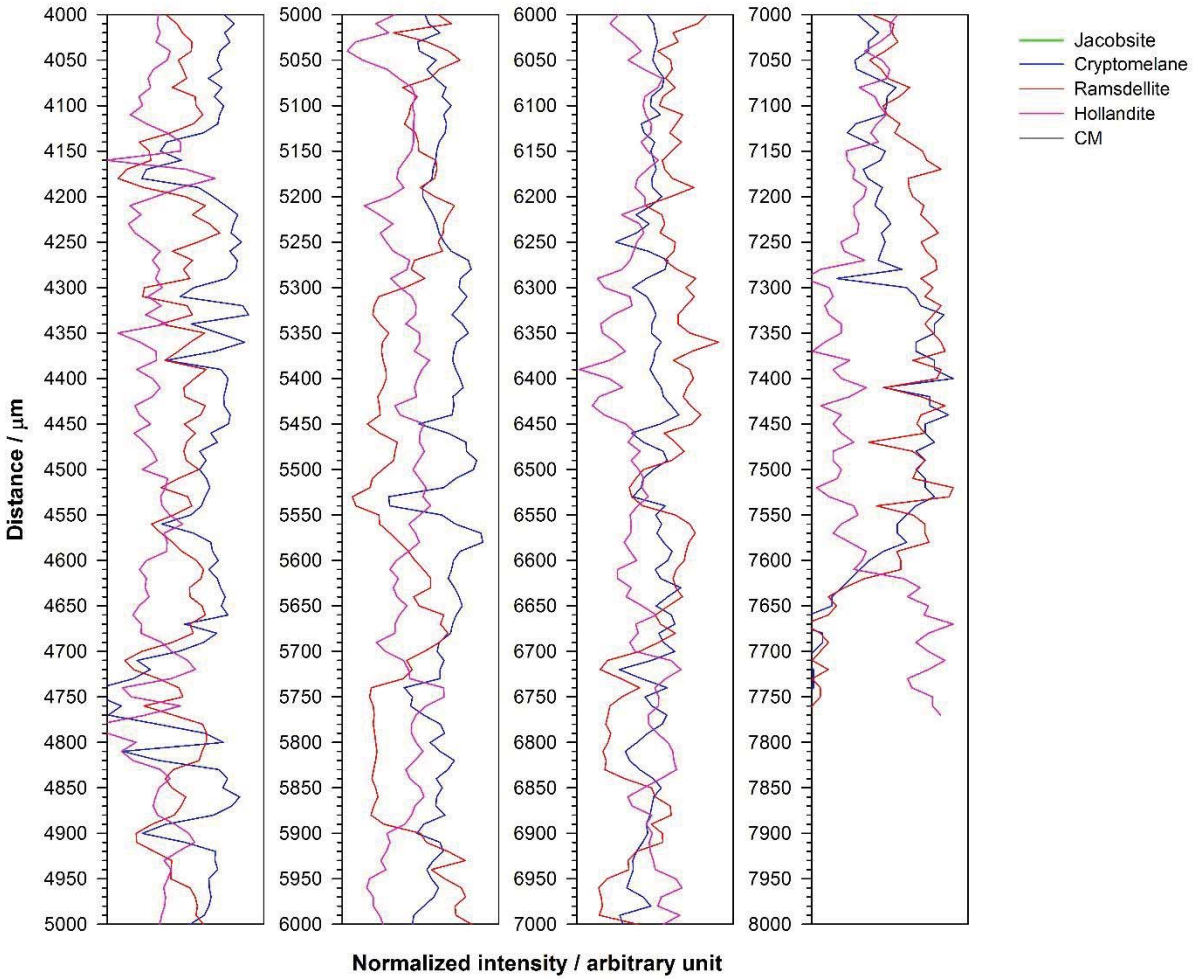
Distance / µm
Normalized intensity / arbitrary unit
Jacobsite
Cryptomelane
Ramsdellite
Hollandite
CM

75-B5 (Mn-2)

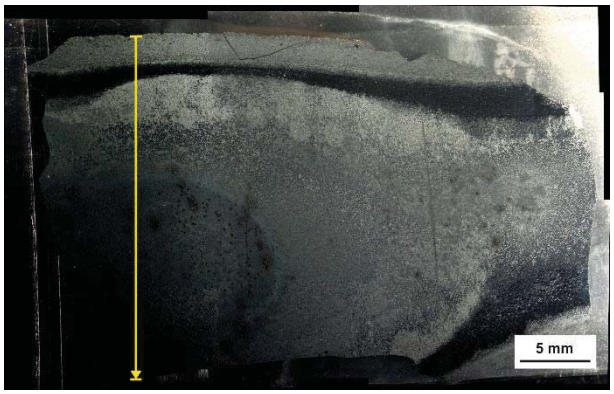
5 mm

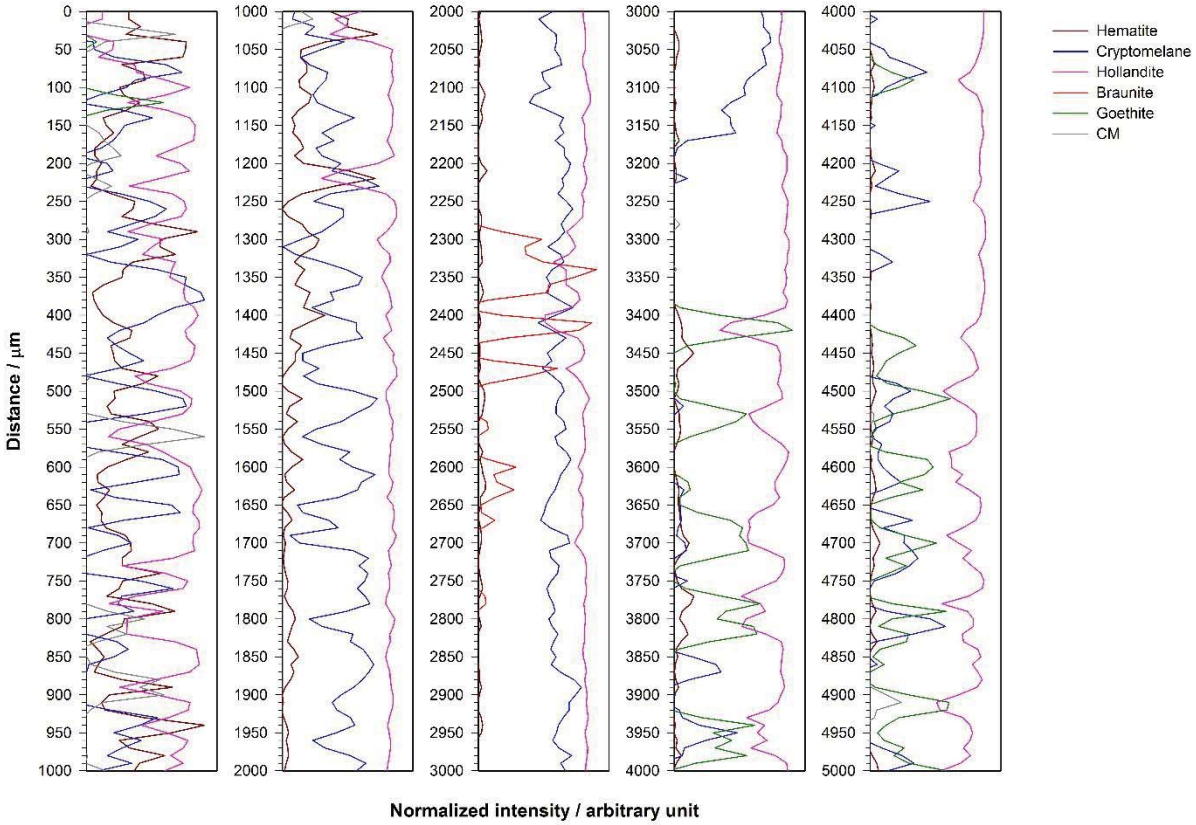
Distance / µm
Normalized intensity / arbitrary unit
Hematite
Cryptomelane
Hollandite
Braunite
Goethite
CM

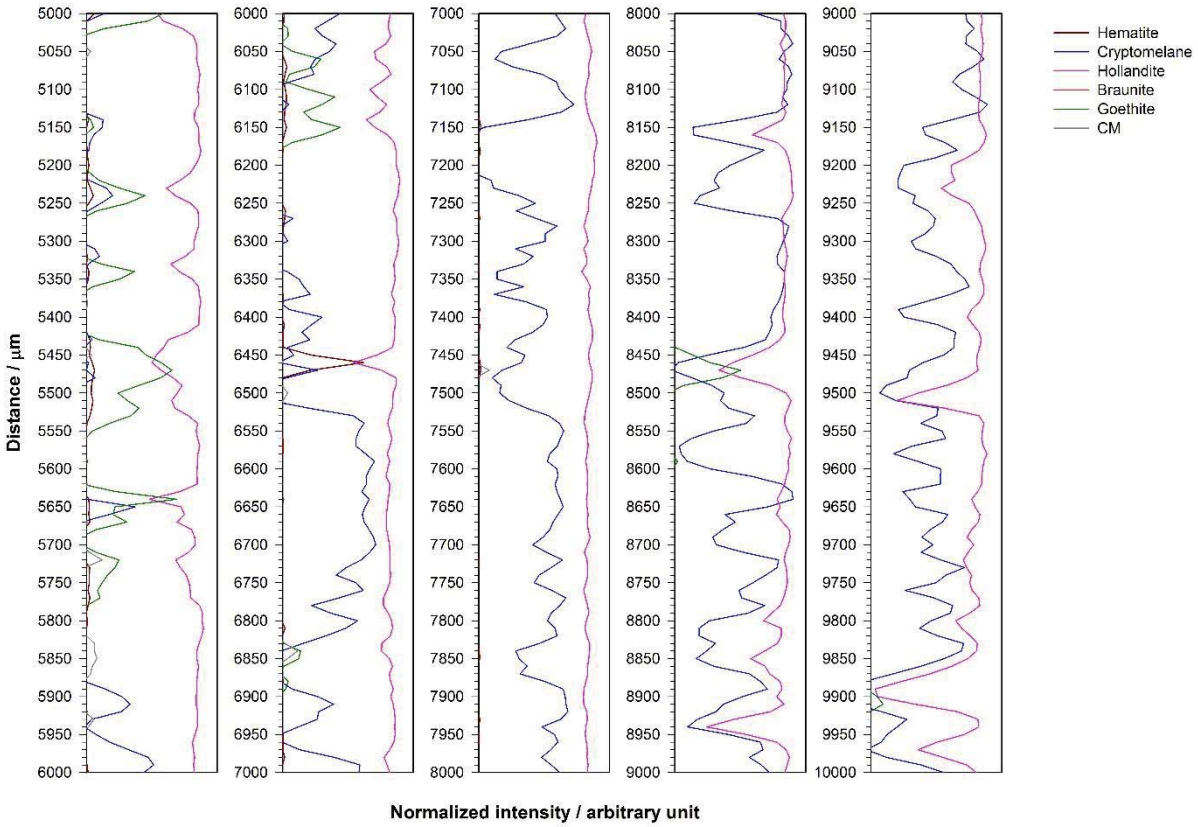
Distance / µm
Normalized intensity / arbitrary unit
Hematite
Cryptomelane
Hollandite
Braunite
Goethite
CM

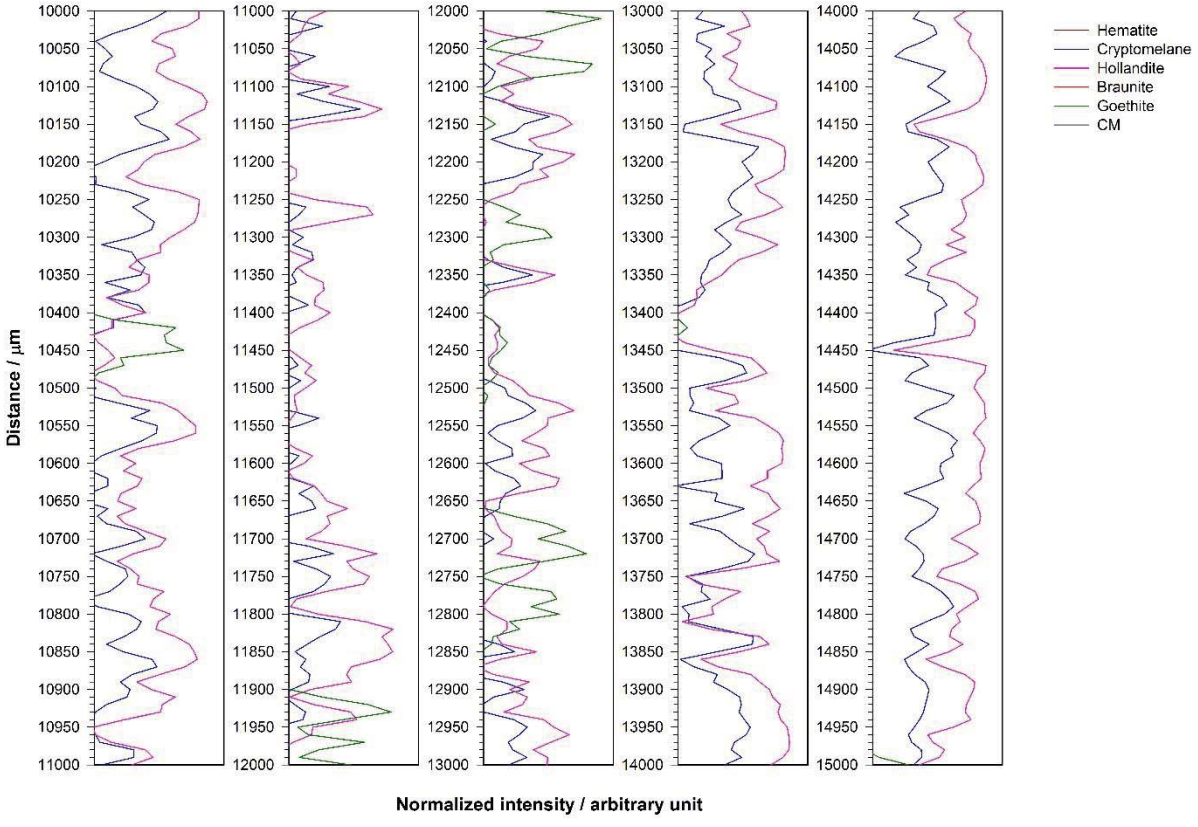
Distance / µm
Normalized intensity / arbitrary unit
Hematite
Cryptomelane
Hollandite
Braunite
Goethite
CM

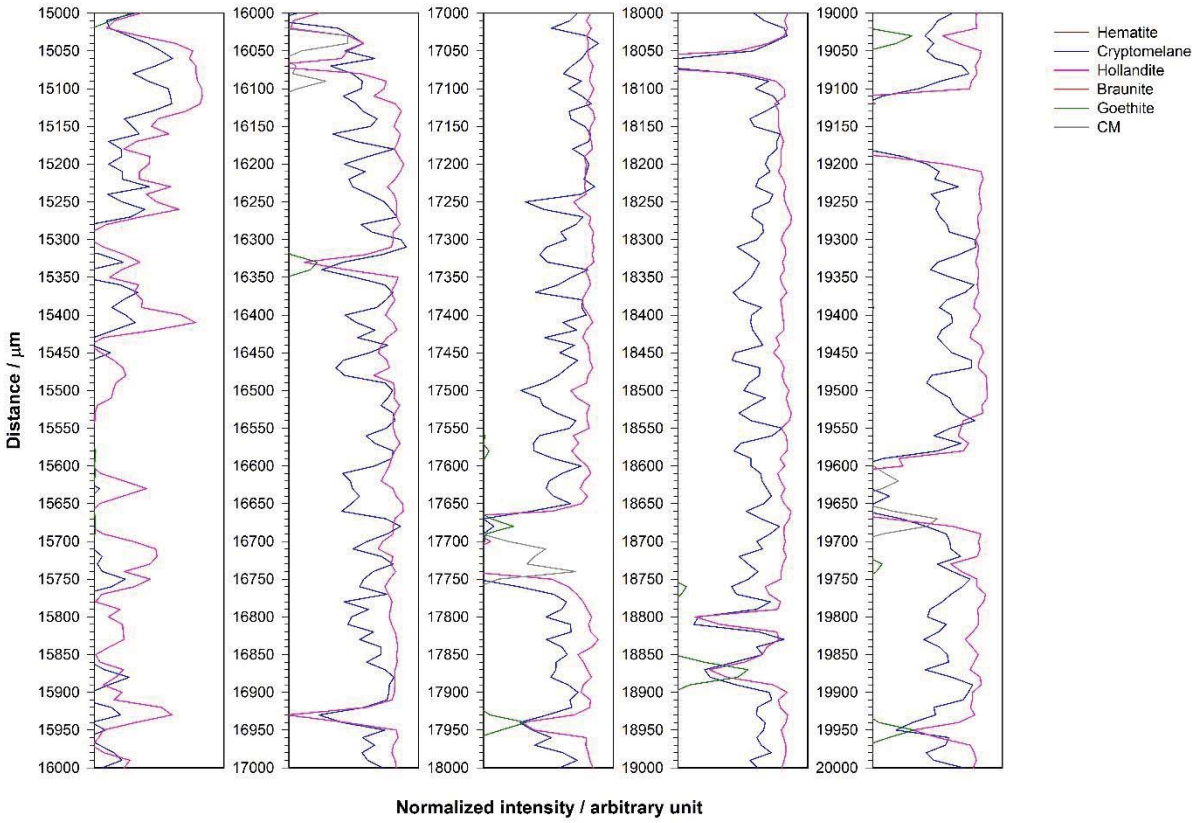
Distance / µm
Normalized intensity / arbitrary unit
Hematite
Cryptomelane
Hollandite
Braunite
Goethite
CM

78-D1 (Mn-2)


5 mm

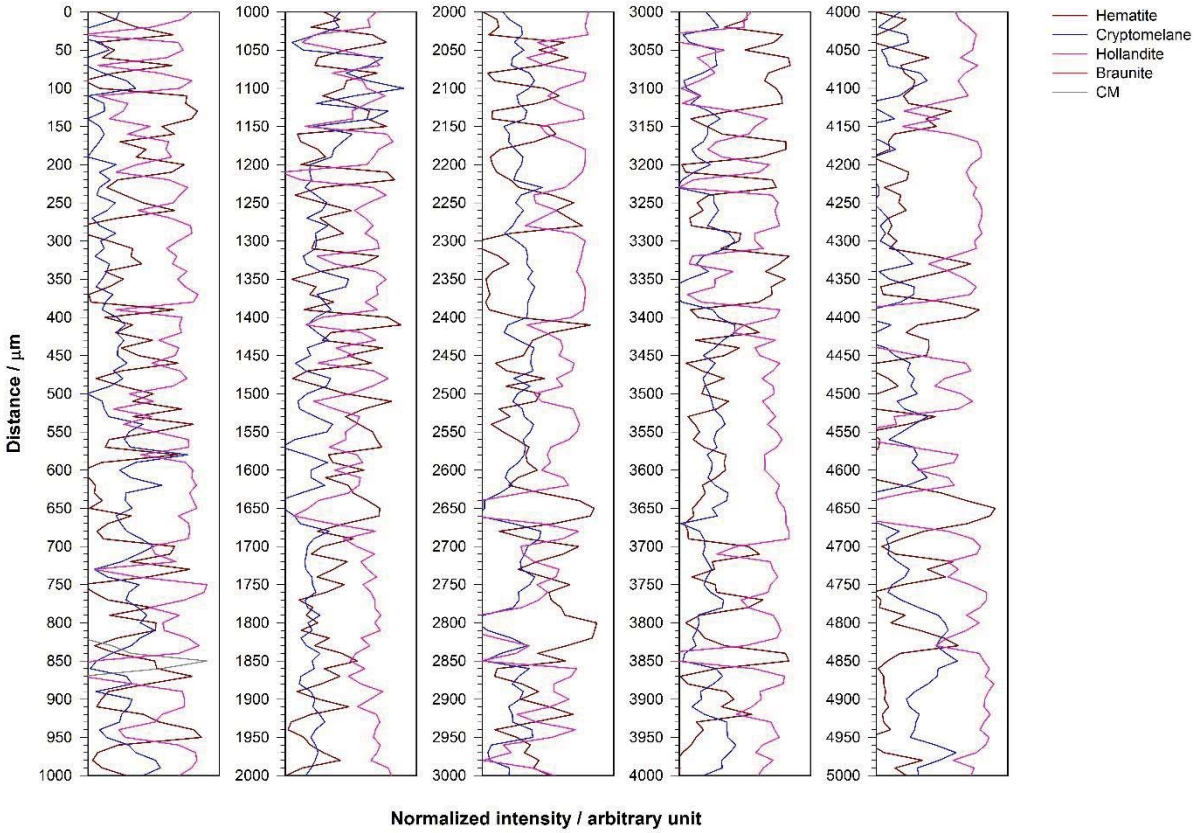
Distance / µm
Normalized intensity / arbitrary unit
Hematite
Cryptomelane
Hollandite
Braunite
CM

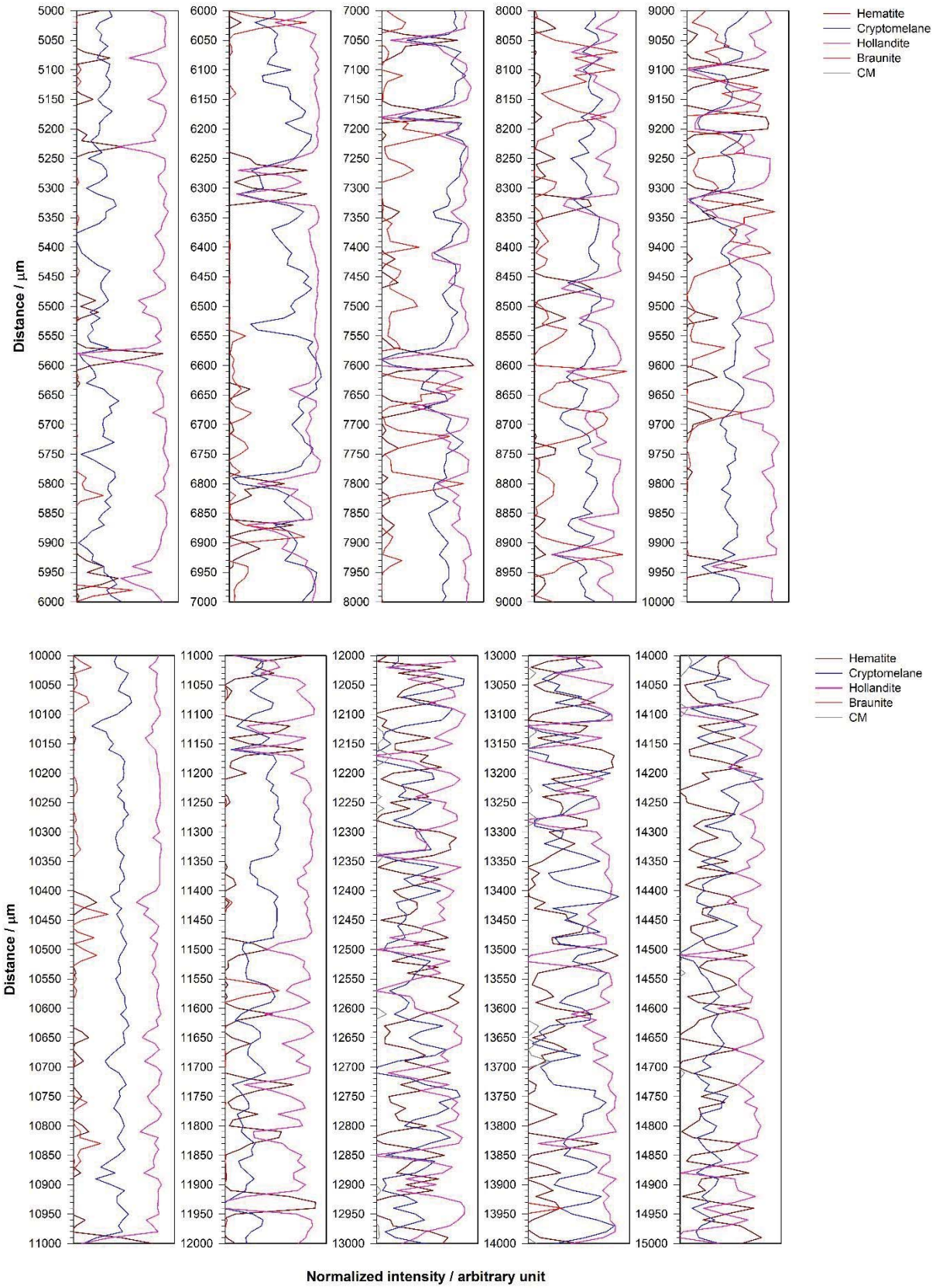
Hematite
Cryptomelane
Hollandite
Braunite
CM
Distance / µm
Normalized intensity / arbitrary unit

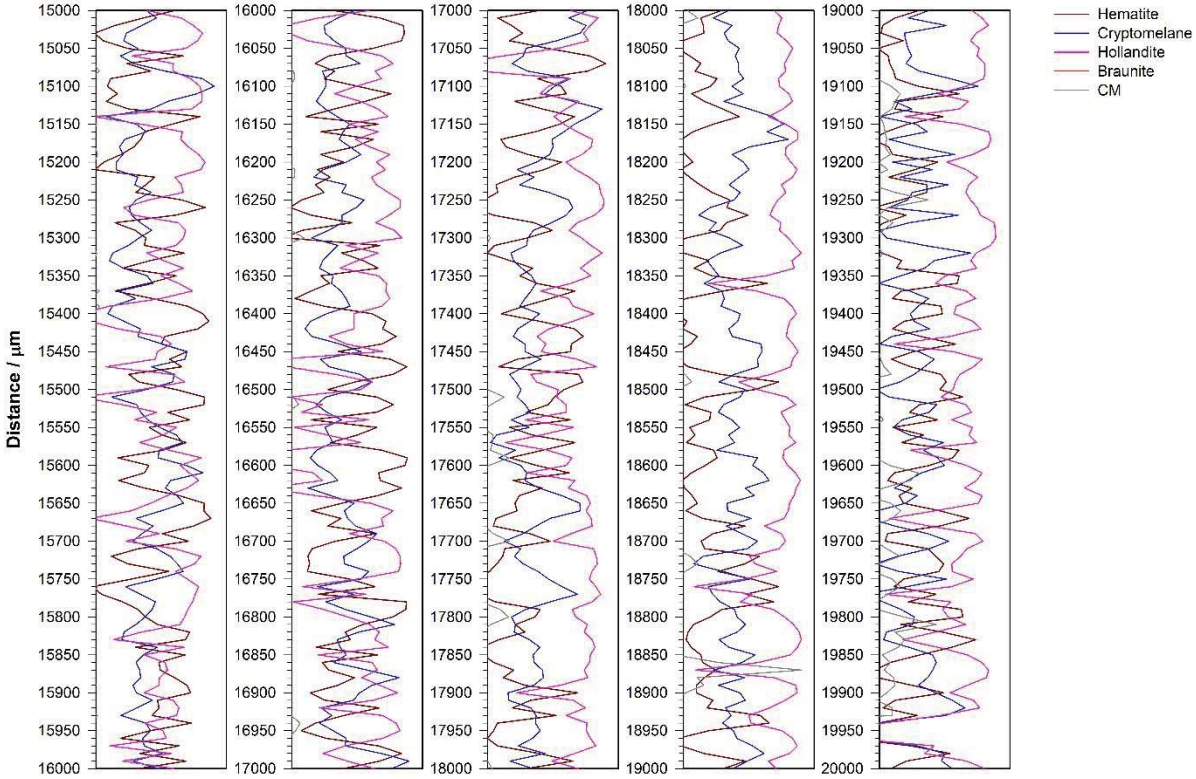

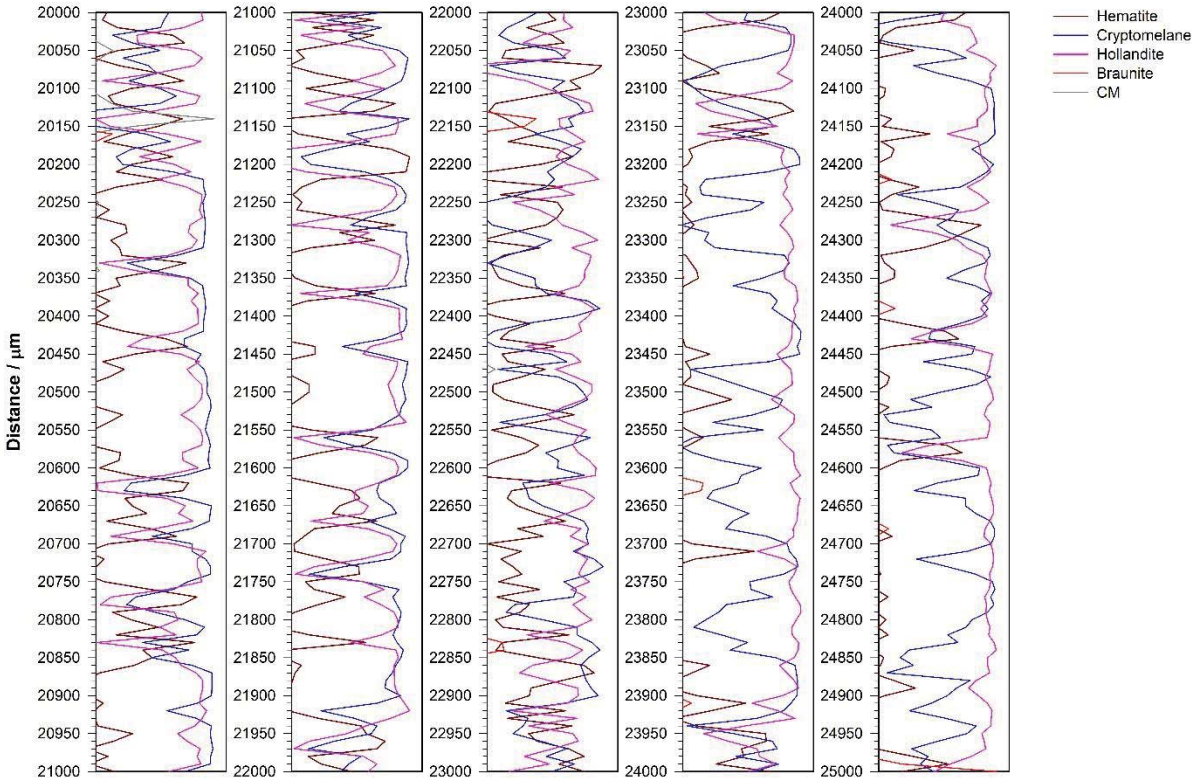

Normalized intensity / arbitrary unit

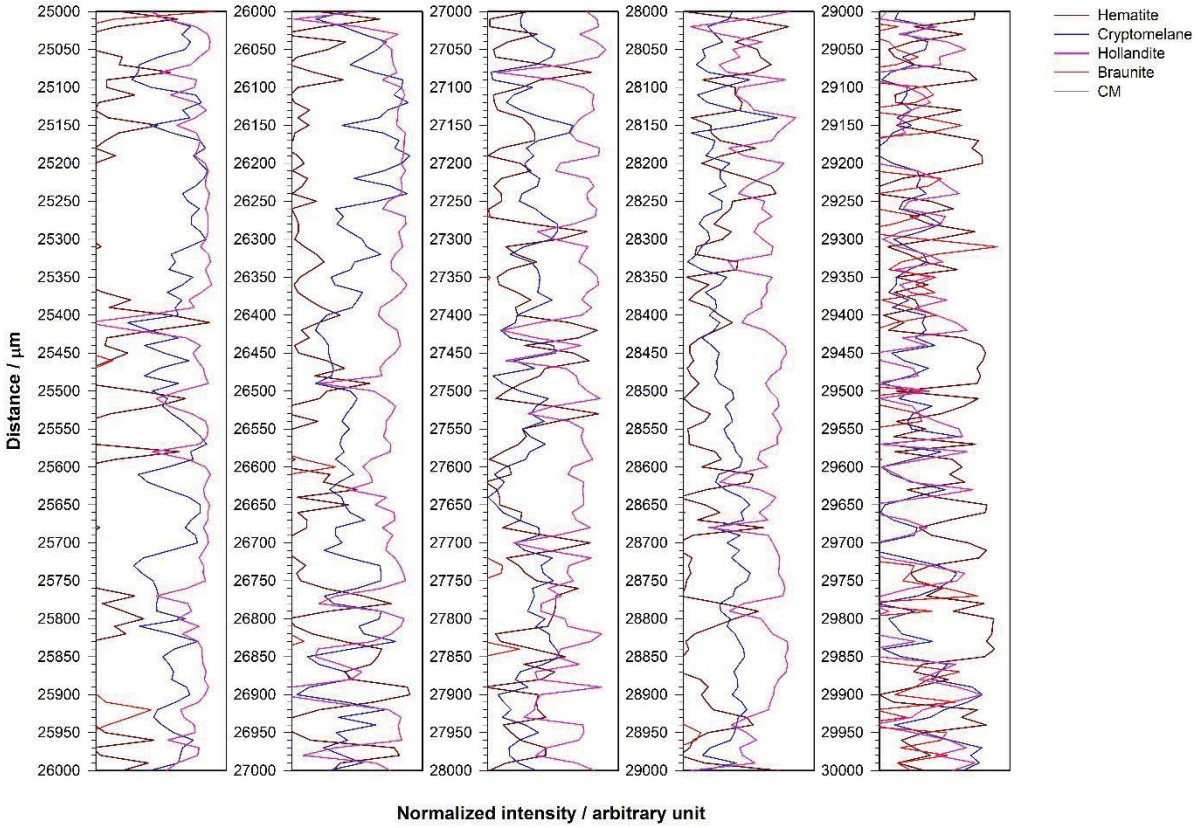
Hematite
Cryptomelane
Hollandite
Braunite
CM
Distance / µm
Normalized intensity / arbitrary unit

81 (Mn-3)

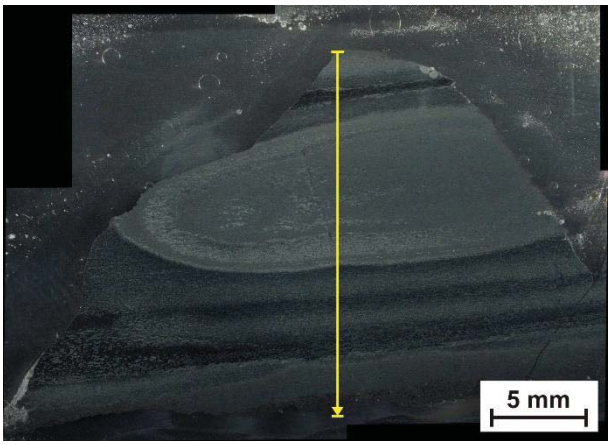
5 mm

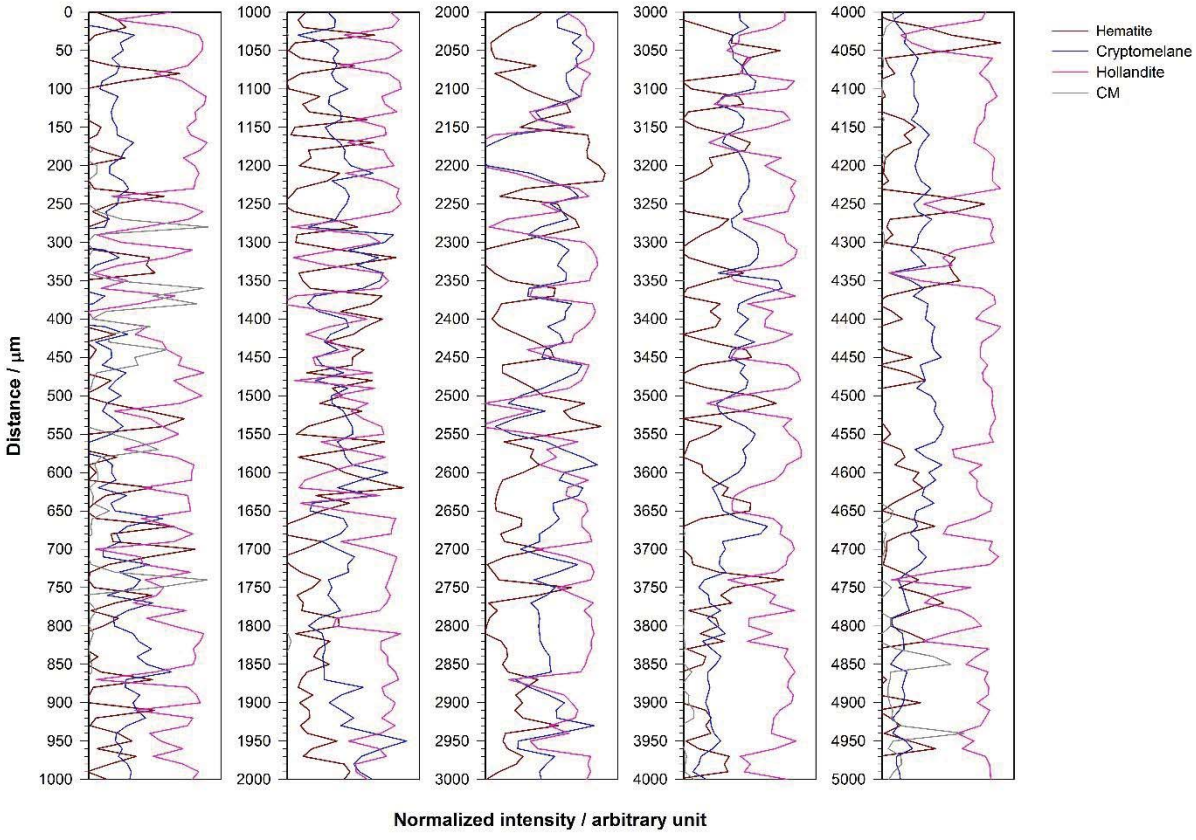
Distance / µm
Normalized intensity / arbitrary unit
Hematite
Cryptomelane
Hollandite
CM

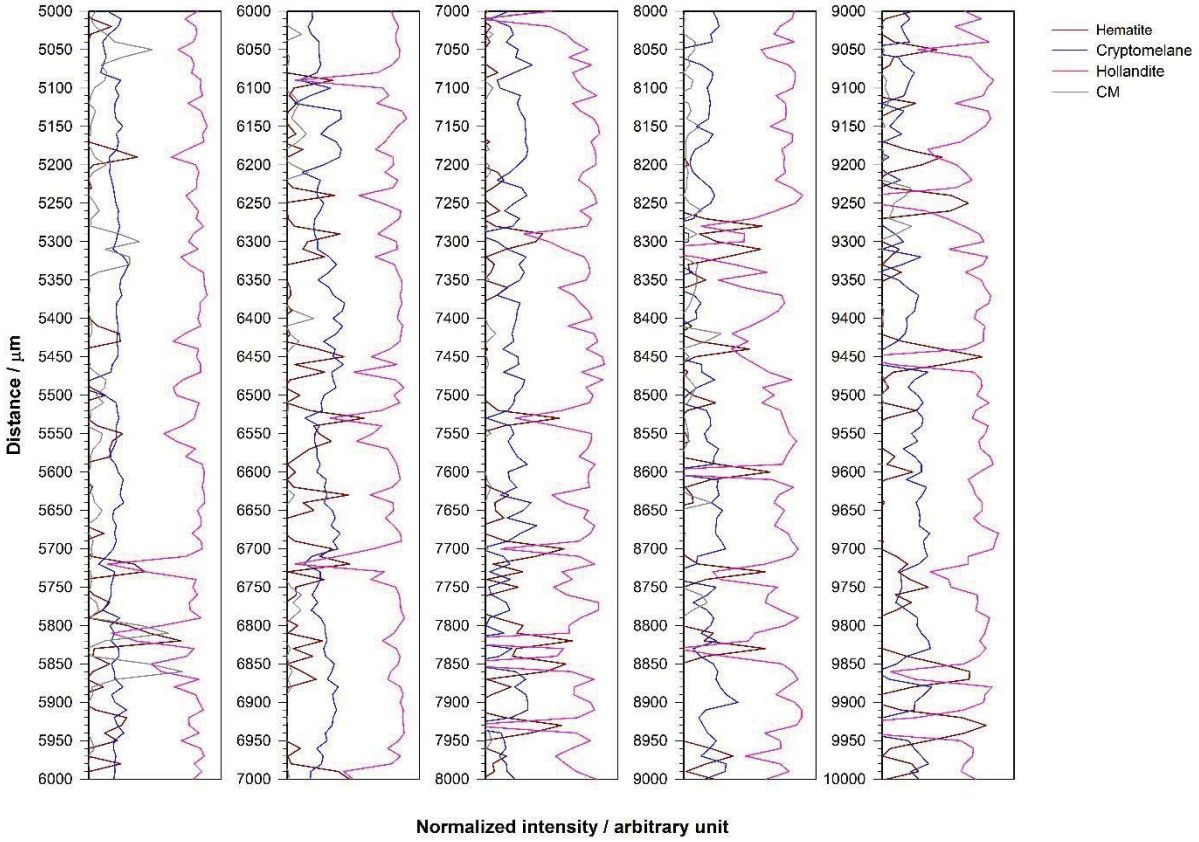
Distance / µm
Normalized intensity / arbitrary unit
Hematite
Cryptomelane
Hollandite
CM

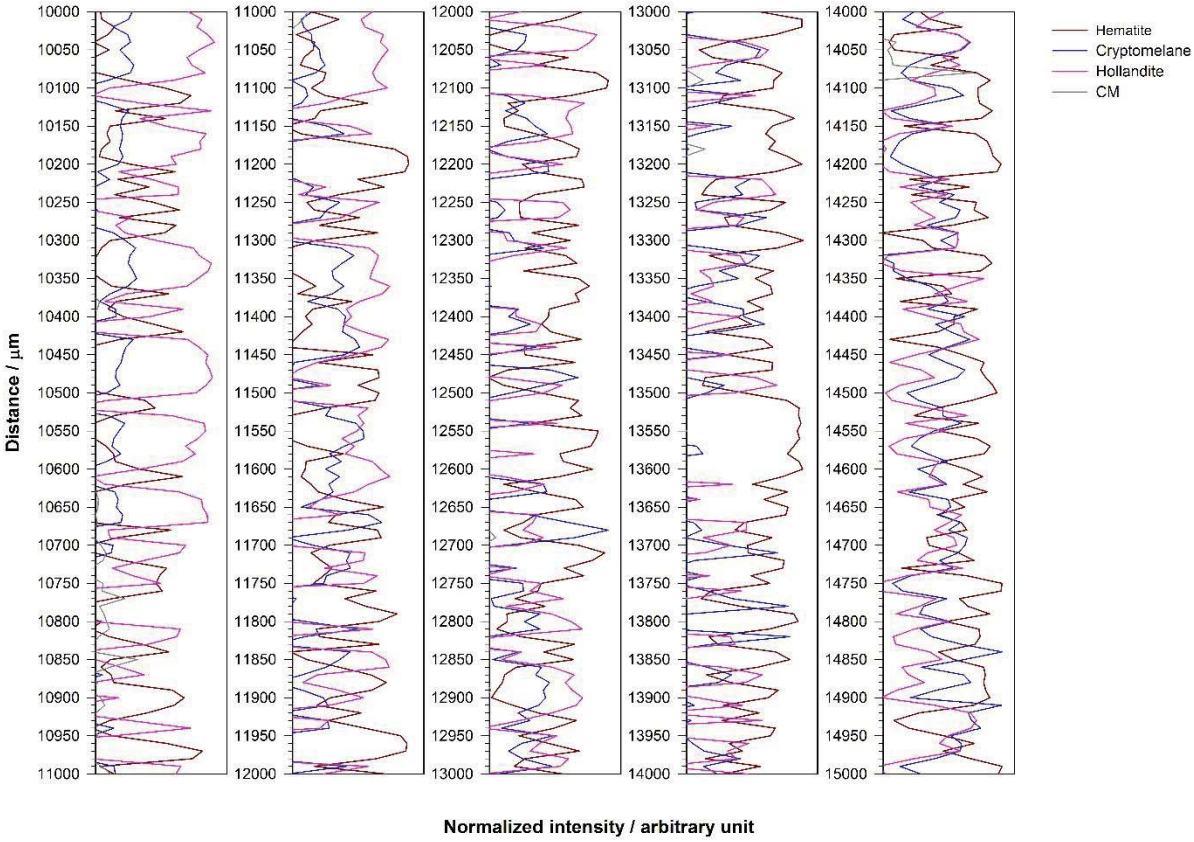
Distance / µm
Normalized intensity / arbitrary unit
Hematite
Cryptomelane
Hollandite
CM

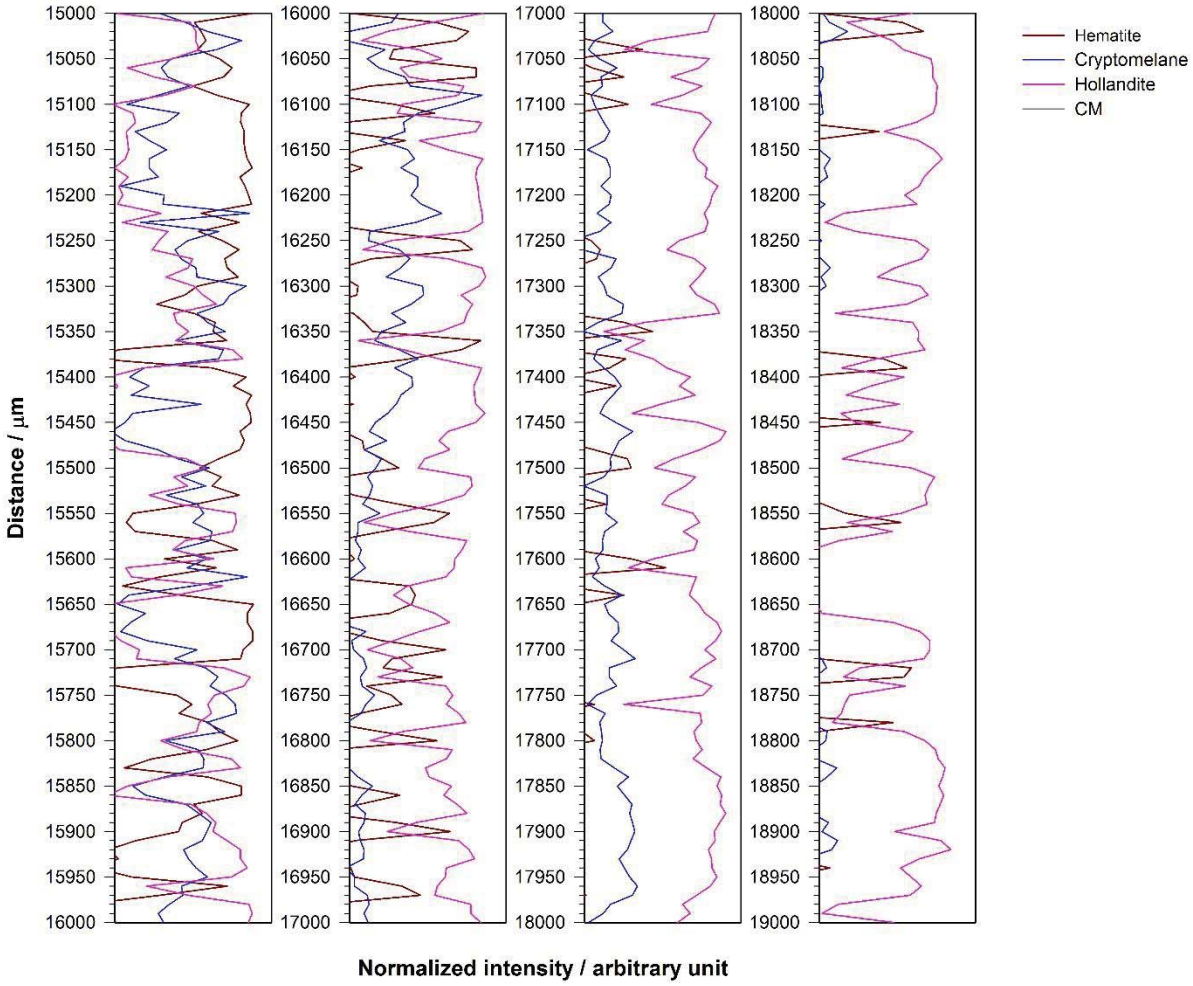
Hematite
Cryptomelane
Hollandite
CM
Distance / µm
Normalized intensity / arbitrary unit

SI 13-Fig. Mineralogical distribution by Raman spectroscopy (sample 75-2)

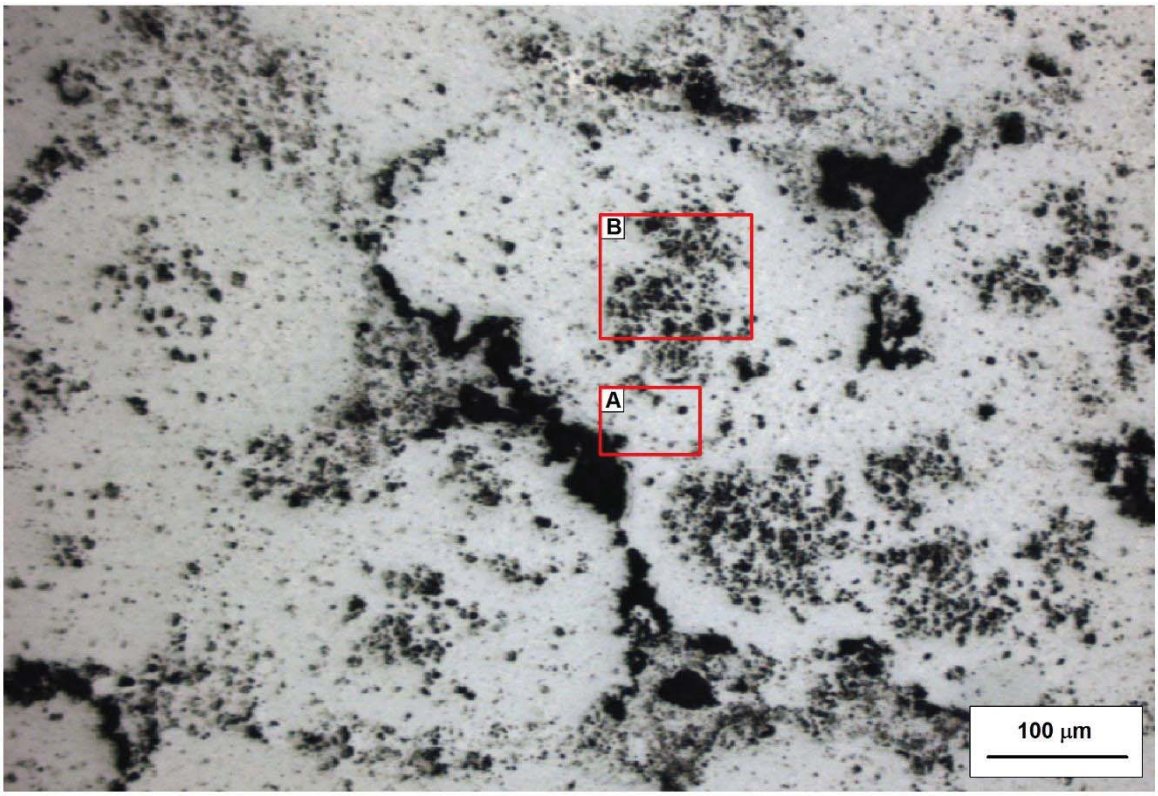

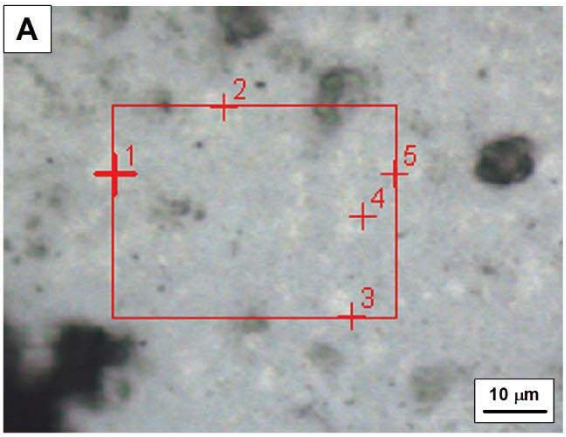

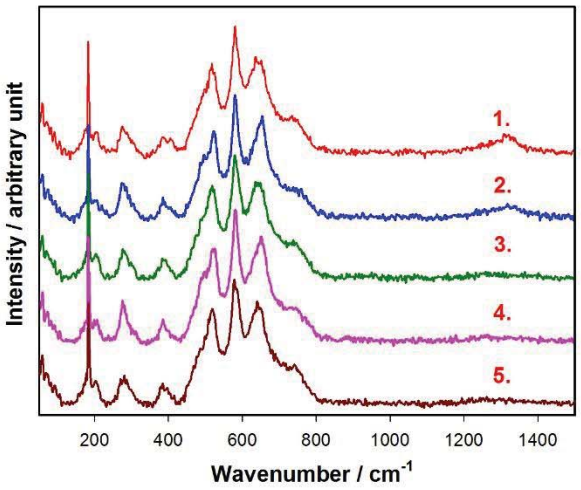

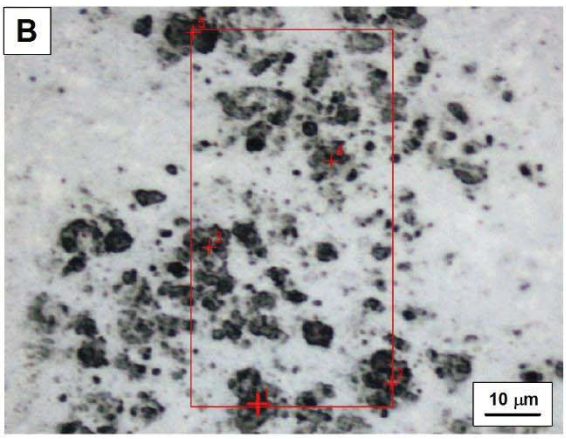

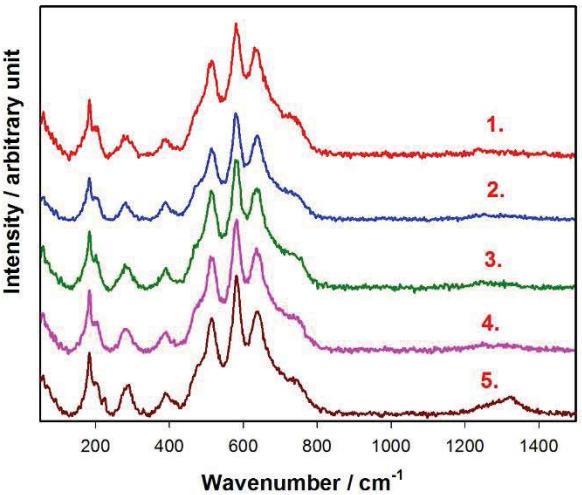

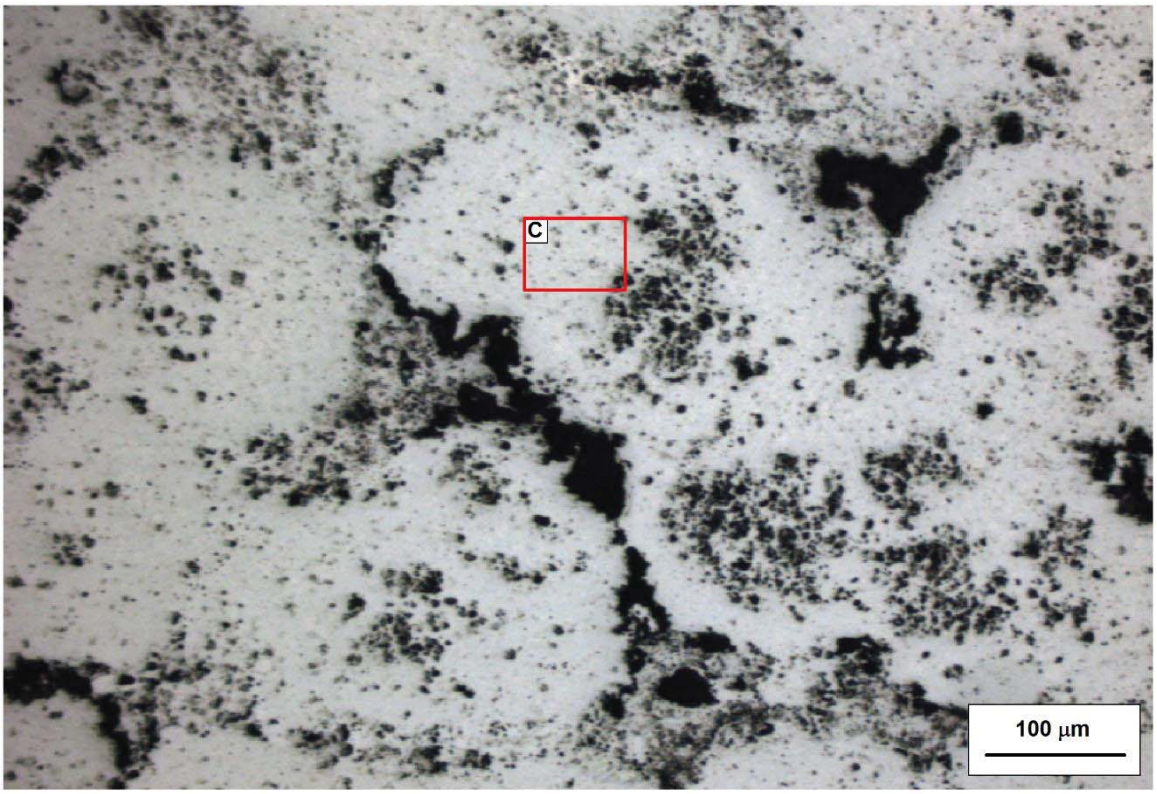
C
100 μm

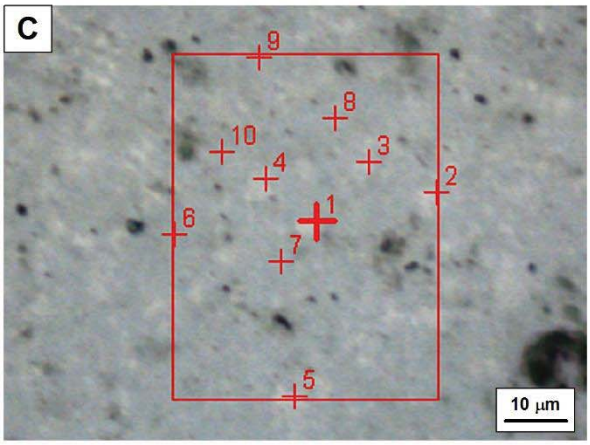
C
9
8
10
3
4
2
1
6
7
5
10 μm

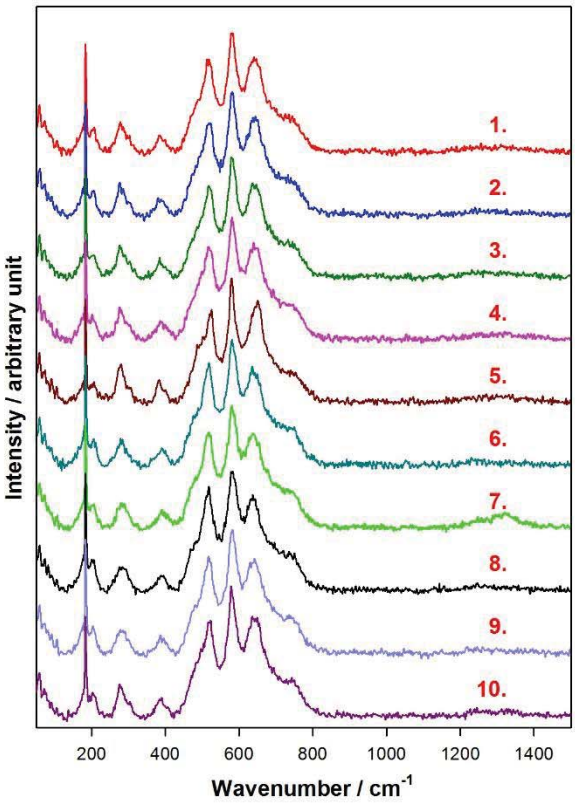
Intensity / arbitrary unit
1.
2.
3.
4.
5.
6.
7.
8.
9.
10.
200
400
600
800
1000
1200
1400
Wavenumber / cm-1

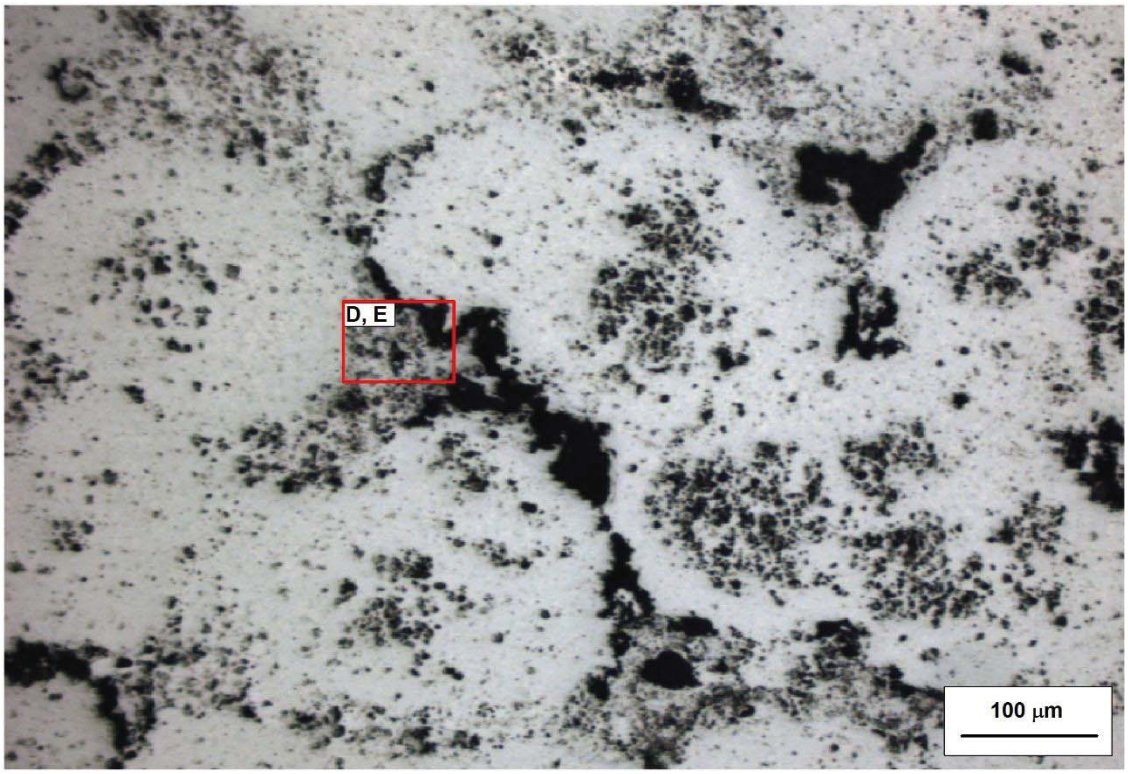
D, E
100 μm

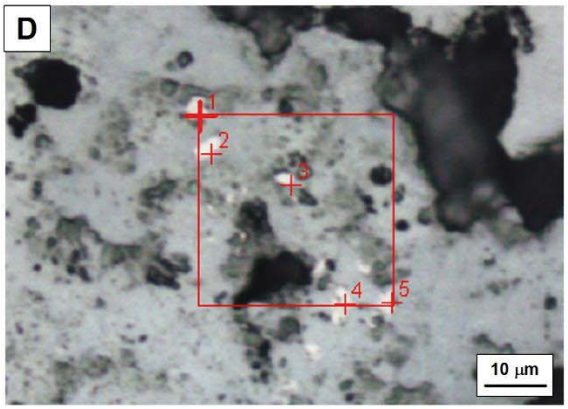
D
1
2
3
4
5
10 μm

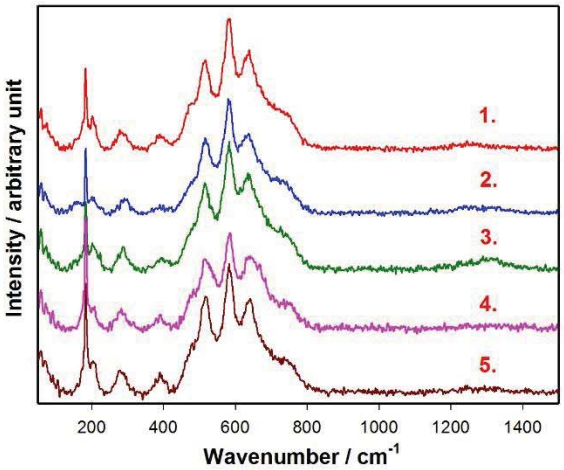
Intensity / arbitrary unit
1.
2.
3.
4.
5.
200
400
600
800
1000
1200
1400
Wavenumber / cm-1

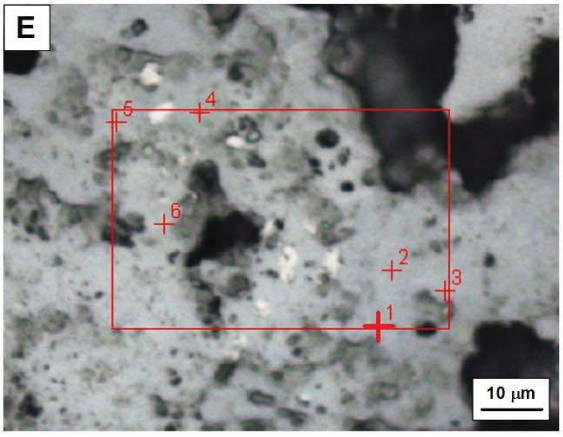
E
5
4
6
2
3
1
10 μm

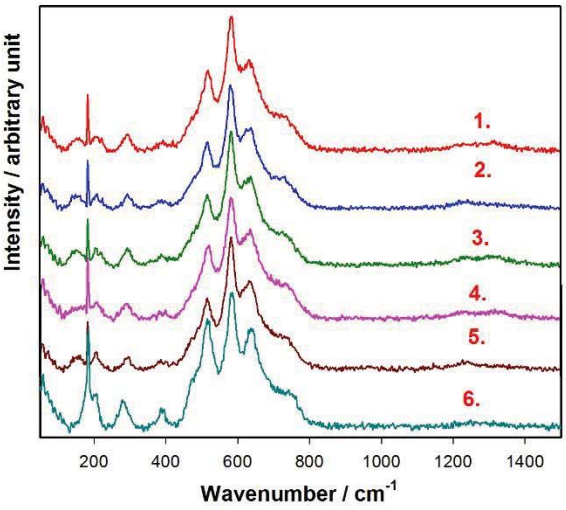
Intensity / arbitrary unit
1.
2.
3.
4.
5.
6.
200
400
600
800
1000
1200
1400
Wavenumber / cm-1

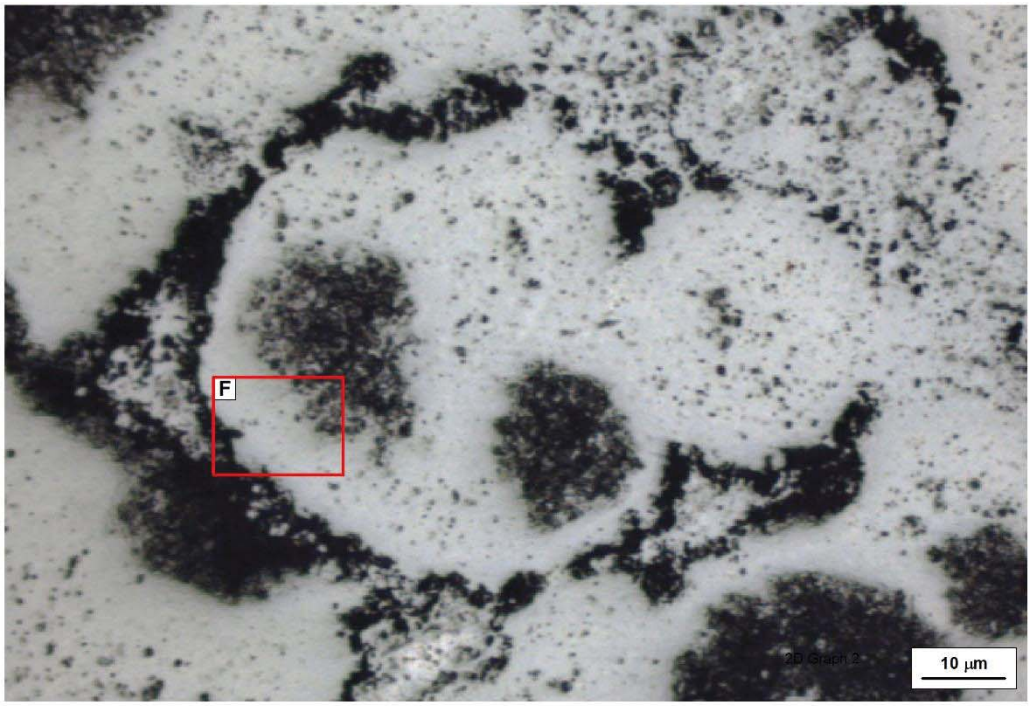
F
10 μm

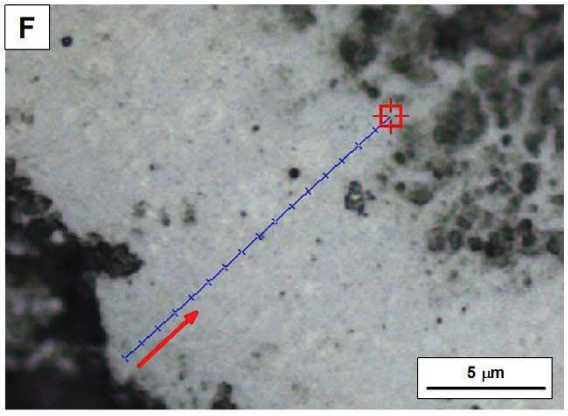
F
5 μm

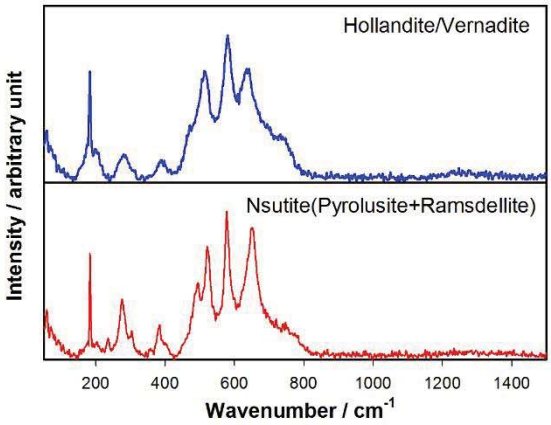
Hollandite/Vernadite
Nsutite(Pyrolusite+Ramsdellite)
Intensity / arbitrary unit
200
400
600
800
1000
1200
1400
Wavenumber / cm-1

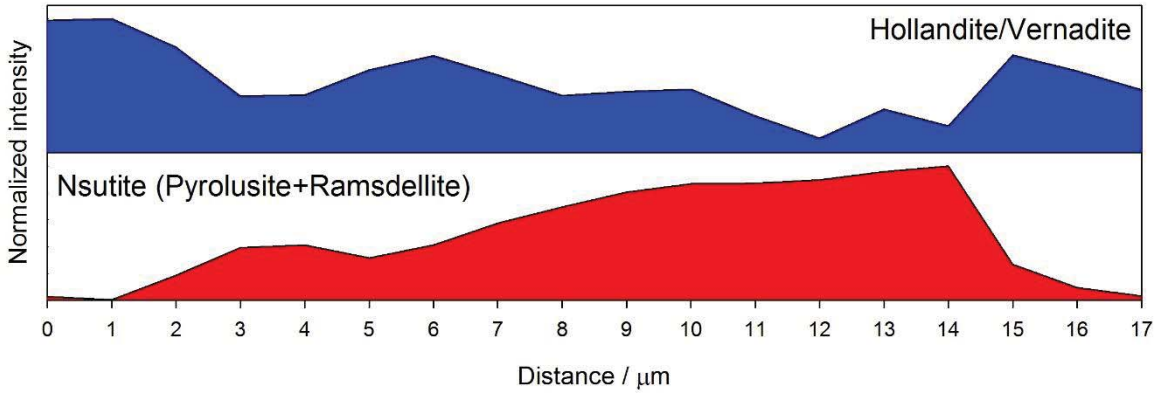
Hollandite/Vernadite
Nsutite (Pyrolusite+Ramsdellite)
Normalized intensity
0
1
2
3
4
5
6
7
8
9
10
11
12
13
14
15
16
17
Distance / μm

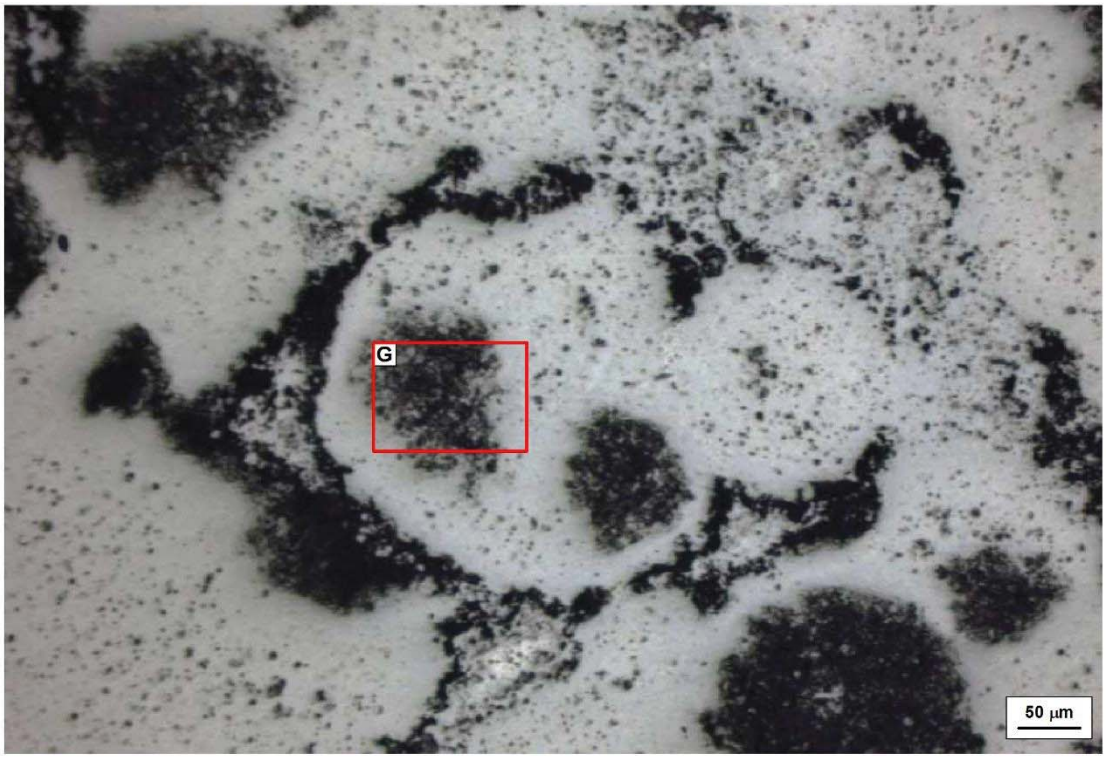
G
50 μm

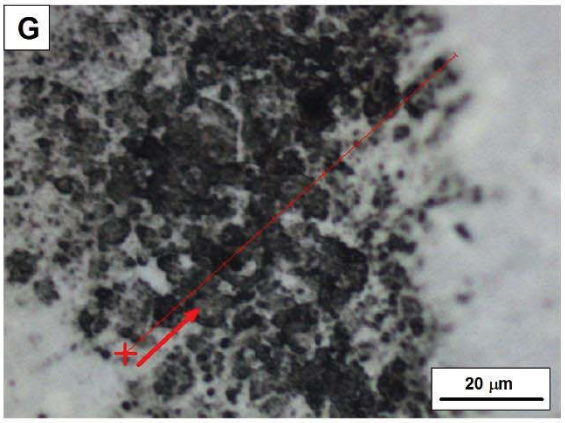
G
20 μm

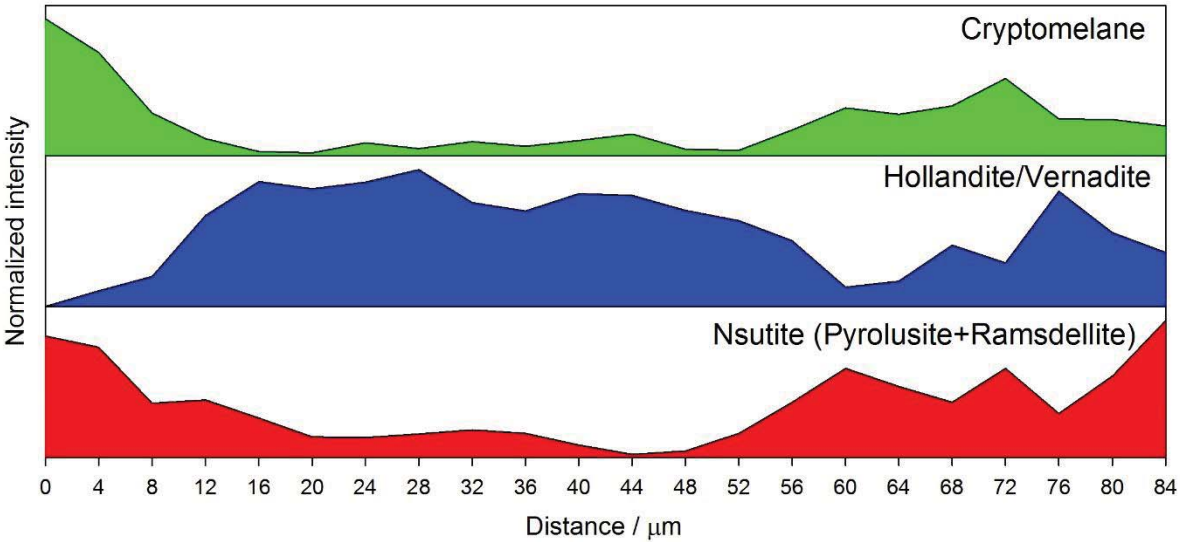
Cryptomelane
Hollandite/Vernadite
Nsutite (Pyrolusite+Ramsdellite)
Normalized intensity
0 4 8 12 16 20 24 28 32 36 40 44 48 52 56 60 64 68 72 76 80 84
Distance / μm

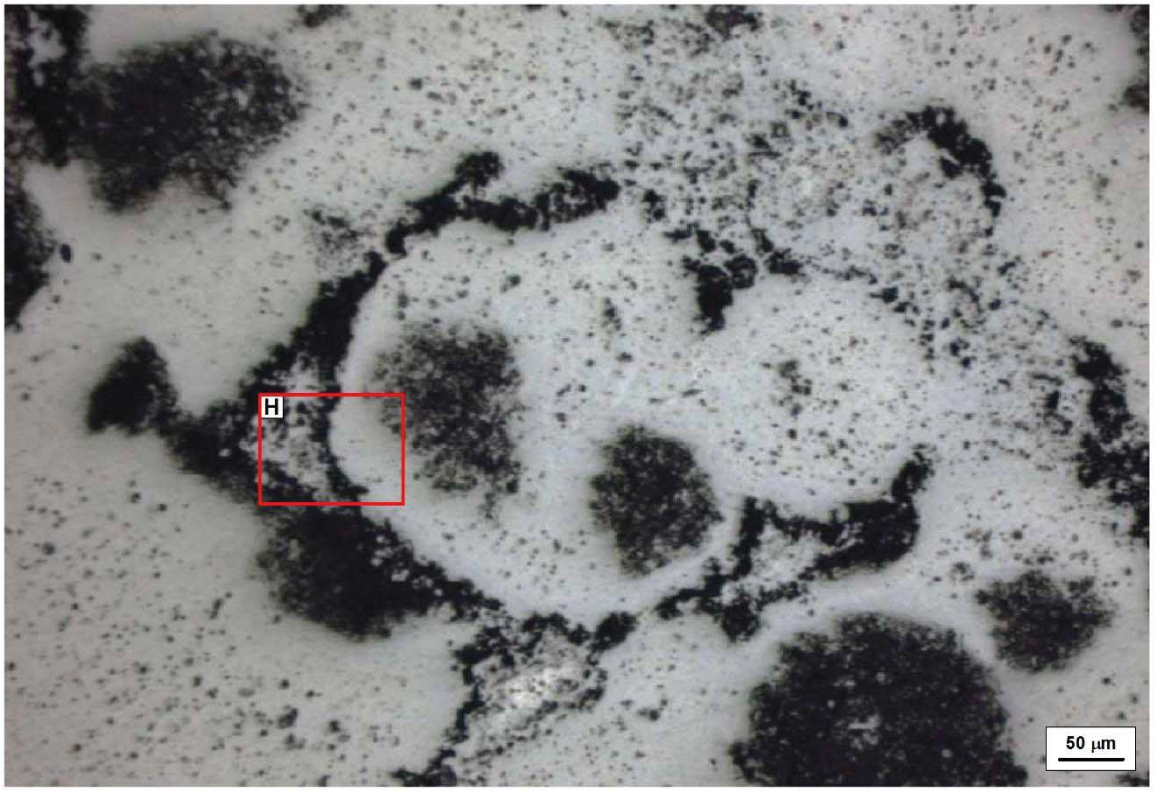
H
50 μm

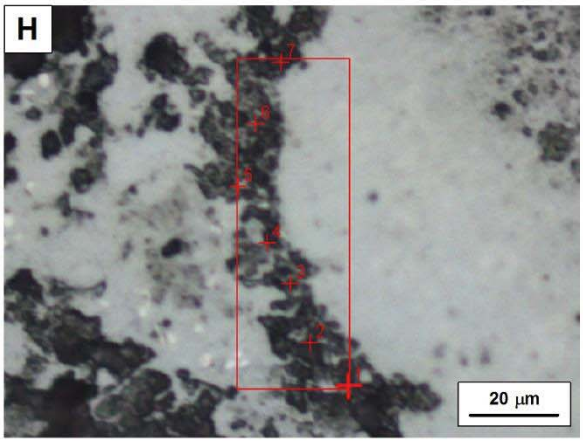
H
20 μm

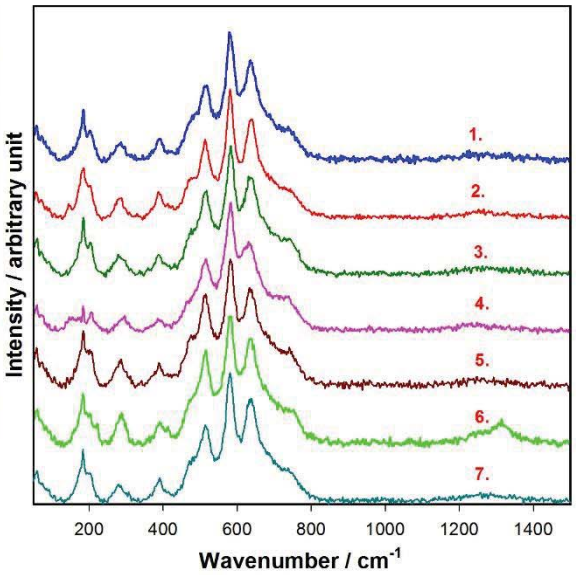
Intensity / arbitrary unit
1.
2.
3.
4.
5.
6.
7.
200
400
600
800
1000
1200
1400
Wavenumber / cm-1

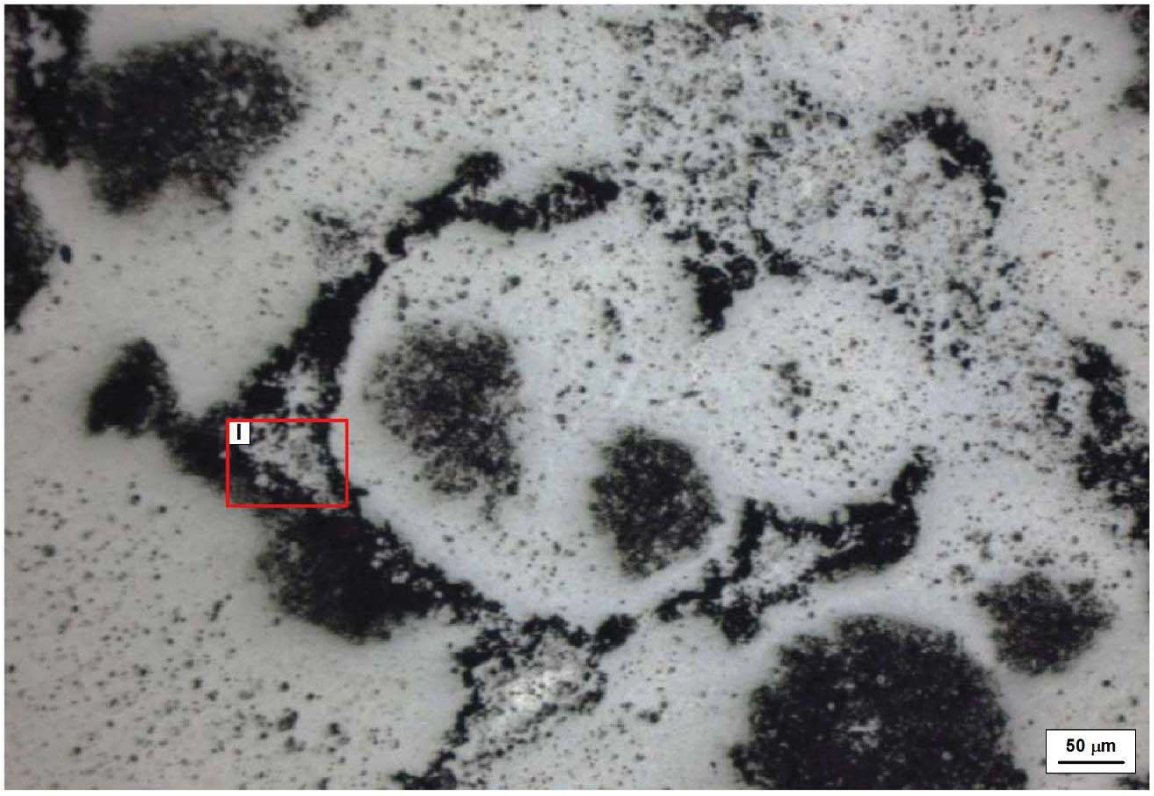
I
50 μm

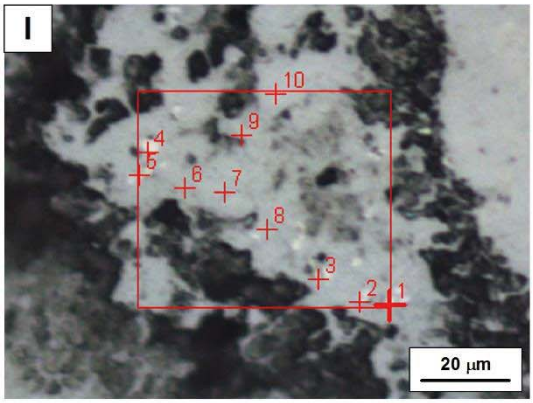
I
10
9
4
5
6
7
8
3
2
1
20 μm

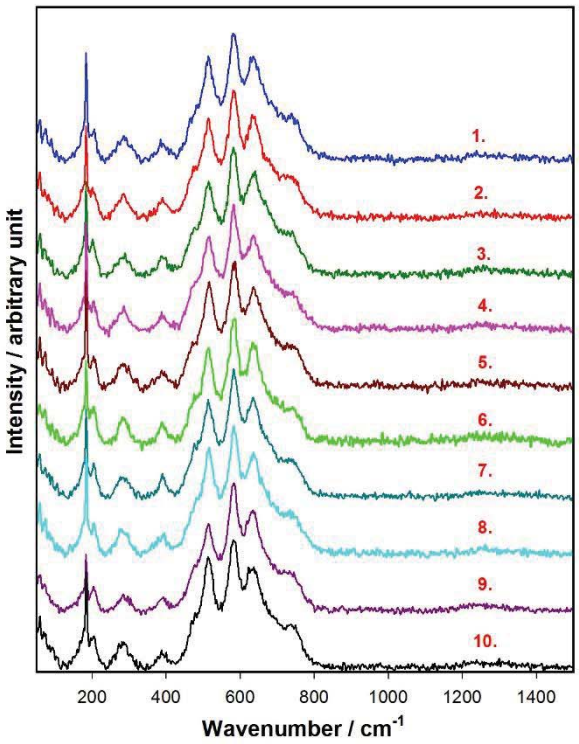
Intensity / arbitrary unit
1.
2.
3.
4.
5.
6.
7.
8.
9.
10.
200
400
600
800
1000
1200
1400
Wavenumber / cm-1

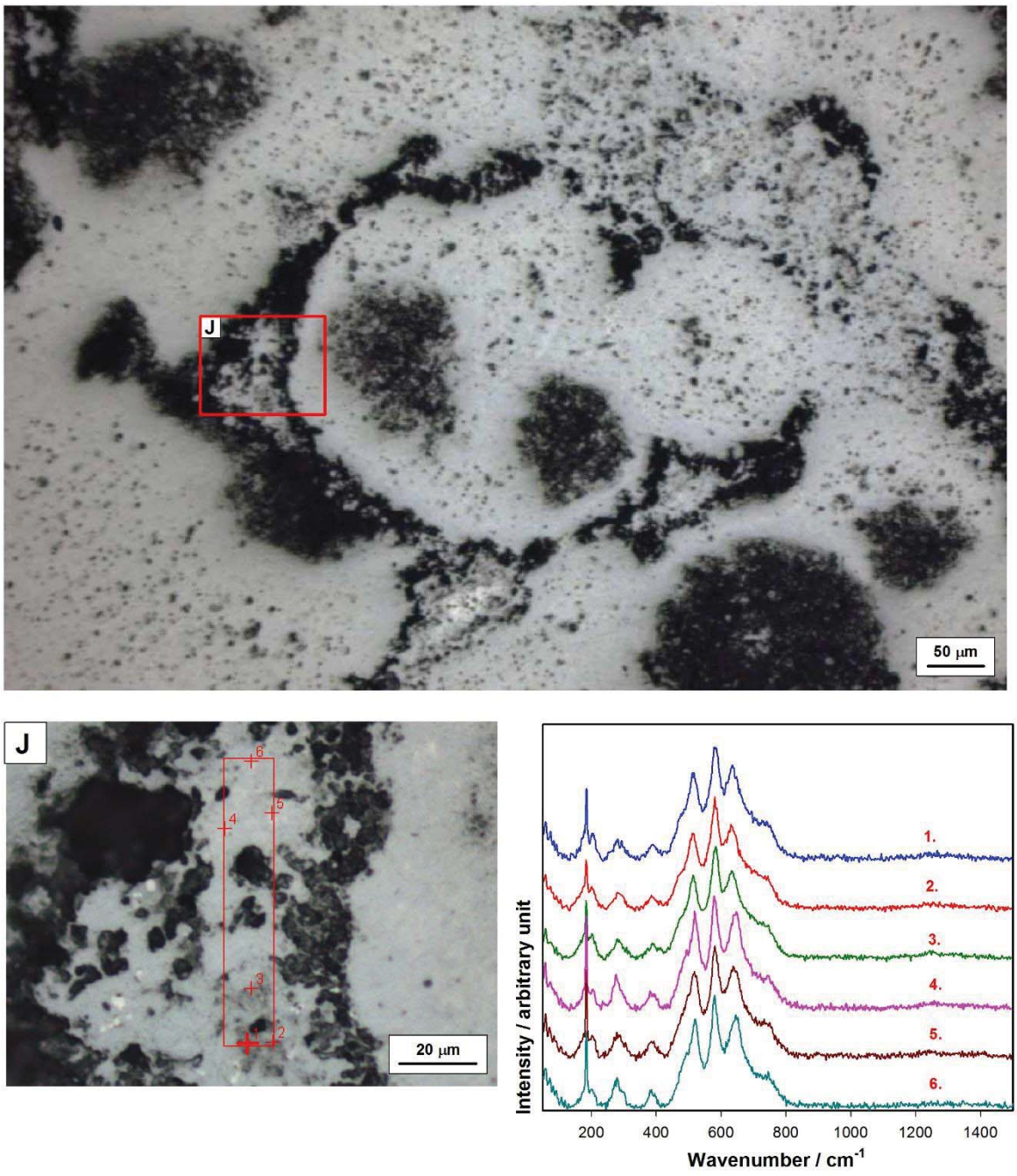

All the spectra taken in the fluffy parts, micronodules (cell colonies) and matrix material show dominant vernadite/hollandite-type Mn-oxides-hydroxides composition and more or less amount of cryptomelane and variable organic matter. The textural differences do not show significant mineralogical differences. The fluffy,micronodules are cell colonies (clusters), the central part consists of hollandite/vernadite (G) and organic matter, around which cryptomelane and nsutite (pyrolusite + ramsdellite) occur.

SI 14-Fig. Mineral phases and distribution in spherical (bubble-like) structures measured by Raman spectroscopy

1. **Outer part**

The **"dark spots"** in the matrix (M2 and M4 on Fig. 1) are mainly empty except dark porous inner rim with various thickness, which consist of hollandite type Mn oxide phase (dominant phase), cryptomelane and goethite (Fig. 2-5). The **matrix** among the "dark spots" (M1 and M3 on Fig. 1) is built up also by hollandite, cryptomelane and goethite (Fig. 2-5). The occurrence and distribution of the three minerals are consistent in the matrix material any trend in their distribution was not observable.

2. **Rim**

The non-porous rim of the spherical structure „bubble-like structure" (001 line on Fig. 1) mainly consists of hollandite and cryptomelane in variable amounts (Fig. 6). Rarely among the hollandite-cryptomelane flakes fine-grained clusters of goethite occur (Fig. 6). The distribution of the mentioned phases are indicative of gradually drop of peak intensity related to hollandite and cryptomelane phases in the direction from the spherical structure ("bubble-like structure)" to the matrix (Fig. 6).

3. **Inner part**

The **matrix** of the inner part of the spherical (bubble-like) structure is composed of very fine grained goethite (ferrihydrite) and little particles of Mn oxides (hollandite, cryptomelane in variable amounts), however hollandite is the dominant in the **dark spots** (Fig. 7-11). The mineral composition of the matrix and the dark spots show a unified distribution, any difference or significant trend in the matrix or in the dark spots was not detected.

Representative sample areas where Raman spectra were acquired (the other measured areas have similar mineral composition and distribution).

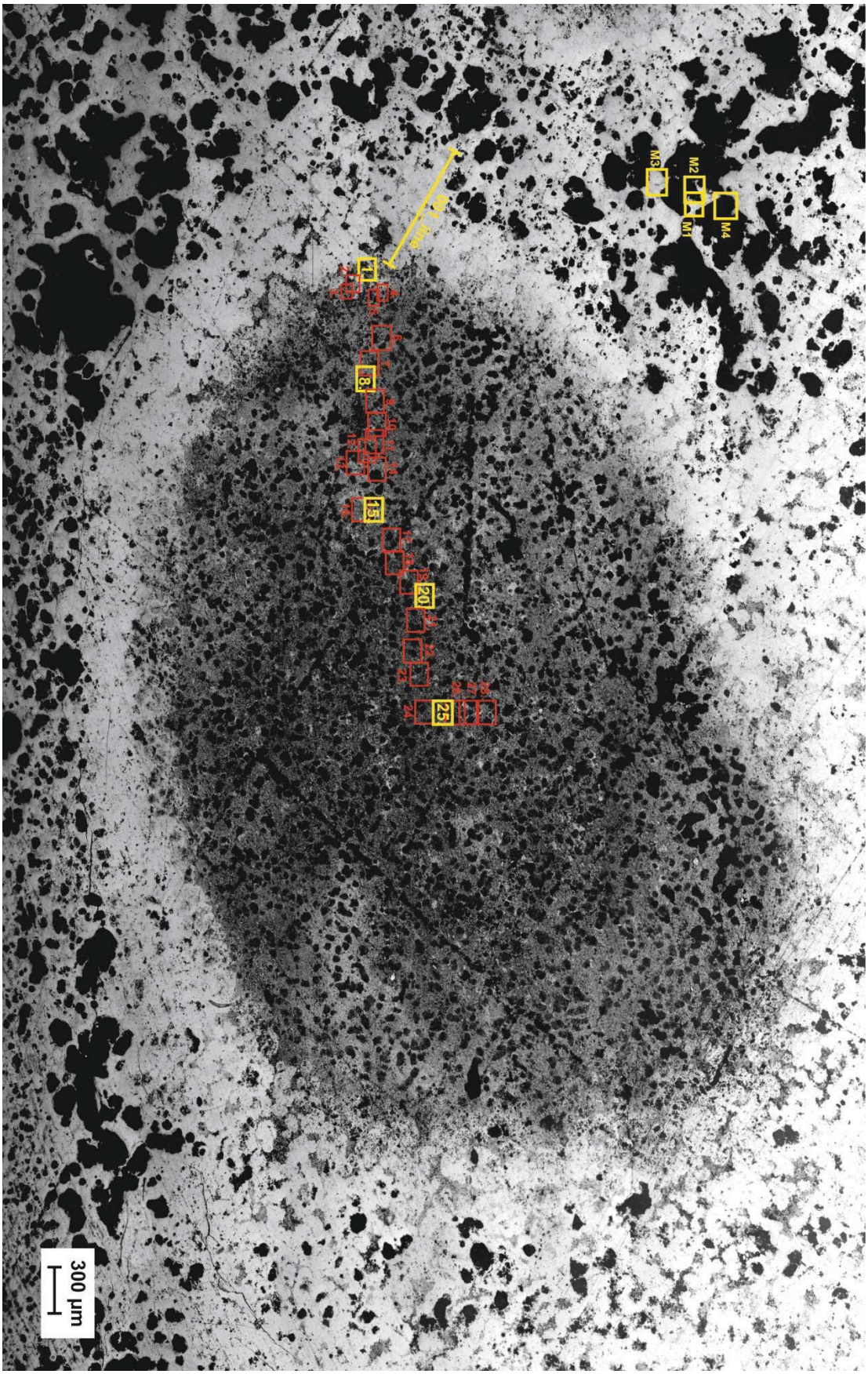

Figure 1.: Composite map from the investigated spherical (bubble-like) structure - measured areas are indicated on the picture (those places are detailed in this short report are in yellow color)

Outer part

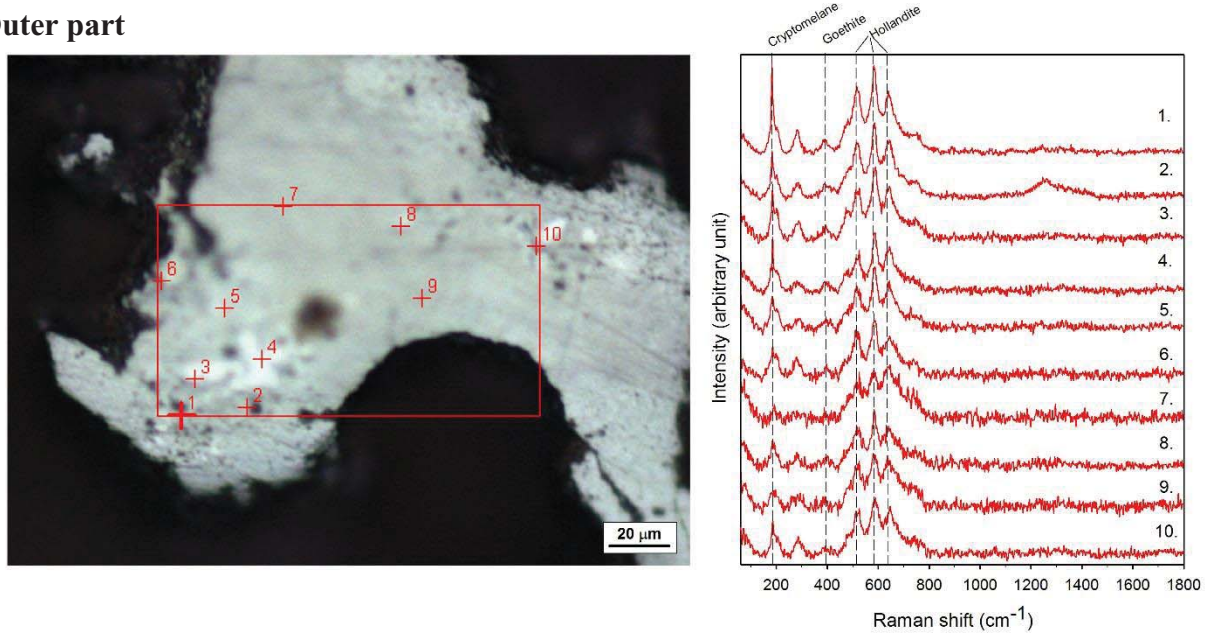

Figure 2.: Measuring points and Raman spectra from place indicated by M1 on Fig. 1.

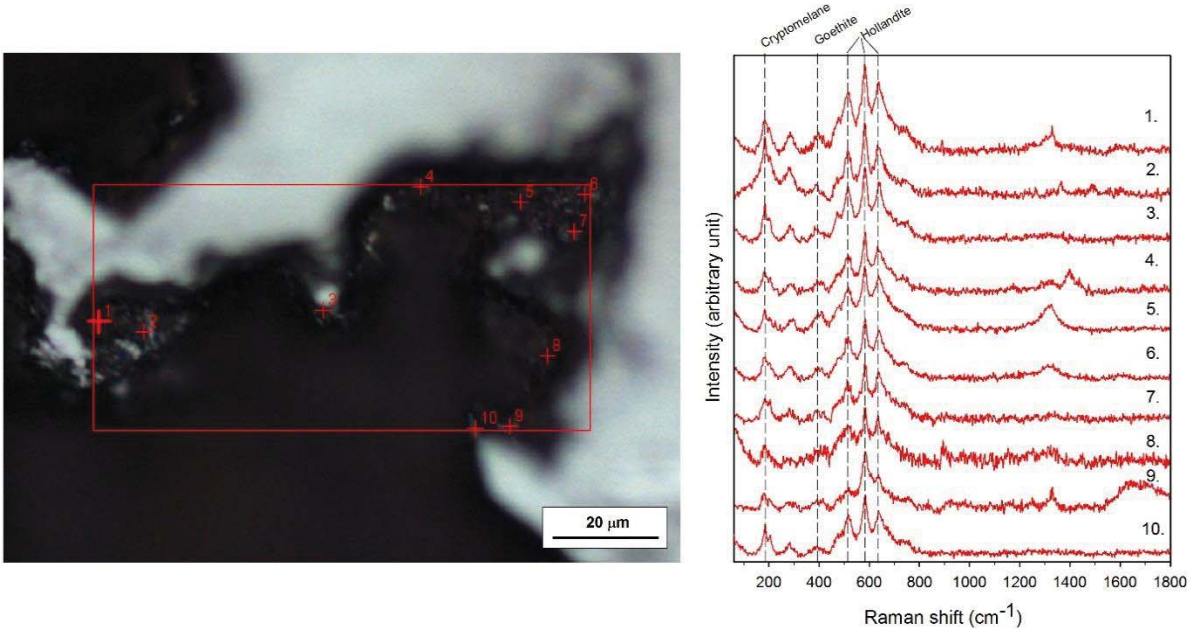

Figure 3.: Measuring points and Raman spectra from place indicated by M2 on Fig. 1.

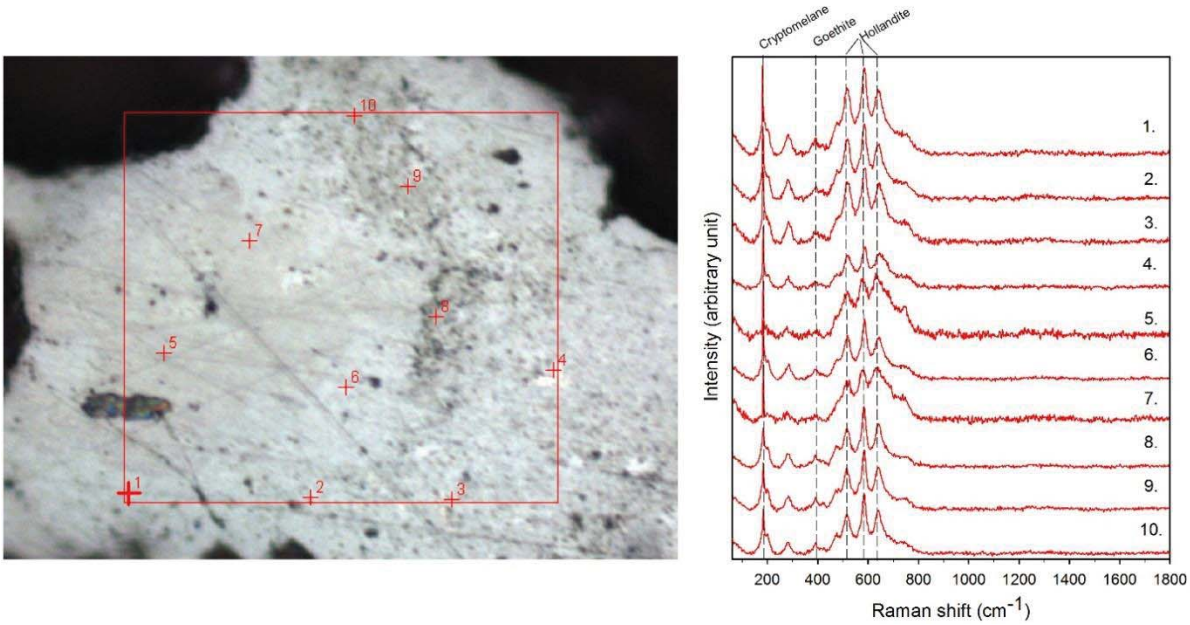

Figure 4.: Measuring points and Raman spectra from place indicated by M3 on Fig. 1.

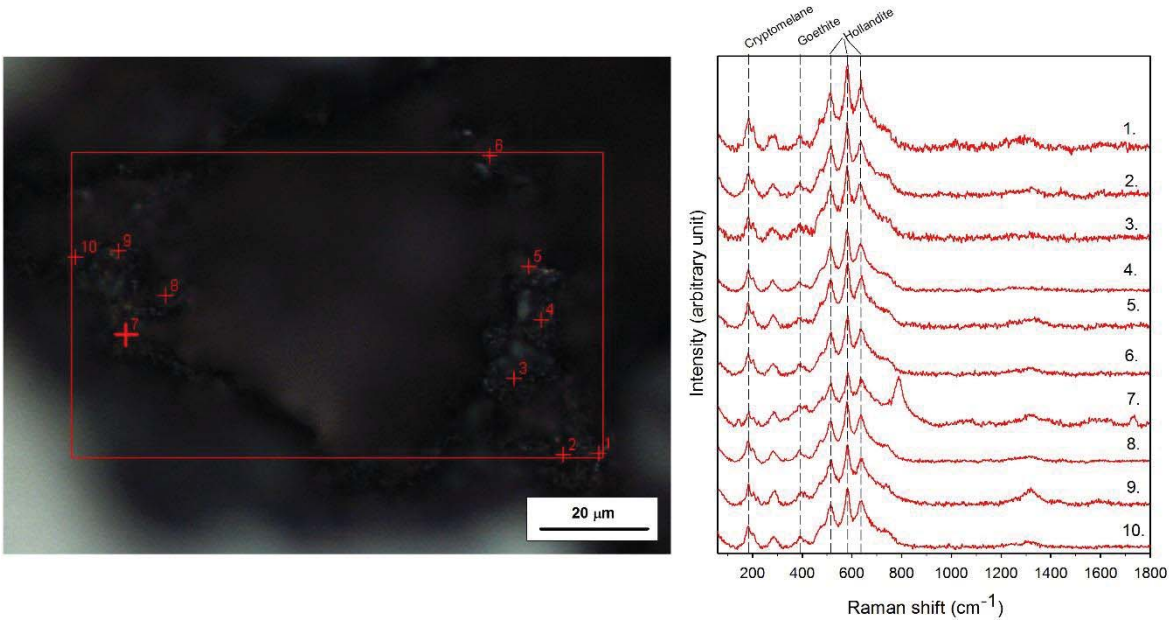

Figure 5.: Measuring points and Raman spectra from place indicated by M4 on Fig. 1.

Peak at 800 cm^{-1} can be UO2 or janhaugite $(Na,Ca)_3(Mn^{2+},Fe^{2+})_3(Ti,Zr,Nb)_2(Si_2O_7)_2O_2(OH,F)_2$

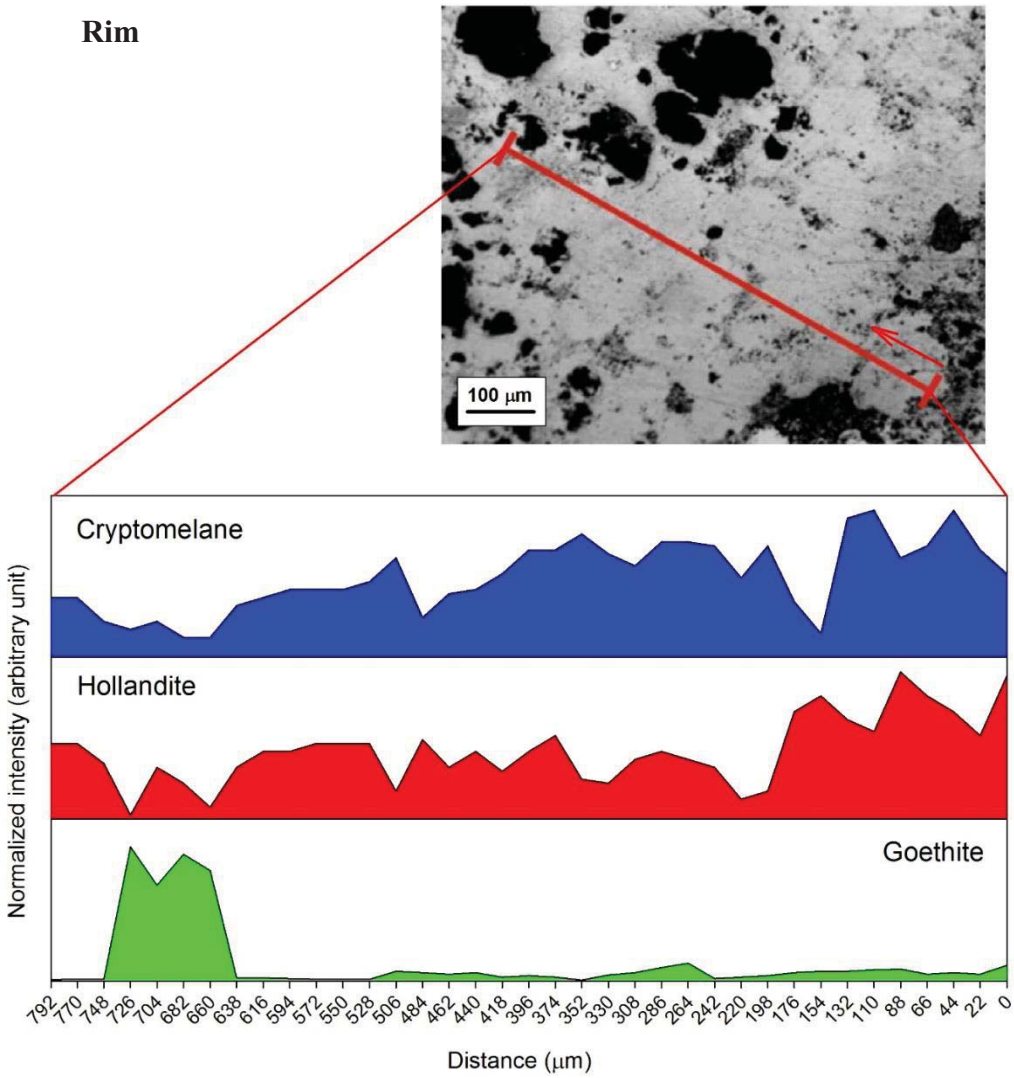

Figure 6.: 001-line map (indicated by yellow line marked with 001_line caption on the image).

Inner part

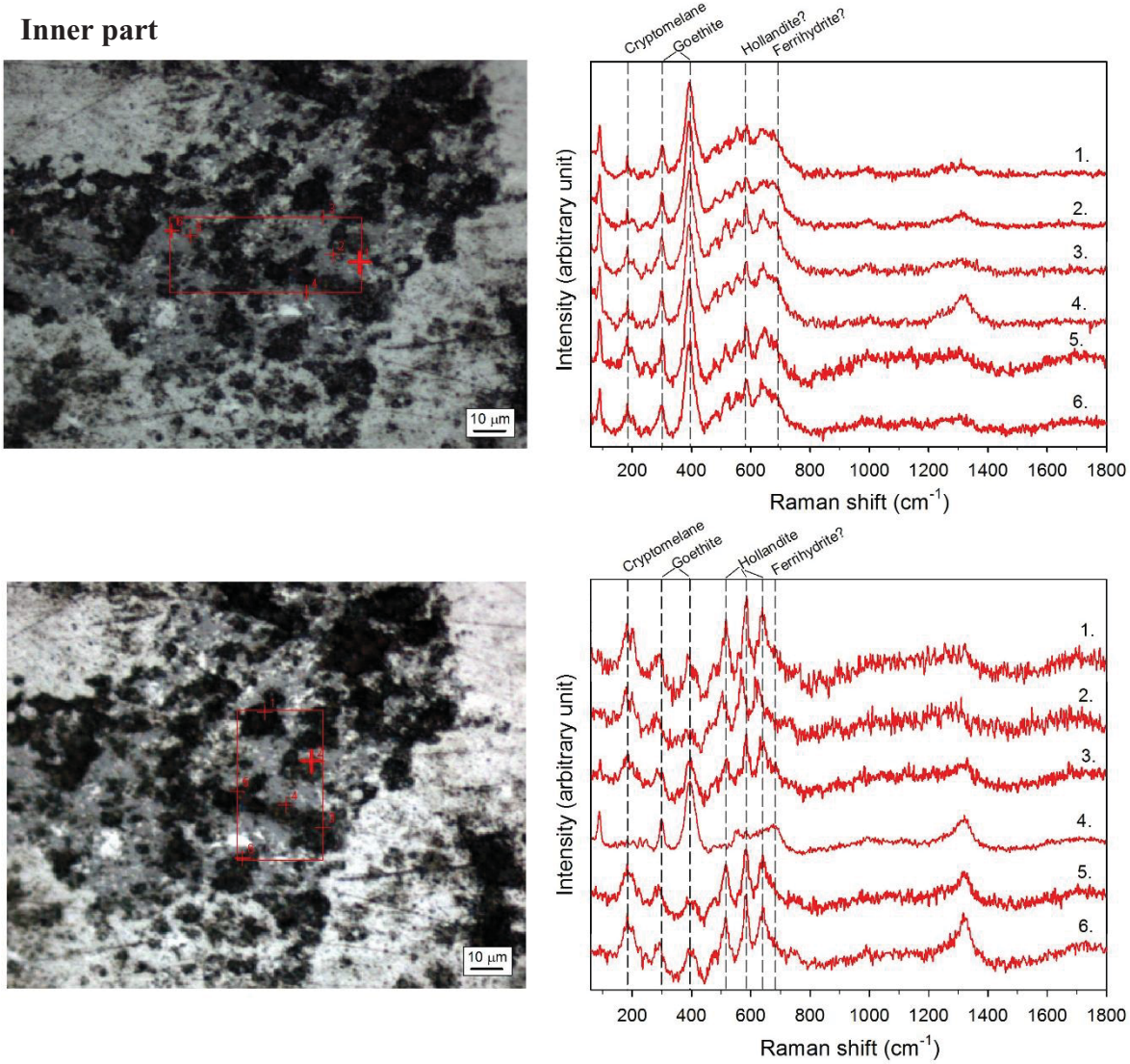

Figure 7.: Map indicated on the composite picture by yellow box marked by number 1.

The leftmost part of the spherical (bubble-like) structure consists of goethite (ferrihydrite) and little particles of Mn oxides (hollandite, cryptomelane in various amount), however hollandite is the dominant in the dark spots.

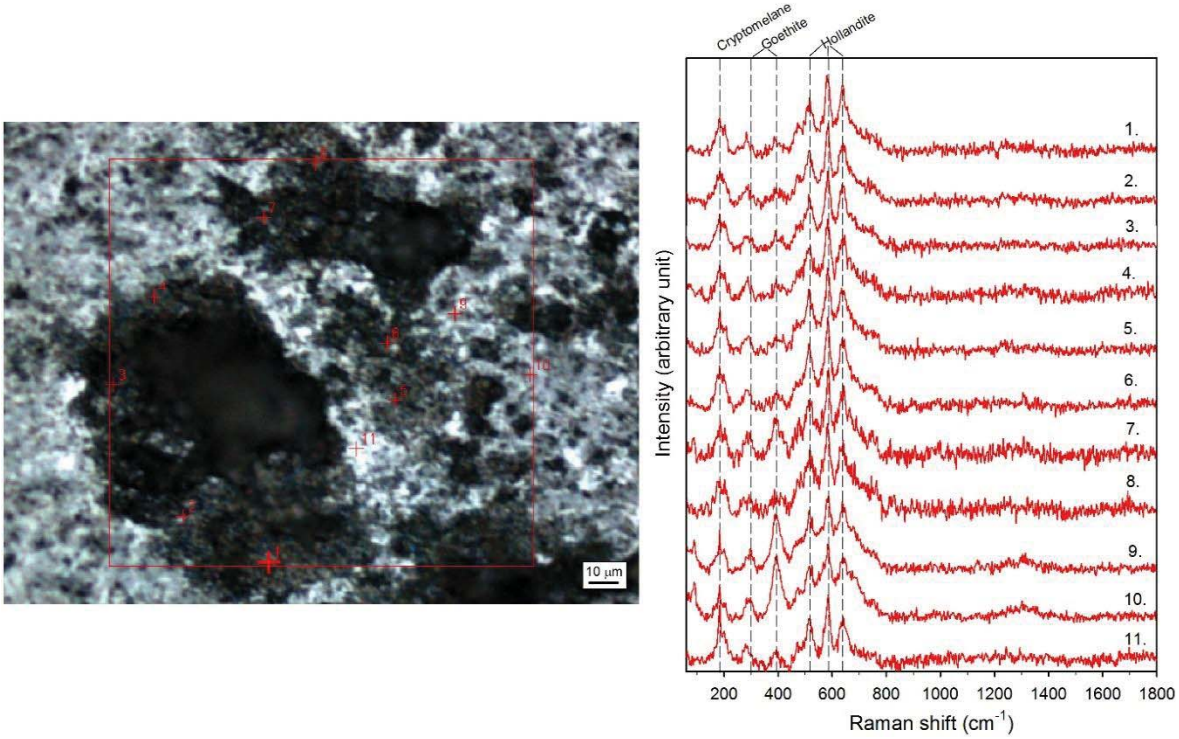

Figure 8.: Map indicated on the composite picture by yellow box marked by number 8. The dark spots have porous hollandite (cryptomelane, goethite) rims indicated on (Fig. 8. 1-4, 7, 8) while in the matrix among dark spots the Mn oxide has higher cryptomelane content (Fig 8. 5, 6, 9-11).

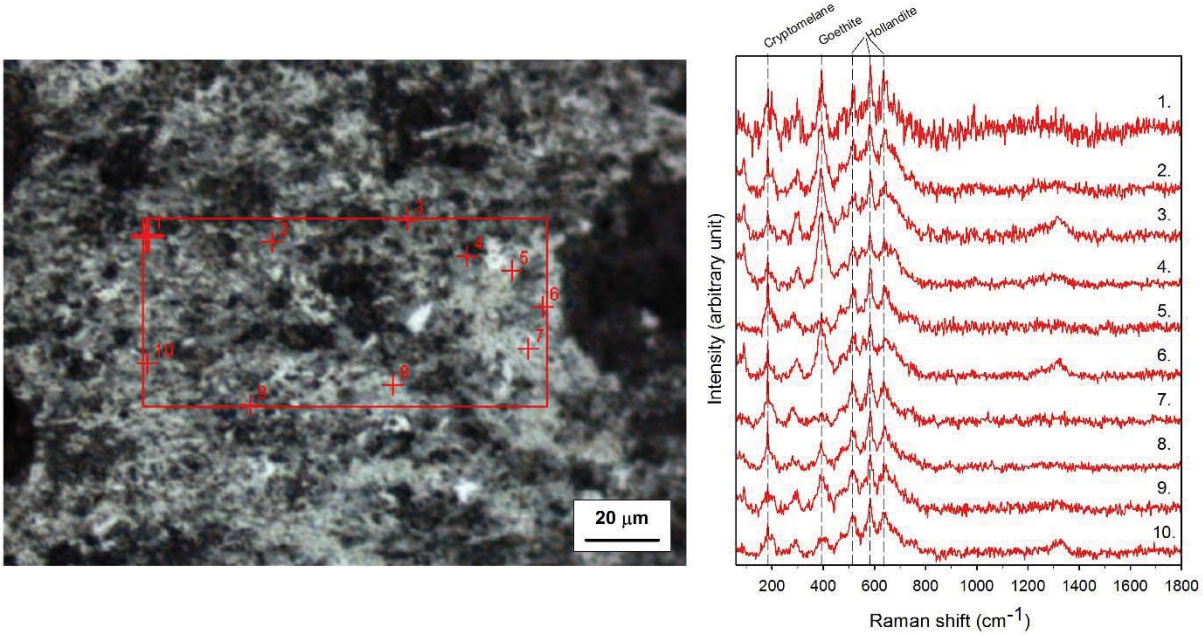

Figure 9.: Map indicated on the composite picture by yellow box marked by number 15.

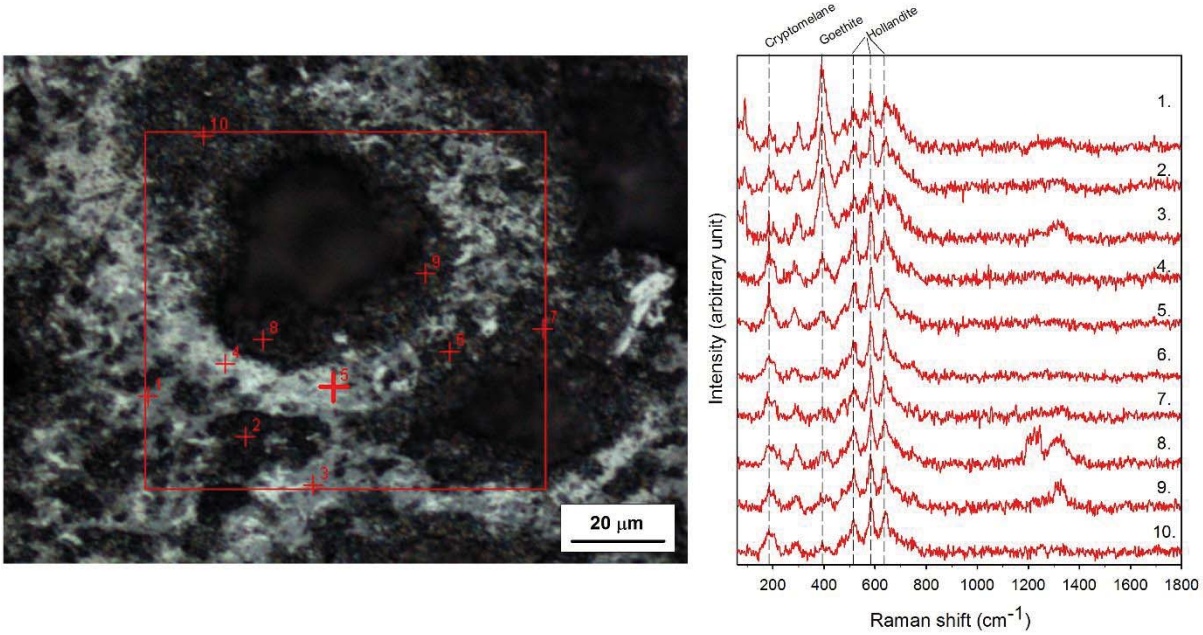

Figure 10.: Map indicated on the composite picture by yellow box marked by number 20.

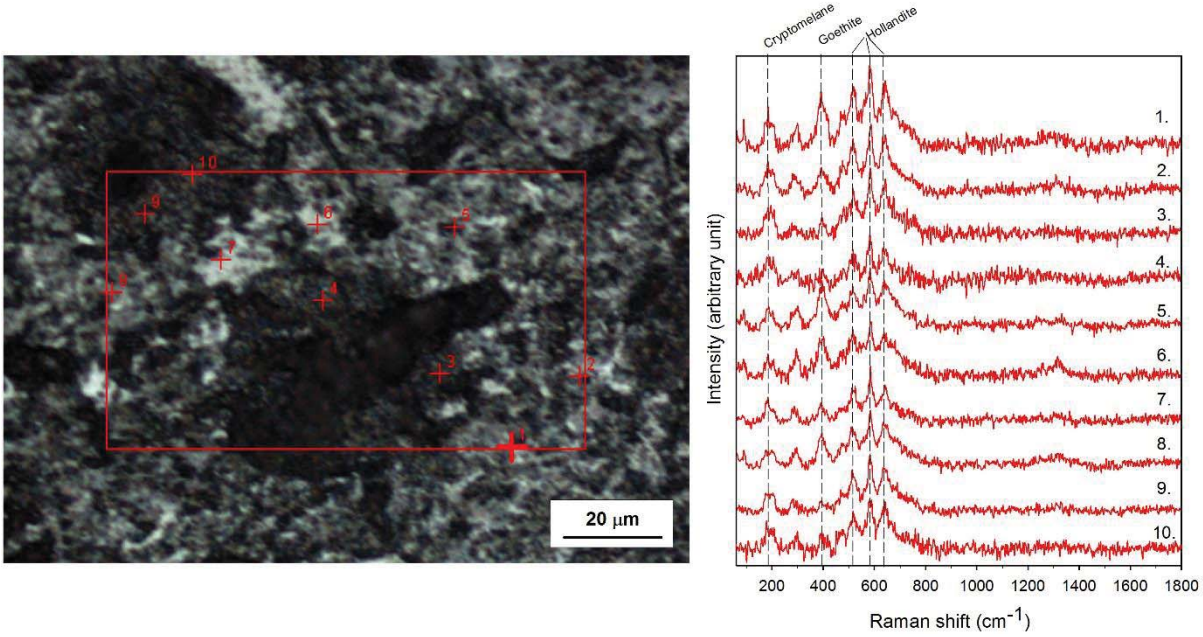

Figure 11.: Map indicated on the composite picture by yellow box marked by number 25.

Comparing the mineral phases and distribution in the outer, inner and rim area of the measured spherical (bubble-like) structure, they are similar.

SI 15-Table A. Summary of formation of Mn-1 ore bed according to structural hierarchy

Structural hierarchy	Fe and Mn in (Mn-1) from the aspect of Fe	Mn oxide ore in Fe oxide system			
		Accumulation of sediment	**Interpretation**	**Origin of rock**	**Interpretation**
	Sediment/rock	Sediment composition: Ferrihydrite+silica, lepidocrocite+silica, initial Mn-oxide-hydroxide referring to start of enzymatic microbial Mn oxidation (δMnO_2, manganite-MnOOH, todorokite, birnessite), organic matter +land derived debris? or syngenetic „clast-like" particles (quartz, feldspar, mica, apatite, carbonate, volcanic debris)	**Primary formation conditions - palaeoenvironment** Low T aquatic system, normal marine salinity, neutrophylic (6-8), suboxic (Eh: +0.3 V) conditions, with dissolved oxygen through dysoxic (DO 0.2–2.0 mL/L), to suboxic (DO 0–0.2 mL/L) conditions. Occasionally reached obligatory oxic conditions (Eh: +0.4-+1.0 V), aerobic system with dissolved oxygen, DO > 2 mL/L) Fe-oxide-hydroxide,Mn-oxide-hydroxide, C_{org}, rare debris **microbial - Step 1. (chemolithoautotrophic cycle I.)** --- **Evidences** filamentous with an inner pearl-necklace-like texture; micromorphology, type of FeOB metabolism; giving a few tens of µm-scale lamination, MMPSS*, series of Fe-rich biomats, and Mn-lamination	Mn oxide-silicate ore embedded in Fe oxide-silica (jasper), Mn-1 bed	**Burial + early diagenesis (lithification) Stabilization of minerals in oxic-suboxic conditions** Cell + EPS material bind: Ca^{2+}, Mg^{2+}, Na^{+}, K^{+}, P, S2-, Si, Co, Zn, Ba, REE (bioessential elements…) liberalization on decay (CO_3^{2-}) (PO_4^{2-}) (SiO_4^{4-}) (SO_4^{2-}) (OH^{-}) etc.…taking part in diagenetic mineralization **FeOB system stabilization via diagenesis** **hematite and goethite forms accompanied by silica seggregation (cyanobacteria also bind silica-stress and radiation prevention)** *Remnants of syngenetic phase (Initial enzymatic microbial)* Ferrihydrite, lepidocrocite occur Fe oxide-hydroxide + silica →aegirine (no CL) **aegirine** also feldspars (albite, orthoclase) Fe oxide-hydroxide + silica →celadonite mica, clay **seggregated silica also forms quartz (jasper, jaspilite-nanopigments of Fe oxide)** Transitional minerals between Fe and Mn phases: hollandite, jacobsite **MnOB system stabilization via diagenesis influenced by the seggregated silica** **braunite, serandite, hollandite** (The occurrance of braunite as main phase refer to Mn oxidation on Fe oxide active surface catalyses, which refer to only suboxic conditions under Mn-1 formation, with
	Texture	Fine grained, filamentous microbial forms, coccoid forms double microbial lamination of ore forming microbes (Fe, Mn)		Double lamination (a few tens of µm-scale Fe and Mn minerals) + preserved microbial biomat texture, fine grained **(aegirine* occurs in biolaminite as the probable diagenetic Fe biomat)** amygdalites (as diagenetic formations)	
	Matrix main complex mineralogy (also accompanying minerals are important) authigenic minerals	Mn-oxide-hydroxide (δMnO_2, manganite-MnOOH, todorokite, birnessite, clay minerals, among them celadonite (Fe-mica), C_{org}, rare debris (K-feldspar, quartz, mica, apatite, carbonate, volcanic debris, etc.)		**Mn minerals:** *Remnants of syngenetic phase (Initial enzymatic microbial)* Vernadite $(Mn^{4+}Fe^{3+}CaNa)(OH)_2*nH_2O$ Todorokite $Na_{0.2}Ca_{0.05}K_{0.02}Mn^{4+}{}_4Mn^{3+}{}_2O_{12}•3(H_2O)$ Birnessit $Na_{0.7}Ca_{0.3}(Mn^{3+}\ Mn^{4+})_7O_{14}.2.8H_2O$ Manganite $Mn^{3+}OOH$ ***Main Mn ore mineral phase (oxide-silicate)(diagenetic)*** **Braunite ($Mn^{2+}Mn^{3+}{}_6SiO_{12}$)** Serandite $NaMn^{2+}{}_{1.5}Ca_{0.5}Si_3O_8(OH)$ hollandite $Ba_{0.8}Pb_{0.2}Na_{0.1}Mn^{4+}{}_{6.1}Fe^{3+}{}_{1.3}Mn^{2+}{}_{0.5}Al_{0.2}Si_{0.1}O_{16}$ *Further diagenetic products* Pyrolusite ($Mn^{4+}O_2$) Ramsdellite ($Mn^{4+}O_2$) Hausmannite $Mn^{3+}{}_3O_4$ Cryptomelane ($\mathbf{K}Mn^{4+}{}_6Mn^{2+}{}_2O_{16}$) Manjiroite $\mathbf{Na}(Mn^{4+}{}_7Mn^{3+})O_{16}$	

				Romanéchite (psilomelane) [(**Ba**,H_2O,Mn_5O_{10}, **Ba**(Mn^{4+}, Mn^{3+})O_{10}.1.4H_2O)] *Can be interpreted as transitional form between Mn and Fe oxide* Jacobsite $Mn^{2+}_{0.6}Fe^{2+}_{0.3}Mg_{0.1}Fe^{3+}_{1.5}Mn^{3+}_{0.5}O_4$ *Carbonates* Ca-rhodochrosite ($MnCO_3$) *(Mn^{4+}→Mn^{2+})* *$CH_2O + 8H^+ + 4MnO_2 \rightarrow Mn^{2+} + CO_2 + 11H_2O$* *$Mn^{2+} + CO_2 + H_2O \rightarrow MnCO_3 + 2H^+$* (early diagenetic sporadic heterotroph microbial mineralization) **Other minerals:** Orthoclase $KAlSi_3O_8$ Albite $NaAlSi_3O_8$ Muscovite $KAl_3Si_3O_{10}(OH)_{1.8}F_{0.2}$ Chlorite $Mg_{3.75}Fe^{2+}_{1.25}Si_3Al_2O_{10}(OH)_8$ Chamosite (Fe-mica –chlorite type) Kaolinite/dickite $Al_2Si_2O_5(OH)_4$ Cancrinite $(NaCa..)_8(Al_6Si_6O_{24})(CO_3,SO_4)_2.2H_2O$ Quartz (SiO_2) Apatite [$(Ca_{10}(PO_4)_6(OH, F, Cl)_2$] Barite $Ba(SO_4)$ Dolomite $CaMg(CO_3)_2$ Strontianite $Sr(CO_3)$ Johannite $Cu(UO_2)_2(SO_4)_2(OH)_2$ $8H_2O$ Organic material	obligatory oxic intervals, when enzymatic Mn oxidation started.) *Remnants of syngenetic phase (Initial enzymatic microbial)* todorokite, birnessite, manganite **Stable Mn oxide-hydroxides referring the start of initial enzymatic Mn oxidation, which composition is influenced by the liberalized cations:** pyrolusite, ramsdellite, cryptomelane, manjiroite, romanéchite (psilomelane), hausmannite Ca-rhodochrosite (early diagenetic sporadic heterotroph microbial mineralization) **Others:** apatite (Ca-phosphate) carbonates (dolomite, ankerite, strontianite) cancrinite (silicate, carbonate, sulfate) sulfate (baryte)- refer to less oxic conditions (together with hematite) + remnants of variable organic matter Pyrite FeS_2 (pyritized biomats in sulfate reduction zone - diagenetic) Oxic (Eh: +0.4-+1.0 V), aerobic system with dissolved oxygen, DO > 2 mL/L) suboxic metabolism (Eh: 0-+0.2 V; with dissolved oxygen through dysoxic (DO 0.2–2.0 mL/L), to suboxic (DO 0–0.2 mL/L) conditions. pH: 6-8 – neutral, slightly alkaline --- **Evidences** **Mineral assemblage** **Fine lamination (a few tens of µm-scale) of variable diagenetic fine grained mineral couples (diagenesis of Fe and Mn microbial system) and other variable products of diagenesis (local Eh-pH and other conditions (concentrations, etc.) determine quality of forming minerals)**
	Micro-mineralogy (authigenic minerals) chosen Fe minerals	Fe-bearing minerals: Ferrihydrite - lepidocrosccite in microbial texture (+silica) **Authigenic mineralization**		**Fe-bearing minerals**: *Remnants of syngenetic phase (Initial enzymatic microbial)* Ferrihydrite (FeOOH) Lepidocrocite $Fe^{3+}O(OH)$ ***Main Fe ore mineral phase (diagenetic)*** **Hematite** (Fe_2O_3) Goethite FeOOH	

				Can be interpreted as transitional form between Mn and Fe oxide Jacobsite $Mn^{2+}_{0.6}Fe^{2+}_{0.3}Mg_{0.1}Fe^{3+}_{1.5}Mn^{3+}_{0.5}O_4$ Pyrite FeS_2 (pyritized biomats in sulfate reduction zone- diagenetic) Celadonite $KMg_{0.8}Fe^{2+}_{0.2}Fe^{3+}_{0.9}Al_{0.1}Si_4O_{10}(OH)_2$ **Aegirine** $Ca_{0.75}Na_{0.25}Mg_{0.5}Fe^{2+}_{0.25}Fe^{3+}_{0.25}(Si_2O_6)$ **Preservation and authigenic mineralization**	**Stabilization and complex diagenesis (including cell and EPS decay) resulted mineral assemblage of variable quality, quantity and size dimensions in a very variable structural and textural distribution.** **Dense typical microbial texture (OM)(MMPT)** **amorphous organic matter remnants** **Most of diagenetic minerals (pyroxene, feldspar, quartz) have no CL. Diagenetic minerals follow the microbial texture (biomats)(EPS)(compulsive shape), diagenetic seggregation forms, and can grow as large as some mm-scale, e.g. aegirine.** **These can cause a tricky situation looking as land derived debris but they are mainly diagenetic minerals.** **Synsediment tectonic movements – destroy slightly lithified biomats forming fragments** **Or** **the previous model exists and older deposits were eroded and resedimented. but no field experiences support that scenario.** **Diagenetic cycle (I)**
	Microbial mediation (variable organic matter molecules) Atom, ion chemistry	Chemolithoautotrophic FeOB microbial mediation (Fe(II) $6Fe^{2+} + 0.5O_2 + CO_2 + 16H_2O \rightarrow CH_2O + 6Fe(OH)_3 + 12\ H^+$			
	Isotopes (bulk)	no data		no data	
		Accumulation of sediment		**Origin of rock**	
Time →					

*: diagenetic aegirine – references are in good agreement with the recent case, also interpret the absence of smectite, and evaporitic conditions also can be raised

What we see in the deposit is the result of complex diagenetic processes, mainly diagenetic minerals what include the decomposition and mineralization of cell (Fe and Mn bacteria, cyanobacteria and other types, etc.) and EPS (extracellular polymeric substance) material

SI 15-Table B. Summary of formation of Mn-2-3 ore beds according to structural hierarchy

Structural hierarchy	Fe and Mn in (Mn-2-3) from the aspect of Fe	Mn oxide ore in Fe oxide system			
		Accumulation of sediment	**Interpretation**	**Origin of rock**	**Interpretation**
	Sediment/rock	Sediment composition: Ferrihydrite+silica, lepidocrocite+silica, initial Mn-oxide-hydroxide referring to start of enzymatic microbial Mn oxidation (δMnO_2, manganite-MnOOH, todorokite, birnessite), organic matter +land derived debris? or syngenetic „clast-like" particles (quartz, feldspar, mica, apatite, carbonate, volcanic debris)	**Primary formation conditions - palaeoenvironment** Low T aquatic system, normal marine salinity, neutrophylic (6-8), suboxic (Eh: +0.3 V) conditions, with dissolved oxygen through dysoxic (DO 0.2–2.0 mL/L), to suboxic (DO 0–0.2 mL/L) conditions. Occasionally reached obligatory oxic conditions (Eh: +0.4-+1.0 V), aerobic system with dissolved oxygen, DO > 2 mL/L) Fe-oxide-hydroxide,Mn-oxide-hydroxide, C_{org}, rare debris **microbial - Step 1. (chemolithoautotrophic cycle I.)** --- **Evidences** filamentous with an inner pearl-necklace-like texture; micromorphology, type of FeOB metabolism; giving a few tens of µm-scale lamination, MMPSS*, series of Fe-rich biomats, and Mn-lamination	Mn oxide-silicate ore embedded in Fe oxide-silica (jasper), Mn-1 bed	**Burial + early diagenesis (lithification) Stabilization of minerals in oxic-suboxic conditions** Cell + EPS material bind: Ca^{2+}, Mg^{2+}, Na^{+}, K^{+}, P, S2-, Si, Co, Zn, Ba, REE (bioessential elements…) liberalization on decay (CO_3^{2-}) (PO_4^{2-}) (SiO_4^{4-}) (SO_4^{2-}) (OH^{-}) etc….taking part in diagenetic mineralization **FeOB system stabilization via diagenesis** **hematite and goethite forms accompanied by silica seggregation (cyanobacteria also bind silica-stress and radiation prevention)** *Remnants of syngenetic phase (Initial enzymatic microbial)* Ferrihydrite, lepidocrocite occur Fe oxide-hydroxide + silica →aegirine (no CL) **aegirine** also feldspars (albite, orthoclase) Fe oxide-hydroxide + silica →celadonite mica, clay **seggregated silica also forms quartz (jasper, jaspilite-nanopigments of Fe oxide)** Transitional minerals between Fe and Mn phases: hollandite, jacobsite **MnOB system stabilization via diagenesis influenced by the seggregated silica** **braunite, serandite, hollandite** (The occurrance of braunite as main phase refer to Mn oxidation on Fe oxide active
	Texture	Fine grained, filamentous microbial forms, coccoid forms double microbial lamination of ore forming microbes (Fe, Mn)		Double lamination (a few tens of µm-scale Fe and Mn minerals) + preserved microbial biomat texture, fine grained **(aegirine* occurs in biolaminite as the probable diagenetic Fe biomat)** amygdalites (as diagenetic formations)	
	Matrix main complex mineralogy (also accompanying minerals are important) authigenic minerals	Mn-oxide-hydroxide (δMnO_2, manganite-MnOOH, todorokite, birnessite, clay minerals, among them celadonite (Fe-mica), C_{org}, rare debris (K-feldspar, quartz, mica, apatite, carbonate, volcanic debris, etc.)		**Mn minerals:** *Remnants of syngenetic phase (Initial enzymatic microbial)* Vernadite ($Mn^{4+}Fe^{3+}CaNa)(OH)_2*nH_2O$ Todorokite $Na_{0.2}Ca_{0.05}K_{0.02}Mn^{4+}{}_4Mn^{3+}{}_2O_{12}•3(H_2O)$ Birnessit $Na_{0.7}Ca_{0.3}(Mn^{3+}\ Mn^{4+})_7O_{14}.2.8H_2O$ Manganite $Mn^{3+}OOH$ ***Main Mn ore mineral phase (oxide-silicate)(diagenetic)*** **Braunite ($Mn^{2+}Mn^{3+}{}_6SiO_{12}$)** Serandite $NaMn^{2+}{}_{1.5}Ca_{0.5}Si_3O_8(OH)$ hollandite $Ba_{0.8}Pb_{0.2}Na_{0.1}Mn^{4+}{}_{6.1}Fe^{3+}{}_{1.3}Mn^{2+}{}_{0.5}Al_{0.2}Si_{0.1}O_{16}$ *Further diagenetic products* Pyrolusite ($Mn^{4+}O_2$) Ramsdellite ($Mn^{4+}O_2$) Hausmannite $Mn^{3+}{}_3O_4$	

				Cryptomelane (**K**$Mn^{4+}_6Mn^{2+}_2O_{16}$) Manjiroite **Na**($Mn^{4+}_7Mn^{3+}$)O_{16} Romanéchite (psilomelane) [(**Ba**,H_2O,Mn_5O_{10}, **Ba**(Mn^{4+}, Mn^{3+})O_{10}.1.4H_2O)] *Can be interpreted as transitional form between Mn and Fe oxide* Jacobsite $Mn^{2+}_{0.6}Fe^{2+}_{0.3}Mg_{0.1}Fe^{3+}_{1.5}Mn^{3+}_{0.5}O_4$ *Carbonates* Ca-rhodochrosite ($MnCO_3$) *(Mn^{4+}→Mn^{2+})* *$CH_2O + 8H^+ + 4MnO_2 \rightarrow Mn^{2+} + CO_2 + 11H_2O$* *$Mn^{2+} + CO_2 + H_2O \rightarrow MnCO_3 + 2H^+$* (early diagenetic sporadic heterotroph microbial mineralization) **Other minerals:** Orthoclase $KAlSi_3O_8$ Albite $NaAlSi_3O_8$ Muscovite $KAl_3Si_3O_{10}(OH)_{1.8}F_{0.2}$ Chlorite $Mg_{3.75}Fe^{2+}_{1.25}Si_3Al_2O_{10}(OH)_8$ Chamosite (Fe-mica –chlorite type) Kaolinite/dickite $Al_2Si_2O_5(OH)_4$ Cancrinite $(NaCa..)_8(Al_6Si_6O_{24})(CO_3,SO_4)_2.2H_2O$ Quartz (SiO_2) Apatite [$(Ca_{10}(PO_4)_6(OH, F, Cl)_2$] Barite $Ba(SO_4)$ Dolomite $CaMg(CO_3)_2$ Strontianite $Sr(CO_3)$ Johannite $Cu(UO_2)_2(SO_4)_2(OH)_2$ 8H_2O Organic material	surface catalyses, which refer to only suboxic conditions under Mn-1 formation, with obligatory oxic intervals, when enzymatic Mn oxidation started.) *Remnants of syngenetic phase (Initial enzymatic microbial)* todorokite, birnessite, manganite **Stable Mn oxide-hydroxides referring the start of initial enzymatic Mn oxidation, which composition is influenced by the liberalized cations:** pyrolusite, ramsdellite, cryptomelane, manjiroite, romanéchite (psilomelane), hausmannite Ca-rhodochrosite (early diagenetic sporadic heterotroph microbial mineralization) **Others:** apatite (Ca-phosphate) carbonates (dolomite, ankerite, strontianite) cancrinite (silicate, carbonate, sulfate) sulfate (baryte)- refer to less oxic conditions (together with hematite) + remnants of variable organic matter Pyrite FeS_2 (pyritized biomats in sulfate reduction zone - diagenetic) Oxic (Eh: +0.4-+1.0 V), aerobic system with dissolved oxygen, DO > 2 mL/L) suboxic metabolism (Eh: 0-+0.2 V; with dissolved oxygen through dysoxic (DO 0.2–2.0 mL/L), to suboxic (DO 0–0.2 mL/L) conditions. pH: 6-8 – neutral, slightly alkaline --- **Evidences** **Mineral assemblage** **Fine lamination (a few tens of µm-scale) of variable diagenetic fine grained mineral couples (diagenesis of Fe and Mn microbial system) and other variable products of diagenesis (local Eh-pH and other**
	Micro-mineralogy (authigenic minerals) chosen Fe minerals	Fe-bearing minerals: Ferrihydrite - lepidocrosccite in microbial texture (+silica) **Authigenic mineralization**		**Fe-bearing minerals**: *Remnants of syngenetic phase (Initial enzymatic microbial)* Ferrihydrite (FeOOH) Lepidocrocite $Fe^{3+}O(OH)$ ***Main Fe ore mineral phase (diagenetic)***	

				Hematite (Fe_2O_3) Goethite FeOOH *Can be interpreted as transitional form between Mn and Fe oxide* Jacobsite $Mn^{2+}_{0.6}Fe^{2+}_{0.3}Mg_{0.1}Fe^{3+}_{1.5}Mn^{3+}_{0.5}O_4$ Pyrite FeS_2 (pyritized biomats in sulfate reduction zone- diagenetic) Celadonite $KMg_{0.8}Fe^{2+}_{0.2}Fe^{3+}_{0.9}Al_{0.1}Si_4O_{10}(OH)_2$ **Aegirine** $Ca_{0.75}Na_{0.25}Mg_{0.5}Fe^{2+}_{0.25}Fe^{3+}_{0.25}(Si_2O_6)$ **Preservation and authigenic mineralization**	**conditions (concentrations, etc.) determine quality of forming minerals)** **Stabilization and complex diagenesis (including cell and EPS decay) resulted mineral assemblage of variable quality, quantity and size dimensions in a very variable structural and textural distribution.** **Dense typical microbial texture (OM)(MMPT)** **amorphous organic matter remnants** **Most of diagenetic minerals (pyroxene, feldspar, quartz) have no CL. Diagenetic minerals follow the microbial texture (biomats)(EPS)(compulsive shape), diagenetic seggregation forms, and can grow as large as some mm-scale, e.g. aegirine.** **These can cause a tricky situation looking as land derived debris but they are mainly diagenetic minerals.** **Synsediment tectonic movements – destroy slightly lithified biomats forming fragments** **Or** **the previous model exists and older deposits were eroded and resedimented. but no field experiences support that scenario.** **Diagenetic cycle (I)**
	Microbial mediation (variable organic matter molecules) Atom, ion chemistry	Chemolithoautotrophic FeOB microbial mediation (Fe(II) $6Fe^{2+} + 0.5O_2 + CO_2 + 16H_2O \rightarrow CH_2O + 6Fe(OH)_3 + 12\ H^+$			
	Isotopes (bulk)	no data		no data	
		Accumulation of sediment		**Origin of rock**	
Time →					

What we see in the deposit is the result of complex diagenetic processes, mainly diagenetic minerals what include the decomposition and mineralization of cell (Fe and Mn bacteria, cyanobacteria and other types, etc.) and EPS (extracellular polymeric substance) material